

Numerical aspects of the application of smoothed point interpolation methods in computational geomechanics

Author:

Tootoonchi, Arash

Publication Date:

2019

DOI:

<https://doi.org/10.26190/unsworks/3639>

License:

<https://creativecommons.org/licenses/by-nc-nd/3.0/au/>

Link to license to see what you are allowed to do with this resource.

Downloaded from <http://hdl.handle.net/1959.4/61513> in <https://unsworks.unsw.edu.au> on 2024-05-03

**NUMERICAL ASPECTS OF THE APPLICATION OF
SMOOTHED POINT INTERPOLATION METHODS
IN COMPUTATIONAL GEOMECHANICS**

Arash Tootoonchi

BSc, MSc

A thesis submitted in fulfilment of the requirements for the degree of
DOCTOR OF PHILOSOPHY



School of Civil and Environmental Engineering

The University of New South Wales

Sydney, Australia

January 2019

COPYRIGHT STATEMENT

'I hereby grant the University of New South Wales or its agents the right to archive and to make available my thesis or dissertation in whole or part in the University libraries in all forms of media, now or here after known, subject to the provisions of the Copyright Act 1968. I retain all proprietary rights, such as patent rights. I also retain the right to use in future works (such as articles or books) all or part of this thesis or dissertation.

I also authorise University Microfilms to use the 350 words abstract of my thesis in Dissertation Abstract International (this is applicable to doctoral theses only).

I have either used no substantial portions of copyright material in my thesis or I have obtained permission to use copyright material; where permission has not been granted I have applied/will apply for a partial restriction of the digital copy of my thesis or dissertation.'

Signed ...Arash Tootoonchi.....

Date27/01/2019.....

AUTHENTICITY STATEMENT

'I certify that the Library deposit digital copy is a direct equivalent of the final officially approved version of my thesis. No emendation of content has occurred and if there are any minor variations in formatting, they are the result of the conversion to digital format.'

Signed ...Arash Tootoonchi.....

Date27/01/2019.....

ORIGINALITY STATEMENT

‘I hereby declare that this submission is my own work and to the best of my knowledge it contains no materials previously published or written by another person, or substantial proportions of material which have been accepted for the award of any other degree or diploma at UNSW or any other educational institution, except where due acknowledgement is made in the thesis. Any contribution made to the research by others, with whom I have worked at UNSW or elsewhere, is explicitly acknowledged in the thesis. I also declare that the intellectual content of this thesis is the product of my own work, except to the extent that assistance from others in the project's design and conception or in style, presentation and linguistic expression is acknowledged.’

Signed ...Arash Tootoonchi.....

Date27/01/2019.....

INCLUSION OF PUBLICATIONS STATEMENT

UNSW is supportive of candidates publishing their research results during their candidature as detailed in the UNSW Thesis Examination Procedure.

Publications can be used in their thesis in lieu of a Chapter if:

- The student contributed greater than 50% of the content in the publication and is the “primary author”, ie. the student was responsible primarily for the planning, execution and preparation of the work for publication
- The student has approval to include the publication in their thesis in lieu of a Chapter from their supervisor and Postgraduate Coordinator.
- The publication is not subject to any obligations or contractual agreements with a third party that would constrain its inclusion in the thesis

Please indicate whether this thesis contains published material or not.

- This thesis contains no publications, either published or submitted for publication (if this box is checked, you may delete all the material on page 2)*
- Some of the work described in this thesis has been published and it has been documented in the relevant Chapters with acknowledgement (if this box is checked, you may delete all the material on page 2)*
- This thesis has publications (either published or submitted for publication) incorporated into it in lieu of a chapter and the details are presented below*

CANDIDATE'S DECLARATION

I declare that:

- I have complied with the Thesis Examination Procedure
- where I have used a publication in lieu of a Chapter, the listed publication(s) below meet(s) the requirements to be included in the thesis.

Name	Signature	Date (dd/mm/yy)
Arash Tootoonchi		26/01/2019

Postgraduate Coordinator's Declaration (to be filled in where publications are used in lieu of Chapters)

I declare that:

- the information below is accurate
- where listed publication(s) have been used in lieu of Chapter(s), their use complies with the Thesis Examination Procedure
- the minimum requirements for the format of the thesis have been met.

PGC's Name	PGC's Signature	Date (dd/mm/yy)

Details of publication #1:					
<i>Full title:</i> A cell-based smoothed point interpolation method for flow-deformation analysis of saturated porous media					
<i>Authors:</i> Tootoonchi, A., A. Khoshghalb, G.R.Liu and N. Khalili					
<i>Journal or book name:</i> Computers and Geotechnics					
<i>Volume/page numbers:</i> 75: 159-173					
<i>Date accepted/ published:</i> 2016					
Status	Published	<input checked="" type="checkbox"/>	Accepted and In press	<input type="checkbox"/>	In progress (submitted)
The Candidate's Contribution to the Work					
Arash has been the principal investigator on his publication and has done the majority of the work.					
Location of the work in the thesis and/or how the work is incorporated in the thesis:					
This publication is the basis for Chapter 3 of the thesis.					
Primary Supervisor's Declaration					
I declare that:					
<ul style="list-style-type: none"> the information above is accurate this has been discussed with the PGC and it is agreed that this publication can be included in this thesis in lieu of a Chapter All of the co-authors of the publication have reviewed the above information and have agreed to its veracity by signing a 'Co-Author Authorisation' form. 					
<i>Supervisor's name</i> Arman Khoshghalb		<i>Supervisor's signature</i>		<i>Date (dd/mm/yy)</i> 25/01/2019	

Details of publication #2:					
<i>Full title:</i> A novel approach for application of smoothed point interpolation methods to axisymmetric problems in poroelasticity					
<i>Authors:</i> Tootoonchi, A., A. Khoshghalb and G.R.Liu					
<i>Journal or book name:</i> Computers and Geotechnics					
<i>Volume/page numbers:</i> 102: 39-52					
<i>Date accepted/ published:</i> 2018					
Status	Published	<input checked="" type="checkbox"/>	Accepted and In press	<input type="checkbox"/>	In progress (submitted)
The Candidate's Contribution to the Work					
Arash has been the principal investigator on his publication and has done the majority of the work.					
Location of the work in the thesis and/or how the work is incorporated in the thesis:					
This publication is the basis for Chapter 4 of the thesis					
Primary Supervisor's Declaration					
I declare that:					
<ul style="list-style-type: none"> the information above is accurate this has been discussed with the PGC and it is agreed that this publication can be included in this thesis in lieu of a Chapter All of the co-authors of the publication have reviewed the above information and have agreed to its veracity by signing a 'Co-Author Authorisation' form. 					
<i>Supervisor's name</i> Arman Khoshghalb		<i>Supervisor's signature</i>		<i>Date (dd/mm/yy)</i> 25/01/2019	

Details of publication #3:			
<i>Full title: A Smoothed Meshfree Method for Simulation of Frictional Embedded Discontinuities</i>			
<i>Authors: Khoshghalb, A. and Tootoonchi, A.</i>			
<i>Journal or book name: Tunnelling and Underground Space Technology</i>			
<i>Volume/page numbers: -</i>			
<i>Date accepted/ published:-</i>			
Status	<i>Published</i>	<input type="checkbox"/>	<i>Accepted and In press</i>
		<input type="checkbox"/>	<i>In progress (submitted)</i>
			<input checked="" type="checkbox"/>
The Candidate's Contribution to the Work			
Arash has been the principal investigator on his publication and has done the majority of the technical work.			
Location of the work in the thesis and/or how the work is incorporated in the thesis:			
This publication is part of the Chapter 6 of the thesis.			
Primary Supervisor's Declaration			
I declare that:			
<ul style="list-style-type: none"> • the information above is accurate • this has been discussed with the PGC and it is agreed that this publication can be included in this thesis in lieu of a Chapter • All of the co-authors of the publication have reviewed the above information and have agreed to its veracity by signing a 'Co-Author Authorisation' form. 			
<i>Supervisor's name</i> Arman Khoshghalb	<i>Supervisor's signature</i>	<i>Date (dd/mm/yy)</i> 25/01/2019	

Abstract

This study examines various numerical aspects of smoothed point interpolation methods (SPIM) in computational geomechanics. The extension of SPIM to flow-deformation analysis of saturated porous media is formulated. The singularity problem encountered when original SPIM formulation is applied to axisymmetric setting is addressed. The proposed SPIM formulation is thoroughly examined through the extensive error analysis performed for the set of benchmark numerical problems in terms of appropriate variables of interest. An unconditionally consistent stabilisation method is then formulated in SPIM framework to mitigate the adverse consequences arising from the violation of the well-known inf-sup condition. The proposed stabilisation method offers absolute stability regardless of the *a priori* chosen scalar value, commonly known as the stabilisation parameter. The proposed stabilisation method allows the use of equal-order linear interpolation functions for both primary variables. The robustness of the stabilised SPIM is shown by the numerical simulation of a number of linear and materially nonlinear problems in saturated porous media. Finally, a mesh-independent representation of SPIM has been developed for flow-deformation analysis of saturated porous media with embedded interfaces. The proposed formulation allows the violation of inner-continuity assumption within supporting domains by enhancing the standard interpolation functions with the physically appropriate enrichment functions. This method enables the attainment of accurate numerical solutions without appealing to time-consuming techniques such as successive re-meshing, leading to a more practical treatment of problems including weak or strong discontinuities. A numerical contact

algorithm is developed to enable the computation of the frictional contact forces stemming from the onset of the closure mode in the cracks. The presence of the fluid flow within the cracks is represented by inclusion of the fluid continuity equation. The proposed mesh-independent method is verified by a number of single-phase and two-phase problems which encompasses different aspects of the existing discontinuities.

Acknowledgement

There are many people I would like to mention and thank for a variety of reasons: I would like to express my deepest gratitude and appreciation to my supervisor Dr. Arman Khoshghalb for without his brilliant ideas, constant support and encouragement, I don't think I ever would have completed this work. He always did his best to find a quick moment to talk when it was needed and responded all my questions and queries so promptly. Arman, I appreciate every single advice and suggestion that you have provided me throughout this research.

The author wishes to express his sincere gratitude and appreciation to his co-supervisor, Professor Nasser Khalili, for his invaluable guidance, and friendly support during the course of this research.

I would also like to thank my research colleagues in the geotechnical engineering group who made my stay at UNSW much more enjoyable and memorable and my old friend in Iran, Aidin, who has always encouraged me to pursue my PhD degree despite difficulties I experienced during this research.

Lastly, my parents and my sister for the supports and the chances they've given me over the years.

I dedicate this thesis to my mother, Parivash, who has been my primary source of motivation for these years to succeed.

Arash Tootoonchi

January 2019

List of publications

The research work presented in this thesis has been performed at the School of Civil and Environmental Engineering at the University of New South Wales, Sydney, Australia; under the supervision of Dr Arman Khoshghalb from August 2014 to January 2019.

During the term of candidature, the following papers have been published from this research:

Journal papers:

- Tootoonchi, A., A. Khoshghalb, G.R.Liu and N. Khalili, *A cell-based smoothed point interpolation method for flow-deformation analysis of saturated porous media*. Computers and Geotechnics, 2016. **75**: p. 159-173.
- Tootoonchi, A., A. Khoshghalb and G.R.Liu, *A novel approach for application of smoothed point interpolation methods to axisymmetric problems in poroelasticity*. Computers and Geotechnics, 2018. **102**: p. 39-52
- Khoshghalb, A. and Tootoonchi, A., *A Smoothed Meshfree Method for Simulation of Frictional Embedded Discontinuities*. Tunnelling and Underground Space Technology, (submitted).

Conference papers:

- Tootoonchi, A., A. Khoshghalb, and N. Khalili, *Meshfree method analysis of Biot's consolidation using cell-based smoothed point interpolation method*. Applied Mechanics & Materials, 2016. 846.
- Tootoonchi, A., A. Khoshghalb, and N. Khalili, *A novel approach of fully smoothed point interpolation methods to axisymmetric problems in poroelasticity*, 16th European Congress on Computational Methods in Applied Sciences and Engineering, Crete, Greece, 2016.

Table of Contents

Abstract	vii
Acknowledgement.....	ix
List of publications.....	x
Table of Contents	xi
List of Figures	xv
List of Tables.....	xx
1 Introduction	1
1.1 Background.....	1
1.2 Problem Statement and research gaps	4
1.3 Objectives and layout of the thesis	9
2 Literature Review.....	13
2.1 Introduction.....	13
2.2 A brief review of meshfree methods.....	13
2.3 Application of MMs in geotechnical engineering	19
2.4 Stabilisation methods in computational geomechanics	25
2.5 Numerical analysis of porous media including interfaces.....	34
2.6 Conclusion	46
3 Application of cell-Based smoothed point interpolation methods in the flow-Deformation analysis of saturated porous media.....	48
3.1 Introduction.....	48
3.2 Governing equations	49
3.3 Constitutive modelling.....	51
3.4 Cell-based smoothed PIM/RPIM.....	52
3.4.1 Construction of shape functions	53
3.4.2 Node selection schemes.....	57
3.5 G Space theory and smoothing operation.....	58
3.5.1 G space theory	58
3.5.2 Smoothing gradient operation	60

3.5.3	Cell-based smoothed strains	61
3.6	Numerical model.....	64
3.6.1	Spatial discretisation.....	65
3.6.2	Temporal discretisation	69
3.7	Numerical examples	70
3.7.1	One-dimensional consolidation.....	71
3.7.2	Two-dimensional consolidation	79
3.7.3	One-dimensional hydraulic pulse test	85
3.8	Conclusions.....	89
4	A novel approach for application of smoothed point interpolation methods to axisymmetric problems in poroelasticity	91
4.1	Preface	91
4.2	Governing equations	92
4.3	Constitutive modelling.....	92
4.4	Variational statement	93
4.5	Domain discretisation and support node selection	95
4.5.1	Domain discretisation.....	95
4.5.2	Support node selection schemes.....	95
4.5.3	Nodal shape functions	95
4.5.4	Smoothed strains	96
4.6	Solution to the singularity problem	97
4.7	Discretisation in space	99
4.8	Discretisation in time	103
4.9	Numerical examples	103
4.9.1	Cryer's problem.....	103
4.9.2	De Leeuw's problem	109
4.9.3	The study of Noordbergum effect	113
4.10	Conclusion	118
5	A stabilized, low-order edge-based smoothed point interpolation method for numerical analyses in geomechanics	120
5.1	Preface	120
5.2	Notation	121
5.3	The smoothed mixed <i>Galerkin</i> method	122
5.3.1	Coupled flow-deformation governing equations.....	122

5.3.2	Constitutive modelling	123
5.3.3	Variational form of the standard mixed <i>Galerkin</i> method	124
5.3.4	Smoothing domains in ESFEM	125
5.3.5	Smoothing gradient operation	126
5.3.6	Generalised smoothed mixed <i>Galerkin</i> formulation	127
5.4	Matrix form of the generalised smoothed mixed <i>Galerkin</i> FEM	129
5.4.1	Creation of linear shape functions and approximated solutions.....	129
5.4.2	Computation of the property matrixes.....	130
5.4.3	Linearisation	133
5.5	Consistently stabilised mixed ESFEM	136
5.5.1	The inf–sup condition.....	137
5.5.2	Consistently stabilised smoothed <i>Galerkin</i> methods.....	137
5.5.3	Stabilisation parameter	142
5.5.4	Spatial and temporal discretisation of the proposed stabilisation method 143	
5.5.5	Computation of the smoothed Gepu and Gelu	145
5.6	Polynomial pressure projection method	152
5.7	Numerical Examples.....	156
5.7.1	One dimensional consolidation	156
5.7.2	Mandel’s problem.....	161
5.7.3	Bearing capacity of a strip footing	166
5.8	Conclusion	172
6	An Enriched smoothed point interpolation method for the flow-deformation analysis of saturated porous media with embedded interfaces	174
6.1	Preface	174
6.2	Governing equations of saturated porous media with interfaces.....	175
6.2.1	Weak forms	177
6.2.2	Fluid flow formulation within a strong discontinuity	180
6.3	Enriched SPIM for saturated porous media with interfaces	184
6.3.1	The signed distance function.....	186
6.3.2	<i>Heaviside</i> function.....	187
6.3.3	Ridge function	187
6.3.4	Domain discretisation.....	189
6.3.5	Supporting node selection schemes.....	189

6.3.6	Creation of standard shape functions	190
6.3.7	Computation of smoothed strain and pressure gradient in Enriched SPIM	190
6.4	Contact behaviour along interfaces.....	194
6.4.1	Contact conditions: the <i>Kuhn–Tucker</i> rule.....	195
6.4.2	Coulomb theory of frictional contact	197
6.4.3	The Enriched SPIM formation for contact modelling.....	202
6.5	The fully discretised Enriched cell-based SPIM formulation for saturated porous media with an embedded interface.....	208
6.6	Numerical verifications.....	213
6.6.1	Single-phase medium with an inclined interface subjected to compressive loading.....	214
6.6.2	Single-phase medium with the horizontal interface subjected to non-uniform compression.....	218
6.6.3	Multi-layered elastic foundation	223
6.6.4	Saturated porous rectangular block with vertical discontinuity	230
6.7	Conclusion	239
7	Conclusions and further work	241
7.1	Contributions and findings.....	242
7.1.1	Application of cell-based smoothed point interpolation methods in the flow-deformation analysis of saturated porous media	242
7.1.2	A novel approach for application of smoothed point interpolation methods to axisymmetric problems in poroelasticity.....	243
7.1.3	A stabilised, low-order smoothed point interpolation method for numerical analyses in geomechanics	244
7.1.4	An enriched smoothed point interpolation method for flow-deformation analysis of saturated porous media with embedded interfaces	246
7.2	Future research.....	247
	References	251

List of Figures

Figure 3.1. T-schemes used in this study to select the supporting nodes, (a) T4 scheme; (b) T2L scheme.	58
Figure 3.2. The schematic representation of smoothing domains in CSPIM and CSRPIIM methods.	62
Figure 3.3. A schematic representation of S_n and S_s for an arbitrary quadrature point of interest assuming a T4 node selection scheme.....	64
Figure 3.4. Schematic locations of the quadrature points used in this study for calculation of the shape functions.....	68
Figure 3.5. Schematic representation of the soil column and its associated smoothing domains for modelling one-dimensional consolidation problem.....	72
Figure 3.6. Numerical analysis of one dimensional consolidation problem: a) Change of the excess pore fluid pressure with time at three different points, and b) variation of surface settlement with time.....	73
Figure 3.7. Displacement error norms at dimensionless time $td = 0.1$ (a) and $td = 1.0$ (b) for one-dimensional consolidation problem.....	76
Figure 3.8. Pore fluid pressure error norms at dimensionless time $td = 0.1$ (a) and $td = 1.0$ (b) for one-dimensional consolidation problem.....	77
Figure 3.9. Energy error norms at dimensionless time $td = 0.1$ (a) and $td = 1.0$ (b) for one-dimensional consolidation problem.	77
Figure 3.10. Strain energy (kJ) versus time for one-dimensional consolidation problem using configuration number 3.	78
Figure 3.11. Representation of a two-dimensional consolidation problem and the background mesh (smoothing domains) used in the numerical analysis.	80
Figure 3.12. Dimensionless excess pore fluid pressure versus depth ratio under the centre of the loaded area at $td = 0.1$	81
Figure 3.13. Displacement error norms at dimensionless times $td = 0.1$ (a) and $td = 1.0$ (b) for two-dimensional consolidation problem.	83
Figure 3.14. Pore fluid pressure error norms at dimensionless times $td = 0.1$ (a) and $td = 1.0$ (b) for two-dimensional consolidation problem.....	84
Figure 3.15. Energy error norms at dimensionless times $td = 0.1$ (a) and $td = 1.0$ (b) for two-dimensional consolidation problem.	84
Figure 3.16. Geometry and background mesh assumed in one-dimensional hydraulic pulse simulation.	86
Figure 3.17. Variation of fluid pressure at $x = 4.6$ mm versus dimensionless time for one-dimensional hydraulic pulse test.....	87
Figure 3.18. Pressure error norms at dimensionless times $td = 0.1$ (a) and $td = 1.0$ (b) for one-	89

Figure 4.1. A schematic illustration of the Gauss points causing singularity problem in the computation of the property matrices.....98

Figure 4.2. Gauss points located on the edges and over a smoothing domain to evaluate the local property matrices..... 100

Figure 4.3. (a) The schematic representation of Cryer’s problem, (b) the background mesh used in the analysis 104

Figure 4.4.The contour of excess pore pressure for Cryer’s problem (case 1) at dimensionless time 0.0529..... 105

Figure 4.5. Solutions to the Cryer’s problem; (a) The distribution of dimensionless excess pore pressure versus dimensionless surface displacement; (b) the variation of dimensionless surface displacement with respect to the square root of the dimensionless time..... 106

Figure 4.6. Displacement error norms for Cryer’s problem at dimensionless time (a) $td=0.1$; and (b) $td=1.0$ 108

Figure 4.7. Excess pore pressure norms for Cryer’s problem at dimensionless time (a) $td=0.1$; and (b) $td=1.0$ 109

Figure 4.8. A schematic representation of (a) the section and (b) the plan view of the cylinder relevant to De Leeuw’s problem..... 110

Figure 4.9. The mesh configuration adopted for the numerical solution of the De Leeuw’s problem..... 110

Figure 4.10. Variation of the dimensionless excess pore pressure versus dimensionless radius at different dimensionless times..... 111

Figure 4.11. Displacement error norms for De Leeuw’s problem at dimensionless time (a) $td = 0.1$; and (b) $td = 1.0$ 112

Figure 4.12. Pressure error norms for De Leeuw’s problem at dimensionless time (a) $td = 0.1$; and (b) $td = 1.0$ 113

Figure 4.13.(a) Illustration of the three-layered medium and its corresponding boundary conditions employed for the numerical simulation of the Noordbergum effect, and (b) representation of a portion ($0m \leq z \leq 10m$, $0m \leq r \leq 110m$) of the background mesh adopted in the study of the Noordbergum effect..... 115

Figure 4.14. The variation in the hydraulic head versus time for the Noordbergum problem. 117

Figure 4.15. The surface and radial displacements at $z = 10m$ for the Noordbergum problem. 118

Figure 5.1. A mesh composed of linear triangular elements and its corresponding smoothing domains. An interior smoothing domain Ω_{ks} corresponding to edge k of the background mesh, and a boundary smoothing domain Ω_{ms} corresponding to edge m of the background mesh are highlighted. 126

Figure 5.2. A schematic representation of (a) the soil column with its assigned boundary conditions (not to scale), and (b) the discretisation used for the numerical analyses. 157

Figure 5.3. A pressure profile, along the height of the soil column, presented with the stabilised ESFEM proposed in this study, the standard ESFEM and the stabilised FEM obtained with the polynomial pressure projection method. 159

Figure 5.4. The contours of the approximated pressure solutions (kPa) for three elements on the top of the soil column obtained by (a) stabilised ES-FEM and (b) standard ES-FEM after three initially subsequent time steps. 161

Figure 5.5. (a) a schematic (not to scale) representation of the geometry of Mandel’s problem (b) the discretisation used for modelling a quarter of the domain. 163

Figure 5.6. The variation of the dimensionless excess pore pressure along the dimensionless length of the soil medium at dimensionless time $t_d = 1 \times 10^{-5}$ for (a) standard and stabilised FEM and (b) for standard ES-FEM and proposed method for the stabilisation of ESFEM. 164

Figure 5.7. The contours of dimensionless pressure distribution after the first time step of $\Delta t_0 = 0.01$ sec for (a) standard ESFEM, and (b) stabilised ESFEM 165

Figure 5.8. (a) The geometry of the strip footing (not to scale) and the saturated porous medium used to estimate the collapse load and (b) the discretisation adopted for the numerical solution. 168

Figure 5.9. Pressure variations along the axis of symmetry beneath the strip footing at the dimensionless time $t_v = 5 \times 10^{-8}$, obtained by (a) standard and stabilised FEM and (b) standard ESFEM and proposed stabilised ESFEM. 170

Figure 5.10. Vertical load variations with respect to vertical displacements just below the strip footing, plotted for (a) the standard and stabilised FEM and (b) the standard ESFEM and the stabilised ESFEM using the method proposed in this study. 171

Figure 5.11. Pressure contours, at the last convergent step, obtained using (a) the proposed stabilised ESFEM at the dimensionless time $t_d = 5.64 \times 10^{-6}$ and (b) the standard ESFEM at the dimensionless time $t_d = 5.4 \times 10^{-6}$ 172

Figure 6.1. A schematic representation of a saturated porous medium Ω with internal boundary Γ_d 176

Figure 6.2. A schematic representation of the geometry and the corresponding local coordinate system in the cavity 183

Figure 6.3. A signed distance function applied to quantify the position of a node with respect to the interface 187

Figure 6.4. Schematic representation of the ridge function to reproduce a weak discontinuity 189

Figure 6.5. A supporting domain cut by an interface and its associated Gauss points used in the numerical integrations 192

Figure 6.6. Schematic representation of two bodies in contact in association with gap functions in normal and transversal directions with the constrained condition [322] .. 196

Figure 6.7. A sliding slave body with respect to a master body undergoing a relative tangential displacement[322] 197

Figure 6.8. A schematic representation of the partitioning of the contact interface and the relevant Gauss points on the contact surface used for the numerical integration. ..207

Figure 6.9. (a) A schematic representation of the unit square geometry with a frictional interface. (b) The discretization used for the computations [261].215

Figure 6.10. The contours of the horizontal displacement associated with the deformed medium with an inclined interface subjected to compressive loading when $\mu < \tan \theta$, slipping state for (a) the Enriched CSRPI-M-T2L of this study, and (b) the numerical result presented in [330].216

Figure 6.11. The contours of the horizontal displacement associated with the deformed medium with an inclined interface subjected to the compressive loading when $\mu > \tan \theta$, stick condition for (a) the Enriched CSRPI-M-T2L of this study and (b) the numerical result presented in [330].217

Figure 6.12. (a) A unit squared medium compressively loaded and sheared at the top edge and fixed at the bottom edge. (b) The underlying discretisation used in this study.219

Figure 6.13. The profile of normal contact stress (a) and the variation of tangential sliding with respect to the interfacial length for the case where the frictional coefficient is $\mu = 0.1$, which corresponds to the slipping condition.220

Figure 6.14. The profile of normal contact stress (a) and the variation of tangential sliding with respect to the interfacial length for the case where the frictional coefficient is taken as $\mu = 0.4$, which corresponds to the stick and slip conditions.220

Figure 6.15. The horizontal displacement contours on the deformed medium of a unit square subjected to non-uniform compression with the frictional coefficient (a) $\mu = 0.1$ and (b) $\mu = 0.4$222

Figure 6.16. The representation of the multi-layered saturated porous medium with interfacial geometries, along with the corresponding boundary conditions [61].223

Figure 6.17. The triangulation adopted for the proposed Enriched CSPIM/CSRPI-M for the simulation of the multi-layered saturated porous medium, together with the coordinates of the nodes of interest for the examination of numerical results.224

Figure 6.18. The variation of excess pore water pressure with time at nodes P1 and P2.226

Figure 6.19. The variation of vertical displacement with respect to time at nodes P1 and P2.227

Figure 6.20. The excess pore pressure contours obtained by (a) FEM and (b) CSRPI-M-T2L at $t = 20.47$ sec.228

Figure 6.21. The displacement contours obtained by (a) FEM and (b) CSRPI-M-T2L at time $t = 20.47$ sec.229

Figure 6.22. (a) Geometry of the discontinuous saturated porous block [65] and (b) the domain discretisation used in the numerical simulation.231

Figure 6.23. The dimensionless excess pore pressure profiles along the strong discontinuity at time (a) $t = 0.0007$ days; (b) $t = 0.0021$ days; (c) $t = 0.0035$ days; and (d) $t = 0.007$ days233

Figure 6.24. The evolution of the opening at the strong discontinuity for time (a) $t = 0.0007$ days; (b) $t = 0.0021$ days; (c) $t = 0.0035$ days; and (d) $t = 0.007$ days, obtained by CSRPI-M-T2L.234

Figure 6.25. The evolution of the consolidation process for time (a) $t = 0.0007$ days;(b) $t = 0.0021$ days;(c) $t = 0.0035$ days; and (d) $t = 0.007$ days in (1) a continuous saturated porous block and (2) a discontinuous saturated porous block. The arrows are flow lines.235

Figure 6.26. The variation of the fluid flux in x_1 direction for time (a) $t = 0.0007$ days; (b) $t = 0.0021$ days; (c) $t = 0.0035$ days; and (d) $t = 0.007$ days for the saturated porous medium (1) without crack and (2) with crack.....239

List of Tables

Table 2-1. The summary of MMs applications in geotechnical engineering and geomechanics discussed in this study.	46
Table 3-1. Properties of different configurations used for the assessment of the error norms for the one-dimensional consolidation problem.....	74
Table 3-2. Comparison of the computational time required by different numerical procedures adopted in example 3.7.1.....	78
Table 3-3. The properties of different configurations adopted for numerical analysis of the two-dimensional consolidation problem.	81
Table 3-4. Comparison of the computational time required by different numerical procedures adopted in example 3.7.2.....	83
Table 3-5. The mesh properties used for one-dimensional hydraulic pulse test.	88
Table 4-1. Soil properties used in the analysis of Cryer’s problem (E is the Young modulus and ν is the Poisson’s ratio).....	104
Table 4-2. The number of field nodes and elements (smoothing domains) for different background meshes adopted for the error analysis of Cryer’s problem.....	107
Table 4-3. The properties of the different background meshes employed in the error analysis of De Leeuw’s problem.....	112
Table 4-4. The soil properties adopted in the simulation of the Noordbergum effect.	116
Table 6-1. The predictor–corrector algorithm for a frictional contact problem (superscript n or n + 1 indicates trial number) [322].	202
Table 6-2. Material properties assigned for the numerical simulation of the multi-layered elastic foundation.	225
Table 6-3. The material properties assigned to the consolidation problem of the discontinues saturated porous medium [65].....	231

1 Introduction

1.1 Background

The interaction between fluids and solids is at the heart of geotechnical engineering problems. Fully coupled flow-deformation analysis requires robust and efficient numerical schemes for reliable simulation of problems in geotechnical engineering. Advances in computing power and computational mechanics over the past three decades have led to the development of a variety of numerical techniques for the solution of geotechnical engineering problems.

One of the most widely used numerical methods applied to geotechnical engineering problems is the finite element method (FEM). FEM is very reliable, well developed, and commonly used in the geotechnical engineering community. Incorporating material nonlinearity using advanced constitutive models, soil–water coupling behaviour, and geometric nonlinearities, some elegant solutions have already been achieved for several complicated geotechnical problems using FEM [1, 2].

Despite its convenience and robustness, FEM has some inherent deficiencies, such as a strong reliance on mesh quality, overly stiff behaviour, volumetric locking, poor derivative solutions, and poor performance in problems with potential mesh distortion, such as large deformation analysis and crack propagation simulations. FEM can be time-consuming in strongly nonlinear analyses with large deformations due to the required successive mesh generations and subsequent data transfers [3, 4]. The re-meshing process might also produce erroneous outputs, as frequently reported in the

literature [4-6]. The root of all these problems can be traced to the high mesh dependency of the FEM formulation and the ensuing numerical results.

One possible approach to overcoming at least some of the difficulties associated with FEM is the recently introduced mesh-free methods (MMs). MMs considerably relax the dependency of the numerical solution on mesh quality by performing numerical operations which extend beyond meshes, offering better convergence rates in numerical solutions as the relatively more complex shape functions and supporting nodes are employed in the approximation of the unknown variables. The sufficient smoothness of the numerical solutions and derivatives provided by MMs in obtaining accurate stress fields paves the way for the elimination of post-processing requirements such as meshadaptivity. This is one of the major advantages of MMs, especially in problems involving geometrical nonlinearity. To date, MMs have been applied in solving many geotechnical engineering problems, including two-dimensional contaminant transport through saturated porous media [7], prediction of subsidence over compacting reservoirs [8], consolidation analysis in saturated porous media [9], soil collapse and erosion processes in excavations [10], and analysis of slope stability and discontinuities [11].

Despite their excellent flexibility, the interpolation functions in MMs may not necessarily create continuous approximation functions over the problem domain as there are a number of overlapping supporting domains for approximating primary unknowns, which may violate the required continuity of the primary unknowns in a C_0 sense. C_0 means that the variable of interest must be continuous over the field and must have no enforcement of the continuity for the derivatives of the variables. This results in difficulties when derivatives of approximation functions are required. A common

approach to overcome this problem is introduction of bell-shaped weight functions in the formulation (for example in Element-free Galerkin Method (EFGM) [12]). However, inclusion of weight functions increases the computational cost of the numerical scheme, mainly because it has complex shape functions calculated using large number of supporting nodes. Not only is the evaluation of the derivatives of such shape functions costly, but the ensuing property matrices have also large bandwidths. The property matrices are ones that mathematically express the certain feature of a porous medium in a discretised way such as stiffness, coupling and compressibility matrices. The globally assembled property matrices then fill the blocks of the global matrix representing the discretised form of the coupled flow-deformation equations. The smoothing strain technique based on the G space theory [13, 14] has been introduced as a relaxation technique to arrive at the weakened weak (W^2) formulation [15, 16] which removes the continuity requirement of the approximation function and therefore the need for weight functions. The weakened weak formulation has been adopted in association with the polynomial interpolation method (PIM) and the radial polynomial interpolation method (RPIM), which led to the development of the smoothed PIM (SPIM) and the smoothed RPIM (SRPIM) [15-20]. In these methods, the conventional compatible strain is replaced by the smoothed strain which is constant over arbitrary smoothing domains. The smoothed strain field construction overcomes the difficulties associated with the compatibility of the approximation functions by eliminating the need for derivatives of the approximation function, as opposed to the conventional numerical methods such as FEM and PIM/RPIM. The smoothing operation also leads to the attainment of more accurate numerical solutions [19, 21]. The elegant performance of SPIM/SRPIM has been shown in engineering problems in a variety of disciplines [21-33]. Smoothed-point interpolation methods also possess greater convergence

properties in terms of primary variables and energy norm compared to most previously adopted MMs [19].

1.2 Problem Statement and research gaps

Despite their excellent features, SPIM/SRPIM have been vastly overlooked by geotechnical engineering community. There are only a few basic studies on the application of these methods for flow-deformation analyses in porous media. The studies presented in [34, 35] used a rudimentary node selection scheme with the involvement of a few supporting nodes, overlooked the possibility of the achievement of further softness by employing more complex node selection schemes. These studies were restricted to exploit very simple nonlinear constitutive models or a linear elastic behaviour without any extension towards more complex problems, frequently encountered in geotechnical practice.

It is, therefore, desirable to develop SPIM/SRPIM formulations for the flow-deformation analysis of saturated porous media to exploit their full potentials in improving currently available numerical methods. First, it is necessary to investigate whether or not the extension of the SPIM/RPIM to the mixed *Galerkin* formulation retains its greater accuracy and convergence rate in terms of both primary variables compared to the conventional numerical methods. Such an investigation requires extensive numerical error analysis in terms of the quantities of interest, for example displacement, pressure, and strain energy, using the numerical solutions obtained from SPIM/RPIM and a conventional numerical method like the standard FEM. Such a thorough investigation is not available in the current literature.

Unlike most conventional numerical methods such as the FEM, the extension of the SPIM/RPIM formulation to axisymmetric problems is not trivial and requires additional adjustments in the formulations, even for single-phase problems. This difficulty is due to the existence of Gauss points along the axis of symmetry in the SPIM/SRPIM formulations, causing the singularity in the calculation of the stiffness matrix. This problem has not been yet properly addressed in the literature. Thus, adjustments must be made to the formulation of SPIM/SRPIM to analyse axisymmetric problems, both in single-phase and multi-phase porous media. because in an axisymmetric setting, the modelling of geotechnical-related problems is of relative importance.

It is known that when conventional numerical techniques are used for analysis of mixed coupled formulations, stability problems may arise, particularly when low permeability or high loading rates are considered [36, 37]. Extensive numerical studies of the roots of these instabilities reveal that the fulfilment of a special relationship between the chosen spaces for the approximation of primary variables is required when (nearly) incompressible constraints are encountered in the standard variational formulation. This criterion corresponds to the famous Ladyzhenskaya–Babuska–Brezzi (LBB) condition, also known as the inf-sup condition [38, 39]. Inappropriate spaces chosen for approximation of primary variables lead to the violation of the inf-sup condition, which can have adverse implications, such as severe pressure oscillation or overestimation of the collapse load in geotechnical engineering practice.

To overcome this problem, several stabilisation techniques have been proposed in the literature to remove the inherent deficiency related to the satisfaction of the inf-sup condition [40-48], and these have frequently been applied to geotechnical engineering problems [49-52]. Among these, one of the most appealing groups includes consistent

stabilisation methods in which the desirable consistency property is preserved by appending the residuals of the relevant strong differential equations to their corresponding variational statements. Consistent stabilisation methods not only eliminate the pressure oscillation but also exhibit optimal convergence in constrained numerical simulations of interest [43, 46, 47, 53].

Unfortunately, the seemingly natural choice of equal linear subspaces for the primary variables leads to the violation of the LBB condition in coupled problems of porous media [36, 37, 54-57]. The consistent stabilisation techniques are able to restore the LBB condition in this case, but leave penalty errors as fail to preserve their consistency features, because the added terms containing second order derivatives are either vanished or poorly approximated rendering the consistent stabilisation technique ineffective in this case. Very few techniques have been proposed to enable the utilisation of equal linear interpolation subspaces, i.e. [58], but they give rise to other adverse consequences, such as increases in computational expense due to the appearance of several additional unknowns.

A technique based on applying an appropriate smoothing gradient operation can potentially retrieve the utilisation of equal-order linear interpolation functions in a consistently stabilised formulation, because derivations of the approximation functions are eliminated by the smoothing operation. Such a consistently stabilised technique based on equal-order linear approximation functions could be very efficient, but has not been yet explored in the literature.

The analysis of coupled problems with interfacial constraints is frequently encountered in geotechnical engineering as well as in the oil and gas industry. The flow-deformation analysis for fractured porous media associated with the possibility of the crack

propagation is relatively common in the oil industry, commonly known as hydraulic fracturing. The existence of the interfaces may arise from a mismatch in material properties or the existence of a jump in the value of a primary variable which may change over time. One of the considerable limitations of the FEM in such problems is the requirement of the alignment of the mesh topology with the configuration of the discontinuities. This leads to a cumbersome and potentially erroneous process when, for example, an evolving discontinuity such as a propagating crack changes its orientation over time or during iterations. One solution is to enrich the approximation functions with appropriate discontinuous functions which can truly capture the existence of interfaces throughout a problem domain. Perhaps the best-known method in this category is the extended finite element method (XFEM), which is based on the augmentation of the shape functions, restoring the partition of unity concept [59]. XFEM has frequently been adapted to various saturated porous media problems with different interfaces [60-69].

The treatment of weak or strong discontinuities in multiphase porous media by MMs has gained very limited attention [70, 71]. In MMs, the formulation can be augmented to reproduce realistic numerical solutions to account for the presence of interfaces. This must be done in such a way that evolving interfaces can be simulated, without resorting to cumbersome techniques such as repeated generation of smoothing domains. The formulation must also be augmented with an appropriate fluid continuity equation, to account for the flow within evolving interfaces in saturated porous media.

There are numerous examples in computational geomechanics, in which two or more bodies are in contact such as retaining walls along with backfill soils, shallow foundations, piles with their surrounding soils and conventional triaxial tests. Thus, the

local contact behaviour can have a major influence on the global stress and deformation patterns over the domain of the problem. Thus, the proper modelling of the soil-structure interaction and the closure mode of crack faces require the accurate implementation of an appropriate contact algorithm. A comprehensive contact algorithm must truly capture both opening/closing mode through the imposition of the contact constraint in the normal direction and stick/slipping mode through introducing a realistic constitutive model to determine the relative displacement of contacting bodies in the tangential direction [72]. Despite the contact modelling importance in geotechnical engineering, very few attempts have been made to include the contact algorithm in meshfree methods.

1.3 Objectives and layout of the thesis

The objectives of this research are as follows:

- 1) Extend the original SPIM/SRPIM formulations to coupled flow-deformation problems frequently encountered in geotechnical engineering, and to study their performance compared to standard numerical methods such as the FEM.
- 2) Remove the inherent deficiency of SPIM/SRPIM formulation in axisymmetric problems when adopting a coupled formulation.
- 3) Recover the utilisation of equal linear interpolation functions for both primary variables while satisfying the inf-sup condition in the context of a consistent stabilisation method.
- 4) Augment the SPIM/SRPIM formulation to allow the inclusion of interfacial geometries without the alignment of smoothing domains and interfacial geometry, and develop a robust contact algorithm to account for tractions induced by closure modes in interfaces.

Chapter 2 presents a comprehensive literature review related to the objectives of the thesis. The literature review includes previous studies related to a brief review of SPIM/SRPIM and other MMs, followed by the introduction of previous studies of MMs in geotechnical engineering. Chapter 2 also reviews stabilisation techniques previously applied in geomechanics and other relevant disciplines, such as Stokes equations, and elucidates their differences. This chapter ends by reviewing previous studies related to the inclusion of interfaces and contact behaviour in geotechnical engineering, especially those approaches which account for the coupled flow-deformation process.

Chapter 3 presents the cell-based SPIM/SRPIM developed on the basis of the generalised gradient smoothing technique for the numerical modelling of saturated porous media. To this end, spatial discretisation of the coupled flow-deformation equations is formulated by adopting the weakened weak (W^2) concept, or the generalised smoothed *Galerkin* method. Both primary variables, displacement and pressure fields, are approximated using the appropriate shape functions PIM and RPIM, which possess the Kronecker property, facilitating the imposition of essential boundary conditions for both primary variables. The validity and robustness of the proposed method is thoroughly assessed via the simulation of a number of benchmark examples and comparison with their reference solutions. The convergence properties and the accuracy of the proposed method are investigated through an extensive error analysis in terms of primary variables and energy, compared with conventional PIM/RPIM methods and the FEM.

Chapter 4 adopts SPIM/SRPIM coupled formulations in axisymmetric settings. The method overcomes a difficulty encountered when using SPIMs in an axisymmetric setting, the inherent deficiency associated with the existence of Gauss points along the symmetry axis. A decomposition technique which differentiates the smoothed from the non-smoothed terms is presented that avoids the singularity problem which would otherwise arise. The proposed method restores the accuracy of the original SPIM/SRPIM formulations and incurs no increase in the required computational effort. The performance of the proposed method is investigated through the simulation of both benchmark and practical axisymmetric problems, accomplished via a set of convergence studies in terms of quantities of interest for various time and mesh densities.

Chapter 5 proposes a consistently stabilised smoothed point interpolation method (SPIM/SRPIM) which encompasses both linear and nonlinear numerical analysis in geomechanics. In the proposed method, equal-order linear interpolations as a natural, practical choice can be adopted for both displacement and pressure variables while circumventing the difficulties associated with the fulfilment of the inf-sup condition and achieving optimal convergence rates in computational geomechanics. The proposed method retains the contributing terms in conjunction with the displacement and its weighting function in order to preserve the consistency of the original formulation. The proposed method offers an unconditionally stable form of the edge-based smoothed finite element method (SFEM), which is used as the simplest representative form of SPIM, regardless of a priori chosen stabilisation parameter. The efficiency and robustness of the proposed method are thoroughly studied for a range of benchmark numerical problems, including material linearity and nonlinearity assumptions.

Chapter 6 develops an Enriched SPIM/SRPIM formulation for flow-deformation analysis of saturated porous media which includes embedded interfaces. In this formulation, the PIM and RPIM shape functions are augmented by appropriate discontinuous functions representing the discontinuity involved in either the primary variables or their gradients within a domain without requiring generation of successive smoothing domains when interfaces change their orientations. The proposed method addresses the difficulties encountered in the standard FEM, SPIM, and SRPIM formulations which require the conformity of surface discontinuities with discretisation topology. Appropriate *Heaviside* and ridge enrichment functions are adopted to properly capture the discontinuities in the primary/secondary fields within supporting domains. The effects associated with the closure modes of discontinuities are included through the adaptation of a nonlinear contact algorithm, accounting for frictional effects in

discontinuities. The contact algorithm is numerically implemented based on the satisfaction of an inequality commonly known as the *Kohn-Tucker* inequality in both the normal and tangential directions. The effect of fluid exchange within discontinuities is formulated by the inclusion of a suitable and realistic form of the fluid continuity equation within the discontinuities, which is discretised and simultaneously solved with the discretised coupled flow-deformation equations of the surrounding medium. A set of numerical examples which accommodate the embedded interfaces due to both a large contrast in material properties and a jump in primary variables is numerically modelled and compared with the solutions proposed by previous studies.

Chapter 7 summarizes the studies which have been done and presents the main findings of this thesis. Potential avenues for future exploration also presented.

2 Literature Review

2.1 Introduction

This chapter is devoted to a comprehensive literature review pertaining to the objectives of the thesis. The literature review carefully elucidates pertinent previous studies relevant to a brief review of SPIM/SRPIM and other MMs, followed by the application of MMs in geotechnical engineering. Chapter 2 also discusses various stabilisation techniques previously applied in geomechanics with their relevant special features and possible deficiencies, such as those methods applied to *Stokes* equations and the Darcy equation. This chapter gives a comprehensive review related to previous studies, devoted to the inclusion of interfaces and contacts in geotechnical engineering, especially those approaches which considers the flow-deformation process in saturated and unsaturated porous media.

2.2 A brief review of meshfree methods

The finite element method (FEM) is widely recognised as one of the most reliable numerical methods for simulation in the geotechnical engineering community. Numerous sophisticated geotechnical simulations have been performed using the FEM [2]. FEM exhibits robustness and accuracy in the majority of practical geotechnical problems. Despite its effectiveness, the FEM application in certain problems can be difficult, mainly due to its heavy reliance on mesh-based interpolations. Problematic cases include large deformation analysis, simulation of discontinuities, analysis of problems involving fragmentation, etc. A number of improvements to the FEM have

been proposed in the literature to overcome these difficulties. However, the proposed techniques have their own implications and most often demand considerably higher computational efforts compared to the standard FEM. In addition, the FEM approximation inherently engenders overly-stiff matrices that might end up with the appearance of volumetric locking if an exact numerical integration scheme is employed and/or Poisson's ratio is taken as 0.5 (the incompressible material) [73].

Over the past three decades, a relatively new class of numerical methods, collectively known as meshfree methods (MMs) has been introduced. MMs have undergone remarkable progress due to their distinct features, with the objective of addressing a major part of the deficiencies attributed to mesh-dependent numerical methods. MMs aim to compensate for at least some of the difficulties associated with the FEM by resorting to more flexible approximation/interpolation techniques created by nodes scattered in a whole domain of interest.

The first MM that can be found in the literature is referred to as smoothed particle hydrodynamics (SPH), which was introduced by Lucy [74] and Gingold and Monaghan [75], to evaluate astrophysics problems. Later, Libersky, Petschek [76] exploited SPH, for the first time, in solid mechanics to demonstrate the application of the method in this field. MMs offer excellent flexibility for adaptation either based on a strong form, such as SPH and its corrected versions, or a global weak form. The element-free *Galerkin* (EFG) [12] was the first MM, formulated based on a global weak form, followed by the reproducing kernel particle method (RKPM) [77] one year later, even though striking similarities exist between EFG and RKPM. While both EFG and RKPM exploit the so-called intrinsic bases, other MM formulations, deduced by utilisation of the extrinsic bases, admitted the partition of unity concept. It is worth mentioning that extrinsic basis

was initially incorporated into a p-refinement method, e.g. hp-cloud [78], and the partition of unity concept (PU) proposed by Melenk and Babuška [59].

MMs can be adapted on local weak forms and formulated on overlapping subdomains rather than global weak forms. The meshless local Petrov-*Galerkin* (MLPG) is one of the well-suited local MMs [79] where the numerical integration is performed on overlapping subdomains leading to a ‘truly’ MM because it eliminates the need for background meshes to perform numerical integration.

MMs can be classified based on how they express approximation forms to represent unknown variables in three general classes, as noted in [80]:

- Finite integral representation methods, in which the approximation of unknown variables is expressed by integral forms. Some well-known MMs are classified in this group, such as SPH [4] and RKPM [7].
- Finite series representation method, in which the approximated variables are represented using a series of polynomial bases. This group includes MMs based on moving least square (MLS) concept [81], the partition of unity methods [59], and the general form of hp-cloud [78].
- Differential representation methods, in which unknown variables are expanded using the Taylor expansion series up to the desired order of accuracy, for example [82, 83].

There are several advantages to using MMs. First, MMs can accommodate some enhancement techniques, such as h-adaptivity, easier than other methods, such as the FEM, which are formulated based on mesh-based interpolation functions. Second, the treatment of evolving interfaces in which the geometry and/or orientation changes over time, such as crack propagation, shear bands and even mismatch in material properties,

can be handled with more ease (compared to the FEM) in most MMs. Third, the enforcement of mesh conformity is relaxed when the inclusion of an interfacial configuration is required [84]. Fourth, the difficulties associated with mesh distortion are easier to handle while performing large deformation analysis. Fifth, MMs ensure higher order continuity by the inclusion of more supporting nodes and a variety of approximation/interpolation functions in comparison to the FEM.

Performing numerical integration in MMs, however, necessitates assigning relatively more quadrature points over a supporting domain of interest to produce solutions with adequate accuracy because MMs often employ non-polynomial functions [85]. Moreover, the imposition of essential boundary conditions in MMs may be complicated by the difficulties that arise from the lack of Kronecker delta properties, which leads to the significant level of computation in MMs [86].

In the point interpolation method (PIM) proposed by Liu and Gu [87], the shape functions possess the Kronecker delta function property, which facilitates imposing the essential boundary conditions. However, the non-singularity associated with the creation of PIM interpolation functions is not guaranteed in this method. The radial point interpolation method (RPIM) was introduced to avoid the singularity problem through the augmentation of PIM shape functions with appropriate radial bases [88]. Nevertheless, in PIM and RPIM, the approximation functions violate continuity across a problem field. A penalty method was exploited to induce a continuous approximation instead of the discontinuous approximation produced by PIM and RPIM, but the increase in computational costs are preventive due to the enlarged bandwidth of the attained algebraic system [86].

In recent years, a novel form of variational statement, together with G space theory, has been introduced to relax the continuity requirement. In this approach, the governing equations are reformed based on an innovative form of the variational statement, the so-called weakened weak formulation (W^2) [20, 89]. The weakened weak formulation is formulated through the replacement of the compatible strain field obtained by the derivative of the displacement field with an equivalent smoothed strain expressed by an integral strain form, commonly known as a strain smoothing operation. Hence, there is no need to compute the derivatives in order to acquire the strain-displacement matrix and other derivative-included matrices. The stability and convergence of the proposed method was mathematically proven by the rigorous properties established by the G space theory [89, 90].

The strain smoothing operation has been also applied to the conventional FEM by [91, 92], which was originally formulated by Chen, Wu [93] to prevent the disappearance of the strain-displacement matrix in an EFG context as nodal integration is to be performed. This is viewed as a robust way to address the difficulties associated with using the FEM. Applying the smoothing gradient technique softens the stiffness matrix attained by the Smoothed FEM (SFEM), preventing the occurrence of volumetric locking and other adverse consequences such as overly-stiff evaluation of resultant matrices. SFEM has various forms, including the cell-based smoothed finite element method (CSFEM) [91], the edge-based smoothed finite element method (ESFEM) [94] and the node-based smoothed finite element method (NSFEM) [95]. The various theoretical aspects of SFEMs were investigated in [92, 96]. The non-local information that is brought in from the neighbouring elements leads to more supporting nodes being involved in the creation of the shape functions, and it therefore increases the bandwidth

of the resulting stiffness matrix in SFEMs. The capability of SFEMs in various fields has been demonstrated by applying them to several numerical problems in [97-100].

The introduction of the strain smoothing technique to PIM/RPIM leads to development of the smoothed point interpolation method (SPIM) and the smooth radial point interpolation method (SRPIM). Applying the smoothing operation technique requires smoothing domains that are properly constructed. The smoothing domains are generally independent from the background mesh, and they are constructed on top of the existing mesh in such a way that the *no sharing rule* is met [15, 16]. Different approaches to constructing permissible smoothing domains have been developed and reported in the literature [16, 20, 101, 102]. Using the strain smoothing operation in the smoothing domain associated with field nodes results in a specific form, known as the node-based smoothed point interpolation method (NSPIM) and the node-based smoothed radial point interpolation method (NSRPIM) [95]. A similar procedure, along with the construction of smoothing domains based on shared boundaries of adjacent meshes, has resulted in the edge-based smoothed point interpolation method (ESPIM) and the edge-based smoothed radial point interpolation method (ESRPIM) [16]. The elements of the background mesh themselves can serve as smoothing domains, resulting in development of the cell-based smoothed point interpolation method (CSPIM) and the cell-based smoothed radial point interpolation method (CSRPIM).

Smoothed point interpolation methods have been applied in a variety of disciplines, proving their appealing features through the use of extensive numerical simulations. A thorough assessment of the numerical properties of different SPIMs/SRPIMs was performed in [19]. A number of novel techniques have been proposed in an NSPIM/NSRPIM context [17] and in a CSPIM context [25] to properly capture the

stress singularity in fracture mechanics. ESPIM and SRPIM have been applied to include the presence of discontinuities stemming from a large contrast in material property in the field of solid mechanics [26]. Various numerical problems associated with plates and shells have been simulated by applying SPIM and SRPIM [23, 24, 103]. SPIM and SRPIM can also be adopted to other mesh forms, such as quadratic forms as implemented in [31], in which a novel technique was employed to create a continuous and piecewise quadratic displacement field over the whole problem domain. The adjustments in SPIM and SRPIM can be extended to the adaptation of the slightly modified versions of PIM and RPIM shape functions, as seen in [27, 33]. Remedial techniques were also adopted in SPIM and SRPIM with the objective of further improvement in the efficiency of the methods, as seen in the adaptivity technique used in ESPIM in [28]. Heat transfer problems have also been simulated using different SPIMs and SRPIMs, as seen in [21, 29]. The application of SPIM and SRPIM has not been restricted to the problems associated with static loading, and SPIM and SRPIM have been successfully applied to vibration problems in solid mechanics [22]. Wave propagation problems and transient thermo-elastic analysis have also been attempted in SPIM/SRPIM contexts as seen in [104] and [30], respectively. SPIM and SRPIM have been so far used in several practical civil engineering problems, e.g., the investigation of thermal effects in concrete dam construction [105].

2.3 Application of MMs in geotechnical engineering

This section presents a comprehensive review of MM studies related to various geotechnical engineering problems. A wide range of MMs has been adopted to solve a number of problems that are frequently confronted in practical geotechnical

engineering. To the extent possible, this review is classified with respect to the MMs adopted in each study.

The pioneering study conducted by Modaressi and Aubert [106] is referred to as the first application of MMs in geotechnical engineering in which the response associated with saturated porous media was investigated with the material elasticity assumption. In another study by Murakami and Kawabata [107], the EFG formulation was adopted for flow-deformation analysis of saturated porous media. A two-dimensional formulation based on EFG method was proposed in [7] for contaminant transport in saturated porous media. Oliaei and Pak [108] proposed a coupled EFG formulation to properly capture the consolidation process in saturated porous media, and that study investigated the numerical issues related to utilisation of EFG in conjunction with the hydro-mechanical analysis presented in [109]. The EFG-coupled formulation was then extended to three-dimensional problems in [9, 110].

Soil properties, such as the friction angle and cohesion, were obtained from the laboratory results of an adaptation of the MLPG method in a set of numerical simulations, along with the Mohr-Coloumb failure criteria used in existing studies such as the study presented in [111]. A modified MLPG was also adopted to simulate saturated porous media using dynamic analysis in [112], followed by an unequal MLPG formulation to suppress the pressure oscillation that arises from the imposition of volumetric constraint in [113].

The material point method (MPM), originally formulated in the early 1990s [111], is one of the prominent types of MMs that has been widely applied to a variety of disciplines. In MPM, the material points are sufficiently small Lagrangian elements to present the problem field of interest, while the gradient of the primary variables is

calculated by the surrounding background mesh/grids. MPM has gained a significant amount of attention in the geotechnical engineering community, which has led to several numerical studies conducted by applying MPM. MPM was used in a dynamic analysis of the slope failure that includes weak layers in [114]. The slope failure study associated with an MPM application was extended to seismic loading in [115]. The soil-structure interaction induced by the existence of anchors in soils was numerically studied in [116]. Investigation of the soil behaviour arising from the coupling interaction of solid grains and fluid flow was performed by Bandara and Soga [117], adopting MPM, which was originally inspired by applying MPM to a general study of granular media behaviour presented in [118]. The coupled flow-deformation analysis of porous media by MPM was extended to a coupled dynamic analysis in [119]. The mass movements frequently encountered in landslides incur large deformation, which was studied in [120]. MPM was also used in the study of cone penetration test with different drainage boundary conditions [121].

The discrete element method (DEM) is a class of numerical methods, often included in the MM category. The main idea behind DEM is to characterise the rotational movements of particles by including the distinguishable degrees of freedom, which appropriately captures the contact states of solid particles in granular media, originally proposed by Cundall and Strack [122]. DEM has been utilised in a number of geotechnical studies, including analysis of a shallow foundation lain on a slope [123]. The effect of tunnel lining on the distribution of the soil pressure within the earth was assessed by the DEM in [124]. A two-dimensional analysis of granular media was extended to three-dimensional simulations in a DEM context in [125]. The structural damage induced by blast loading with inclusion of soil-structure interaction was simulated by DEM in [73].

The finite point-set method (FPM) is another example of MMs that has been extensively applied in fluid dynamics. Several FPM geotechnical applications can also be found in the literature. In FPM, a continuous medium is represented by a sufficient number of points, to which local properties, such as temperature, density and velocity, are assigned. The prominent feature of FPM is that it possesses the flexibility to express the problem of interest in Lagrangian, Eulerian or mixed Lagrangian-Eulerian description with ease of implementation. Therefore, representative points can either be moved or fixed in a space. The influence of a vehicle travelling through saturated porous media was studied by adopting a FPM in [126]. Other examples of the adaptation of FPM to soil mechanics are the study of tri-axial tests adopted by FPM together with a nonlinear constitutive model presented in [127] and the investigation relevant to the simulation of avalanches in [128]. The influence of cutting on the variations of stress and strain induced in soil media was investigated in [129].

Blanc and Pastor [130] applied a two dimensional SPH model to simulate debris flows. Bui and Fukagawa [131] proposed an improved version of SPH to properly capture the possible failure modes of embankments with the inclusion of the flow-deformation process in porous media, followed by the extension to large deformation analysis to evaluate the post-peak behaviour of segmental retaining walls in [132]. The use of SPH in large deformation analysis was also investigated in a study involving a hypo-plastic constitutive model developed in [133]. The coupling of fluid flow with soil particles was also considered in the numerical simulation of reservoirs by SPH in [134]. Hu, Liu [135] developed an SPH application in geotechnical engineering to conduct a three-dimensional analysis to simulate the flow-like behaviour of soil particles under landslide conditions. The flow-like behaviour was also investigated by a combined technique referred to as the depth-integrated SPH, proposed by Blanc and Pastor [130].

Another novel technique by combining SPH and DEM was proposed to properly model the brittle-viscous deformation in practical problems, such as hydro-fracturing in [136].

The particle finite element method (PFEM) refers to a MM that utilises the FEM discretisation to integrate the partial differential equations, while allowing the corresponding nodes to move based on the adaptation of the motion equation in a Lagrangian sense. The balanced forces along with all the associative physical properties are transferred with the nodes that are moving as if they are behaving as particles. This unique feature has contributed to solving a number of complex geotechnical problems. The influence of the tunnelling process by rock cutting tool was presented by applying PFEM in [137]. The coupled flow-deformation process was also simulated in a study conducted by Oñate and Idelsohn [138].

PIM and RPIM have been frequently used to solve in geotechnical engineering problems due to their ease of implementation, Kronecker delta properties and striking similarities to the conventional FEM without mesh-dependent restrictive issues. Wang and Liu [139, 140] extended the application of PIM and RPIM to solve Biot's equation. Wang and Wang [141] formulated an unequal order PIM/RPIM to eliminate the pressure oscillation arising from the violation of inf-sup condition. Then, Khoshghalb and Khalili [142] proposed a coupled flow-deformation formulation together with the utilisation of PIM and RPIM associated with a novel three-point temporal discretisation method [143] to alleviate the temporal insatiability that occurs during numerical simulation of the consolidation process. Khoshghalb and Khalili [144] also extended the PIM/RPIM formulation to model unsaturated porous media including hydraulic hysteresis, followed by the extension of the formulation to large deformation problems

[145]. PIM and RPIM were also involved in the assessment of wave-seabed interaction in [146, 147].

Despite the fact that SPIM/SRPIM possesses desirable properties, the application of SPIM and SRPIM in geotechnical engineering has received little attention. Soares [34] proposed an iterative algorithm adopted to a simplified version of ESPIM to simulate linear and nonlinear geotechnical problems, followed by another study to include the dynamic effects [35]. Nonetheless, these studies were restricted to simple node selection schemes and some simplifications in the calculation of the coupling matrix of the system. To address these deficiencies, Ghaffaripour and Khoshghalb [148] proposed a novel algorithm to properly capture the coupling effects related to the response of saturated porous media when material nonlinear models are adopted. In this study, more sophisticated nodal selection techniques, together with both PIM and RPIM shape functions, were adopted.

A soft particle method was developed to simulate granular media in [149], followed by the simulation of shear bands by Schneider-Muntau and Chen [150]. Among the various MMs methods that could not be classified under abovementioned well-known MMs, the first application of the maximum entropy shape functions in MM for elasto-static problems were introduced by Ullah and Augarde [151]. Later, the formulation of EFG, along with the FEM that exploit the maximum entropy concept was presented in [152] including both small and large deformation analysis. The local maximum entropy formulation was consequently developed in [153]. It was extended to include material nonlinearity in a study presented by Kardani and Nazem [154] associated with an adaptive version which the FEM along with EFG employed the local maximum entropy shape functions in [155]. The material nonlinearity was also considered in a meshless

natural neighbour method developed in [156]. More sophisticated constitutive models were adopted in [157] to simulate cemented sand incorporating a bonded-particle method in [158] to capture the lateral spreading due to the liquefaction phenomenon using the Lattice Boltzman method. A Lagrangian MM was also proposed to allow for the movement of nodes by Wu and Chen [159].

2.4 Stabilisation methods in computational geomechanics

The ever-increasing applications of coupled flow-deformation analysis in porous media have garnered a great deal of attention in the literature. The first theoretical contribution to the consolidation problem was described in the pioneering work by Terzaghi [160], in which the consolidation process was formulated for a one-dimensional soil column under a constant load. Later, the theory of the flow-deformation analysis of porous media was extended to a generalised three-dimensional formulation by Biot [161]. Biot's formulation presents coupled equations of the time-dependent stress distributions and displacements in the solid phase in conjunction with the attendant pore-pressure dissipation in the fluid phase. This theory has provided a fundamental basis for subsequent studies in a wide variety of fields, such as geomechanics, biomechanics and rock mechanics.

The necessity of analysing and understanding complex flow-deformation processes in porous media has led to the development of competent numerical methods to solve the governing equations. The first application of Biot's theory using numerical methods was presented in [162], and it was later extended by Zienkiewicz in [56, 163]. The incremental forms of Biot's equations, which are required for material and geometrical nonlinear analysis, were developed in [3, 57, 164]. The assumption of fully saturated

porous media was originally made in Biot equations. However, understanding the mechanism of the interactions among different phases in three-phase problems, such as unsaturated soils or oil–gas–soil reservoir simulation, necessitated further development of the coupled formulation into a more generalised approach that accommodates three coupled equations, each of which representing a certain phase [54, 144, 165, 166].

A mixed \mathbf{u}/p formulation is often used for numerical analysis of coupled flow-deformation problems to obtain simultaneous approximations of the displacement of the solid phase in conjunction with the relevant fluid phase pressure distribution. The \mathbf{u}/p formulations employ the mixed finite element method context, in which both primary variables are simultaneously obtained by introduction of the coupling effects through non-diagonal matrices to the global discretised equation. However, mixed formulations encounter difficulties, particularly when the flow-deformation problem is met with the constraints of low permeability or a high loading rate. To investigate the origins of these challenges, the mixed variational form of Biot's equations can be scrutinised, revealing that a special relationship between displacement and pressure spaces must be fulfilled in the presence of (nearly) incompressibility constraints. This relationship assures the coincidence of the pressure space with the range of the Divergence operator. This crucial requirement corresponds to the famous Ladyzhenskaya-Babuska-Brezzi (LBB) condition [38], also known as the inf-sup condition [39, 167]. It can be shown that the stability of mixed finite element approximations is ensured by the fulfilment of a discrete version of the inf-sup condition as a requirement to yield stable solutions [38, 168]. This enforces the pressure and displacement spaces of the approximations to satisfy a special relationship that imitates continuous cases.

Unfortunately, the seemingly natural choice of equal-order approximating spaces for both displacement and pressure fields violates the inf-sup condition. This violation causes oscillation in the numerical fluid pressure results and overestimation of the collapse load due to a tendency of the volumetric locking phenomenon in numerical simulations of (nearly) incompressible porous media when approaching a collapse state. Standard safe elements, such as the Taylor-Hood element families, in which the displacement field is approximated one order higher than the pressure field, have often been employed in the literature to this problem. A wide range of more sophisticated similar elements has been proposed in [40, 169] to overcome this problem. Nonetheless, from the point of view of implementation, it is desirable to adopt the same equal low-order elements for both displacement and pressure approximations. In doing so, it is possible to generate uniform data structures to conduct large-scale computations easily and cost-effectively by generating property matrices of manageable sizes with small bandwidths in three-dimensional problems for both pairs of unknown field variables. Taylor-Hood elements tend to result in the convergence of the numerical solutions, but either with a major loss of optimal convergence rate or without the convergence of the Divergence of the rate of displacement[170].

The adverse implications associated with the violation of the inf-sup condition can be circumvented, or at least ameliorated, by the regularisation of the mixed problem, leading to the stabilised *Galerkin* methods [41, 171-173]. Although a unified classification of these stabilisation schemes would be difficult, they are formulated based on the modification or relaxation of the incompressibility constraint by adding stabilising terms to the mass balance equation(s). This stabilises the mixed formulations and retains the convergence properties of the solutions.

Many stabilised methods have been previously developed and applied in the fluid dynamics context, encompassing all the features of a constraint problem. Numerous stabilisation techniques can be found in the literature for *Stokes* [44-46, 172, 174-176] and Darcy equations [43, 48, 170, 177-181].

Time-stepping stabilising techniques are considered to be one of the pioneering stabilisation methods dating back to late 1990s [182]. The main idea behind these methods is to project the pressure gradient into the velocity space and to introduce this projection as an additional dependent variable. Consequently, the incompressibility constraint in the continuity equation is relaxed by subtracting the discontinuous pressure gradient from the additional projected variable. This technique, which is known as the fractional step method, has been applied in dynamic analysis of geotechnical problems [37, 55, 183]. The time-stepping technique was also introduced in an MM context as an appealing feature of this class of numerical methods to exhibit stability subjected to large deformation, frequently accompanied by dynamic loading, as proposed in [83, 184]. Nonetheless, this class of stabilisation technique is not well-suited for quasi-static consolidation analysis because the intrinsic assumption in its formulation is more suitable for dynamic analysis [36].

Another prominent stabilisation technique is the finite increment calculus (FIC), or simply finite calculus [185-188], based on the pioneering work of Oñate [185]. In this technique, equations for the balance of mass and momentum in a space-time domain are reformulated using the Taylor-series expansion to account for higher-order terms, presenting variations of the transported variables within the balance domain.

FEM formulations stabilised with the FIC technique, which express the first-order form of the FIC balance equation in space, have been applied frequently in the context of

computational fluid and solid mechanics [185-188]. FIC has also been successfully applied to both one- and two-dimensional coupled flow-deformation analyses of porous media [36]. Recently, a second-order FIC form of the mass balance equation [189, 190] was applied to two- and three-dimensional consolidation analyses of porous media, thus facilitating the ability to obtain a more stable form of the mass balance equation [191]. However, in a comprehensive assessment of the performance of stabilised *Galerkin* methods in geomechanics reported in [49], it was shown that the first-order form of the FIC technique failed to converge at early stages of a nonlinear stability analysis of a vertical cut using both the associated and non-associated nonlinear constitutive models. In [49], FIC was unable to make further improvements to the bearing capacity analysis of a strip footing in comparison to other classical stabilisation methods. Further investigations are required to assess the robustness and accuracy of the FIC approach in cases of a nonlinear numerical analysis of porous media.

Several other stabilisation methods proposed in the literature can be classified as residual-based techniques. Residual-based stabilisation methods work based on the relaxation or modification of compressibility constraints by adding additional terms to the mixed variational formulations. These methods, collectively known as consistently stabilised *Galerkin* methods, provide consistency, in general, because the stabilising terms eventually vanish. These methods involve a positive parameter that must be *a priori*-specified, i.e. the stabilisation parameter. Based on the stability achieved for a range of the stability parameter in consistently stabilised *Galerkin* methods, these methods are categorised into two distinctive groups [192]: methods that yield conditionally stable solutions with a set of restricted stability parameters and methods that offer unconditional stability with respect to all mesh-dependent stability parameter values. In a comprehensive theoretical investigation [53], where the consistently

stabilised finite element methods proposed for the *Stokes* equation were assessed, the *Galerkin* least-squares (GLS) [47] and pressure-*Poisson Galerkin* methods [46] were considered to be conditionally stable, while the stabilisation method initially proposed for *Stokes* equations in [172] was shown to be unconditionally stable. Consistently stabilised *Galerkin* methods have been successfully applied in computational geomechanics. For example, Truty [193] developed a GLS approach for the consolidation analysis of saturated soils. However, the proposed method fails to completely suppress pressure oscillations when a non-zero value of the fluid compressibility is assigned in a numerical simulation. The proposed method also used a transient stability parameter with the inclusion of the current time-step that might cause, on the basis of the authors' investigations and according to the theoretical investigations in [53], either a faster onset of pressure oscillation or abrupt deviation from the exact solution by a small perturbation of the properly chosen stability parameter. The pressure-*Poisson Galerkin* like method was adapted to EFG in [194], which can be considered as the first application of a consistent stabilisation technique in MMs.

Truty and Zimmerman then derived a formulation for *Stokes* problems based on the method presented in [44] and compared it with GLS and pressure-*Poisson* methods for fully saturated soils [50]. They later extended their approach to the analysis of unsaturated soils [51]. Good agreement was achieved with respect to the reference solutions in both linear and nonlinear cases, but their proposed method was only conditionally stable [53]. That could lead to the appearance of pressure oscillations or volumetric locking when an inappropriate stability parameter value is chosen. The same stabilisation technique was also adopted in [195], but with the stability parameter assumed independent from the time-step size.

It is frequently reported that consistently stabilised *Galerkin* methods, such as the formulations applied in [50, 51, 193, 195], are not well-behaved when equal low-order interpolations are used for both primarily unknown variables. This is because these methods are often formulated based on the residual of the strong form of the governing equation, which results in the appearance of second-order derivatives in variational forms in their corresponding formulations. Second-order derivatives are either vanished or poorly approximated when equal-order linear interpolations are employed [52, 53, 177, 178, 192, 196] rendering the stabilising terms ineffective. A possible heuristic technique could be a reformulation that transforms the governing coupled equations into a first-order system of equations [171]. However, this might engender more unknown variables and larger algebraic problems that must be numerically solved. Other strategies include replacing a discrete operator with the Laplace operator [192] or reconstructing higher order derivatives [58] that have striking similarities and are referred to as weakly consistent methods. A global L^2 projection is needed in both cases, which precludes the applicability of the previously mentioned remedial methods from the implementation of stabilising terms at the element level. The global projection refers to the projection that project the variable of interest itself on the whole domain of interest to the functional space, not on each background mesh/cell; thus, it would dramatically increase computational expenses.

The method proposed in [192] is claimed to be an unconditional stable variant of the pressure-*Poisson Galerkin* stabilised method. However, according to the numerical investigation to assess the performance of stabilised *Galerkin* methods in geomechanics reported in [49], the added stabilising term relevant to the weighting function of the displacement has a negligible stabilising effect on the results. Hence, it was proposed that the corresponding term could be omitted from the proposed formulation for

practical simplification. This suggestion makes the proposed method similar to a pressure-*Poisson Galerkin* method; however, the elimination of the aforementioned term may cause considerable error by a small perturbation of the stability parameter. This error is especially notable for fluid pressure distribution because a large deviation could be observed in its approximated solutions [49]. Therefore, it is beneficial to develop an unconditional stabilisation technique irrespective of an *a priori*-specific stabilisation parameter similar to the absolute stable method proposed in [172].

Non-residual pressure projection stabilisation techniques have also been proposed as a possible remedy for applying equal low-order pair of spaces to a wide range of applications [42, 174, 197]. These techniques are motivated by the fractional step schemes for the optimal use of equal lowest-order interpolations without resorting to residuals of governing equations and the appearance of higher-order derivatives. Multiple stabilised pressure projection methods, which have been extensively applied to Darcy and *Stokes* equations, have been proposed, including global pressure gradient stabilisation [175, 198, 199], local pressure gradient stabilisation [174], polynomial pressure projection-based methods [177, 200] and local and global pressure jump formulations [197, 201]. The basic idea behind the pressure projection methods is to supplement the deficiency associated with the fulfilment of the inf-sup condition by imposing an additional term on the variational formulation, compensating for pressure deviations. The use of pressure projection methods eliminates the need to compute high-order derivatives, and it preserves the symmetry of the resulting original global matrix obtained from the mixed formulation.

Despite the striking similarities between the fractional step schemes and the polynomial pressure projection methods, the latter involves fewer computations because many of

the projections are implemented at the element level [200]. In geomechanics, the applications of the polynomial pressure projection method in numerical analysis have been investigated for fully coupled flow-deformation in linear and nonlinear saturated porous media [52] and porous media with double porosity [202]. The effectiveness of the polynomial pressure projection method in numerical hydraulic fracturing analysis was also confirmed in [203]. It was applied to RKPM as the application of polynomial pressure projection in MMs, which exhibited good agreement with reference solutions but with the assumption of elasticity; thus, an assessment of the capability of the proposed method for nonlinear problems was overlooked [204]. However, it was revealed that the polynomial pressure projection stabilisation method fails to remove the pressure oscillation in the vicinity of the drainage boundary where the presence of intensive pressure gradient exists [36].

The variational multiscale method is another approach that results in the general form of consistent stabilisation techniques that employ bubble functions to account for the approximation of the fine scale within each element. The first method in this category can be traced back to [205], which attempted to solve the *Stokes* problem. This method has also been applied to the numerical flow-deformation analysis of porous media for one- and two-dimensional benchmark problems [36]. The aforementioned study shows that the method results in stabilised matrices that are identical to those attained by the application of the *pressure-Poisson Galerkin* stabilised methods, provided that an appropriate bubble function is carefully selected. However, [36] shows that the bubble function method is not well-behaved for stabilising a one-dimensional flow-deformation analysis in geomechanics.

The concept of the softening effect introduced in [93] associated with G space theory [14, 89] was exploited in SFEM and SPIM/SRPIM to induce the desired softening effects needed to mitigate the overly-stiff behaviour of the FEM and SPIM/SRPIM. However, SFEMs and SPIM/SRPIM are not completely well-behaved when subjected to incompressible constraints [94]. Hence, some stabilisation techniques have been adapted to SFEMs to develop a fully locking-free form of SFEMs, e.g., the utilisation of bubble functions in SFEMs for single-phase problems subjected to an incompressible constraint [206-208]. The bubble functions are, however, inadequate to stabilise the general coupled flow-deformation variational statement in computational geomechanics [36]. Similar to the FEM, the original SFEMs also suffer from the inability to utilise equal linear order interpolation functions for both primary variables in a consistent stabilisation framework. To date, the application of a stabilised SFEM in computational geomechanics has not been studied.

2.5 Numerical analysis of porous media including interfaces

In geotechnical engineering, the load acting on structures is generally transferred to soil through the areas where the soil and structures are in contact. Such surfaces in contact can be generally modelled assuming either natural boundary conditions, including the flexibility of adjacent structures in the analysis of interest, or essential boundary condition relevant to a primary displacement variable, assuming fully rigid adjacent structures. These simplifications are, however, rudimentary and might yield erroneous predictions that are far from realistic behaviour and might only be applicable when the surfaces in contact are already known. Several complexities from the field of contact mechanics, such as frictional sliding accompanied by large deformations and opening or

closing of crack surfaces of hydro-fracturing phenomena, are needed to simulate the contacting surfaces. The quality of the prediction of the overall behaviour of the soil-structure interactions is influenced by the attainment of the realistic response where the surfaces are in contact. In geotechnical engineering, frictional contact between soil and structure is important in many applications including foundations, piles, soil anchors, retaining walls, and geotextile reinforcements in embankments and retaining structures.

The zero-thickness model can be thought of as the simplest and earliest technique for numerical modelling of contacts in geotechnical engineering because of the simplicity of implementing zero-thickness elements in conventional FEM codes. A simple double-noded interface element capable of accounting for fluid flow within a crack in fractured rock, but only in a tangential direction was formulated by Ng and Small [209] and by Noorishad and Ayatollahi [210]. Later on, in a study by Segura and Carol [211], the zero-thickness model was extended to incorporate transversal fluid flow. The theoretical framework for zero-thickness elements that assumes a discontinuous pressure field was established in [212] and its accuracy and robustness in coupled flow-deformation analysis were demonstrated in [213]. A horizontally aligned crack with the assumption of non-propagation was numerically simulated by a triple-noded zero-thickness element developed by Guiducci and Pellegrino [214]. Following this, Centeno Lobão and Eve [215] proposed a constrained interface formulation across which pressure continuity was preserved. The enforcement of pressure continuity across the element was also established by using Lagrange multipliers, developed in [216]. A zero-thickness element that assumed the discontinuity fields for both the pressure field and its gradient was developed in [60]. A zero-thickness element for stationary hydraulic fracturing, including a traction-displacement relationship in a two-dimensional setting, was also presented in [217], which, through imposing an additional degree of freedom, exploited

the partition of unity concept to properly capture the displacement discontinuity across interfaces. The zero-thickness element proposed in [218] enables incorporation of the hardening behaviour of soils, including interfaces, and can be expressed in an incremental form, but it has limitations relevant to the geometrical predefinition of zero-thickness elements.

The geometrical restriction attributed to the use of zero thickness element was, for the first time, addressed as an application to soil-structure interaction problems in a pioneering study by Van den Berg [219], in which a soil mass streaming past a fixed cone was simulated by formulating of zero-thickness elements under an Eulerian setting that is able to handle large deformations. However, this study failed to capture a penetration procedure that starts from the ground surface. Liyanapathirana and Deeks [220] proposed a novel method that, through a set of predefined pile-soil interface elements that are successively activated with corresponding pile elements, simulates the installation process of displacement of open-ended piles with negligible wall thickness under circumstances of large deformation. Nonetheless, the extension of the proposed method to the simulation of closed-ended piles and piles with considerable thickness is not feasible because the pile and interface elements are not able to fill space while inactive. Despite the simplicity attributed to using zero-thickness elements in modelling discontinuities, their applicability is often restricted to problems where only pre-existing interfaces with previously known configurations exist. Thus, zero-thickness elements fail to produce qualitative solutions for boundary value problems in which interfaces move with time in an unpredicted fashion.

In computational contact mechanics, and in particular in the FEM framework, the simplest way of treating interacting objects is perhaps an algorithm commonly known

as node-to-surface (NTS). NTS has been extensively employed in commercial and academic FEM codes. In this approach, the enforcement of constraints is effectively established through a node of one contact surface, commonly named the slave, and the corresponding surface (master), which effectively involves collocating the contact integrals at the slave nodes. This approach is able to include large deformation analysis.

NTS was first applied in finite element modelling to Hertzian contact problems [221]. The first implementation of NTS in soil-structure interaction was due to [222], in which an NTS formulation associated with a Lagrange multiplier was applied to simulate the interaction between a buried culvert and the surrounding soil in order to address the difficulties associated with surface separation and re-closure. Nonetheless, the study was restricted to problems under the small sliding assumption between contacting nodes. A cantilever sheet-pile wall interaction in conjunction with the concept of frictional contact constrained by the NTS technique was modelled in [223, 224]. Despite its simplicity, the NTS method in general fails to pass the patch test, due to non-uniformity of nodal forces arising from using high-order interpolation functions, even when the problem involves a uniform stress field [225]. In addition, the NTS method may induce the deterioration of mesh quality near the surfaces of the contacting bodies.

Another well-established technique, known as the surface-to-surface (STS) algorithm, was subsequently proposed in which contact constraints are expressed in a weak form. As a result, the computation of contact integrals is not performed at slave nodes any longer. The STS technique was first formulated as an integration technique over contact segments for two-dimensional applications. It was firstly introduced as a segment-to-segment approach in [226], followed by extension to two-dimensional settings in [227]. A frictional contact formulation accompanied by the STS algorithm was employed to

model pile installation in normally consolidated undrained soils with low permeability in [228]. This study successfully simulated a number of realistic features of pile penetration for piles of a finite depth, but could simulate only pre-bored piles under the small sliding assumption. Unlike NTS, the completion of the patch test in conjunction with the STS algorithm was ensured, but STS was not able to satisfy the inf-sup condition [38, 167].

The mortar technique was then proposed as a possible alternative for constraining contacting bodies. It is similar to STS but retains the consistency of variational statements subject to contact constraints, maintaining the optimal convergence rate for the primary variables. The mortar technique passes the patch test and meets the inf-sup stability condition. It has very frequently been applied to various solid mechanic problems [229-232] and has been extended to simulate the influence of interfaces on nonlinear saturated porous media [233], to analyse torpedo anchors [234], and to apply a quadratic mortar-like discretisation to model the pile installation process [235], in which a frictional contact formulation was introduced. In this study, a possible large deformation between piles and the surrounding soils was consistently considered by using quadratic solid elements. However, the mortar technique involves considerable computational expense due to the need to evaluate mortar integrals [236].

Contact mechanics has been incorporated into a number of soil-structure interaction problems associated with the FEM. The cone penetration test in cohesionless soils was simulated in [237]. There, the mechanism of penetration and the prominent factors that may influence the penetrating process were comprehensively investigated. The evaluation of the stress and strain distributions induced by pushed-in piles being installed and loaded was studied in [238]. In this study, contact constraints were

enforced by minimising the total potential energy by introducing an additional Lagrange multiplier. In another geotechnical application, a frictional contact formulation within a FEM framework was employed to evaluate the performance of piles with enlarged ends, resulting in an improved formulation for estimating the capacity of such piles [239].

The contact constraints between two interacting bodies can, in general, be imposed through two main methods: the method of “Lagrange multipliers” and the “penalty method”. In the Lagrange multipliers method, the contact condition is imposed as a constraint on the governing variational formulation of the continuum problem. This way, the Lagrange multipliers can be interpreted as primary unknowns, by which the enforcement of the contact constraint is exactly imposed [240]. The Lagrange multipliers as primary variables are, therefore, to be treated like other primary variables and approximated in a similar fashion. Consequently, the introduction of the Lagrange multipliers as primary variables results in the increase of the algebraic system size and in the loss of the likely original symmetry of a formulation. In addition, the issues concerning the fulfilment of the inf-sup condition to ensure stability remain when employing Lagrange multipliers to introduce contact forces as primary variables [38]. The most convenient pair of choices associated with the approximation of primary variables, i.e., displacement and Lagrange multipliers, is ruled out by the inf-sup condition. Although several stabilisation remedies have been proposed to circumvent the inf-sup condition when Lagrange multipliers are introduced, e.g., see [241], they would likely either reduce numerical accuracy or impose difficulties when identifying and specifying the scale stabilisation parameter at an element level [85, 242, 243].

In the penalty method, the amplitude of stiffness at the contact surface between two bodies is assigned *a priori* at the places where the contact constraints are to be imposed.

As a result, the introduction of penetration between two contacting boundaries is inevitably admitted; this is related to the normal contact force through the contact stiffness, commonly known as the penalty parameter [244]. The accuracy of numerical solutions associated with fulfilling the contact constraints relies heavily on the magnitude of the contact stiffness, which must be large enough to satisfy the constraint condition, but not too large; otherwise, ill-conditioning problems would ensue. Benefiting from the advantages of both these techniques, other constraint algorithms have been proposed and successfully applied to contact problems. One of these well-established improved techniques is the augmented Lagrange multipliers method [240].

The concept of adaptive re-meshing has been used in a wide range of disciplines to accurately obtain numerical solutions to problems that involve moving discontinuities. The idea behind adaptive re-meshing is to enforce the conformity of mesh topology to evolving discontinuities by creating successively ever more conforming meshes and their subsequent projections of data over time or during iterations. Simoni and Secchi [245] introduced a two-dimensional cohesive crack relationship along with an adaptive re-meshing technique based on Delaunay mesh generation. They used this combination in an FEM framework for saturated porous media, followed by a study of the application of the method for a gravity concrete dam subjected to cyclic loading. A study that accounted for the thermo-mechanical coupling was proposed by Schrefler and Secchi [246], in which optimal mesh size was assured by repeated re-meshing. An adaptive technique was then proposed in [247] with an appropriate mapping operator that ensures a priori local satisfaction of balance equations is directly applied to nodal forces and fluxes. The mesh adaptivity and the cohesive crack concept were also extended to three-dimensional porous media problems in [248]. Generally, the difficulties of the FEM due to the restriction of interfacial configurations to element

boundaries and the preservation of inner element continuities result in significant computational costs when modelling moving discontinuities. In addition, projection of data between successive re-meshing may produce numerical errors.

Recently, much attention has been given to the “embedded” methods for simulation of interface problems. “Embedded” refers to problems where the interface geometry is allowed to be independent of some underlying bulk mesh. Related studies have extensively focused on the eXtended Finite Element Method (XFEM) and its application to a wide range of interface problems. XFEM can be seen as an extension of the finite element method for handling boundary value problems with moving discontinuities in which the conformity of the element boundaries to an interfacial geometry is not necessarily required. Conformity is satisfied through introducing enrichment functions to capture discontinuities inside elements representing cracks, material interfaces and even voids. The enrichment procedure exploits the partition of unity (PU) technique, originally proposed by Melenk and Babuška [59]. The PU property states that the sum of the interpolation functions must be unity. XFEM eliminates the necessity of successive mesh generations and the difficulties frequently encountered in the re-meshing procedure associated with the FEM. XFEM was first proposed for modelling two-dimensional cracks in [249, 250], followed by an extension to the three-dimensional setting in [251, 252]. Tangential discontinuities were modelled in [253, 254]. XFEM was applied to the modelling of voids in [255] and to material interfaces in [256].

The modelling of frictional contact across interfaces in XFEM framework has gained relatively less attention compared to the FEM. An XFEM formulation was presented by Khoei and Nikbakht [257] and by Liu and Borja [258] to properly simulate the frictional

contact problem constrained by the penalty technique. Liu and Borja [258] proposed an XFEM formulation, including embedded frictional contacts, for a finite deformation analysis that accommodated finite stretching and rotation. Nistor and Guiton [259] introduced a contact search algorithm that allowed systematic updates of contacting bodies in a hybrid X-FEM framework, formulated as XFEM coupled with a Lagrange large sliding contact algorithm under the assumption of large deformation. Recently, an NTS contact algorithm was formulated in [260] based on XFEM including large deformation employing the penalty technique. A stabilised augmented Lagrange multiplier was investigated in the XFEM framework in [261] in which the stabilisation technique previously employed by Béchet and Moës [241] was reformulated to alleviate the traction oscillation across a crack obtained by a constrained XFEM framework.

In a pioneering study, De Borst, Réthoré [262] presented the application of XFEM in modelling a propagating discontinuity, such as a crack or a shear band, in saturated porous media under a biaxial plane-strain condition. This was followed by an extension to dynamic analysis in [263]. The studies presented in [262, 263] assumed two pressure degrees of freedom across the discontinuity, without permission of possible fluid movement and storage in the discontinuity. The latter phenomenon was included in the coupled flow-deformation equation for the surrounding medium later, through a modified fluid continuity equation that represents the fluid transport and storage within the interface in [264] under the assumption of linear elastic fracture mechanics. Later on, the cohesive crack model [265, 266] and large deformation analysis [68] were also studied. The formulation was then extended to coupled problems in unsaturated porous media [63, 267, 268] and extended to include thermo-hydro-mechanical analysis in a two-dimensional setting by Khoei and Moallemi [64] and in a three-dimensional setting by Prevost and Sukumar [269]. An uncoupled approach in conjunction with modelling

of a single crack propagation pressurised by fluid was investigated in [270] by introducing a special treatment for the enrichment of crack tips, and in [271-273] by assuming an impervious surrounding medium. A three-dimensional impervious medium with cracks induced by fluid pressurisation was evaluated by Gupta and Duarte [274]. Remij, Remmers [275] also modelled a crack propagation induced by fluid pressure in a porous medium. They assumed an independent pressure variable for fluid within the discontinuity by including three independent pressure degrees of freedom at the interface.

Khoei and Vahab [65] presented a coupled hydro-mechanical variational statement for saturated porous media, with the XFEM framework, subject to the contact constraints arising from the participation of the crack closure mode. The proposed method exploited the penalty method to account for the contact constraint and for the fluid flow ceasing within the crack where the closure mode of the crack appears. The influence of hydraulic fracturing in gravity dams was investigated by the adoption of XFEM with a proper cohesive crack model in [276]. Using the XFEM framework, a steady-state analysis of the fluid flow leaking into a layered soil medium with wells was performed in [277].

An XFEM formulation was proposed in order to include weak discontinuities with arbitrary orientations arising from a large contrast in material properties in [61] in which the proposed formulation was verified by the simulation of a layered dam subjected to dynamic loading. Watanabe, Wang [217] proposed a novel method to represent the influence of pre-existing interfaces in rocks by employing lower-dimensional interfaces with locally defined enrichment functions. Two approaches relevant to the systematic computation of fluid flow and its corresponding interfacial forces within a cavity were

compared in [66] which accounted for the mixed mode of fractures, that necessitates to formulate a contact algorithm appropriately. Taleghani and Olson [278] formulated an enriched numerical method in order to simulate the hydraulic fracturing phenomenon in porous media and consider natural discontinuities in a medium, but they failed to introduce an appropriate enrichment function when the induced fractures is intersected by natural interfaces. Accordingly, the proposed method is valid only up to the threshold of an interfacial junction.

Although XFEM has shown robustness and accuracy in computational geomechanical applications, it possesses a number of inherent deficiencies. Numerical integration of discontinuous functions, used for reproducing the discontinuities in XFEM, complicates the numerical implementation of XFEM due to the necessary partitioning of elements intersected by an interface, reducing the accuracy of the numerical solutions. XFEM necessitates some recovery techniques, i.e., the derivative recovery proposed in [279] or the a posteriori treatment formulated in [280], in order to improve the computation of stress and its association with the stress intensity factor.

The numerical simulation of interfaces in geomechanics by MMs has gained little attention. Aimene and Nairn [281] proposed an MPM formulation to investigate the interaction of induced hydraulic fractures with natural interfaces, within the framework of linear fracture mechanics. In this study, crack propagation was governed by the maximum hoop stress criterion, and, through the adaptation of continuous fracture modelling proposed in [282].

In [283], SPH was applied to model rock fracturing stemming from magma intrusion. Oliaei, Pak [284] proposed a fully-coupled EFG formulation for the simulation of induced fractures in saturated porous media. This was followed by an improved form of

EFG, proposed in [285]. However, the numerical solutions obtained in the presence of discontinuities exhibited a slight oscillation, as previously reported for solid mechanics applications in [85, 286]. Thus, an enriched EFG formulation that incorporated weak discontinuities was proposed for both saturated and unsaturated porous media in [70] in order to restore the accuracy of the numerical solutions. In this study, various applicable enrichment functions relevant for the presence of a weak discontinuity were compared in term of accuracy. The previous study was then extended, in [71], to simulate a strong discontinuity due to a jump in the primary variable (displacement) and to compute its proportional cohesive forces, inspired by the formulation in [69]. Nonetheless, the term associated with fluid leakage in the fluid continuity equation arising from the transport or storage of fluid in cavity was overlooked. A novel DEM-SPH method was formulated in [136] to simulate induced fractures pressurised by a fluid. In this method, the displacement variable was represented by DEM while SPH adopted to simulate the fluid phase. This approach is however very computationally demanding. Some advanced MMs, e.g., SPIM and SRPIM, have not been yet applied in simulation of moving discontinuities in multiphase media.

The Table 2-1 summarizes almost MMs applications in geotechnical engineering as well as geomechanics mentioned in this study.

Table 2-1. The summary of MMs applications in geotechnical engineering and geomechanics discussed in this study.

Method	Applications in geotechnical engineering and geomechanics
EFG	[106],[107],[287],[108],[284],[9],[110],[152],[153],[285],[70, 71].
MPLG	[111],[112],[288].
MPM	[114],[115],[116],[117],[118],[119],[120],[121],[281].
DEM	[123],[124],[125],[136].
FPM	[126],[127],[128],[129].
SPH	[130],[131],[132],[133],[134],[135],[283],[136].
PFEM	[137],[138].
PIM/RPIM	[141],[142],[144],[145],[147],[146].
SPIM/SRPIM	[35],[289],[148].
Soft Particle Method	[149],[150]

2.6 Conclusion

In this chapter, a general classification of MMs has been presented in terms of their representation of the variable approximation, followed by their relative deficiencies compared to the recently proposed MMs such as PIM/RPIM. This chapter has also discussed a comprehensive application of MMs in geotechnical engineering and computational geomechanics which is more or less classified based on the methods used. Various stabilisation techniques have been discussed and classified. The special features of discussed stabilisation methods as well as their deficiencies have been highlighted in this chapter. It has been shown that the adoption of a consistent

stabilisation technique accompanied by the smoothing gradient technique would facilitate the use of equal order linear interpolation while obtaining theoretical consistency features. This needs to an extension of SPIM/SRPIM towards the coupled flow-deformation analysis of saturated porous media at first. The end section of this chapter has presented the various applications of numerical methods when interfaces are included in geotechnical engineering problems. These applications include soil-structure interactions and the saturated and unsaturated porous media with the propagating or pre-existing cracks as well as the material interfaces. It has shown that various numerical techniques were applied to different interfacial configurations involved in geotechnical problems, some of which have addressed difficulties associated with inserting the interfacial geometries independent of the underlying discretisation such as XFEM.

3 Application of cell-Based smoothed point interpolation methods in the flow-Deformation analysis of saturated porous media

3.1 Introduction

In this chapter, the numerical techniques adopted for numerical analysis of the problems in this study is described in detail. These methods, called cell-based smoothed point interpolation methods (CSPIM), are based on the generalised gradient smoothing technique recently developed by Liu and his coworkers [13, 15, 16, 20, 89, 101, 105]. In the proposed methods, the problem domain is first discretised with the use of a simple triangular background mesh. The purpose of the background mesh is twofold: (i) it is used to select the supporting nodes for each point of interest for the construction of nodal shape functions, and (ii) the cells of the background mesh serve as the smoothing domains. Spatial discretisation of the coupled partial differential equations is derived by applying the weakened weak (W^2) formulation referred to as the Generalised Smoothed Galerkin method. Both displacement and pressure fields are interpolated using the point interpolation shape functions (polynomial and radial) which are described in detail in this chapter. In the formulations proposed, shape function differentiations are eliminated with the use of the smoothed gradient technique, leading to the definition of the smoothed strains and pressure gradients. Temporal discretisation is performed with a three-point time discretisation scheme with variable time steps. Different node selection schemes, known as T-schemes, to guarantee the non-singularity of the moment matrices

in creating shape functions are described. The methods are presented in this chapter for the solution of the fully coupled equations governing the behaviour of a fully saturated porous media. The accuracy and convergence rate of the methods are investigated through comparison of the numerical results of the proposed methods with those obtained using analytical/semi-analytical solutions, point interpolation methods, and standard finite element methods. The formulation presented in this chapter is adopted for further developments in the subsequent chapters.

3.2 Governing equations

The partial differential equations governing the fluid flow and deformation in elastic saturated porous media, first developed by Biot [161], are presented here. The saturated medium is presented by two interacting continuum phases, i.e. soil skeleton and fluid phase. The coupling of the two phases is described by the effective stress principle. Inertia effects are neglected, and homogeneity is assumed. The compact matrix-vector notation is used, with bold imprints denoting vectors and matrices, and an over-dot representing the time derivative. Throughout this thesis, for the soil skeleton, tensile stresses are assumed to be positive according to the sign convention of continuum mechanics. However, the pore fluid pressure is considered positive in compression according to soil mechanics convention.

The combination of the overall equation of equilibrium, linear momentum balance and mass balance equations for the fluid phase results in the governing coupled differential equations for the domain as follows [161]:

$$\mathbf{L}_d^T(\boldsymbol{\sigma}' - \eta p \boldsymbol{\delta}) + \rho \mathbf{g} = \mathbf{0} \quad (\text{Equilibrium}) \quad (3-1)$$

$$\nabla \cdot \left[\frac{\mathbf{k}_f}{\mu_f} (-\nabla p + \rho_f \bar{\mathbf{g}}) \right] + \alpha_f \dot{p} + \nabla \cdot \dot{\mathbf{u}} = 0 \text{ (Continuity)} \quad (3-2)$$

in which the differentiation operator \mathbf{L}_d is defined as:

$$\mathbf{L}_d = \begin{bmatrix} \frac{\partial}{\partial x_1} & 0 \\ 0 & \frac{\partial}{\partial x_2} \\ \frac{\partial}{\partial x_2} & \frac{\partial}{\partial x_1} \end{bmatrix} \quad (3-3)$$

with x_1 and x_2 being space coordinates. ∇ is the gradient operator expressed as $\nabla = \mathbf{L}_d^T \boldsymbol{\delta}$, with $\boldsymbol{\delta} = [1 \ 1 \ 0]^T$. Equation 3-1 is derived from the equilibrium equation for the solid phase, while Equation 3-2 represents the continuity condition for the fluid phase obtained by inserting Darcy's law for fluid flow within porous media into the fluid mass balance equation. $\boldsymbol{\sigma}'$ denotes the effective stress acting on the solid phase which is linked to the total stress $\boldsymbol{\sigma}$ by Terzaghi's effective stress principle. $\mathbf{g} = [0 \ g \ 0]^T$ and $\bar{\mathbf{g}} = [0 \ g]^T$ express two different representations of the gravity acceleration vectors with g denoting the gravitational constant. \mathbf{u} represents the displacement field of the solid phase; p is the fluid pressure; \mathbf{k}_f indicates the intrinsic permeability of the porous media; μ_f is the dynamic viscosity of the fluid phase; ρ_f is the density of the fluid; and ρ is the buoyant porous medium density. $\alpha_f = n(C_f - C_s) + \eta C_s$, in which $\eta = 1 - \frac{C_s}{C}$. n is the porosity, and C_f , C_s and C are the compressibility of the fluid phase, the compressibility of the solid grains, and the drained compressibility of the porous medium, respectively.

The adequate essential and natural boundary conditions that are required for the sake of the solvability of Equation 3-1 and Equation 3-2 are presented in the following forms:

$$\mathbf{u}(\mathbf{x}, t) = \bar{\mathbf{u}}(t) \quad \text{specified displacement} \quad \text{on } \Gamma_u \quad (3-4)$$

$$\mathbf{n}^T \boldsymbol{\sigma}'(\mathbf{x}, t) = \bar{\mathbf{t}}(t) \quad \text{specified traction} \quad \text{on } \Gamma_t \quad (3-5)$$

$$p(\mathbf{x}, t) = \bar{p}(t) \quad \text{specified pressure} \quad \text{on } \Gamma_p \quad (3-6)$$

$$-\mathbf{n}^T \mathbf{w}(\mathbf{x}, t) = \bar{q}(t) \quad \text{specified flux} \quad \text{on } \Gamma_q \quad (3-7)$$

where \mathbf{n} is the outward unit normal vector, expressed in a matrix form as:

$$\mathbf{n} = \begin{bmatrix} n_{x_1} & 0 & n_{x_2} \\ 0 & n_{x_2} & n_{x_1} \end{bmatrix}^T \quad (3-8)$$

in which n_{x_1} and n_{x_2} are the unit normal components at the point of interest in the x_1 and x_2 directions, respectively. The formulation presented here is developed for two-dimensional setting.

In the standard fashion, Γ_u , Γ_t , Γ_p , and Γ_q are restricted regions of the boundary of the domain such that:

$$\Gamma = \Gamma_u \cup \Gamma_t = \Gamma_p \cup \Gamma_q \quad (3-9)$$

$$\Gamma_u \cap \Gamma_t = \Gamma_p \cap \Gamma_q = \emptyset \quad (3-10)$$

3.3 Constitutive modelling

For the sake of simplicity, isotropic elastic behaviour has been assumed for the solid phase throughout this thesis except some parts where other assumptions are emphasised. The stress–strain relationship expressing the interaction between the soil skeleton and the fluid phase is given by

$$\dot{\boldsymbol{\sigma}} = \mathbf{D} \dot{\boldsymbol{\epsilon}} - \eta \dot{p} \boldsymbol{\delta} \quad (3-11)$$

in which $\boldsymbol{\sigma}$ is the total stress tensor. The over dot here indicates the rate form of the stress-strain relationship due to the possible nonlinearity of the constitutive behaviour of the porous media. It does not mean the real time derivative. For isotropic elastic media, the stress-strain relationship can be written in the following form

$$\dot{\boldsymbol{\sigma}} = 2G\dot{\boldsymbol{\varepsilon}} - (\lambda \text{tr}\dot{\boldsymbol{\varepsilon}} + \eta \dot{p})\boldsymbol{\delta} \quad (3-12)$$

where $G = \frac{E}{2(1+\nu)}$ and $\lambda = \frac{\nu E}{(1+\nu)(1-2\nu)}$ are Lamé constants, with E being the elasticity modulus and ν being the Poisson's ratio. tr is the trace operator, with $\text{tr}\dot{\boldsymbol{\varepsilon}}$ representing the soil volumetric strain.

3.4 Cell-based smoothed PIM/RPIM

As discussed in the previous chapter, the SPIM and SRPIM are powerful meshfree methods that are recently developed. In these methods, instead of a compatible strain field, the smoothing operation is used to construct the smoothed strain field. Not only does the strain field construction solve the problem associated with the compatibility of approximation functions, it also increases the accuracy of the numerical solution, mainly through elimination of the need for the derivatives of the shape functions. To apply smoothing operation techniques, smoothing domains need to be constructed. The smoothing domains are generally independent from the background mesh and are constructed on top of the existing mesh in such a way that the *no sharing rule* is met [15, 16]. Different approaches to construct permissible smoothing domains have been developed in the literature [16, 20, 101, 102]. In the simplest case, the cells of the background mesh can be directly used to serve as the smoothing domains [20]. This process leads to one of the simplest SPIMs, called the cell-based SPIM (CSPIM). In this

method, no additional operation is needed to construct smoothing domains. This is adopted in this study and is fully described in the subsequent sections.

3.4.1 Construction of shape functions

Two types of shape functions, formulated with different basis functions, can be considered in cell-based smoothed methods: polynomial point interpolation method (PIM) shape functions which use polynomial basis functions [87], and radial point interpolation method (RPIM) shape functions which use both polynomial and radial basis functions (RBFs) [88].

For PIM shape functions, the arbitrary field approximation function of interest, $v(\mathbf{x})$, in the space coordinates $\mathbf{x} = [x_1, x_2]$ is approximated at any point in the problem domain with the following series representation:

$$v(\mathbf{x}) = \sum_{i=1}^p b_i p_i(\mathbf{x}) = \mathbf{p}^T(\mathbf{x}) \mathbf{b} \quad (3-13)$$

where $p_i(\mathbf{x})$ is the polynomial basis function (monomial terms), and p is the number of nodes in the compact support domain (the supporting nodes) of the point of interest (referred to as set S_n for each point of interest). b_i is the coefficient for the corresponding monomial term $p_i(\mathbf{x})$, which forms vector \mathbf{b} , as shown in Equation 3-13.

The explicit forms of \mathbf{b} and $\mathbf{p}(\mathbf{x})$ are as follows:

$$\mathbf{b}^T = [b_1 \quad b_2 \quad \cdots \quad b_p] \quad (3-14)$$

$$\mathbf{p}^T(\mathbf{x}) = [1 \quad x_1 \quad x_2 \quad x_1^2 \quad x_1 x_2 \quad x_2^2 \quad \cdots] \quad (3-15)$$

The monomial terms of \mathbf{p} , $p_i(\mathbf{x})$, are selected from Pascal's triangle starting from lower orders to ensure completeness of the basis to a desired order, and also to satisfy the consistency requirement of the shape functions.

In RPIM, radial basis functions augmented with polynomials are used to approximate the field function in the following way:

$$v(\mathbf{x}) = \sum_{i=1}^p a_i R_i(\mathbf{x}) + \sum_{j=1}^l b_j p_j(\mathbf{x}) = \mathbf{R}^T(\mathbf{x})\mathbf{a} + \mathbf{p}^T(\mathbf{x})\mathbf{b} \quad (3-16)$$

in which $R_i(\mathbf{x})$ and $p_j(\mathbf{x})$ are the RBFs and monomial terms, respectively. a_i is the coefficient for radial basis $R_i(\mathbf{x})$, and b_j is the coefficient for the polynomial basis $p_j(\mathbf{x})$. p is again the number of nodes in the compact support domain of the point of interest (set S_n), and l is the number of monomial terms. In a 2D setting, at least three monomial terms ($l = 3$) are needed to ensure the linear consistency of the approximation function. From Equation 3-16, it is clear that if no RBF is adopted and $l = p$ is assumed, RPIM formulation is reduced to PIM formulation.

A number of different RBFs, such as the Multi-Quadric basis (MQ) function, the Gaussian function, the thin plate spline function, and the compactly supported RBF can be used in construction of RPIM shape functions. In this thesis, MQ is adopted resulting in the following definition for $R_i(\mathbf{x})$:

$$R_i(\mathbf{x}) = (r_i^2 + (\alpha_c d_c)^2)^q, \quad \alpha_c \geq 0 \quad (3-17)$$

in which r_i is the distance between the point of interest $\mathbf{x} = (x_1, x_2)$ and the field node

$$\mathbf{x}_i = (x_{1i}, x_{2i}) \quad (r_i = \sqrt{(x_1 - x_{1i})^2 + (x_2 - x_{2i})^2}), \text{ and } \alpha_c \text{ and } q \text{ are dimensionless}$$

parameters that control the shape of the approximation function. The shape parameters can be tuned to improve the performance of the numerical method. They are assumed as

$\alpha_c=1$ and $q = 1.03$ in this study in accordance with the recommendations in [290]. d_c implies the average nodal spacing.

The unknown coefficients a_i and b_j in Equation 3-16 are now determined by enforcing the approximation function to pass through all the nodes in the local support domain of the point of interest. Assuming only one degree of freedom per node for the sake of simplicity, p equations are obtained as follows

$$v_h = v(\mathbf{x}_h) = \sum_{i=1}^p a_i R_i(\mathbf{x}_h) + \sum_{j=1}^l b_j p_j(\mathbf{x}_h) \quad , \quad h = 1, 2, \dots, p \quad (3-18)$$

where v_h represents the nodal value of the independent variable at the h th node in the support domain. l more equations are needed to uniquely quantify a_i and b_j . The following extra l constraints are enforced:

$$\sum_{i=1}^p a_i p_j(\mathbf{x}_i) = 0 \quad j = 1, 2, \dots, l. \quad (3-19)$$

The matrix form of Equations 3-18 and 3-19 takes the following form:

$$\begin{bmatrix} \mathbf{R}_0 & \mathbf{P} \\ \mathbf{P}^T & \mathbf{0} \end{bmatrix} \begin{bmatrix} \mathbf{a} \\ \mathbf{b} \end{bmatrix} = \mathbf{G} \begin{bmatrix} \mathbf{a} \\ \mathbf{b} \end{bmatrix} = \begin{bmatrix} \mathbf{u} \\ \mathbf{0} \end{bmatrix} \quad \left(\mathbf{G} = \begin{bmatrix} \mathbf{R}_0 & \mathbf{P} \\ \mathbf{P}^T & \mathbf{0} \end{bmatrix} \right) \quad (3-20)$$

where

$$\mathbf{R}_0 = \begin{bmatrix} R_1(r_1) & R_2(r_1) & \dots & R_p(r_1) \\ R_1(r_2) & R_2(r_2) & \dots & R_p(r_2) \\ \vdots & \vdots & \ddots & \vdots \\ R_1(r_p) & R_2(r_p) & \dots & R_p(r_p) \end{bmatrix}_{(p \times p)} \quad (3-21)$$

$$\mathbf{P} = \begin{bmatrix} P_1(\mathbf{x}_1) & P_2(\mathbf{x}_1) & \dots & P_l(\mathbf{x}_1) \\ P_1(\mathbf{x}_2) & P_2(\mathbf{x}_2) & \dots & P_l(\mathbf{x}_2) \\ \vdots & \vdots & \ddots & \vdots \\ P_1(\mathbf{x}_p) & P_2(\mathbf{x}_p) & \dots & P_l(\mathbf{x}_p) \end{bmatrix}_{(p \times l)} = \begin{bmatrix} 1 & x_{1_1} & x_{2_1} & \dots & P_l(\mathbf{x}_1) \\ 1 & x_{1_2} & x_{2_2} & \dots & P_l(\mathbf{x}_2) \\ 1 & x_{1_3} & x_{2_3} & \dots & P_l(\mathbf{x}_3) \\ \vdots & \vdots & \ddots & \vdots & \vdots \\ 1 & x_{1_p} & x_{2_p} & \dots & P_l(\mathbf{x}_p) \end{bmatrix}_{(p \times l)} \quad (3-22)$$

\mathbf{G} is the combined moment matrix and \mathbf{v} is the vector of nodal values with the following explicit form

$$\mathbf{v}^T = [u_1 \quad u_2 \quad u_3 \quad \dots \quad u_p] \quad (3-23)$$

Using Equation 3-20, the approximation function can be presented as follows

$$v(\mathbf{x}) = \mathbf{R}^T(\mathbf{x})\mathbf{a} + \mathbf{p}^T(\mathbf{x})\mathbf{b} = \{\mathbf{R}^T(\mathbf{x}) \quad \mathbf{p}^T(\mathbf{x})\} \begin{bmatrix} \mathbf{a} \\ \mathbf{b} \end{bmatrix} = \{\mathbf{R}^T(\mathbf{x}) \quad \mathbf{p}^T(\mathbf{x})\} \mathbf{G}^{-1} \begin{bmatrix} \mathbf{u} \\ \mathbf{0} \end{bmatrix} \quad (3-24)$$

Finally, the RPIM shape functions, $\phi_i(\mathbf{x})$, can be obtained from Equation 3-24 as

$$\phi_i(\mathbf{x}) = \sum_{j=1}^p R_j(\mathbf{x})G_{j,i}^{-1} + \sum_{j=1}^l p_j(\mathbf{x})G_{j+p,i}^{-1} \quad (3-25)$$

in which $G_{j,i}^{-1}$ stands for the components of \mathbf{G}^{-1} . Invertibility of \mathbf{G} matrix can be guaranteed in all practical cases by adopting appropriate node selection schemes for determination of the supporting nodes at each point of interest and also by imposing $l < p$ [90].

The shape functions constructed using PIM or RPIM possess the Kronecker delta function property, which results in an easy implementation of the essential boundary conditions. The shape functions also satisfy the partition of unity (PU) condition at each point of interest, \mathbf{x} , which is expressed as $\sum_{i=1}^p \phi_i(\mathbf{x}) = 1$. When the point of interest moves across the problem domain, the nodes in the compact support domain of the point of interest are updated accordingly. This involves sudden inclusion or exclusion of new nodes in the support domain which results in the approximation function created using RPIM/PIM shape functions being discontinues across the problem domain. This issue will be thoroughly addressed later in the study.

3.4.2 Node selection schemes

In the CSPIM and CSRPIIM, the cells of the triangular background mesh are used for the selection of the supporting nodes at each point of interest within the problem domain. A set of supporting node selection schemes, known as T-schemes, has been proposed to provide automatic node selection algorithms using the background mesh that ensure the invertibility of the combined moment matrix. A salient feature of the T-schemes is that supporting domains could be automatically and efficiently constructed without any manual operation. The node selection scheme must also be compatible with the smoothing domains selected to satisfy the *no sharing rule*. This rule stipulates that the selection of the smoothing domains and the T-scheme must be in such a way to ensure that boundary of the smoothing domains do not share any line segment on which the assumed displacement field is discontinues [291]. A good overview of the different node selection schemes permissible for CSPIM and CSRPIIM and their properties can be found in [20]. In this chapter and other relevant chapters, two of the node selection schemes developed for CSPIM and CSRPIIM, referred to as T4 and T2L, are adopted. T4 can be used in both CSPIM and CSRPIIM, whereas T2L works only with CSRPIIM. The schematic representation of the T4 and T2L node selection schemes is depicted in Figure 3.1. In all T-schemes, for any point of interest on the boundary of the problem domain, linear interpolation using the two boundary points adjacent to the point of interest is always used [20]. This is needed so that the numerical scheme can pass the standard patch test [4].

As shown in **Figure 3.1**, for a point of interest (quadrature point) inside the domain, the T4 scheme selects four nodes of the two cells sharing the edge hosting the point of interest, as opposed to the T2L scheme which selects two layers of nodes around the point of interest. The first layer is the same as those nodes selected in the T4 scheme,

and the second layer are comprised of the nodes directly connected to the first-layer nodes.

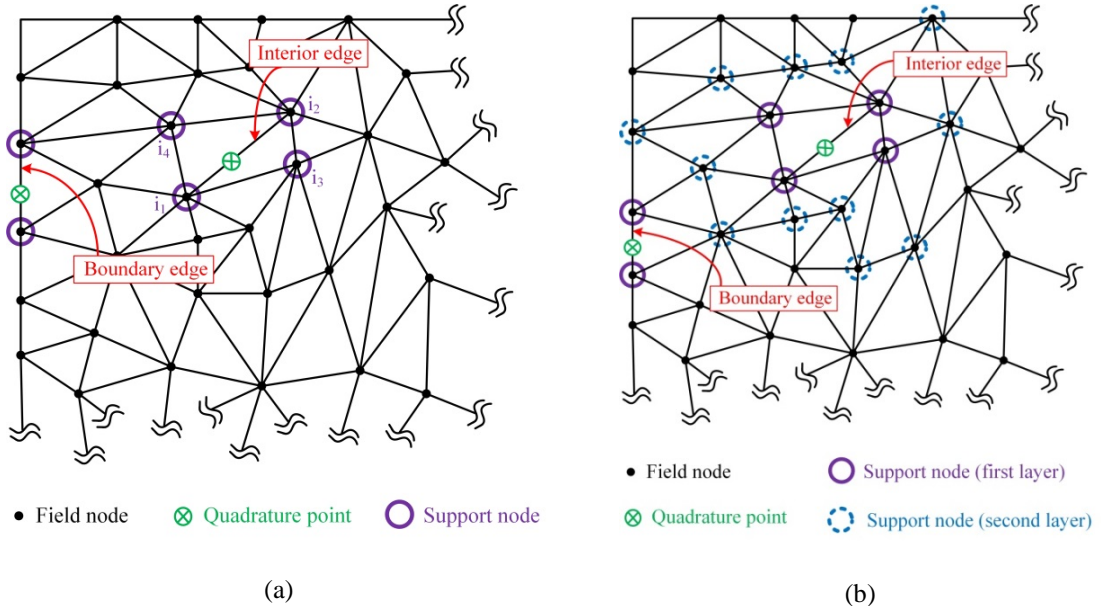


Figure 3.1. T-schemes used in this study to select the supporting nodes, (a) T4 scheme; (b) T2L scheme.

3.5 G Space theory and smoothing operation

3.5.1 G space theory

A G space containing a set of discrete functions has recently been proposed by Liu [13, 14] and Liu and Zhang [20]. This space was introduced to include not only piecewise continuous functions, but also some discontinuous functions which allows a wider range of numerical techniques to be utilised for the solution of the equations of interest. The inclusion of some discontinuous functions in the G space allows the use of the smoothing gradient technique in the numerical procedure which has some attractive features discussed later throughout this thesis. The G_h^1 that is used throughout this thesis can then be expressed as follows:

$$G_h^1(\Omega) = \begin{cases} v|_v(\mathbf{x}) = \sum_{n=1}^N \phi_n(\mathbf{x})e_n = \boldsymbol{\phi}(\mathbf{x})\mathbf{e}, \mathbf{e} \in \mathbf{R}^N \\ v \in L^2(\Omega), \\ \sum_{k=1}^{N_s} (\int_{\Gamma_k^s} v(S) n_i ds)^2 > 0 \Leftrightarrow v \notin \mathbb{R}; i = 1, \dots, d \end{cases} \quad (3-26)$$

in which v is the field variable of interest, approximated by a set of shape functions ϕ_n in terms of the yet unknown nodal values of the variable of interest e_n , globally collected in $\boldsymbol{\phi}(\mathbf{x})$ and \mathbf{e} vectors, respectively. N is the number of supporting nodes; N_s denotes the number of boundary segments of the domain of interest; ds is the length of the k th boundary segment of the boundary; Ω is the domain of interest, \mathbb{R} symbolises the functional space, of which ϕ_n is the basis.

The major difference between the G_h^1 space and the H_h^1 space is that the H_h^1 space necessitates that the function as well as its first gradient be square integrable, while for the G_h^1 space, only the function itself must be square integrable. Therefore, the functional requirement is now further weakened in addition to the already weakened requirement for functions in H_h^1 space. Hence, the G_h^1 space can be referred to as a space of a set of functions, each of which fulfils the weakened weak (W^2) requirements on continuity. In H_h^1 space, the continuity of the function is ensured by inducing the bounded condition upon the first derivatives of the function. Therefore, in numerical techniques that are cast in H_h^1 space, like the FEM for example, the nodal shape functions need to be continuous over the problem domain. Thanks to the *Poincare-Friedrichs'* inequality, numerical stability is automatically guaranteed when approximation functions belong to H_h^1 space, provided that the desired degree of smoothness is satisfied. However, in G_h^1 space, the bounded condition is only enforced for the function. It can be shown that the numerical stability in the G_h^1 space is guaranteed by proper creation of sufficient smoothing domains [92].

A function in the G_h^1 space is also a member of the L^2 space, therefore, G_h^1 space is indeed a subspace of L^2 space. Any function interpolated by the FEM shape functions fulfils the aforementioned three conditions for the inclusion in G_h^1 space, and therefore is a member of the G_h^1 space with the fulfilment of the minimum number of constructed smoothing domains. The proof is presented in [89]. Therefore, all the conjectures proven for functions in a G_h^1 space also remain valid for those in H_h^1 .

3.5.2 Smoothing gradient operation

In SPIM/SRPIM, the gradient of the displacement field is approximated over smoothing domain by an integral representation, which is given by:

$$\tilde{\nabla} \mathbf{u} = \int_{\Omega} \nabla \mathbf{u}(\xi) W(\mathbf{x} - \xi) d\xi, \quad (3-27)$$

in which $W(\mathbf{x} - \xi)$ is a pre-described smoothing function and $\tilde{\nabla} \mathbf{u}$ represents the smoothed form of the gradient of the displacement field. \mathbf{u} is assumed to be square integrable, in which Ω is the area of any taken arbitrary domain in a two-dimensional setting in the sense of *Lebesgue* integration that allows occasional discontinuity at finite points within the domain of interest. ξ implies the dependency of the pre-described smoothing function and the gradient of the displacement field, together commonly known as Convolution integral. For simplicity, the *Heaviside* function is conventionally adopted as the smoothing function:

$$W(\mathbf{x} - \xi) = \begin{cases} \frac{1}{A_k^s} & \xi \in \boxed{\Omega}_x \\ 0 & \xi \notin \boxed{\Omega}_x \end{cases}, \quad (3-28)$$

where $\boxed{\Omega}_x$ denotes the field domain accompanied by its boundary associated with the point of interest $\mathbf{x} \in \Omega$ and A_k^s is the area of the corresponding smoothing domain Ω_k^s . Knowing the displacement field, the smoothed gradient of the displacement field can be obtained for any smoothing domain using Equations 3-27 and 3-28, and the Divergence theorem, resulting in:

$$\tilde{\boldsymbol{\varepsilon}} = \frac{1}{A_k^s} \int_{\Omega} \nabla \mathbf{u}(\mathbf{x}) d\Omega = \frac{1}{A_k^s} \int_{\Gamma} \mathbf{L}_n \mathbf{u}(\mathbf{x}) d\Gamma, \quad (3-29)$$

where \mathbf{L}_n stands for the matrix composed of the components of the unit outward normal vector, with the arrangement of entries as:

$$\mathbf{L}_n = \begin{bmatrix} n_{x_1} & 0 \\ 0 & n_{x_2} \\ n_{x_2} & n_{x_1} \end{bmatrix}. \quad (3-30)$$

3.5.3 Cell-based smoothed strains

To overcome the problem of discontinuity of the approximation function over the problem domain, smoothed strains are utilised in CSPIM and CSRPI in place of compatible strains. The smoothed strains are obtained using the generalised smoothing operation (Equation 3-29). To this end, the problem domain, Ω , is divided into a number of linearly independent smoothing domains, Ω_k^s , which satisfy the following conditions:

$$\Omega = \bigcup_{k=1}^{N_{SD}} \Omega_k^s \quad (3-31)$$

$$\Omega_i^s \cap \Omega_j^s = \emptyset, i \neq j \quad (3-32)$$

where Ω_k^s ($k = 1, \dots, N_{SD}$) is the k th smoothing domain, and N_{SD} is the total number of smoothing domains in the problem domain. As mentioned before, in CSPIM and

CSRPIIM, the cells of the background mesh are directly used as the smoothing domains as depicted in Figure 3.2.

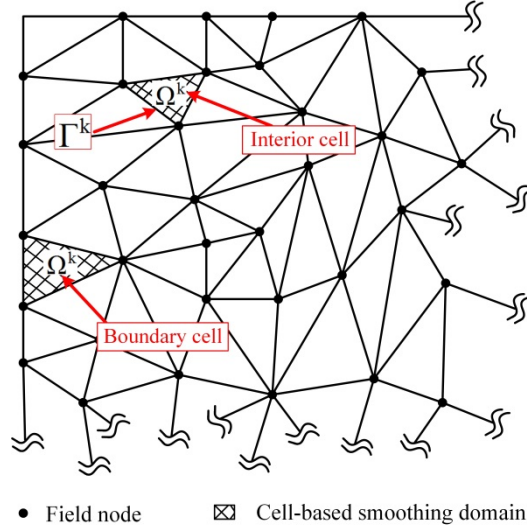


Figure 3.2. The schematic representation of smoothing domains in CSPIM and CSRPIIM methods.

The smoothed strain can be expressed in terms of the nodal displacement values for each smoothing domain in the following familiar format:

$$\tilde{\boldsymbol{\epsilon}}^{(k)} = \tilde{\mathbf{B}}_1 \mathbf{u} \quad (3-33)$$

where $\tilde{\mathbf{B}}_1$ is the smoothed strain-displacement matrix for each smoothing domain, which is obtained by the summation of the smoothed strain-displacement matrices computed at the quadrature points on the edges of the smoothing domains, as follows

$$\tilde{\boldsymbol{\epsilon}}^{(k)} = \sum_{i=1}^q \tilde{\mathbf{B}}_{1i} \mathbf{u}_i \quad i \in S_s \quad (3-34)$$

in which S_s is the set of q support nodes which includes all the nodes involved in the interpolation of quadrature points located on all segments of boundary Γ_k^S for each

smoothing domain Ω_k^S . S_n which is defined earlier is always a subset of S_s at each point of interest (quadrature point). An illustration of these two sets based on a T4 node selection scheme for an arbitrary quadrature point of interest is shown in Figure 3.3.

The smoothed matrices $\tilde{\mathbf{B}}_{1l}$ and $\tilde{\mathbf{B}}_1$ are in fact of the following forms, respectively:

$$\tilde{\mathbf{B}}_{1l} = \begin{bmatrix} \tilde{b}_{lx_1} & 0 \\ 0 & \tilde{b}_{lx_2} \\ \tilde{b}_{lx_2} & \tilde{b}_{lx_1} \end{bmatrix} \quad (3-35)$$

$$\tilde{\mathbf{B}}_1 = \begin{bmatrix} \tilde{b}_{1x_1} & 0 & & \tilde{b}_{qx_1} & 0 \\ 0 & \tilde{b}_{1x_2} & \cdots & 0 & \tilde{b}_{qx_2} \\ \tilde{b}_{1x_2} & \tilde{b}_{1x_1} & & \tilde{b}_{qx_2} & \tilde{b}_{qx_1} \end{bmatrix}_{3 \times 2q} \quad (3-36)$$

in which the components of $\tilde{\mathbf{B}}_1$ are obtained by summation over all the quadrature points along the segments of the boundary of each smoothing domain,

$$\tilde{b}_{il} = \frac{1}{2A_k^S} \sum_{m=1}^{N_{seg}} \left[L_m^k \sum_{n=1}^{N_{gau}} w_n \phi_l(\mathbf{x}_{mn}) n_l(\mathbf{x}_{mn}) \right] \quad (l = x_1, x_2) \quad (3-37)$$

where N_{seg} is the number of line segments of the boundary Γ_k^S , L_m^k is the length of the m th segment of Γ_k^S , n_l represents the component of the unit outward normal to the corresponding segment of Γ_k^S and N_{gau} is the number of quadrature points used in each segment of Γ_k^S , which is taken two for both CSPIM and CSRPI in this study. \mathbf{x}_{mn} is the n th quadrature point of the m th segment of Γ_k^S , and w_n is the Gauss integration weight of the corresponding quadrature point. $\phi_i(\mathbf{x}_{mn})$ is the shape function value for node $i \in S_s$ at the point of interest \mathbf{x}_{mn} . If the current quadrature point $i \notin S_n$, then $\phi_i(\mathbf{x}_{mn}) = 0$.

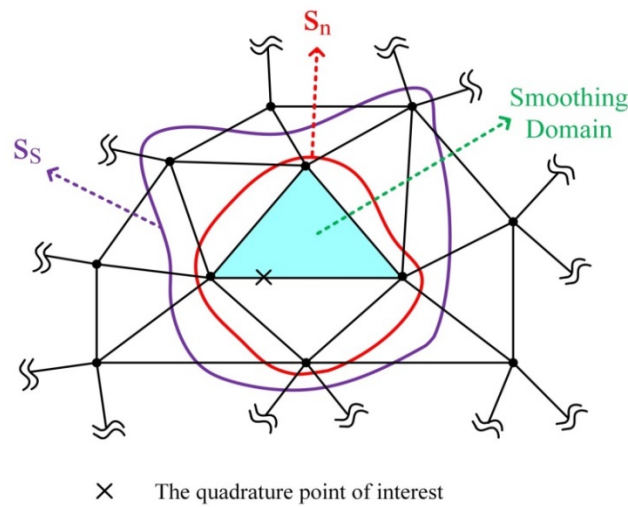


Figure 3.3. A schematic representation of S_n and S_s for an arbitrary quadrature point of interest assuming a T4 node selection scheme.

Note that the formulation of the smoothed strains does not contain shape function derivatives. Therefore, the discontinuity of the approximation function over the problem domain does not pose any problem in calculation of the smoothed strains. Moreover, this implies that compared to the standard weak formulation, the consistency requirement to shape functions is further reduced which is why the formulation is called a weakened weak (W^2) formulation [15, 16].

3.6 Numerical model

In this section, the Generalised Smoothed Galerkin (GS Galerkin) approach is used for spatial discretisation of the governing equations to obtain the weekend weak forms of the coupled flow-deformation equations. The weekend weak forms are then discretised in time to yield the fully discretised form of the governing equations. The unknown

variables are presented in terms of their nodal values with the use of PIM/RPIM shape functions. The unknown variables are solid phase displacements and excess pore fluid pressure in the domain.

3.6.1 Spatial discretisation

Applying the GS Galerkin method to governing Equations 3-1 and 3-2 yields the spatially discretised forms of the governing equations for saturated porous media in the following form [292]:

$$\tilde{\mathbf{K}}\mathbf{U} - \eta\tilde{\mathbf{C}}\mathbf{P} = \mathbf{F} \quad (3-38)$$

$$\eta\tilde{\mathbf{C}}^T\dot{\mathbf{U}} + \tilde{\mathbf{H}}\mathbf{P} + a_f\mathbf{M}\dot{\mathbf{P}} = \mathbf{T} \quad (3-39)$$

where \mathbf{U} is the global nodal displacement vector, \mathbf{P} is the nodal excess pore fluid pressure values, \mathbf{F} is the vector of nodal forces, \mathbf{T} is the vector of nodal fluxes, and $\tilde{\mathbf{K}}$, $\tilde{\mathbf{C}}$, $\tilde{\mathbf{H}}$ and \mathbf{M} are the global property matrices. These matrices are derived from assembly of the corresponding local property matrices obtained from each smoothing domain as follows:

$$\tilde{\mathbf{K}}_k^s = \int_{\Omega_k^s} \tilde{\mathbf{B}}_1^T \mathbf{D} \tilde{\mathbf{B}}_1 d\Omega \quad (3-40)$$

$$\tilde{\mathbf{C}}_k^s = \int_{\Omega_k^s} \tilde{\mathbf{B}}_1^T \delta \mathbf{N}^p d\Omega \quad (3-41)$$

$$\tilde{\mathbf{H}}_k^s = \int_{\Omega_k^s} \frac{k_f}{\mu_f} \tilde{\mathbf{B}}_2^T \tilde{\mathbf{B}}_2 d\Omega \quad (3-42)$$

$$\mathbf{M}_k = \int_{\Omega_k^s} \mathbf{N}^p{}^T \mathbf{N}^p d\Omega \quad (3-43)$$

$$\mathbf{T}_k = \int_{\Gamma_k^s} \mathbf{N}^p{}^T \bar{q} d\Gamma \quad (3-44)$$

$$\mathbf{F}_k = \int_{\Omega_k^s} \mathbf{N}^{uT} \rho \mathbf{g} d\Omega + \int_{\Gamma_k^s} \mathbf{N}^{uT} \bar{\mathbf{t}} d\Gamma \quad (3-45)$$

The entries of $\tilde{\mathbf{K}}$ are calculated as follows:

$$\tilde{\mathbf{K}} = \sum_{k=1}^{N_{SD}} \tilde{\mathbf{K}}_k^s = \sum_{k=1}^{N_{SD}} \tilde{\mathbf{B}}_1^T \mathbf{D} \tilde{\mathbf{B}}_1 A_k^s \quad (3-46)$$

in which summation indicates the conventional assembly procedures to construct the global stiffness matrix of the system. Equation 3-46 shows that no transformation to the natural coordinates is required in the CSPIM/CSRPIM because the smoothed strain-displacement matrix ($\tilde{\mathbf{B}}_1$) is constant over the corresponding smoothing domain.

For the fluid phase, the gradient of pore fluid pressure is constant over each smoothing domain. Applying the smoothing gradient operator, i.e. Equation 3-29, to the pore fluid pressure gradient, we have

$$\tilde{\nabla} P = \frac{1}{A_k^s} \int_{\Omega_k^s} \nabla p(\mathbf{x}) d\Omega = \sum_{i=1}^q \tilde{\mathbf{B}}_{2i} p_i = \tilde{\mathbf{B}}_2 \mathbf{p} \quad (3-47)$$

in which $\tilde{\nabla} P$ is the smoothed gradient of the pore fluid pressure change, p_i is the pore fluid pressure at node i , and \mathbf{p} is the vector of pore fluid pressures for the supporting nodes of the current smoothing domain (set S_s). $\tilde{\mathbf{B}}_2$ takes the following form at each point of interest:

$$\tilde{\mathbf{B}}_2 = \sum_{i \in S_s} \tilde{\mathbf{B}}_{2i} = \sum_{i \in S_s} \begin{bmatrix} \tilde{b}_{ix_1} \\ \tilde{b}_{ix_2} \end{bmatrix} = \begin{bmatrix} \tilde{b}_{1x_1} & \dots & \tilde{b}_{qx_1} \\ \tilde{b}_{1x_2} & & \tilde{b}_{qx_2} \end{bmatrix}_{2 \times q} \quad (3-48)$$

As can be seen, the entries of $\tilde{\mathbf{B}}_2$ are the same as those of $\tilde{\mathbf{B}}_1$, so $\tilde{\mathbf{B}}_2$ is readily available at no extra computational cost. In fact, by application of the smoothing technique, the integration of the pore fluid pressure gradient over the domain is converted to the sum of integrations along the boundaries of the smoothing domains. The smoothed fluid

flow matrix, $\tilde{\mathbf{H}}$, can then be evaluated by summation (assembly) of the local smoothed fluid flow matrixes of all the smoothing domains:

$$\tilde{\mathbf{H}} = \sum_{k=1}^{N_{SD}} \tilde{\mathbf{H}}_k^s = \sum_{k=1}^{N_{SD}} \frac{k_f}{\mu_f} \tilde{\mathbf{B}}_2^T \tilde{\mathbf{B}}_2 A_k^s \quad (3-49)$$

The smoothed coupling matrix is obtained by assembly of the coupling matrices of smoothing domains in the form of

$$\tilde{\mathbf{C}} = \sum_{k=1}^{N_{SD}} \tilde{\mathbf{C}}_k^s = \sum_{k=1}^{N_{SD}} \int_{\Omega_k^s} \tilde{\mathbf{B}}_1^T \boldsymbol{\delta} \mathbf{N}^p d\Omega \quad (3-50)$$

in which \mathbf{N}^p is the shape function matrix for pore fluid pressure at each point of interest defined as (for set S_s)

$$\mathbf{N}^p = [\phi_1(\mathbf{x}) \quad \phi_2(\mathbf{x}) \quad \cdots \quad \phi_q(\mathbf{x})]_{1 \times q} \quad (3-51)$$

According to Equation 3-41, the integrand in the definition of $\tilde{\mathbf{C}}_k^s$ contains the shape function matrix for pore fluid pressure which is not constant over the smoothing domain. Therefore, unlike the calculations of $\tilde{\mathbf{K}}_k^s$ and $\tilde{\mathbf{H}}_k^s$, the integration in Equation 3-50 cannot be readily evaluated for each smoothing domain. A simple approach is adopted in this study to overcome this problem to calculate $\tilde{\mathbf{C}}_k^s$ and finally $\tilde{\mathbf{C}}$ in CSPIM and CSRPIIM. Knowing that $\tilde{\mathbf{B}}_1$ is constant over each smoothing domain, Equation 3-50 can be written in the following form,

$$\tilde{\mathbf{C}} = \sum_{k=1}^{N_{SD}} \left(\tilde{\mathbf{B}}_1^T \boldsymbol{\delta} \left(\int_{\Omega_k^s} \mathbf{N}^p d\Omega \right) \right) \quad (3-52)$$

The integration $\int_{\Omega_k^s} \mathbf{N}^p d\Omega$ in Equation 3-52 needs to be evaluated over each smoothing domain with $\boldsymbol{\delta} = [1 \quad 1 \quad 0]^T$. This can be done with the standard Gauss integration method over the triangular smoothing domain. The number of quadrature points per

smoothing domain depends on the degree of nonlinearity of the shape functions, as well as the accuracy required. In this chapter, three quadrature points per smoothing domain are adopted, but any other selection can be equally used. If the total number of quadrature points per smoothing domain is denoted by g , then the coupling matrix can be evaluated as follows:

$$\tilde{\mathbf{C}} = \sum_{k=1}^{N_{SD}} \left(\tilde{\mathbf{B}}_1^T \boldsymbol{\delta} \left(\sum_{j=1}^g 2A_k^s w_g \mathbf{N}^p \right) \right) \quad (3-53)$$

in which w_g is the weight corresponding to the quadrature of interest. Figure 3.4 schematically shows the locations of the quadrature points used for the computation of the coupling matrix for each smoothing domain.

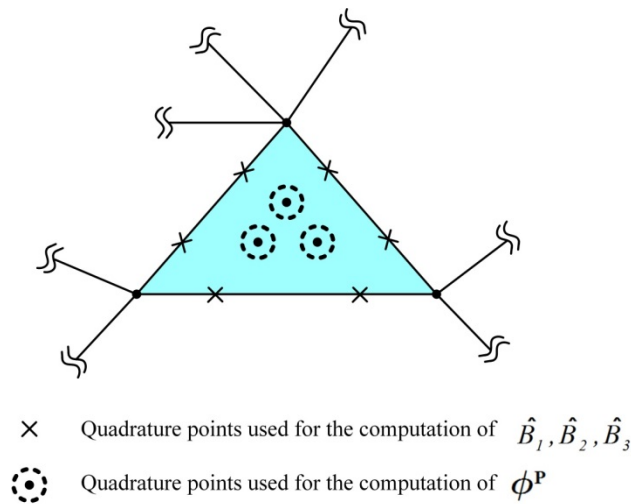


Figure 3.4. Schematic locations of the quadrature points used in this study for calculation of the shape functions.

In a similar fashion, the other global matrices that do not include derivatives of the shape functions (\mathbf{M} , \mathbf{T} and \mathbf{F}) are calculated by assembly of the local matrixes (\mathbf{M}_k , \mathbf{T}_k and \mathbf{F}_k) obtained for each smoothing domain similar to the standard practice in the FEM. The shape function matrix \mathbf{N}^u at each point of interest in a smoothing domain is

defined in the following form to make use of the values already computed for N^p and therefore to keep the computational cost at minimum,

$$N^u = \begin{bmatrix} \phi_1(\mathbf{x}) & 0 & \dots & \phi_q(\mathbf{x}) & 0 \\ 0 & \phi_1(\mathbf{x}) & & 0 & \phi_q(\mathbf{x}) \end{bmatrix}_{2 \times 2q} \quad (3-54)$$

in Equation 3-44, \bar{q} is the fluid flux across the boundary. $\rho \mathbf{g}$ and $\bar{\mathbf{t}}$ in the definition of \mathbf{F}_k in Equation 3-45 are the body force vector and the boundary traction, respectively.

3.6.2 Temporal discretisation

Time discretisation is performed with the use of the three-point time discretisation scheme with variable time steps [143]. This method is unconditionally stable, has second-order accuracy and avoids spurious oscillation on the numerical results. In this method, the calculation starts with an initial time step (Δt_0), and then each subsequent time step grows by a constant growth factor of α ($\alpha > 1$). The time derivatives of an arbitrary function f at time $t + \alpha \Delta t$ can then be estimated in terms of the function values at times $t + \alpha \Delta t$, t and $t - \Delta t$,

$$\dot{f}^{t+\alpha\Delta t} \approx \frac{A f^{t+\alpha\Delta t} - B f^t + C f^{t-\Delta t}}{\Delta t} \quad (3-55)$$

where A , B and C are the constant coefficients obtained by the following equations:

$$A = \frac{2\alpha+1}{\alpha(\alpha+1)}, \quad B = \frac{\alpha+1}{\alpha}, \quad C = \frac{1}{B} \quad (3-56)$$

Applying the three-point time discretisation scheme to Equations 3-38 and 3-39 over the time increment $(1 + \alpha)\Delta t$ (from $t - \Delta t$ to $t + \alpha \Delta t$) gives

$$\tilde{\mathbf{K}} \mathbf{U}^{t+\alpha\Delta t} - \eta \tilde{\mathbf{C}} \mathbf{P}^{t+\alpha\Delta t} = \mathbf{F}^{t+\alpha\Delta t} \quad (3-57)$$

$$A\eta\tilde{\mathbf{C}}^T\mathbf{U}^{t+\alpha\Delta t} + (\Delta t\tilde{\mathbf{H}} + Aa_f\mathbf{M})\mathbf{P}^{t+\alpha\Delta t} = \Delta t\mathbf{T}^{t+\alpha\Delta t} + B\eta\tilde{\mathbf{C}}^T\mathbf{U}^t - C\eta\tilde{\mathbf{C}}^T\mathbf{U}^{t-\Delta t} + Ba_f\mathbf{M}\mathbf{P}^t - Ca_f\mathbf{M}\mathbf{P}^{t-\alpha\Delta t} \quad (3-58)$$

The overall matrix equation of the system is therefore expressed as

$$\mathbf{E}\mathbf{W} = \mathbf{Y} \quad (3-59)$$

$$\mathbf{E} = \begin{bmatrix} A\tilde{\mathbf{K}}_{2N \times 2N} & -A\eta\tilde{\mathbf{C}}_{2N \times N} \\ A\eta\tilde{\mathbf{C}}^T_{N \times 2N} & (\Delta t\tilde{\mathbf{H}} + Aa_f\mathbf{M})_{N \times N} \end{bmatrix}_{3N \times 3N} \quad (3-60)$$

$$\mathbf{W} = \begin{bmatrix} \mathbf{U}^{t+\alpha\Delta t}_{2N \times 1} \\ \mathbf{P}^{t+\alpha\Delta t}_{N \times 1} \end{bmatrix}_{3N \times 1} \quad (3-61)$$

$$\mathbf{Y} = \begin{bmatrix} A(\mathbf{F}^{t+\alpha\Delta t})_{2N \times 1} \\ (\Delta t\mathbf{T}^{t+\alpha\Delta t} + B\eta\tilde{\mathbf{C}}^T\mathbf{U}^t - C\eta\tilde{\mathbf{C}}^T\mathbf{U}^{t-\Delta t} + Ba_f\mathbf{M}\mathbf{P}^t - Ca_f\mathbf{M}\mathbf{P}^{t-\alpha\Delta t})_{N \times 1} \end{bmatrix}_{3N \times 1} \quad (3-62)$$

where N is the total number of field nodes. The three point time discretisation can be used only from the second time step onward. The first time step should be solved with a conventional two-point finite difference scheme. The backward implicit scheme is used for this purpose in this study.

3.7 Numerical examples

The formulation presented above is adopted as the base framework for the subsequent developments in this study. Therefore, in this section, the presented formulation is thoroughly verified, and the performances of different cell-based smoothed MMs are investigated for coupled flow-deformation problems in saturated media. A set of

benchmark examples is studied and the numerical results are compared to analytical or reference solutions. For the sake of comparison, the numerical results of PIM/RPIM with a T4 node selection scheme, and the standard linear FEM using the same background mesh are also provided for all presented problems. For the sake of comparison, the identical \mathbf{u}/p formulation is adopted to the FEM. The constant strain triangular elements have been used throughout this thesis whenever the FEM analysis is required to compare the adequacy and efficiency of the FEM with CSPIM/CSRPIM as these methods employ triangular background mesh associated with three nodes to perform node selection schemes.

3.7.1 One-dimensional consolidation

The benchmark problem of Terzaghi's one-dimensional consolidation is first analysed as shown in Figure 3.5, in association with its boundary conditions and material properties. Figure 3.5 also shows the background mesh constituting cell-based smoothing domains. The height and width of the domain are assumed to $h = 30$ m and $a = 1$ m, respectively. $w = 1$ kPa is assumed to suddenly apply on the top edge of the model. The analytical solution for this problem is available in [161].

This problem is studied here using all the smoothed MMs presented in this study. The same background triangular mesh (presented in Figure 3.5) is used for all cases. The initial dimensionless time step adopted was $\Delta t_D = 1.2$ sec, with the time step growth factor taken as $\alpha = 1.3$. The numerical results are presented in terms of dimensionless surface settlement, u/u_{ult} (u_{ult} is the final settlement obtained using the analytical solution), and dimensionless excess pore pressure, p_f/w , with respect to dimensionless

time, $t_d = \frac{Ek_f(1-\nu)}{\mu(1+\nu)(1-2\nu)h^2} t$. The results of the numerical analysis are shown in Figure 3.6 for three field nodes whose coordinates are presented in Figure 3.5. As can be seen in Figure 3.6, there are excellent agreements between the results of the proposed methods and the analytical solution in terms of the surface displacement and excess pore fluid pressure.

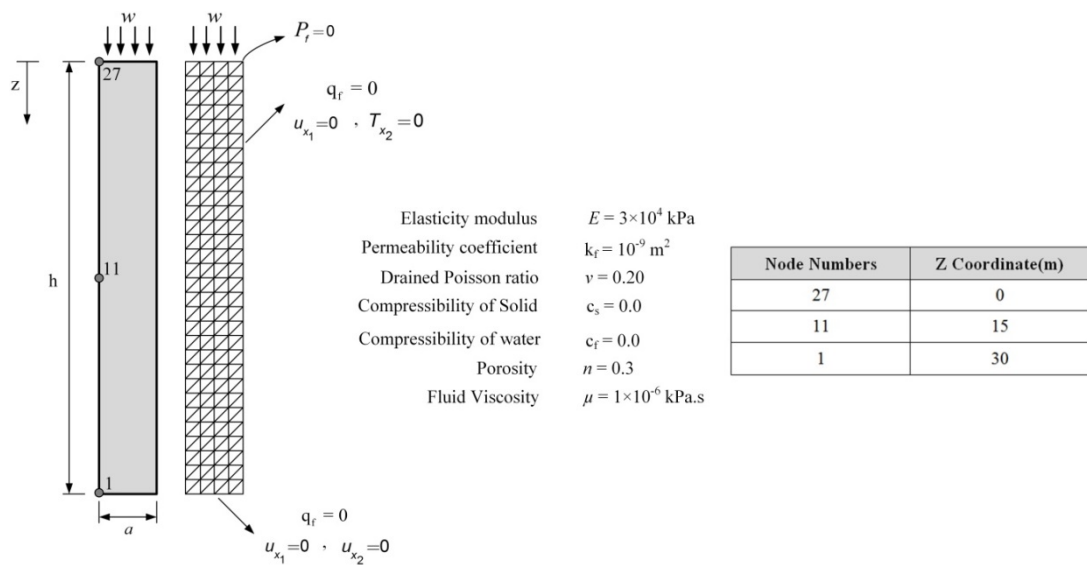


Figure 3.5. Schematic representation of the soil column and its associated smoothing domains for modelling one-dimensional consolidation problem.

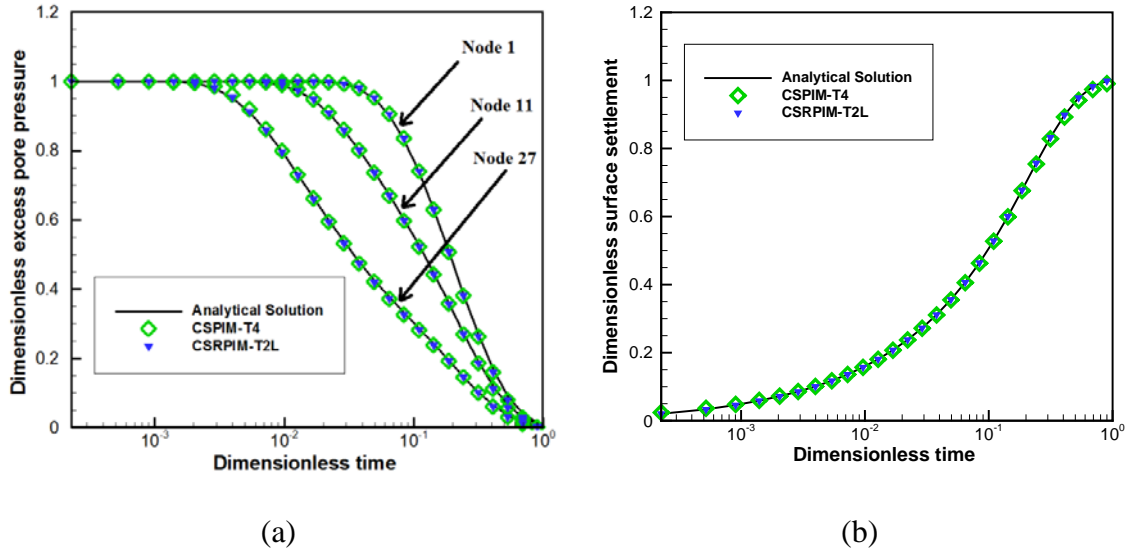


Figure 3.6. Numerical analysis of one dimensional consolidation problem: a) Change of the excess pore fluid pressure with time at three different points, and b) variation of surface settlement with time.

To assess the accuracy and convergence rate of the proposed methods, the error norms of different solutions are precisely examined. Four different background meshes with different densities are used to investigate the convergence rate of the numerical solutions. Three types of error norms are adopted in this chapter, namely displacement error norm (E_d), pore fluid pressure error norm (E_f) and energy error norm (E_e). These are defined as follows:

$$E_d = \sqrt{\frac{\sum_{i=1}^N \left((\mathbf{u}_i^{exc} - \mathbf{u}_i^{num})^T (\mathbf{u}_i^{exc} - \mathbf{u}_i^{num}) \right)}{\sum_{i=1}^N \left((\mathbf{u}_i^{exc})^T \mathbf{u}_i^{exc} \right)}} \quad (3-63)$$

$$E_p = \sqrt{\frac{\sum_{i=1}^N (p_i^{exc} - p_i^{num})^2}{\sum_{i=1}^N (p_i^{exc})^2}} \quad (3-64)$$

$$E_e = \frac{1}{A_k^s} \sqrt{\frac{1}{2} \sum_{k=1}^{N_{SD}} \int_{\Omega_k^s} (\boldsymbol{\varepsilon}_k^{exc} - \boldsymbol{\varepsilon}_k^{num})^T \mathbf{D} (\boldsymbol{\varepsilon}_k^{exc} - \boldsymbol{\varepsilon}_k^{num}) d\Omega} \quad (3-65)$$

where \mathbf{u}_i^{exc} is the exact solution for the displacements at node i , \mathbf{u}_i^{num} is the displacement vector resulting from the numerical solution at node i (both \mathbf{u}_i^{exc} and \mathbf{u}_i^{num} are 2×1 matrices), p_i^{exc} is the exact solution for pore fluid pressure at node i and p_i^{num} is the numerical result for the pore fluid pressure at node i . Similarly, $\boldsymbol{\varepsilon}_k^{exc}$ and $\boldsymbol{\varepsilon}_k^{num}$ are the exact and numerical strains corresponding to each smoothing domain.

The properties of the models used for the error norm assessment of the one-dimensional consolidation problem are listed in Table 3-1. The background mesh shown in Figure 3.5 corresponds to configuration number 2.

Table 3-1. Properties of different configurations used for the assessment of the error norms for the one-dimensional consolidation problem.

Configuration number	Number of field nodes	Number of smoothing domains
1	22	20
2	31	30
3	63	80
4	93	120

Figure 3.7 to Figure 3.9 illustrate the convergence rate of the numerical solutions in terms of the different error norms for the proposed methods at two dimensionless times: $t_d = 0.1$ and $t_d = 1.0$. In these figures, h stands for average nodal spacing and R denotes the convergence rate calculated as the average slopes of all segments for each convergence graph. As can be seen from these figures, all the solutions using CSPIMs/CRPIMs, the FEM and PIM/RPIM converge to the exact solution with the increasing number of smoothing domains. Figure 3.7 to Figure 3.9 show that

CSPIMs/CSRPIMs are more accurate compared to the FEM and PIM/RPIM in terms of all the error norms. In terms of both displacement and pressure norms, CSPIM-T4 is found to yield the most accurate results, while CSRPIM-T2L showing the highest convergence rate among all of the methods studied. In general, it can be seen that the cell-based smoothed methods show higher convergence rates and better accuracy in terms of the energy error norm compared to the FEM. For this example, the energy error norm convergence rates of the proposed smoothed cell-based methods are between 0.8 and 1.0, while the convergence rate of the FEM is between 0.3 and 0.4.

Figure 3.10 shows the variation of strain energy with time for the FEM solution and also for the three smoothed cell-based methods proposed in this study, obtained using configuration number 3. The strain energy is defined by replacing $\boldsymbol{\varepsilon}_k^{exc} - \boldsymbol{\varepsilon}_k^{num}$ with $\boldsymbol{\varepsilon}_k^{num}$ in Equation 3-65. In all methods, the strain energy converges to 0.002175kJ, which is the theoretical value corresponding to the strain energy of a single-phase medium with the same dimensions under a similar load. It can be clearly observed that among the methods studied, CSPIM-T2L has the lowest strain energy at any time during the analysis. This indicates that in this method, consolidation rate is slower and therefore, according to Biot's theory [161], the soil behaviour is softer compared to other methods.

This softness in the behaviour could be due to the use of higher-order shape functions in CSRPIM-T2L resulting in a more accurate strain approximation over the smoothing domains compared to linear FEM, as also reported in [15]. There is also a softening effect due to the reduced integration used in the computation of the numerical integrations [42]. However, these softening effects are compounded by the stiffening effect due to the presence of boundary cells, given that only linear interpolation is used

in boundary cells according to CSRPIIM-T2L formulation. As a result, when the background mesh is coarse, far fewer supporting nodes are, on average, involved in the computation of the shape functions compared to a fine background mesh. Thus, CSRPIIM-T2L may no longer manifest its soft behaviour and in fact often errs on the stiff side when a coarse background mesh is used. That is why CSRPIIM-T2L is very sensitive to background mesh density in all the cases studied and, specially, performs poorly compared to other studied methods in terms of displacement and pressure error norms when the background mesh is relatively coarse. However, according to Figure 3.7 to Figure 3.9 , CSRPIIM-T2L yields very accurate numerical solution in terms of all error norms, especially energy error norm, when a fine background mesh is used.

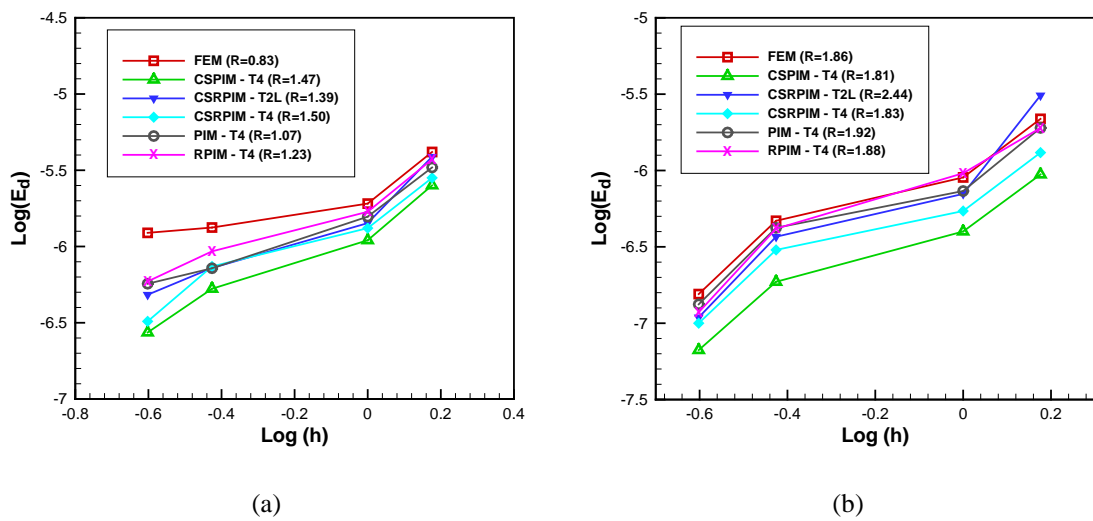


Figure 3.7. Displacement error norms at dimensionless time $t_d = 0.1$ (a) and $t_d = 1.0$ (b) for one-dimensional consolidation problem.

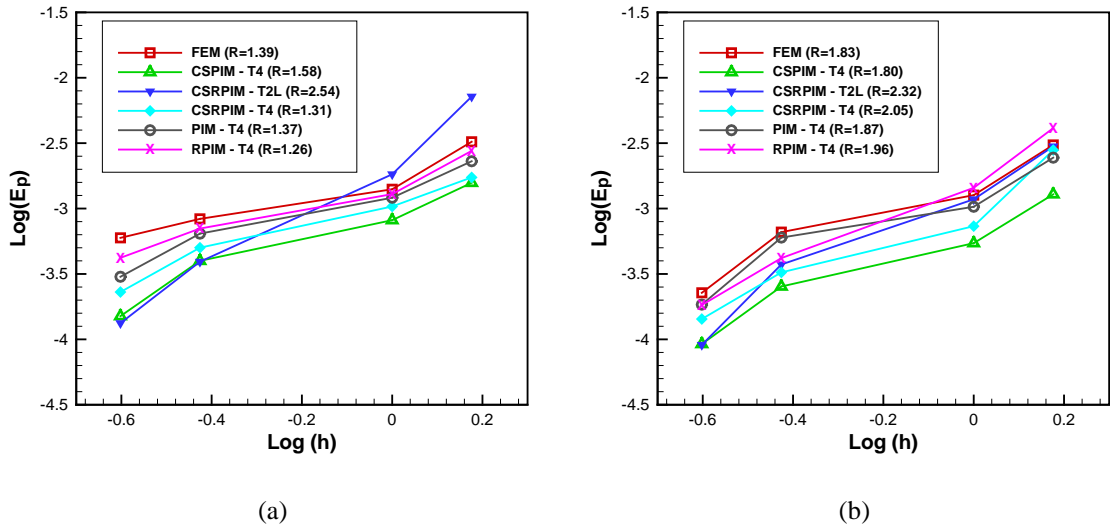


Figure 3.8. Pore fluid pressure error norms at dimensionless time $t_d = 0.1$ (a) and $t_d = 1.0$ (b) for one-dimensional consolidation problem.

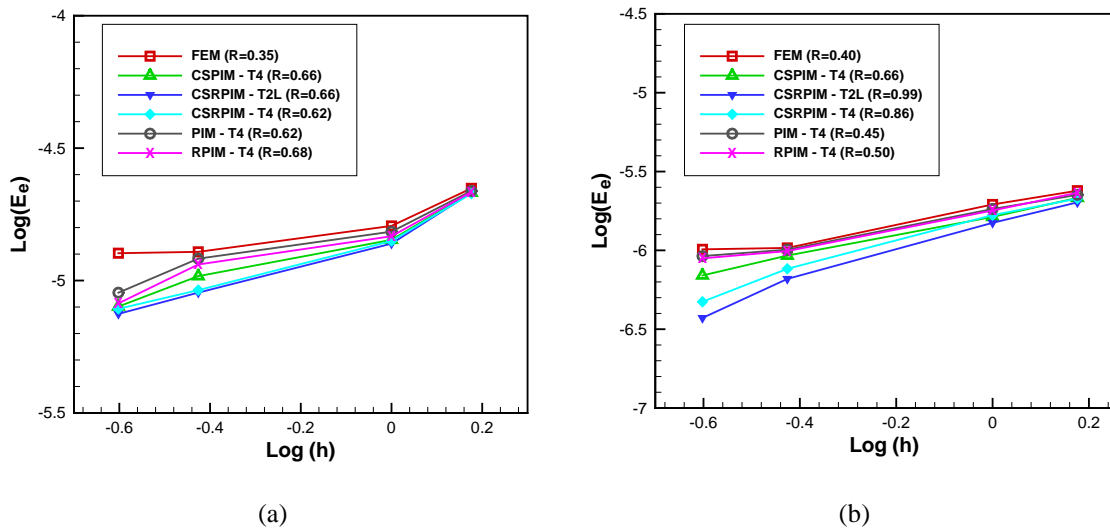


Figure 3.9. Energy error norms at dimensionless time $t_d = 0.1$ (a) and $t_d = 1.0$ (b) for one-dimensional consolidation problem.

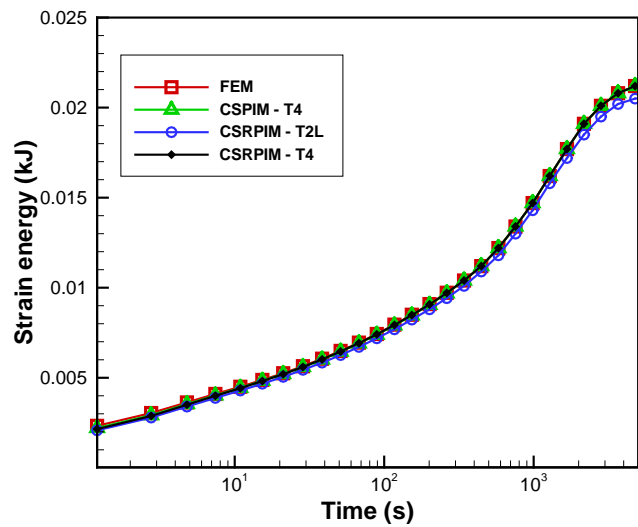


Figure 3.10. Strain energy (kJ) versus time for one-dimensional consolidation problem using configuration number 3.

Table 3-2. Comparison of the computational time required by different numerical procedures adopted in example 3.7.1.

Method	Total time of the analysis with respect to that of the FEM
FEM	1
CSPIM-T4	1.133
CSRPIIM-T2L	1.2 41

Table 3-2 compares the computational efficiency of various CSPIM/CSRPIIMs with respect to that of the FEM. The total times for the analyses for the various methods are normalised with respect to the FEM [90]. As can be seen, despite the fact that CSPIM/CSRPIIM are more computationally expensive, there is little difference between the total times for the numerical analyses using different methods because the geometry of the soil column enforces different CSPIM/CSRPIIMs to create linear-interpolation functions.

3.7.2 Two-dimensional consolidation

The second example involves two-dimensional consolidation of a saturated soil layer subjected to a strip loading. A unit thickness of soil is taken assuming a plane strain condition. A strip loading of $q = 10$ kPa is suddenly applied on the surface of the soil. Due to the symmetry, only half of the domain with a width of $6a$ and a height of $9a$ is modelled here, with a being the width of the loaded area. All boundaries are taken to be impervious except the top surface of the domain. Along the vertical boundaries, the horizontal displacements are constrained and all displacements are fixed along the bottom of the domain. A schematic model of the problem and its associated background mesh (smoothing domains) are shown in Figure 3.11.

The values of the model parameters are taken as follows: $\mu_f = 1 \times 10^{-6}$ kPa s, $k_f = 1 \times 10^{-15}$ m², $E = 10,000$ kPa, $\nu = 0$ and $a = 1$ m. The initial time step adopted is $\Delta t_0 = 1000$ sec, which is equivalent to the dimensionless time step of $\Delta t_d = 0.01$, with the dimensionless time step defined as $t_d = \frac{Ek_f}{(1+\nu)\mu_f a^2} t$. The time step growth factor is assumed $\alpha = 1.1$.

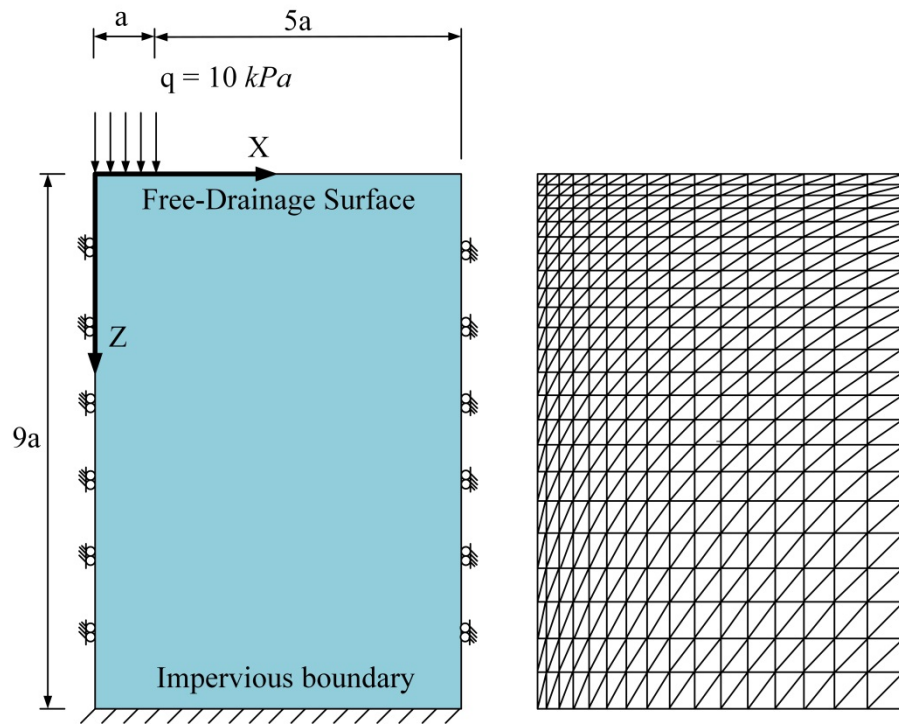


Figure 3.11. Representation of a two-dimensional consolidation problem and the background mesh (smoothing domains) used in the numerical analysis.

The numerical results of excess pore fluid pressure, with respect to the depth ratio (z/a) under the centre of the loading strip, at dimensionless time $t_D = 0.1$ are presented in Figure 3.12. Also presented in this figure are the semi-analytical solution [293], and solutions obtained using the FEM and PIM/RPIM. As can be seen from this figure, all the cell-based smoothed MMs produce accurate results. CSPIM-T4 provides the closest solution to the semi-analytical solution amongst all the methods studied. To investigate the convergence rate of different methods, again, four different models with irregularly disturbed nodes of different densities are adopted in this example. The mesh densities are listed in Table 3-2. The background mesh shown in Figure 3.11 corresponds to configuration number 2.

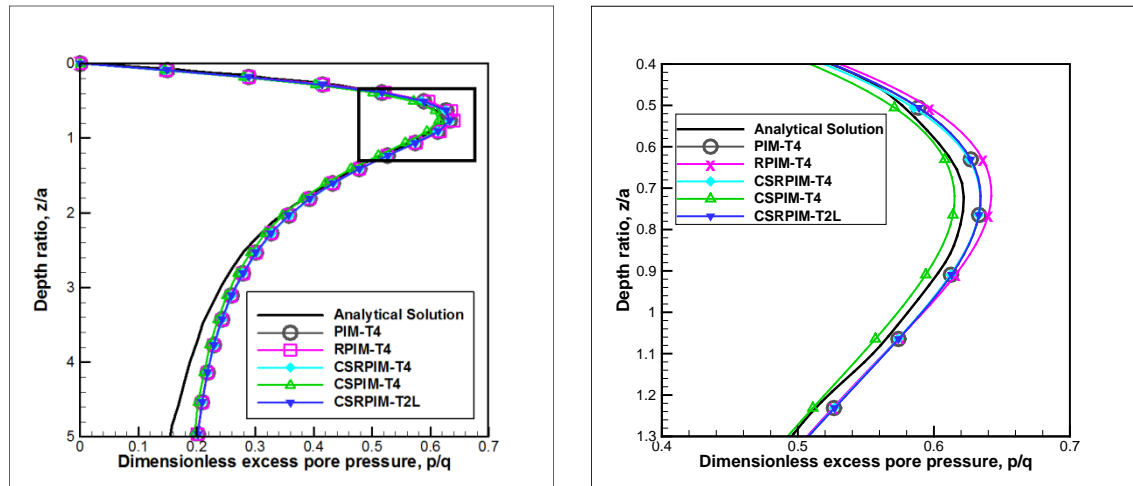


Figure 3.12. Dimensionless excess pore fluid pressure versus depth ratio under the centre of the loaded area at $t_d = 0.1$

Table 3-3. The properties of different configurations adopted for numerical analysis of the two-dimensional consolidation problem.

Configuration number	Number of field nodes	Number of smoothing domains
1	66	100
2	384	736
3	651	1,200
4	925	1,728

Figure 3.13 to Figure 3.15 depict a comparison of the convergence rate and accuracy of different methods in terms of displacement, pressure and energy error norms, respectively, for the two-dimensional consolidation problem at dimensionless times $t_D = 0.1$ and $t_D = 1$. In general, smoothed cell-based methods presented in this study are more accurate than the FEM and PIM/RPIM, regardless of the mesh density and node selection scheme adopted. However, the difference between different smoothed cell-based methods are almost negligible in terms of all error norms, although CSPIM-T4 is

slightly more accurate in general compared to the other two. From Figure 3.13 to Figure 3.15, it can be seen that the convergence rates of all the methods examined in this example are almost similar with an average value of slightly above 2.0 in terms of displacement and pore fluid pressure error norms, and slightly below 1.0 in terms of energy error norm.

The flat segments in Figure 3.13(a) can be attributed to the nature of the consolidation process, which produces the very negligible values of the displacement field at the very early stage in many places of the soil medium. Therefore, the mesh sizes with increasing density do not affect the accuracy of the displacement norm. As the mesh sizes attain the values smaller than a certain threshold, the accuracy of the displacement field would be improved. Because of the medium geometry, the development of the displacement field is restricted to the relative small region beneath the foundation. Therefore, the flat segments can be even seen in Figure 3.13(b) even though the consolidation process has been almost completed.

For the sake of comparison, the total time of the analysis for various CSPIM/CSRPIM normalised with that of the FEM are presented in Table 3-4. The CSRPIM-T2L is the most time-consuming analysis as the more complex shape functions are created by much more supporting nodes compared to CSPIM-T4. CSPIM-T4 has less computational efficiency in comparison with the FEM because CSPIM-T4 is able to have more than twice supporting nodes compared to the FEM to create the polynomial shape functions.

Table 3-4. Comparison of the computational time required by different numerical procedures adopted in example 3.7.2

Method	Total time of the analysis with respect to that of the FEM
FEM	1
CSPIM-T4	1.211
CSRPIIM-T2L	1.315

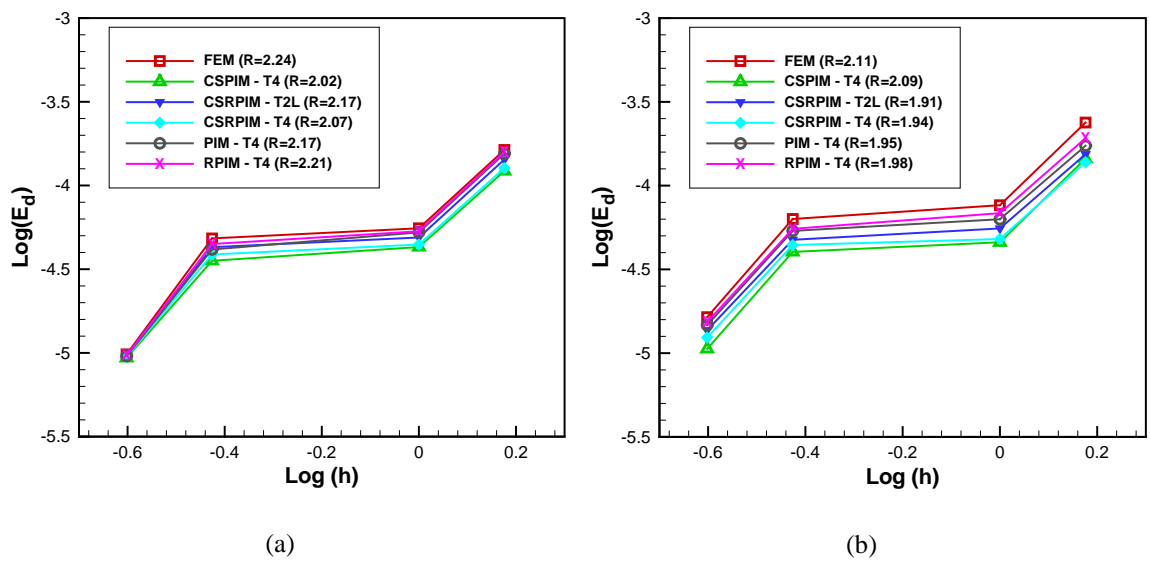


Figure 3.13. Displacement error norms at dimensionless times $t_d = 0.1$ (a) and $t_d = 1.0$ (b) for two-dimensional consolidation problem.

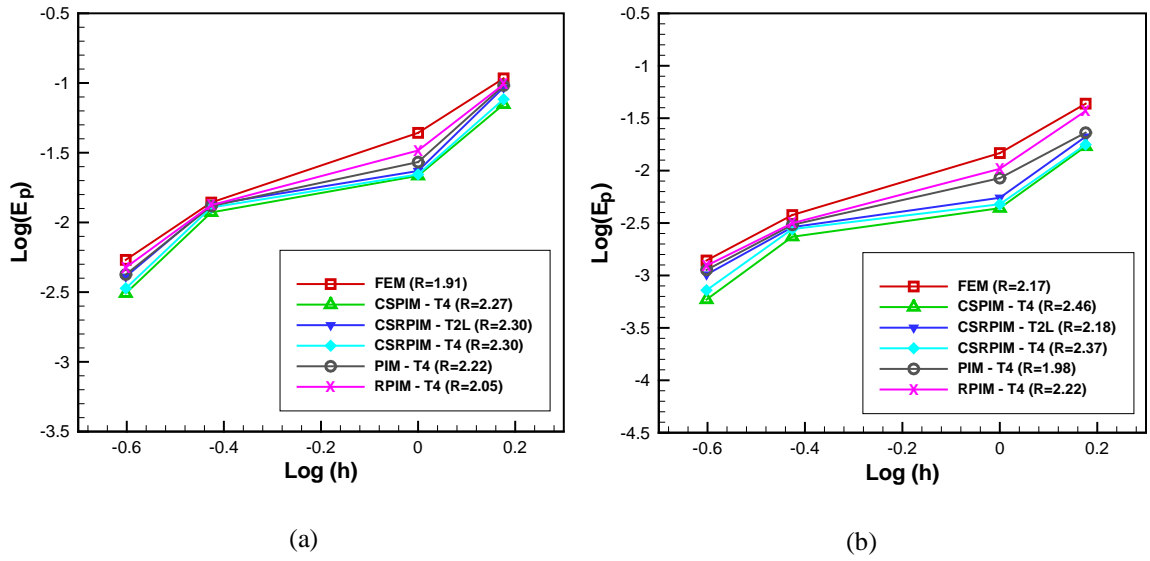


Figure 3.14. Pore fluid pressure error norms at dimensionless times $t_d = 0.1$ (a) and $t_d = 1.0$ (b) for two-dimensional consolidation problem.

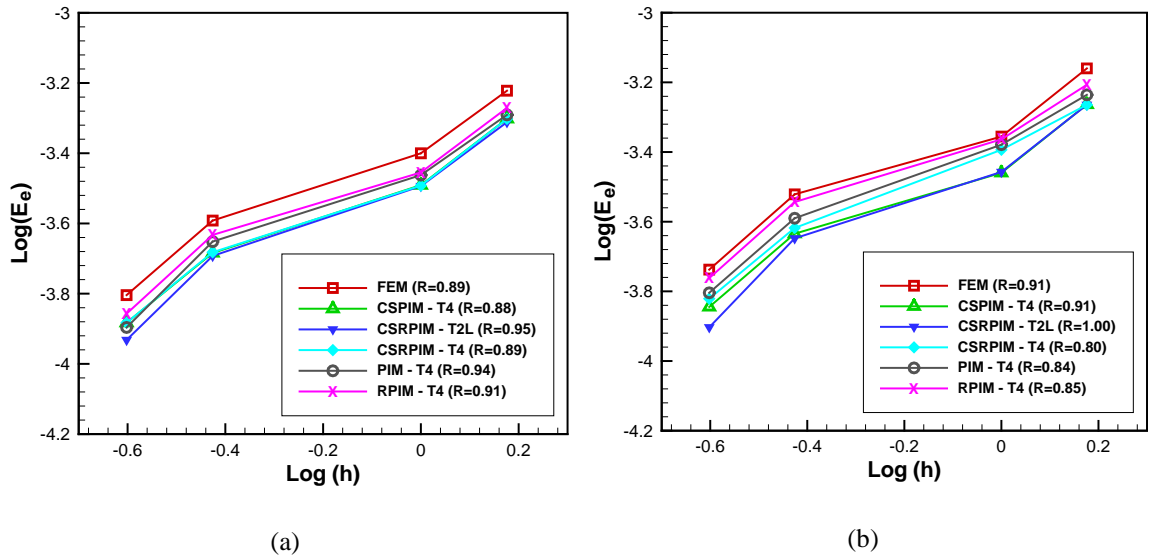


Figure 3.15. Energy error norms at dimensionless times $t_d = 0.1$ (a) and $t_d = 1.0$ (b) for two-dimensional consolidation problem.

The flat segments in Figure 3.14(a) can be due to the severe pressure oscillations at the early stage of the consolidation process because of employing equal order interpolation functions for both displacement and pressure fields. Consequently, the use of the relatively coarse meshes along with the adopted time steps fails to eliminate pressure oscillations. A stabilisation technique is required to eliminate the oscillations, which is fully addressed in chapter 5 of this study. On the other hand, the reduction of the mesh size in Figure 3.14(b) fails to achieve more accurate results since almost all the excess pore water pressure has been dissipated at that time of interest. Therefore, moderate mesh refinement does not produce meaningfully more accurate results up to a certain threshold where the mesh is very fine and increase in the accuracy of the excess pore pressure estimation is finally observed.

3.7.3 One-dimensional hydraulic pulse test

The last example concerns a one-dimensional hydraulic pulse test which involves sudden hydraulic loading of a longitudinal saturated soil sample to investigate its hydraulic properties. As shown in Figure 3.16, the saturated medium is connected to a rigid water chamber which is suddenly pressurised. This pressure pulse is then conveyed through the saturated soil sample. The time-dependent water pressure change within the sample is used for estimation of the permeability of the soil. More details on the test can be found in [294, 295].

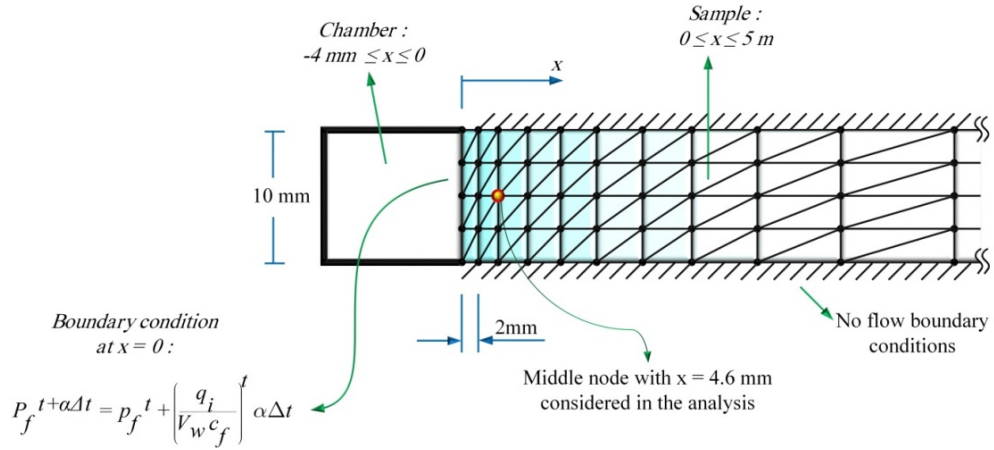


Figure 3.16. Geometry and background mesh assumed in one-dimensional hydraulic pulse simulation.

A soil sample of 5m in length and 10mm in diameter is considered in this example. A very large aspect ratio for the sample is considered in the numerical modelling since the semi-analytical solution for this problem assumes semi-infinite media. The parameters used in this example are as follows: $k_f = 1 \times 10^{-19} \text{ m}^2$, $\mu_f = 1 \times 10^{-6} \text{ kPa s}$, $E = 10,000 \text{ kPa}$ and $\nu = 0.3$. The chamber width is assumed 4mm with an initial pressure of $p_{f0} = 100 \text{ kPa}$. The compressibility of water in the chamber is assumed to be $c_f = 4.45 \times 10^{-10} \text{ Pa}^{-1}$.

The essential boundary condition on the left side of the soil sample needs to be updated at each time step according to the following [294, 295]

$$P_f^{t+\alpha\Delta t} = P_f^t + \left(\frac{q_i}{V_w c_f}\right)^t \alpha\Delta t \quad (3-66)$$

in which V_w is the volume of the rigid chamber and q_i is the nodal flux. Figure 3.17 shows the dimensionless pore fluid pressure, p_f/p_0 , with respect to dimensionless time

$$(\Psi^2 t \text{ with } \Psi^2 = \left(\frac{k_f}{\mu_f}\right) a_f \left(\frac{A_c}{V_w c_f}\right)^2 \text{ in which } A_c \text{ is the cross section area of the soil normal}$$

to the flow direction according to [295]), at the middle row field node with $x = 4.6 \text{ mm}$

obtained using CSPIM-T4, CSRPIIM-T2L and the FEM in association with the semi-analytical solution. The numerical analyses are performed using an initial time step of $\Delta t_0 = 1\text{sec}$, equivalent to the dimensionless time step of $\Psi^2 t = 2.33 \times 10^{-3}$; and a time step growth factor of $\alpha = 1.1$. As can be seen from Figure 3.17, while all the solutions agree well with the semi-analytical solution, CSPIM-T4 and CSPIM-T2L are clearly more accurate than the FEM.

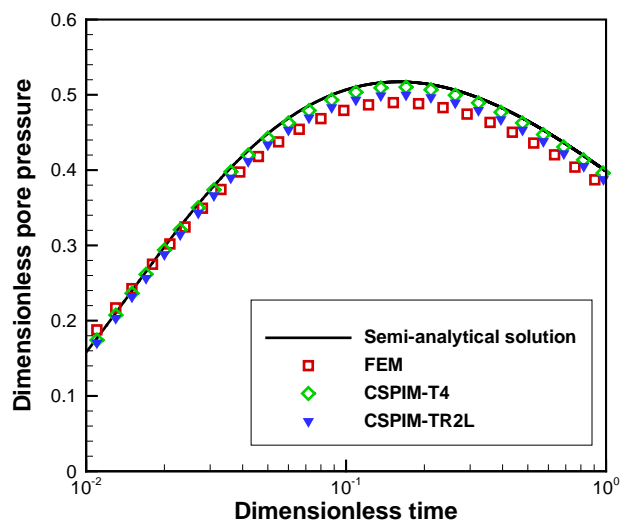


Figure 3.17. Variation of fluid pressure at $x = 4.6$ mm versus dimensionless time for one-dimensional hydraulic pulse test.

Convergence rates of the different numerical methods are investigated in this example too using different mesh densities. The mesh densities used for the error assessments are listed in Table 3-3. The background mesh shown in Figure 3.16 is associated with configuration number 2.

Table 3-5. The mesh properties used for one-dimensional hydraulic pulse test.

Configuration Number	Number of field nodes	Number of smoothing domains
1	505	800
2	1,255	2,000
3	2,505	4,000
4	3,050	4,700

In the simulation of the one dimensional hydraulic pulse test, all the field nodes are constrained with zero displacement. Therefore, only the error norm in terms of pore fluid pressure is investigated. Figure 3.18 shows the results of the numerical investigation at two different times during the analysis. As can be seen from this figure, while the convergence rates are more or less the same for all the methods investigated, cell-based smoothed methods again result in more accurate solutions compared to the FEM and PIM/RPIM for all different mesh densities. Among the cell-based smoothed methods, the CSPIM-T4 performs the best with accuracies almost an order of magnitude higher than those of the FEM.

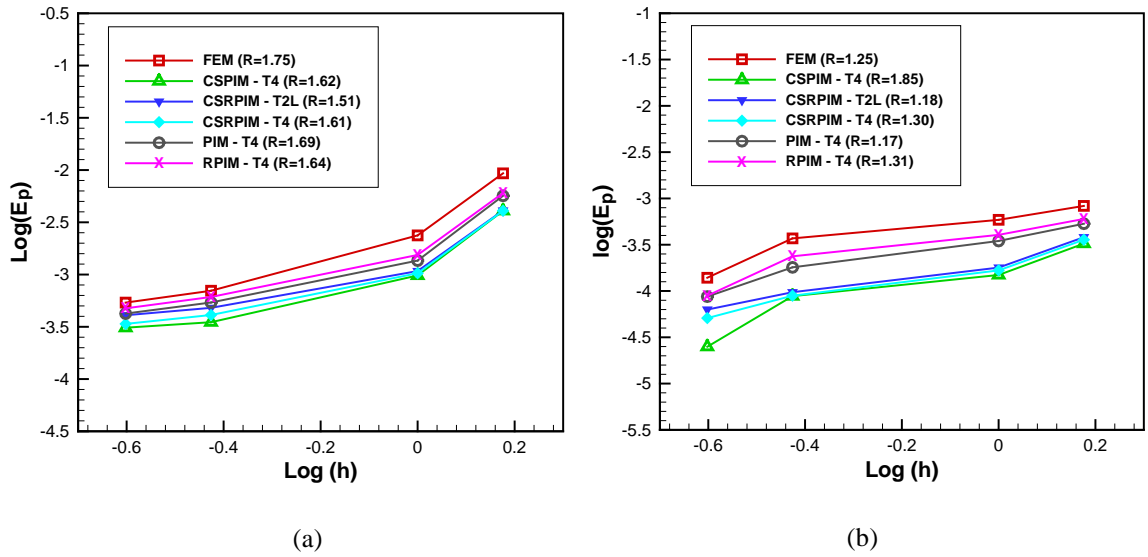


Figure 3.18. Pressure error norms at dimensionless times $t_d = 0.1$ (a) and $t_d = 1.0$ (b) for one-dimensional hydraulic pulse test.

3.8 Conclusions

In this chapter, a group of cell-based smoothed point interpolation methods were proposed for the flow-deformation analysis of saturated porous media, in which displacement and pressure fields are approximated using PIM shape functions (polynomial PIM or radial PIM) and strains and pressure gradients are smoothed over smoothing domains using the generalised gradient smoothing technique. A set of T-schemes for the node selection were applied to guarantee non-singularity of the moment matrix used in the construction of shape functions. According to node selection schemes and PIM/RPIM shape functions, three cell-based MMs have been proposed for coupled numerical analysis of two phase media incorporating a novel approach for calculation of flow property matrices. A number of benchmark examples have been studied to investigate the properties of the presented models and to compare its performance with the FEM and PIM/RPIM. Based on these investigations, the following conclusions can be drawn:

- All the proposed cell-based meshfree methods provide more accurate results in terms of displacement, pore fluid pressure and energy error norms compared to the FEM and PIM/RPIM for flow-deformation analysis of saturated porous media.
- In terms of displacement and pore fluid pressure accuracy, CSPIM-T4 stands out among all the numerical methods studied, with CSRPIM-T4 being a close second. All the proposed cell-based methods show higher convergence rates in comparison with the FEM and PIM/RPIM.
- In terms of energy error norm, CSRPIM-T2L provides the best results in terms of both accuracy and convergence rate. The high accuracy of the CSRPIM-T2L is because both high order shape functions and reduced integration adopted in the method increase the softness of the model, often resulting in a close-to-exact stiffness. The accuracy of CSRPIM-T2L is, however, highly affected by the fineness of the background mesh as the softening effects are considerably hampered when a coarse mesh is used due to a high number of boundary cells (compared to total number of cells) which stiffen the behaviour of the model.

4 A novel approach for application of smoothed point interpolation methods to axisymmetric problems in poroelasticity

4.1 Preface

The application of the smoothed point interpolation methods (SPIM) is extended to axisymmetric problems in poroelasticity in this chapter. A novel, yet simple, approach is presented to overcome the difficulty encountered when using the standard SPIMs in an axisymmetric setting. The problem is related to the presence of Gauss points along the symmetry axis which is inherent in the original SPIM/SRPIM formulations. The approach proposed involves decomposition of the property matrices to smoothed terms and non-smoothed terms which avoids the singularity problem that would otherwise arise. Here, the cell-based SPIM/SRPIM (CSPIM/CSRPIM) are used for the presentation of the proposed method since they offer the simplest form for the creation of the smoothing domains. The approach presented is, however, applicable if other forms of the SPIM are selected. The salient feature of the proposed method is that it neither incurs additional computation nor compromises on the accuracy of the method. In this chapter, the proposed method is detailed and investigated by numerical modelling of a number of benchmark axisymmetric problems, along with a set of convergence studies in terms of various quantities of interest for various time and mesh densities.

4.2 Governing equations

A two-phase porous medium consisting of a solid matrix and a saturating fluid is considered. As presented in Chapter 3, in isothermal conditions, the linear momentum and mass balance equations for the medium are Equation 3-1 and 3-2. The polar coordinate system ($\mathbf{x}=[r \ z]$) is, however, adopted in this chapter instead of the Cartesian coordinate system $\mathbf{x}=[x_1 \ x_2]$ of Chapter 3, as the polar coordinate system is appropriate for problems in axisymmetric settings. Furthermore, the differentiation operator must be redefined for axisymmetric setting, as follows,

$$\mathbf{L}_d = \begin{bmatrix} \frac{\partial}{\partial r} & 0 & \frac{\partial}{\partial z} & \frac{1}{r} \\ 0 & \frac{\partial}{\partial z} & \frac{\partial}{\partial r} & 0 \end{bmatrix}^T \quad (4-1)$$

The solvability of the coupled flow-deformation equations can be ensured by imposing the sufficient and appropriate boundary and initial conditions as defined in Equations 3-4 to 3-7.

4.3 Constitutive modelling

A constitutive model is needed to relate the effective stress to the strain of the solid phase. For simplicity, small strains and elastic behaviour are assumed for the solid skeleton, and therefore, the stress-strain relationship has a similar form as Equation 3-11 and 3-12; however, with the following definitions for the stress and strain, given by:

$$\boldsymbol{\sigma}' = [\sigma'_r \ \sigma'_z \ \tau'_{rz} \ \sigma'_\theta]^T \quad (4-2)$$

$$\boldsymbol{\varepsilon} = [\varepsilon_r \ \varepsilon_z \ \gamma_{rz} \ \varepsilon_\theta]^T = \left[\frac{\partial u_r}{\partial r} \ \frac{\partial u_z}{\partial z} \ \frac{\partial u_r}{\partial z} + \frac{\partial u_z}{\partial r} \ \frac{u_r}{r} \right]^T \quad (4-3)$$

in which, u_r and u_z are displacement components in r and z directions, respectively. σ'_θ is the effective stress in θ direction in an axisymmetric setting

4.4 Variational statement

The variational forms of the governing Equations 3-1 and 3-2 are explicitly derived in this section. The variational form of the governing equations are confined to a pair of sub spaces S_u and S_p , defined as follows:

$$S_u = \{\mathbf{u}: \Omega \rightarrow \mathbf{R}^2 | \mathbf{u} \in G_h^1, \mathbf{u} = \bar{\mathbf{u}} \text{ on } \Gamma_u\} \quad (4-4)$$

$$S_p = \{p: \Omega \rightarrow R | p \in G_h^1, p = \bar{p} \text{ on } \Gamma_p\}, \quad (4-5)$$

The corresponding kinematically admissible subspaces, $V_{v,0}$ and $V_{q,0}$ respectively, are defined as follows:

$$V_{v,0} = \{\mathbf{v}: \Omega \rightarrow \mathbf{R}^2 | \mathbf{v} \in G_{h,0}^1, \mathbf{v} = \mathbf{0} \text{ on } \Gamma_u\} \quad (4-6)$$

$$V_{q,0} = \{q: \Omega \rightarrow R | q \in G_{h,0}^1, q = 0 \text{ on } \Gamma_p\}. \quad (4-7)$$

As discussed in the previous chapter, in general, shape functions constructed by the PIM and RPIM methods are not continuous over the problem domain. Such shape functions are not in H^1 , but are in G^1 which does not require compatibility of shape functions. Therefore, the continuity requirement of the functions in G^1 is further weakened compared to the already weakened requirement for functions in H^1 . Hence, G^1 can be viewed as the space of functions with weakened weak (W^2) requirements on continuity [90].

Again, the approximation of the displacement and excess pore fluid pressure fields are obtained as follows:

$$\mathbf{u} = \mathbf{N}^u \bar{\mathbf{u}}, \quad p = \mathbf{N}^p \bar{p} \quad (4-8)$$

where \mathbf{N}^u and \mathbf{N}^p represent the matrix of displacement and excess pore fluid pressure shape functions, respectively, as presented in Equations 3-54 and 3-51. The *Galerkin's* weighting functions may be represented as:

$$\mathbf{v} = \mathbf{N}^u \mathbf{c}, \quad q = \mathbf{N}^p \bar{c} \quad (4-9)$$

where, \mathbf{c} and \bar{c} are arbitrary unknown weights for the displacement and pressure field approximations, respectively. The weak form of the problem seeks to find $\{\mathbf{u}, p\} \in S_u \times S_p$ such that for all $\{\mathbf{v}, q\} \in V_{u,0} \times V_{p,0}$, we have:

$$\int_{\Omega} \mathbf{v} \mathbf{L}_d^T \boldsymbol{\sigma}' r d\Omega - \eta \int_{\Omega} \mathbf{v} \mathbf{L}_d^T p \boldsymbol{\delta} r d\Omega - \int_{\Omega} \mathbf{v} \rho \mathbf{g} r d\Omega = 0 \quad (4-10)$$

$$\int_{\Omega} q \nabla \cdot \left(\frac{k_f}{\mu_f} (-\nabla p + \rho_f \bar{\mathbf{g}}) \right) r d\Omega + \int_{\Omega} q \nabla \cdot \dot{\mathbf{u}} r d\Omega + \alpha_f \int_{\Omega} q \dot{p} r d\Omega = 0 \quad (4-11)$$

where the integrations are written for 1 *rad* rotation of the domain about the axis of symmetry. Applying Divergence theorem to Equations 4-10 and 4-11, the equivalent weak forms are expressed in the following forms:

$$\int_{\Omega} (\nabla \mathbf{v})^T \boldsymbol{\sigma}' r d\Omega - \eta \int_{\Omega} (\mathbf{v})^T \nabla p \boldsymbol{\delta} r d\Omega - \int_{\Omega} (\mathbf{v})^T \rho \mathbf{g} r d\Omega - \int_{\Gamma_t} (\mathbf{v})^T \bar{\mathbf{t}} r d\Gamma = 0 \quad (4-12)$$

$$\eta \int_{\Omega} q \nabla \cdot \dot{\mathbf{u}} r d\Omega + \int_{\Omega} \frac{k_f}{\mu_f} (\nabla q)^T \nabla p r d\Omega - \int_{\Gamma_q} q \bar{q} r d\Gamma + \alpha_f \int_{\Omega} q \dot{p} r d\Omega = 0 \quad (4-13)$$

For SPIM implementations, Equations 4-12 and 4-13 must be fully discretised in space and time.

4.5 Domain discretisation and support node selection

4.5.1 Domain discretisation

In SPIM/SRPIM, the problem domain is partitioned into N_{SD} smoothing domains that satisfy the conditions expressed by Equations 3-31 and 3-32. The smoothing domains can be created using a triangular background mesh in different ways, resulting in different types of SPIMs [15, 16, 20, 101, 105]. Following the formulation presented in the previous chapter, the cells of the background mesh are directly used as the smoothing domains in this study, resulting in the development of the cell-based SPIM/SRPIM (CSPIM/CSRPIM).

4.5.2 Support node selection schemes

In CSPIM/CSRPIM, selection of supporting nodes at each point of interest is not arbitrary and has to be performed in such a way so that the resulting approximation function is square integrable on the boundary of the smoothing domains [101]. Two node selection schemes, T4 and T2L described in section 3.4.2, are adopted in this chapter. A linear approximation is again applied where the Gauss point of interest is located on the boundary of the domain.

4.5.3 Nodal shape functions

In this chapter, the PIM and RPIM [88] are adopted for the construction of the nodal shape functions. A similar procedure as presented in section 3.4.1 is performed to obtain the shape functions in an axisymmetric setting.

Having computed the nodal shape functions, the displacement and excess pore fluid pressure can be obtained at each point of interest, as follows:

$$\mathbf{u} = \mathbf{N}^u \bar{\mathbf{u}} = \sum_{i=1}^q \begin{bmatrix} \phi_i(\mathbf{x}) & 0 \\ 0 & \phi_i(\mathbf{x}) \end{bmatrix} \begin{Bmatrix} u_{r_i} \\ u_{z_i} \end{Bmatrix} \quad (4-14)$$

$$p = \mathbf{N}^p \bar{p} = \sum_{i=1}^q \phi_i(\mathbf{x}) p_i \quad (4-15)$$

where u_{r_i} and u_{z_i} are the components of nodal displacements, and \mathbf{N}^u and \mathbf{N}^p can be explicitly presented as:

$$\mathbf{N}^u = \begin{bmatrix} \phi_1(\mathbf{x}) & 0 & \dots & \phi_q(\mathbf{x}) & 0 \\ 0 & \phi_1(\mathbf{x}) & \dots & 0 & \phi_q(\mathbf{x}) \end{bmatrix}_{2 \times 2q} \quad (4-16)$$

$$\mathbf{N}^p = [\phi_1(\mathbf{x}) \quad \phi_2(\mathbf{x}) \quad \dots \quad \phi_q(\mathbf{x})]_{1 \times q} \quad (4-17)$$

4.5.4 Smoothed strains

Given that the cells of the background mesh serve as the smoothing domains in CSPIM/CSRPIM, the smoothed gradient of the displacement field (i.e., smoothed strain) is computed for each cell by the smoothing operation technique [90] and the Divergence theorem, as presented by Equation 3-29. However, the matrix containing the components of the unit outward normal vector is defined in the polar coordinate system, as:

$$\mathbf{L}_n = \begin{bmatrix} n_r & 0 \\ 0 & n_z \\ n_z & n_r \end{bmatrix} \quad (4-18)$$

in which n_r and n_z denote the components of the unit outward normal to the boundary of the k th smoothing domain at the Gauss point of interest. The relationship between

smoothed strain and nodal displacements is established as Equation 3-33, with the smoothed strain displacement matrix under an axisymmetric setting taking the following form:

$$\tilde{\mathbf{B}}_1 = \sum_{i=1}^q \tilde{\mathbf{B}}_{1i} = \sum_{i=1}^q \begin{bmatrix} \tilde{b}_{ir} & 0 \\ 0 & \tilde{b}_{iz} \\ \tilde{b}_{iz} & \tilde{b}_{ir} \\ \frac{\phi_i}{r} & 0 \end{bmatrix} \quad i \in S_s \quad (4-19)$$

where the smoothed strain-displacement matrix terms are computed according to Equation 3-37.

4.6 Solution to the singularity problem

In SPIM/SRPIM formulations, the term $\frac{\phi_i}{r}$ in Equation 4-19 leads to a singularity problem due to the Gauss points located on the axis of symmetry as shown in Figure 4.1. To overcome this problem, a novel, yet simple idea is proposed here, in which the smoothed strain-displacement matrix is decomposed into two matrices:

$$\tilde{\mathbf{B}} = \tilde{\mathbf{B}}_{1s} + \mathbf{B}_\theta \quad (4-20)$$

where

$$\tilde{\mathbf{B}}_{1s} = \sum_{i \in S_s} \tilde{\mathbf{B}}_{1si} = \sum_{i \in S_s} \begin{bmatrix} \tilde{b}_{ir} & 0 \\ 0 & \tilde{b}_{iz} \\ \tilde{b}_{iz} & \tilde{b}_{ir} \\ 0 & 0 \end{bmatrix} \quad i = 1, \dots, q \in S_s \quad (4-21)$$

$$\mathbf{B}_\theta = \sum_{i \in S_s} \mathbf{B}_{\theta i} = \sum_{i \in S_s} \begin{bmatrix} 0 & 0 \\ 0 & 0 \\ 0 & 0 \\ \frac{\phi_i}{r} & 0 \end{bmatrix} \quad i = 1, \dots, q \in S_s \quad (4-22)$$

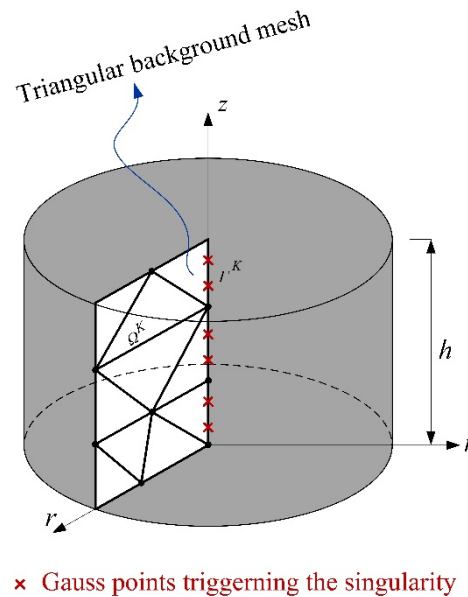


Figure 4.1. A schematic illustration of the Gauss points causing singularity problem in the computation of the property matrices.

The decomposition separates the terms causing the singularity from the rest of the strain-displacement matrix. Given that no smoothing is required for $\frac{\phi_i}{r}$ terms, the integrations involving this term can be carried out over the smoothing domains rather than the boundary of the smoothing domains, resulting in the removal of the singularity problem (see Figure 4.2). The procedure involves no additional computational cost as in any case, the shape function values are required at the Gauss points inside the smoothing domains for the calculation of the property matrices, as detailed in the following sections. The accuracy of the approach is considerably higher compared to using the coordinates of the centroid of the background triangular mesh [37], especially when non-linear nodal shape functions (e.g., radial point interpolation shape functions) or high number of support nodes (e.g., T2L node selection scheme) are used in the

computation of the property matrices. Furthermore, benefiting from the separation technique proposed, the smoothed part of the strain displacement matrix, $\tilde{\mathbf{B}}_{1s}$, remains constant over each smoothing domain, preserving the unique features of the SPIM/SRPIM formulations [13].

4.7 Discretisation in space

Using the Generalised Smoothed *Galerkin* (GS *Galerkin*) approach [90], the spatial discretisation of Equations 3-1 and 3-2 in the axisymmetric setting are obtained as presented in Equations 3-38 and 3-39.

The property matrices of stiffness, coupling, permeability and mass are obtained from the contributions of each smoothing domain through a standard assembly procedure in the following form:

$$\tilde{\mathbf{K}}_k^s = \int_{\Omega_k^s} (\tilde{\mathbf{B}}_{1s} + \mathbf{B}_\theta)^T \mathbf{D} (\tilde{\mathbf{B}}_{1s} + \mathbf{B}_\theta) r d\Omega \quad (4-23)$$

$$\tilde{\mathbf{C}}_k^s = \int_{\Omega_k^s} (\tilde{\mathbf{B}}_{1s} + \mathbf{B}_\theta)^T \boldsymbol{\delta} \mathbf{N}^p r d\Omega \quad (4-24)$$

$$\tilde{\mathbf{H}}_k^s = \int_{\Omega_k^s} \frac{1}{\mu_f} \tilde{\mathbf{B}}_2^T \mathbf{k}_f \tilde{\mathbf{B}}_2 r d\Omega \quad (4-25)$$

$$\mathbf{M}_k = \int_{\Omega_k^s} \mathbf{N}^p{}^T \mathbf{N}^p r d\Omega \quad (4-26)$$

For the global stiffness matrix, Equation 4-23 is rewritten in an expanded form as follows:

$$\begin{aligned}
 \tilde{\mathbf{K}}_k^s &= \int_{\Omega_k^s} (\tilde{\mathbf{B}}_{1s})^T \mathbf{D} (\tilde{\mathbf{B}}_{1s}) r d\Omega + \int_{\Omega_k^s} (\tilde{\mathbf{B}}_{1s})^T \mathbf{D} (\mathbf{B}_\theta) r d\Omega \\
 &+ \int_{\Omega_k^s} (\mathbf{B}_\theta)^T \mathbf{D} (\tilde{\mathbf{B}}_{1s}) r d\Omega + \int_{\Omega_k^s} (\mathbf{B}_\theta)^T \mathbf{D} (\mathbf{B}_\theta) r d\Omega
 \end{aligned} \tag{4-27}$$

The smoothed stiffness matrix is, therefore, divided into four sub-matrices. $\tilde{\mathbf{K}}_{k1}^s$ is calculated similar to the computation of the stiffness matrix in CSPIM/CRPIM of plane strain problems (Equation 3-46) [20]:

$$\tilde{\mathbf{K}}_{k1}^s = \tilde{\mathbf{B}}_{1s}^T \mathbf{D} \tilde{\mathbf{B}}_{1s} \int_{\Omega_k^s} r d\Omega = 2 \tilde{\mathbf{B}}_{1s}^T \mathbf{D} \tilde{\mathbf{B}}_{1s} A_k^s \sum_{i=1}^{N_{gau}} w_i r_i \tag{4-28}$$

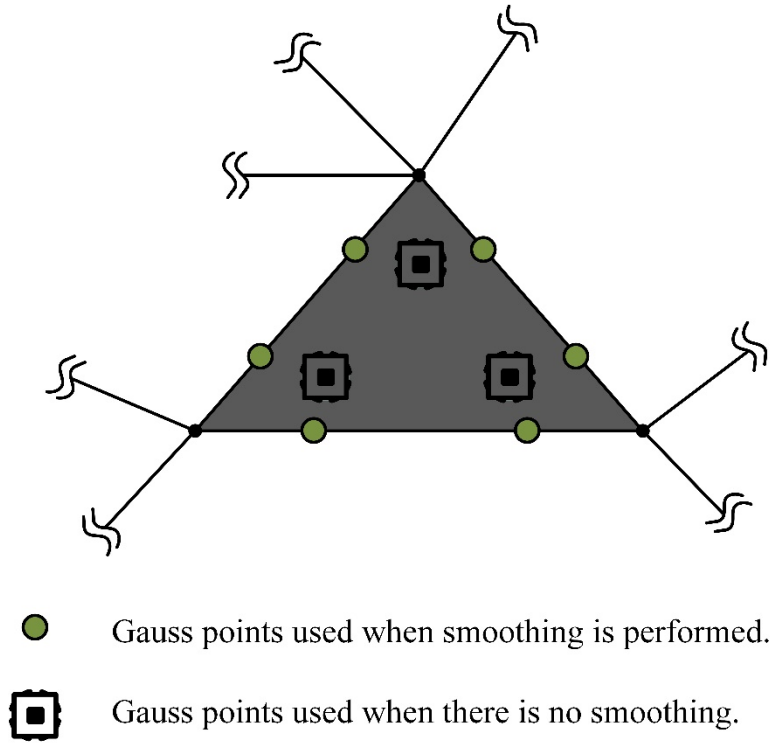


Figure 4.2. Gauss points located on the edges and over a smoothing domain to evaluate the local property matrices.

where \sum stands for both summation and the standard assembly process, and subscript i indicates that the corresponding parameter is calculated at the i th Gauss point (of the

k th smoothing domain), e.g. w_i and r_i are the Gauss integration weight and radius corresponding to the i th Gauss point.

The second and third terms are calculated by adopting an approach similar to that proposed in Equation 3-52 [296] for the calculation of the $\tilde{\mathbf{C}}^{SD}$ matrix, as follows:

$$\tilde{\mathbf{K}}_{k2}^s = \tilde{\mathbf{K}}_{k3}^{sT} = \tilde{\mathbf{B}}_{1s}^T \mathbf{D} \int_{\Omega_k^s} (\mathbf{B}_\theta) r d\Omega = 2\tilde{\mathbf{B}}_{1s}^T \mathbf{D} A_k^s \sum_{j=1}^g \mathbf{B}_{\theta j} w_j r_j \quad (4-29)$$

where, g is the number of Gauss points used over smoothing domains for the computation of non-smoothed terms, which is taken as three in this study as shown in Figure 4.2. w_j is the corresponding weight used in the Gaussian integration rule. This procedure avoids singularity because the non-smoothed strain-displacement matrix, \mathbf{B}_θ , does not involve calculations over the boundary of the smoothing domains. The last term of the stiffness matrix does not involve any smoothing and is calculated over the smoothing domains using the standard Gauss integration approach, as follows:

$$\tilde{\mathbf{K}}_{k4}^s = \int_{\Omega_k^s} (\mathbf{B}_\theta)^T \mathbf{D} (\mathbf{B}_\theta) r d\Omega = 2A_k^s \sum_{j=1}^g (\mathbf{B}_{\theta j})^T \mathbf{D}_i \mathbf{B}_{\theta j} r_j w_j \quad (4-30)$$

Once $\tilde{\mathbf{K}}_{k1}^s$ to $\tilde{\mathbf{K}}_{k4}^s$ are calculated, the global stiffness matrix is evaluated as follows:

$$\tilde{\mathbf{K}} = \sum_{k=1}^{N_{SD}} (\tilde{\mathbf{K}}_{k1}^s + \tilde{\mathbf{K}}_{k2}^s + \tilde{\mathbf{K}}_{k3}^s + \tilde{\mathbf{K}}_{k4}^s) \quad (4-31)$$

where \sum stands for the standard assembly process.

The coupling matrix is obtained as follows

$$\tilde{\mathbf{C}} = \sum_{k=1}^{N_{SD}} \tilde{\mathbf{C}}_k^s = \sum_{k=1}^{N_{SD}} \left(\int_{\Omega_k^s} (\tilde{\mathbf{B}}_{1s} + \mathbf{B}_\theta)^T \delta \mathbf{N}^p r d\Omega \right) \quad (4-32)$$

The contribution of each smoothing domain to the coupling matrix can be written in the following form:

$$\tilde{\mathcal{C}}^{SD} = \underbrace{\left(\int_{\Omega_k^s} (\tilde{\mathbf{B}}_{1s})^T \delta \mathbf{N}^p r d\Omega \right)}_{\tilde{\mathcal{C}}_{k1}^s} + \underbrace{\left(\int_{\Omega_k^s} (\mathbf{B}_\theta)^T \delta \mathbf{N}^p r d\Omega \right)}_{\tilde{\mathcal{C}}_{k2}^s} \quad (4-33)$$

It is noted that $\tilde{\mathcal{C}}_{k1}^s$ has a form similar to $\tilde{\mathbf{K}}_{k2}^s$ or $\tilde{\mathbf{K}}_{k3}^s$, and therefore can be obtained with minor modifications to the formulation of either $\tilde{\mathbf{K}}_{k2}^s$ or $\tilde{\mathbf{K}}_{k3}^s$:

$$\tilde{\mathcal{C}}_1^{SD} = \int_{\Omega_k^s} (\tilde{\mathbf{B}}_{1s})^T \delta \mathbf{N}^p r d\Omega = 2A_k^s \tilde{\mathbf{B}}_{1s}^T \delta \sum_{j=1}^g \mathbf{N}_j^p w_j r_j \quad (4-34)$$

$\tilde{\mathcal{C}}_2^{SD}$ is calculated as follows:

$$\tilde{\mathcal{C}}_2^{SD} = \int_{\Omega_k^s} (\mathbf{B}_\theta)^T \delta \mathbf{N}^p r d\Omega = 2A_k^s \sum_{j=1}^g (\mathbf{B}_\theta)^T \delta \mathbf{N}^p r_j w_j \quad (4-35)$$

The permeability matrix ($\tilde{\mathbf{H}}$) includes only smoothed terms because the fluid flows in either z or r directions, with no flow in θ direction. Thus, the terms associated with \mathbf{B}_θ vanishes from the evaluation of the permeability matrix over each smoothing domain.

We therefore have:

$$\tilde{\mathbf{H}}_k^s = \frac{1}{\mu_f} \tilde{\mathbf{B}}_2^T \mathbf{k}_f \tilde{\mathbf{B}}_2 \int_{\Omega_k^s} r d\Omega = 2 \frac{A_k^s}{\mu_f} \tilde{\mathbf{B}}_2^T \mathbf{k}_f \tilde{\mathbf{B}}_2 \sum_{i=1}^{N_{gau}} w_i r_i \quad (4-36)$$

in which the entries of $\tilde{\mathbf{B}}_2$ are obtained by omitting the components in the 4th row of $\tilde{\mathbf{B}}_s$, as explicitly presented in Equation 3-48.

The global permeability matrix is then assembled in the conventional way:

$$\tilde{\mathbf{H}} = \sum_{k=1}^{N_{SD}} \tilde{\mathbf{H}}_k^s \quad (4-37)$$

The compressibility matrix (\mathbf{M}) does not involve any smoothing and can, therefore, be computed following the standard assembly procedure, as follows:

$$\mathbf{M} = \sum_{k=1}^{N_{SD}} \mathbf{M}_k \quad (4-38)$$

$$\mathbf{M}_k = \int_{\Omega_k^s} \mathbf{N}^{pT} \mathbf{N}^p r d\Omega = 2A_k^s \sum_{i=1}^{N_{gau}} \mathbf{N}_i^{pT} \mathbf{N}_i^p w_i r_i \quad (4-39)$$

The global matrix of external forces and flux can also be computed by assembling the local external force vectors and flux, respectively, which in turn can be calculated for each smoothing domain from as computed for the plain strain condition.

4.8 Discretisation in time

The three-point time discretization scheme [143] is adopted in this chapter for time discretisation of the governing equations as explained in section 3.6.2. The discretised form of the governing equations will be identical to those presented in Equations 3-59 to 3-62.

4.9 Numerical examples

The formulation presented is adopted in this section to solve three benchmark examples to evaluate the accuracy and performance of the scheme suggested. The numerical results are compared with the analytical solutions (when available) and the solution obtained from the standard linear FEM using the same background mesh through a comprehensive error norm and convergence rate analysis.

4.9.1 Cryer's problem

The benchmark consolidation problem of Cryer [297] is adopted here for verification purposes. In this problem, a uniformly distributed surface load of $p_0 = 1$ kPa is concentrically applied to a saturated porous sphere with a radius of $a = 1.0$ m. Only one-quarter of the sphere cross-section was modelled because of the symmetry. The outer boundary of the sphere was assumed to be permeable, and the permeability of the sphere was assumed to be $k = 1$ m/sec. The geometry and boundary conditions of the

problem, along with the triangular background mesh used for the spatial discretisation of the problem domain, are shown in Figure 4.3. The background mesh shown consists of 840 elements and 475 field nodes. Three different cases are studied using three different sets of elastic properties as presented in Table 4-1. Case 3 approximates an incompressible material ($\nu = 0.5$). In all the cases, the initial dimensionless time step ($t_d = \frac{Ek(1-\nu)}{\mu_f(1+\nu)(1-2\nu)a^2} t$) is taken 0.0005 with a time step growth factor of $\alpha = 1.2$.

Table 4-1. Soil properties used in the analysis of Cryer’s problem (E is the Young modulus and ν is the Poisson’s ratio)

Case Number	ν	E (kPa)
1	0.0	1.0
2	0.333	0.666
3	0.496	0.0299

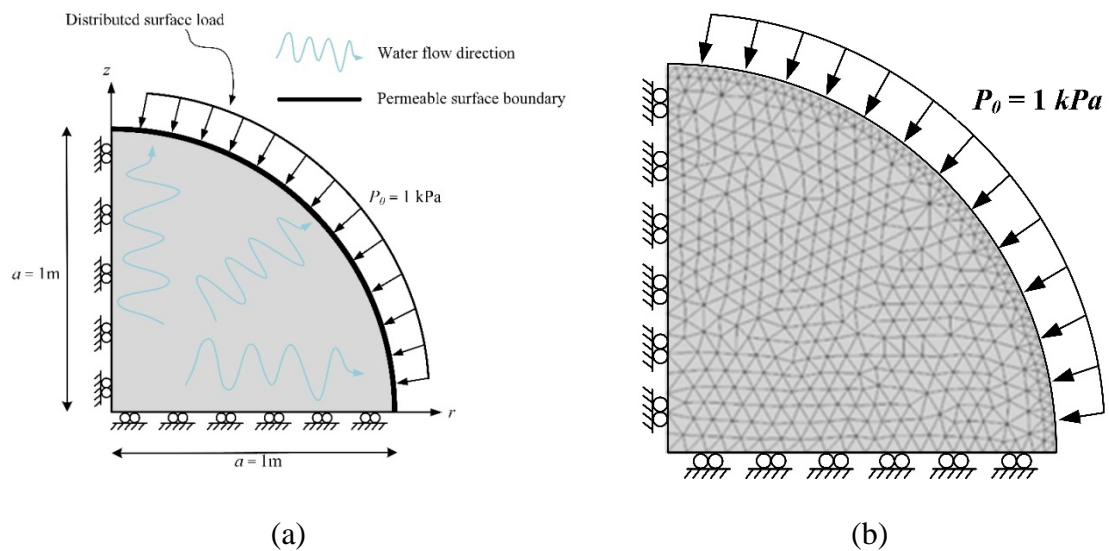


Figure 4.3. (a) The schematic representation of Cryer’s problem, (b) the background mesh used in the analysis

As an example, the numerical results for the excess pore water pressure contours from the analysis of case 1 at dimensionless time 0.0529 are shown in Figure 4.4. As expected, the symmetry of the geometry and the applied load results in the symmetry of the excess pore water pressure contour about the centre of the sphere. Similar results are also obtained for other cases studied (not presented due to similarity with Figure 4.4).

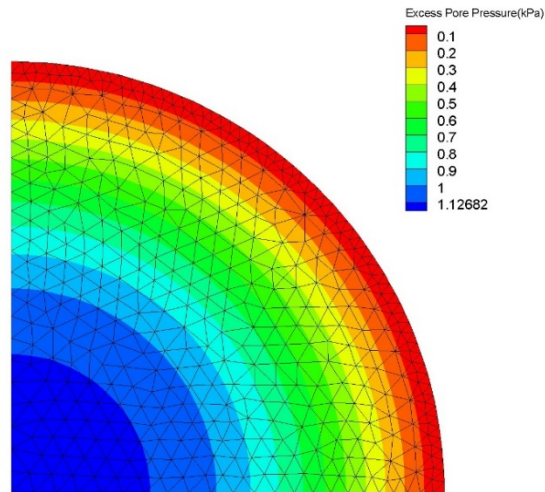


Figure 4.4. The contour of excess pore pressure for Cryer’s problem (case 1) at dimensionless time 0.0529.

The results of the numerical analyses in terms of the dimensionless excess pore water pressure ($P_c = \text{excess pore pressure}/p_0$) at the centre of the sphere versus the dimensionless radial displacement of the surface of the sphere ($U_r = \text{surface settlement}/a$), and the variation of the dimensionless surface settlement with dimensionless time are compared with the analytical solutions presented in [35] for all three cases, as shown in Figure 4.5. Both SPIM and SRPIM with different node selection schemes are adopted as identified in the Figure 3.1. As can be seen from Figure 4.5, there is excellent agreement between the results of the numerical solution and the analytical solution for all three cases studied. In all cases, the pore pressure increases over the entire sphere to the value of the applied load upon the application of

the load. The pore pressure then initially increases at the centre of the sphere in cases 1 and 2 before decreasing due to the consolidation process. This effect, known as the Mandel–Cryer effect [297, 298], is perfectly captured in the numerical analyses. For case 3, where the soil is incompressible, no increase in pore water pressure at the centre of the sphere is observed, which also agrees with the analytical solution for this case. The Mandel–Cryer effect cannot be captured using the original Terzaghi formulation for consolidation and can only be simulated when the governing equations for the solid and water phases are properly coupled. More discussion on this matter can be found in [299].

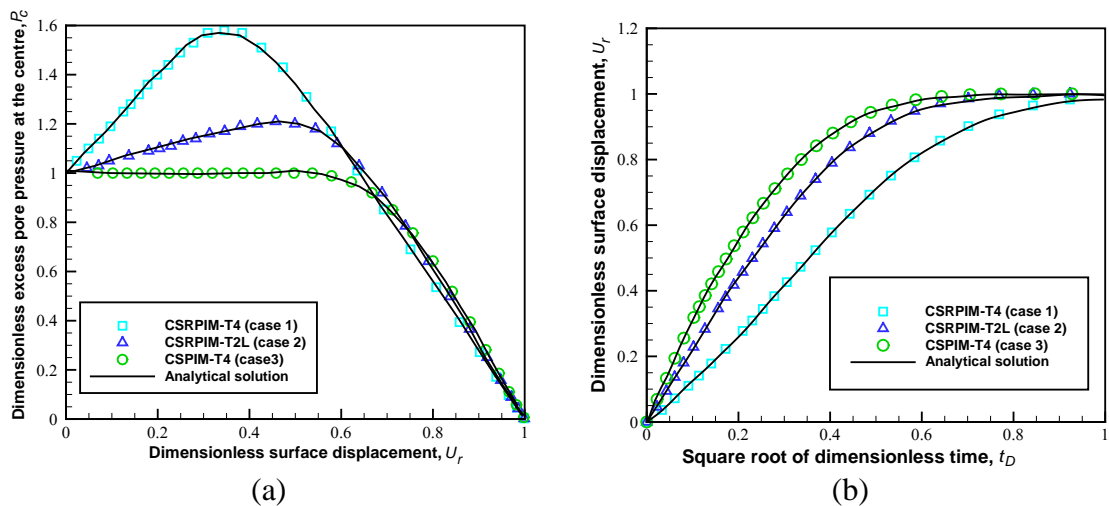


Figure 4.5. Solutions to the Cryer’s problem; (a) The distribution of dimensionless excess pore pressure versus dimensionless surface displacement; (b) the variation of dimensionless surface displacement with respect to the square root of the dimensionless time.

To quantitatively scrutinise the proposed methods, an error analysis is performed using four background meshes with different densities. The accuracy and convergence rate of the proposed method are studied, and also compared with those of the conventional linear FEM with the same background meshes. To this end, two types of error norms, namely the displacement and the pore pressure error norms, are defined as presented by

Equation 3-63 and 3-64, respectively: The properties of the non-uniform background meshes used for the error analysis of the Cryer's problem are listed in Table 4-2.

Table 4-2. The number of field nodes and elements (smoothing domains) for different background meshes adopted for the error analysis of Cryer's problem.

Configuration number	Number of field nodes	Number of smoothing domains
1	30	50
2	108	200
3	387	730
4	1722	2920

A comparison of the convergence rate (shown with R) and accuracy of the different methods proposed in this study, and also the standard linear FEM, with respect to the various mesh densities at two different dimensionless times, $t_d = 0.1$ and $t_d = 1.0$, is depicted in Figure 4.6 and Figure 4.7, for displacements and pressures, respectively. As can be seen, all the methods presented in this study are in general more accurate compared to the FEM, in terms of both displacement and pore fluid pressure calculations. In terms of convergence rates, again CSPIMs/CSRPIMs are in general superior to the FEM, although the difference between the convergence rates of the different methods are not considerable in some cases. Considering the error analysis in terms of displacements, CSRPIM-T2L produces the most accurate results and shows better convergence rates. However, the difference in accuracy and the convergence rate between CSRPIM-T2L and CSRPIM-T4 in terms of displacements at $t_d = 0.1$ is not

considerable. The relatively similar performances of CSRPIIM-T2L and CSRPIIM-T4 in this case may be attributed to the limited dissipation of the excess pore water pressure at $t_d = 0.1$. This results in a displacement field which is mainly concentrated to a small layer at the surface of the sphere. The approximated displacement field in the T2L scheme has therefore very similar accuracy to that of the T4 node selection scheme because most of the additional nodes involved in the T2L scheme have negligible displacements. This effect diminishes as time passes, and the difference between the solutions of CSRPIIM-T2L and CSRPIIM-T4 becomes more meaningful at $t_d = 1.0$, as seen from Figure 4.6. In general, it can be concluded that CSRPIIM-T2L yields the most accurate results and exhibits the highest convergence in terms of both displacements and pressures for the Cryer's problem.

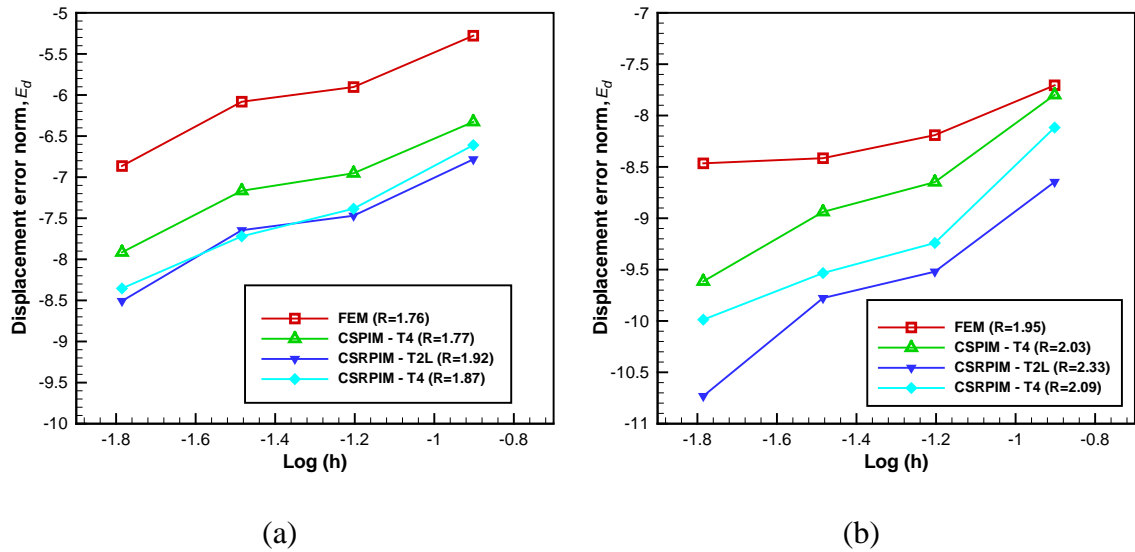


Figure 4.6. Displacement error norms for Cryer's problem at dimensionless time (a) $t_d=0.1$; and (b)

$t_d=1.0$.

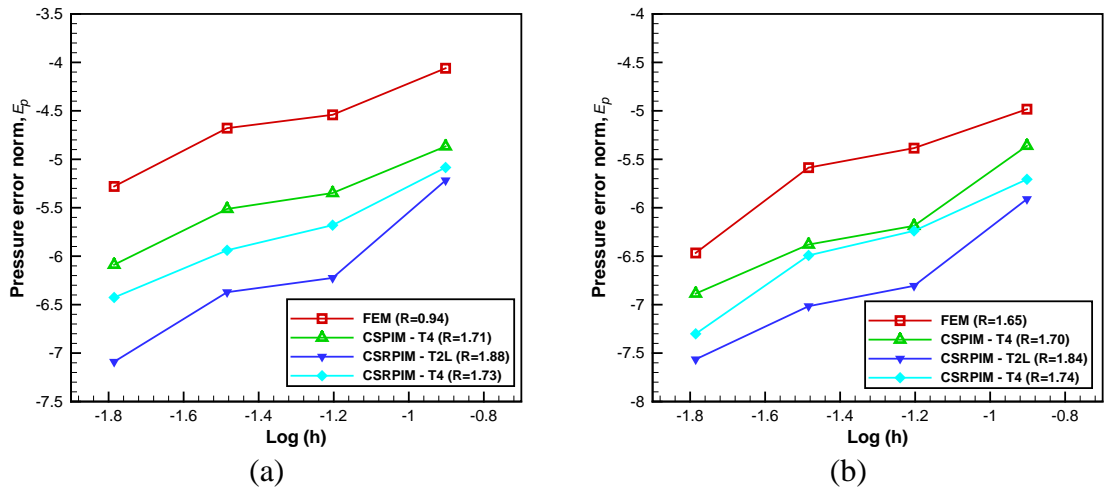


Figure 4.7. Excess pore pressure norms for Cryer's problem at dimensionless time (a) $t_d=0.1$; and (b) $t_d=1.0$.

4.9.2 De Leeuw's problem

The second problem studied here is the De Leeuw's problem, originally considered in [300], which involves a cylindrical saturated porous medium (with radius and height of $a = 1$ m) constrained between two rigid horizontal plates so that the vertical displacements at the top and the bottom of the model are zero, as shown in Figure 4.8. The outer radial boundary of the sample is drained. A uniform compressive radial stress with a magnitude of $p_0 = 1$ kPa is applied to the sample at the outer boundary. The soil properties are taken $E = 1$ kPa and $\nu = 0$, and $k = 1$ m/sec, in accordance with those adopted in [301]. Both solid grains and water are assumed to be incompressible. The first time step is taken as $t_d = 0.001$, and the time step growth factor is assumed $\alpha = 1.05$. For the numerical analysis, an axisymmetric section of the medium was discretised by a background mesh with 450 elements and 256 nodes, as shown in Figure 4.9.

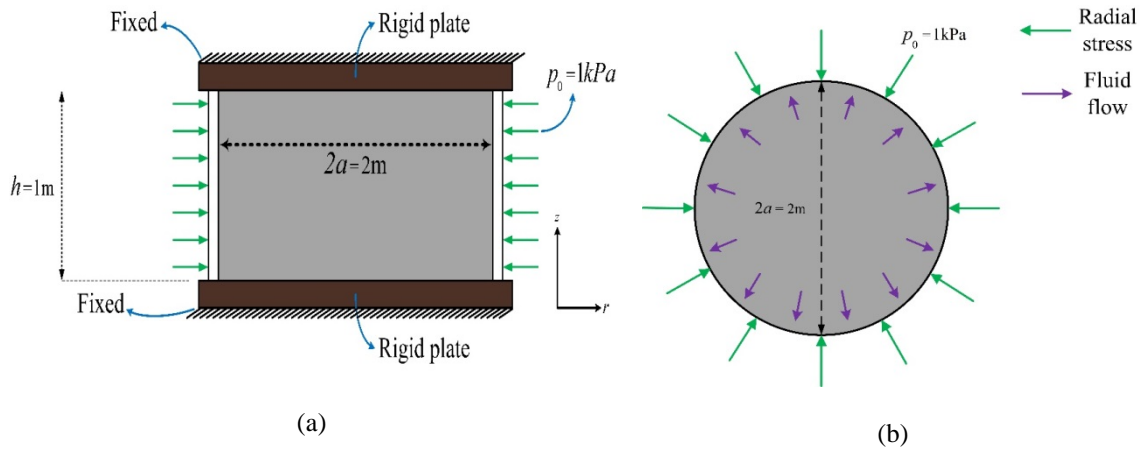


Figure 4.8. A schematic representation of (a) the section and (b) the plan view of the cylinder relevant to De Leeuw's problem.

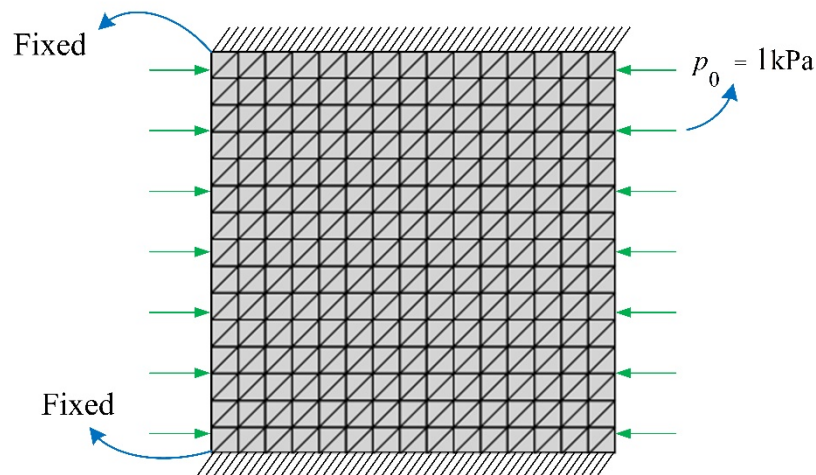


Figure 4.9. The mesh configuration adopted for the numerical solution of the De Leeuw's problem.

The numerical results in terms of dimensionless excess pore pressure ($P_c = \text{excess pore pressure}/p_0$) at different dimensionless radii (r/a) and different dimensionless times, along with their corresponding analytical solutions taken from [301], are presented in Figure 4.10. It is seen from this figure that the numerical results using both CSPIM-T4 and CSRPIIM-T2L perfectly match the analytical solutions at all times. The Mandel-Cryer effect is again evident from Figure 4.10, with excess pore

water pressure initially increasing beyond the initial applied pressure at the centre of the cylinder, before dissipating due to consolidation.

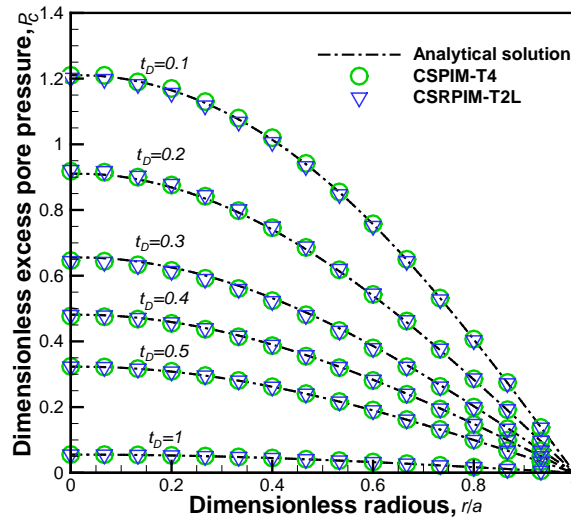


Figure 4.10. Variation of the dimensionless excess pore pressure versus dimensionless radius at different dimensionless times.

A thorough error analysis in terms of displacement and pressure solutions is again performed for this example using four different background meshes, whose properties are listed in Table 4-3.

Table 4-3. The properties of the different background meshes employed in the error analysis of De Leeuw's problem.

Configuration number	Number of field nodes	Number of smoothing domains
1	121	200
2	256	450
3	441	800
4	676	1250

Figure 4.11 and Figure 4.12 illustrate the results of the error analysis of De Leeuw's problem in terms of the displacement and pressure error norms, respectively.

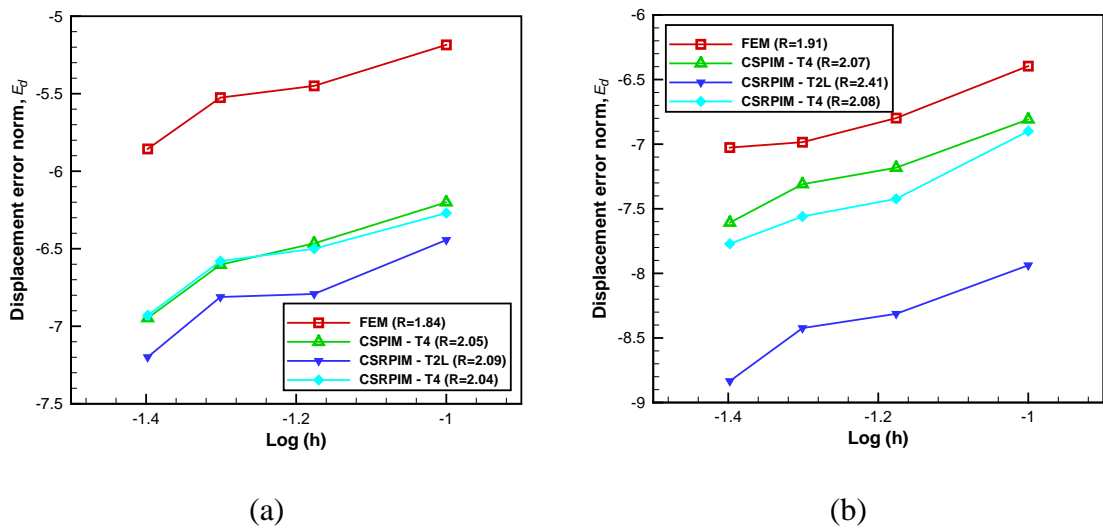


Figure 4.11. Displacement error norms for De Leeuw's problem at dimensionless time (a) $t_d = 0.1$; and (b) $t_d = 1.0$.

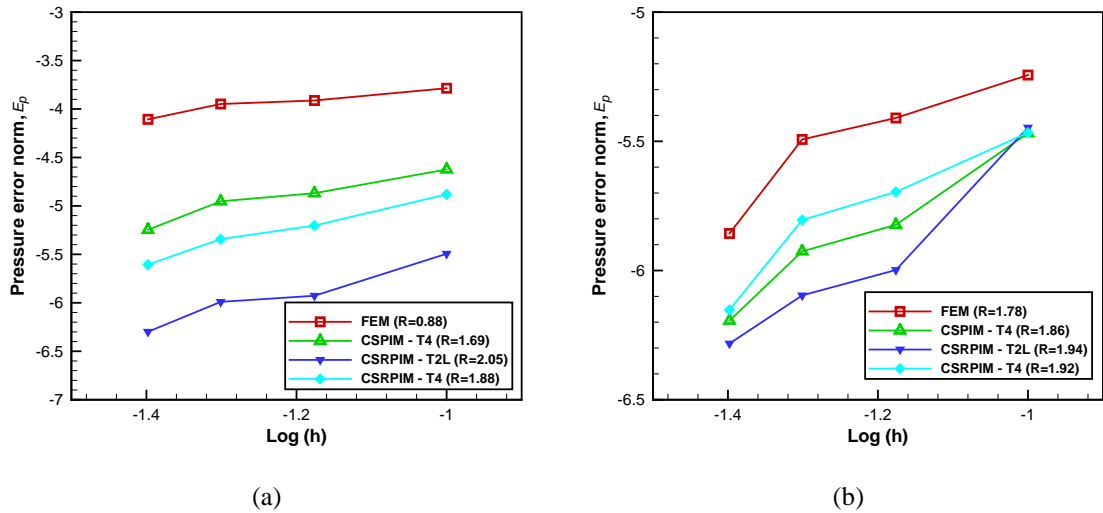


Figure 4.12. Pressure error norms for De Leeuw's problem at dimensionless time (a) $t_d = 0.1$; and (b) $t_d = 1.0$.

All the proposed methods yield more accuracy compared to the FEM in terms of displacement and pressure error norms. In terms of convergence rate, again the methods presented in this study outperform the standard FEM. Among all CSPIMs, CSPIM-T2L achieves the most accurate results in terms of both displacement and pressure. Consistent with the pervious example, the superiority of CSPIM-T2L is less evident in terms of displacement at dimensionless time $t_d = 0.1$, perhaps due to the same reasons discussed in the previous example.

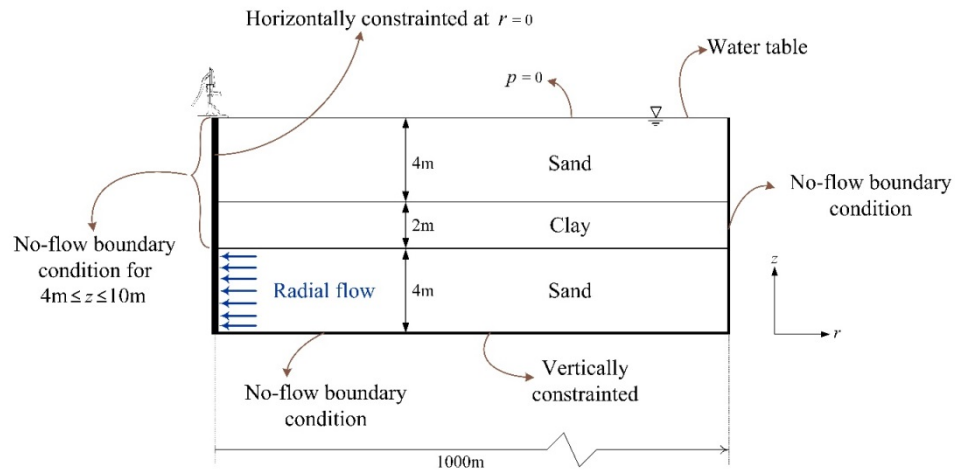
4.9.3 The study of Noordbergum effect

The last numerical example concerns the Noordbergum effect, first observed in a field well in the small village of Noordbergum in the Netherlands [302]. The observation showed that in a three-layered soil medium composed of a clay layer sandwiched between two sand layers, when the pumping of water from the lower sand layer is stopped, the water level in the aquifer quickly increased, as expected. However, in the upper sand layer, the water level initially decreased for a period of time, before starting

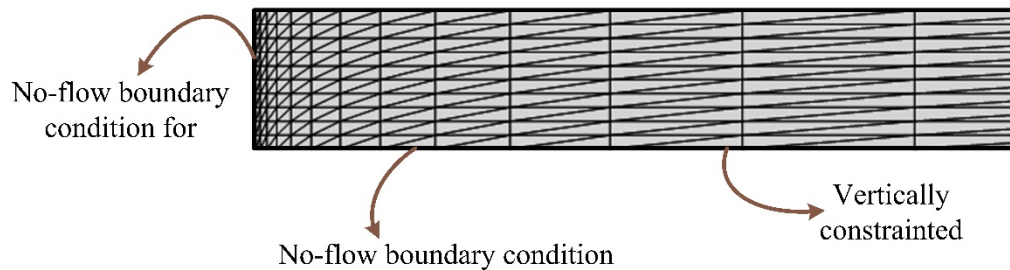
to increase. A similar effect was observed when pumping from the lower sand layer resumed, with the water level in the upper aquifer increased for a while before it was decreased. This phenomenon is also referred to as a reverse groundwater level fluctuation [303]. The Noordbergum effect can be attributed to the radial displacement of the clay layer around the well stemming from the Poisson's ratio effect. The extraction of water from the bottom sand layer causes decrease in pore water pressure in the bottom sand layer, and therefore in the bottom of the clay layer. This suction initiates consolidation process in the clay layer, resulting in an increase in the effective stress, initially in the lower part of the clay layer, and therefore compression of the clay layer, in both horizontal and vertical directions. The radial displacements, in turn, apply confining pressure to the upper part of the clay layer and also the upper sand layer around the well resulting in an increase in pore water pressure in those layers. The pore water pressure increase is more pronounced in the clay layer due to its lower hydraulic permeability compared to the upper sand layer.

For the numerical simulation of the Noordbergum effect, a 2m thick clay layer confined by two 4m thick sand layers is simulated. The schematic geometry of the problem and its relevant boundary conditions are depicted in Figure 4.13. The properties of the two sand layers are identical. The soil parameters used in the simulations are listed in Table 4-4, in accordance to those assumed in [304]. The clay and sand layers were assumed to be homogeneous and isotropic. A vertical well is drilled through all three layers. The water is extracted from the lower sand layer at a constant rate of $\bar{q} = 2 \times 10^{-2} \text{ m}^3/\text{sec}$, as depicted in Figure 4.13. At $r = 0$, the flux boundary condition is assumed for the lower sand layer, while no-flow boundary condition is prescribed for the clay and the upper sand layers. The radial extension of the domain is assumed $r = 1000 \text{ m}$, to approximate infinite lateral extension and minimise the boundary effects. The

compressibility of water is taken $5 \times 10^{-10} \text{ m}^2/N$, and the solid grains are assumed incompressible. The wall of the well is free to move in the vertical direction, but is fixed in horizontal direction.



(a)



(b)

Figure 4.13.(a) Illustration of the three-layered medium and its corresponding boundary conditions employed for the numerical simulation of the Noordbergum effect, and (b) representation of a portion ($0\text{m} \leq z \leq 10\text{m}$, $0\text{m} \leq r \leq 110\text{m}$) of the background mesh adopted in the study of the Noordbergum effect.

Table 4-4. The soil properties adopted in the simulation of the Noordbergum effect.

Parameter	Sand	Clay
n	0.44	0.66
k ($\frac{m}{sec}$)	9.06×10^{-4}	2.29×10^{-6}
ν	0.25	0.35
E (kPa)	8.33×10^3	3.12×10^2

To simulate the problem, an unstructured triangular background mesh composed of 310 elements and 180 nodes is adopted, as partially shown in Figure 4.13. As can be seen from this figure, the background mesh is very fine near the pumping well and becomes coarser steadily as r increases. The first time step is taken as 0.1 sec and increases by a factor of $\alpha = 1.5$ throughout the analysis. The numerical solution in terms of the hydraulic heads and displacements at different points and times are obtained using the proposed CSPIM and CSRPIIM. The results from the FEM using a very fine mesh is also obtained and used as the benchmark solution. Figure 4.14 shows the variation of the hydraulic head versus time at three different levels of $z = 2m$, $z = 5m$, and $z = 8m$. The hydraulic head is defined as $z + \frac{p_t}{\rho_f g}$ in which p_t is the total pore water pressure. A comparison of the numerical results for excess pore pressure is made at two different radial distances: $r = 10$ m and $r = 100$ m. As can be seen from Figure 4.14, the numerical results for CSPIM-T4 and CSRPIIM-T2L properly capture the benchmark solutions at all different levels and radial distances. Also included in Figure 4.14 are the numerical results obtained by Kim and Parizek [304] for the same problem, but with slightly different assumptions (e.g., volume change dependent coefficient of permeabilities, suction effects in the unsaturated zone, etc.). That is why although both

solutions are qualitatively similar and show similar trends, the values obtained in the two solutions are not the same. Comparison of the numerical results at $r = 10$ m and $r = 100$ m for CSPIMs and the FEM shows that the Noordbergum effect is mainly observed in the regions close to the pumping well.

Figure 4.15 depicts the surface settlement and the radial displacement at $z = 10$ m with respect to the radial distance at $t = 86400$ sec = 24 hr, using CSPIM-T4, CSRPIIM-T2L and the benchmark FEM, along with the results obtained by [304]. Again, both CSPIM solutions are in very good agreement with the benchmark solution and show similar trends to the results obtained by [304]. The variation of the horizontal displacement is of special interest in Figure 4.15. As it can be seen, the horizontal displacement increases with radial distance and picks at some point, before decreasing for points farther from the well. This lateral compression around the well is the main reason for the unexpected increase in the pore water pressure and leads to the Noordbergum effect.

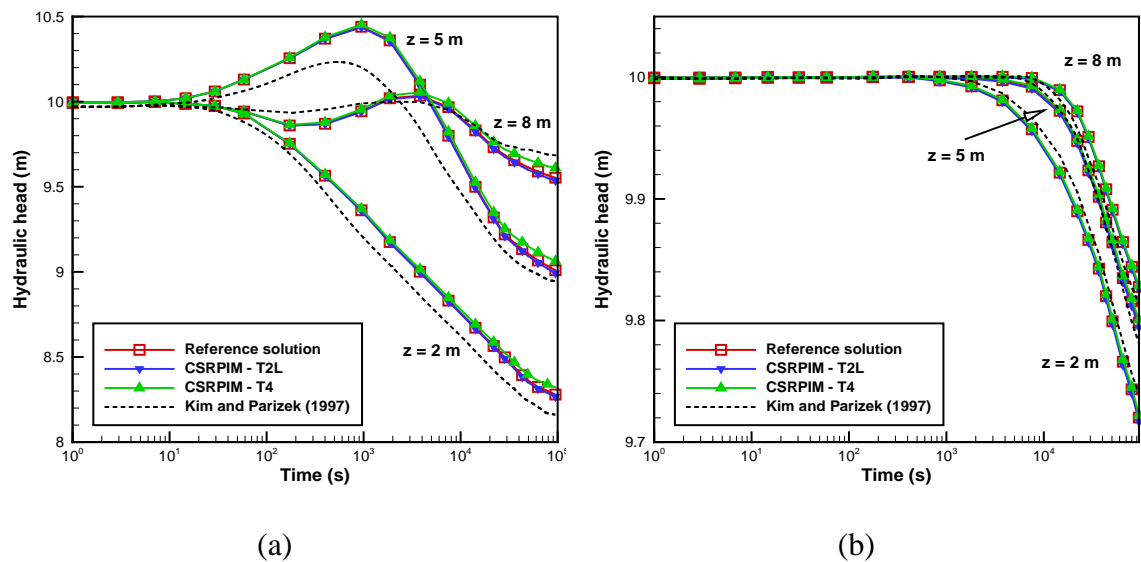


Figure 4.14. The variation in the hydraulic head versus time for the Noordbergum problem.

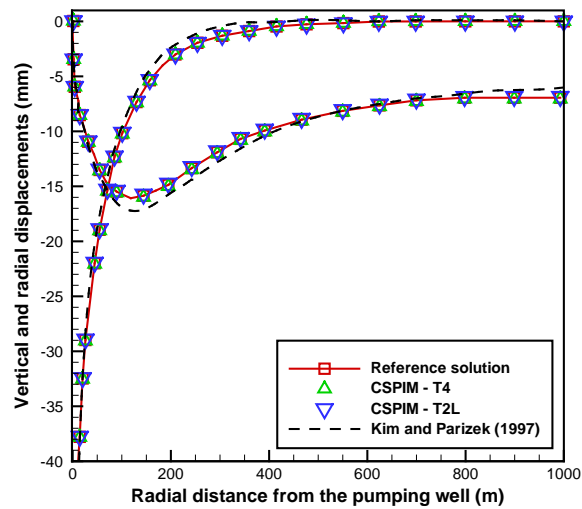


Figure 4.15. The surface and radial displacements at $z = 10\text{m}$ for the Noordbergum problem.

4.10 Conclusion

A novel approach was proposed in this chapter to solve the singularity condition associated with the application of the smoothed point interpolation methods to axisymmetric problems. In the method proposed, the property matrices of the discretised form of the coupled flow–deformation equations are decomposed into submatrices that either contain, or do not contain differentiation of the independent variables. The smoothing operation is then applied only to those submatrices that contain differentiation, while the rest of the submatrices are calculated using the Gauss integration method, very similar to the standard finite element method. The approach proposed gracefully avoids any singularity in the clay formulation, with no need for additional computations compared to the formulation in the plain strain conditions. The applicability and performance of the proposed method to solve axisymmetric coupled problems were studied through simulation of three benchmark problems. The numerical solutions were compared with the analytical solutions or benchmark solutions. In all cases, the numerical results of the proposed method showed excellent agreement with

the analytical or the reference solutions. The robustness and accuracy of the proposed method were further investigated by performing error norm analyses in terms of displacement and excess pore pressure. It was shown that the proposed methods outperform the linear finite element method in terms of both accuracy and convergence rate. Among the proposed methods, CSRPIM-T2L generally exhibited the best performance in terms of both displacement and excess pore pressure, with CSPIM-T4 being a close contestant.

5 A stabilized, low-order edge-based smoothed point interpolation method for numerical analyses in geomechanics

5.1 Preface

A stabilised smoothed point interpolation method for both linear and nonlinear numerical analysis in geomechanics is proposed. The presented method retrieves the use of equal-order linear interpolations as a natural, practical choice in the context of consistently stabilised *Galerkin* methods in computational geomechanics. The formulation presented avoids numerical instabilities and sub-optimal convergence rates often observed when (nearly) incompressible conditions are studied. In this study, the smoothing gradient technique is adopted to preserve the consistency of the proposed method for equal-order linear interpolations while discretising the field domain with a set of triangular elements. The proposed technique is generic in nature and can be applied to any SPIM/SRPIM, however, for the sake of simplicity, a special case of the edge-based SPIM with linear shape functions, often referred to as the edge-based smoothed FEM (ESFEM)[91, 92], has been adopted in this chapter for the presentation of the method and obtaining the numerical solutions. The proposed smoothed formulation retains consistency by eliminating all derivatives that appear in consistently stabilised formulations by employing the smoothing gradient operator, in which integrations of the interested quantities over the smoothing domains are transformed into those over the boundaries of the smoothing domains using the Divergence theorem. SFEMs are mathematically proven to possess greater accuracy and super convergence

than the FEM in a variety of disciplines [17, 94, 97-99, 206]. An unconditionally stabilised *Galerkin* method is applied to the ESFEM, which is used as a representative form of the smoothed FEM (SFEM) and in general SPIM, to demonstrate the applicability of the proposed method in a numerical coupled flow-deformation analysis in computational geomechanics that offers unconditional stability irrespective of *a priori* chosen mesh-dependent stabilisation parameter. This is the first time that such an unconditionally stabilised method is implemented to coupled flow-deformation problems in geomechanics. The robustness and accuracy of the proposed method are examined by comparing the attained numerical results with respect to the reference solutions of several benchmark coupled problems that encompass both linear and nonlinear material behaviour. The numerical results are also compared with those obtained by the stabilised polynomial pressure projection FEM, which has been applied previously in geomechanics [52].

5.2 Notation

In the following sections the domain Ω represents a d -dimensional connected bounded region in \mathbf{R}^d ($d = 2, 3$) with a sufficiently smooth, in the *Lipschitz* sense, boundary Γ . The usual notations $H^p(\Omega)$, $\|\cdot\|_p$ and $(\cdot, \cdot)_p$ are used (with p being a nonnegative integer) to characterise Sobolev spaces, including all functions that have square integrable derivatives up to order p on Ω , the standard Sobolev norm, and the inner product, respectively. $L^2(\Omega)$ is replaced by $H^0(\Omega)$ when $p = 0$, and the inner product designation index is dropped. The symbol $|\cdot|_k, 0 < k \leq p$ represents the k th seminorm on $H^p(\Omega)$. $H_0^p(\Omega)$ stands for the closure of $C_0^\infty(\Omega)$ with respect to the norm $\|\cdot\|_p$. G^l represents the G space, whose associated norm and inner product are shown by $\|\cdot\|_{G^1}$

and $(\cdot, \cdot)_{G^1}$, respectively. Vectors, matrices and spaces that include vector-valued functions are shown in boldface. The Euclidean inner product and norm are denoted by $\langle \cdot, \cdot \rangle$ and $|\cdot|$, respectively. The over-dot indicates the time derivative.

The symbol X^h stands for a finite dimensional space (denoted by the superscript 'h') of function X which approximates it with respect to a regular subdivision \mathcal{T}_h (which is triangulation in this study) of the domain Ω into \mathcal{K} finite subdomains, each denoted by Ω_e . $\tilde{\blacksquare}$ denotes that \blacksquare is smoothed over the smoothing domains.

5.3 The smoothed mixed *Galerkin* method

The variational statement of the coupled flow-deformation equations originally proposed by Biot [161], including material nonlinearity and with small deformation assumption, are briefly described in this section. The generalized weak form that includes the smoothed strain concept is presented. The edge-based smooth finite element method (ESFEM) is briefly discussed. Subsequently, the resulting smoothed global matrix system is linearised with the standard Newton-Raphson iterative scheme.

5.3.1 Coupled flow-deformation governing equations

The coupled equations that govern a two-phase saturated porous medium consisting of solid and fluid phases are expressed by Equation 3-1 and Equation 3-2 in conjunction with the similar definition for \mathbf{L}_d as presented in Equation 3-3. The adequate essential and natural boundary conditions that are required for the solvability of Equations 3-1 and 3-2 are defined in Equations 3-4 to 3-7 with the identical notations associated with

the definitions of the disjointed boundaries for introducing the appropriate essential and natural boundary conditions as prescribed by Equation 3-9 and Equation 3-10.

5.3.2 Constitutive modelling

It is necessary to introduce a constitutive model in a general rate form to characterise the relation between the field variables, that are the displacement and pressure fields of a porous medium, and the effective stress and volume change of the porous media. In its general form, a constitutive relation in a porous medium can be stated as:

$$\dot{\boldsymbol{\sigma}}' = \mathbf{D}^{ep} \dot{\boldsymbol{\varepsilon}} \quad (5-1)$$

in which $\boldsymbol{\varepsilon}$ is the infinitesimal strain defined as follows:

$$\boldsymbol{\varepsilon} = \mathbf{L}_d \mathbf{u} \quad (5-2)$$

and \mathbf{D}^{ep} is the tangent elasto-plastic constitutive matrix. When material nonlinearity is assumed, a strain decomposition is required for the strain rate, such that:

$$\dot{\boldsymbol{\varepsilon}} = \dot{\boldsymbol{\varepsilon}}^e + \dot{\boldsymbol{\varepsilon}}^p \quad (5-3)$$

where $\boldsymbol{\varepsilon}^e$ is the elastic (reversible) part of the strain and $\boldsymbol{\varepsilon}^p$ denotes the plastic (irreversible) part of the strain. To obtain the plastic strain, a flow rule must be adopted.

In general, the calculation of the plastic strain is expressed as:

$$\dot{\boldsymbol{\varepsilon}}^p = \dot{\gamma} \frac{\partial w}{\partial \boldsymbol{\sigma}} = \dot{\gamma} \mathbf{r}(\boldsymbol{\sigma}) \quad (5-4)$$

in which $\dot{\gamma}$ is the scalar plastic multiplier and w denotes the plastic potential function, which can be different from the yield function if non-associativity is assumed. Finally, the consistency condition implies the following condition:

$$f(\boldsymbol{\sigma}) = 0 \quad (5-5)$$

in which f stands for the yield function. In the examples presented in this study, both elastic isotropic materials and nonlinear materials are considered. For nonlinearity, Mohr-Coulomb behaviour is assumed along with both associative and non-associative flow rules. For the sake of brevity, the related yield and potential functions of Mohr-Coulomb constitutive model and their relevant implementation details are not discussed here, and interested readers are referred to [2].

5.3.3 Variational form of the standard mixed *Galerkin* method

The variational form of the coupled flow-deformation equations with the assumption of the isotropic permeability is obtained by seeking $(\mathbf{u}, p) \in \mathbf{H}_0^1(\Omega) \times H_0^1(\Omega)$ such that:

$$A(\mathbf{u}, \mathbf{v}) - \eta B(\mathbf{v}, p) = F(\mathbf{v}) \quad \forall \mathbf{v} \in \mathbf{H}_0^1(\Omega) \quad (5-6)$$

$$\eta B(\dot{\mathbf{u}}, q) + \frac{k_f}{\mu_f} H(q, p) + \alpha_f M(q, p) = T(q) \quad \forall q \in H_0^1(\Omega) \quad (5-7)$$

where $A(\cdot, \cdot)$, $B(\cdot, \cdot)$, $F(\cdot)$ and $H(\cdot)$ are defined by:

$$A(\mathbf{u}, \mathbf{v}) = \int_{\Omega} \boldsymbol{\varepsilon}^T(\mathbf{v}) \boldsymbol{\sigma}'(\boldsymbol{\varepsilon}(\mathbf{u})) d\Omega \quad (5-8)$$

$$B(\mathbf{v}, p) = \int_{\Omega} p \nabla \cdot \mathbf{v} d\Omega \quad (5-9)$$

$$H(q, p) = \int_{\Omega} (\nabla q)^T \nabla p d\Omega \quad (5-10)$$

$$M(q, p) = \int_{\Omega} q \dot{p} d\Omega \quad (5-11)$$

$$F(\mathbf{v}) = \int_{\Gamma_t} (\mathbf{v})^T \bar{\mathbf{t}} d\Gamma + \int_{\Omega} \rho(\mathbf{v})^T \mathbf{g} d\Omega \quad (5-12)$$

$$T(q) = \int_{\Gamma_q} q \bar{q} d\Gamma \quad (5-13)$$

In the interest of formulations offered in the next sections, Equations 5-6 and 5-7 are rewritten in the following form:

$$Q(\mathbf{u}, p; \mathbf{v}, q) = L(\mathbf{v}, q) \quad \forall (\mathbf{v}, q) \in \mathbf{H}_0^1(\Omega) \times H_0^1(\Omega), \quad (5-14)$$

where

$$Q(\mathbf{u}, p; \mathbf{v}, q) = A(\mathbf{u}, \mathbf{v}) - \eta B(\mathbf{v}, p) + \eta B(\dot{\mathbf{u}}, \mathbf{q}) + \frac{k_f}{\mu_f} H(q, p) + \alpha_f M(q, p) \quad (5-15)$$

and

$$L(\mathbf{v}, q) = F(\mathbf{v}) + T(q) \quad (5-16)$$

The global bilinear form of the equations presented above is based on Sobolev spaces, which are conventionally used in spatial discretisation used in the FEM to adopt the smoothing gradient technique for application in ES-FEM.

5.3.4 Smoothing domains in ESFEM

In this chapter, a linear ESFEM is adopted for the developments that follow; thus, the smoothing domains are constructed based only on the shared boundaries of neighbouring elements. However, other forms of the SFEM and also SPIM can also be implemented in a similar fashion.

The creation of smoothing domains for ESFEM analysis requires a subdivision of the problem domain. Triangulation is adopted as it is perhaps the simplest method of domain discretisation which can be performed automatically, similar to the meshing method used in the standard FEM. The mesh is assumed to be composed of N_e non-

overlapping elements, such that $\Omega = \bigcup_{e=1}^{N_e} \Omega_e$, N nodes, and N_s edges. In ESFEM, a set of smoothing domains must be created on top of the background mesh. To this end, an internal node is first added at the centroid of each element Ω_e , as shown in Figure 5.1. The partitioning of the problem domain Ω into a set of N_{SD} smoothing domains (Ω_k^s) is then performed such that $\Omega = \bigcup_{k=1}^{N_{SD}} \Omega_k^s$ and $\Omega_i^s \cap \Omega_j^s = \emptyset, i \neq j$. The smoothing domain Ω_k^s pertaining to edge k is created by connecting two end-edge points to the internal nodes of neighbouring elements, as shown in Figure 5.1.

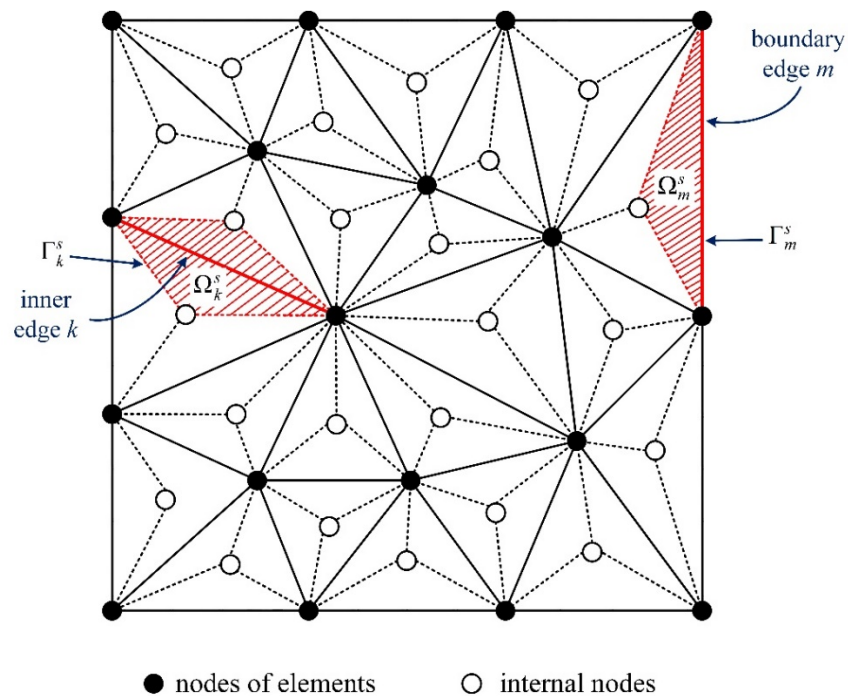


Figure 5.1. A mesh composed of linear triangular elements and its corresponding smoothing domains. An interior smoothing domain Ω_k^s corresponding to edge k of the background mesh, and a boundary smoothing domain Ω_m^s corresponding to edge m of the background mesh are highlighted.

5.3.5 Smoothing gradient operation

In SFEMs, the gradient of the displacement field is approximated over a smoothing domain by an integral representation, similar to that presented in Equation 3-27. The

smoothed gradient of the displacement field can be obtained for any smoothing domain using Equation 3-29.

5.3.6 Generalised smoothed mixed *Galerkin* formulation

The generalised smoothed *Galerkin* formulation for the coupled flow-deformation equations can now be developed. The variational form of the governing Equations 5-6 and 5-7 are confined to a pair of spaces \mathcal{S}_u and \mathcal{S}_p , defined as follows:

$$\mathcal{S}_u = \{\mathbf{u}: \Omega \rightarrow \mathbf{R}^2 | \mathbf{u} \in \mathbf{G}_h^1, \mathbf{u} = \bar{\mathbf{u}} \text{ on } \Gamma_u\} \quad (5-17)$$

$$\mathcal{S}_p = \{p: \Omega \rightarrow R | p \in G_h^1, p = \bar{p} \text{ on } \Gamma_p\} \quad (5-18)$$

The corresponding kinematically admissible spaces, $\mathbf{V}_{v,0}$ and $V_{q,0}$ respectively, are defined as follows:

$$\mathbf{V}_{v,0} = \{\mathbf{v}: \Omega \rightarrow \mathbf{R}^2 | \mathbf{v} \in \mathbf{G}_{h,0}^1, \mathbf{v} = \mathbf{0} \text{ on } \Gamma_u\} \quad (5-19)$$

$$V_{q,0} = \{q: \Omega \rightarrow R | q \in G_{h,0}^1, q = 0 \text{ on } \Gamma_p\} \quad (5-20)$$

Applying the smoothing operation technique to Equations 5-6 and 5-7, the corresponding discrete problems are obtained, which is to seek $(\mathbf{u}^h, q^h) \in \mathcal{S}_u \times \mathcal{S}_p$ such that

$$\tilde{A}(\mathbf{u}, \mathbf{v}) - \eta \tilde{B}(\mathbf{v}, p) = F(\mathbf{v}) \quad \forall \mathbf{v} \in \mathbf{V}_{u,0} \quad (5-21)$$

$$\eta \tilde{B}(\dot{\mathbf{u}}, q) + \frac{k_f}{\mu_f} \tilde{H}(q, p) + \alpha_f M(q, p) = \mathbf{T}(q) \quad \forall q \in V_{p0} \quad (5-22)$$

Alternately, the general smoothed form of the governing equations can be demonstrated as:

$$\tilde{Q}(\mathbf{u}, p; \mathbf{v}, q) = L(\mathbf{v}, q) \quad \forall (\mathbf{v}, q) \in \mathbf{V}_{u,0} \times V_{p,0} \quad (5-23)$$

where

$$\tilde{Q}(\mathbf{u}, p; \mathbf{v}, q) = \tilde{A}(\mathbf{u}, \mathbf{v}) + \eta \tilde{B}(\mathbf{v}, p) + \eta \tilde{B}(\mathbf{u}, q) + \frac{k_f}{\mu_f} \tilde{H}(q, p) + \alpha_f M(q, p) \quad (5-24)$$

$$L(\mathbf{v}, q) = \mathbf{F}(\mathbf{v}) + \mathbf{T}(q), \quad (5-25)$$

where the smoothed bilinear forms are as follows:

$$\tilde{A}(\mathbf{u}, \mathbf{v}) = \int_{\Omega} \tilde{\boldsymbol{\varepsilon}}(\mathbf{v}) \boldsymbol{\sigma}'(\tilde{\boldsymbol{\varepsilon}}(\mathbf{u})) d\Omega \quad (5-26)$$

$$\tilde{B}(\mathbf{v}, p) = \int_{\Omega} p \tilde{\nabla} \cdot \mathbf{v} d\Omega \quad (5-27)$$

$$\tilde{H}(q, p) = \int_{\Omega} (\tilde{\nabla} q)^T \tilde{\nabla} p d\Omega. \quad (5-28)$$

Equation 5-23 is referred to as the weakened weak (W^2) form [13, 14, 89, 305], because only the displacement and pressure fields, and not their derivatives, are required to be square integrable in this form. Using this form, computation of derivatives of the primary variables is no longer required. It can be proved [40] that the globally smoothed bilinear form (Equation 5-23) has a unique solution when edge-based smoothing domains are used.

It is worth mentioning that the functionals $F(\mathbf{v})$ and $T(q)$ are not involved in employing the smoothing gradient technique and have exactly the same form as the linear functionals existing in FEM variational forms.

5.4 Matrix form of the generalised smoothed mixed *Galerkin* FEM

5.4.1 Creation of linear shape functions and approximated solutions

The shape functions used in ESFEM are identical to those applied in the standard FEM associated with linear triangular elements [92]. They are computed directly using the three nodes of the triangular element hosting the point of interest. Accordingly, the pair of equal-order subspaces \mathbf{S}_u^h and S_p^h of trial functions and the subspaces $\mathbf{V}_{v,0}^h$ and $V_{q,0}^h$ of weighting functions contain piecewise linear functions for the interpolation of the field variables, and are defined as follows:

$$\mathbf{S}_u^h = \{\mathbf{u}^h \in \mathbf{G}_h^1, \mathbf{u}^h|_{\Omega_e} \in \mathbf{P}_1(\Omega_e)\} \quad (5-29)$$

$$S_p^h = \{p^h \in G_h^1, p^h|_{\Omega_e} \in P_1(\Omega_e)\} \quad (5-30)$$

$$\mathbf{V}_{v,0}^h = \{\mathbf{v}^h \in \mathbf{G}_{h,0}^1, \mathbf{v}^h|_{\Omega_e} \in \mathbf{P}_1(\Omega_e)\} \quad (5-31)$$

$$V_{q,0}^h = \{q^h \in G_{h,0}^1, q^h|_{\Omega_e} \in P_1(\Omega_e)\} \quad (5-32)$$

where $P_1(\Omega_e)$ possesses a set of polynomials of up to degree one.

Having calculated the shape functions, the approximated displacement and pressure field variables at an arbitrary point of interest $\mathbf{x} \in \Omega_e$ are interpolated in the following forms:

$$\mathbf{u}^h(\mathbf{x})|_{\Omega_e} = \mathbf{N}^u(\mathbf{x})\bar{\mathbf{u}} = \sum_{I=1}^3 \begin{bmatrix} \phi_I(\mathbf{x}) & 0 \\ 0 & \phi_I(\mathbf{x}) \end{bmatrix} \begin{Bmatrix} \bar{u}_I \\ \bar{v}_I \end{Bmatrix} \quad (5-33)$$

$$p^h(\mathbf{x})|_{\Omega_e} = \mathbf{N}^p(\mathbf{x})\bar{p} = \sum_{I=1}^3 \phi_I(\mathbf{x})\bar{p}_I \quad (5-34)$$

in which, similar to the previous chapters, \bar{u}_I and \bar{v}_I are the components of nodal displacement field values, \bar{p}_I is the nodal fluid pressure, and $\phi_I(\mathbf{x}) \in P_1(\Omega_e)$ is the

linear shape function associated with node I . $\mathbf{N}^u(\mathbf{x})$ is the shape function matrix related to the displacement field defined in the expanded form as:

$$\mathbf{N}^u(\mathbf{x})|_{\Omega_e} = \begin{bmatrix} \phi_1(\mathbf{x}) & 0 & \phi_2(\mathbf{x}) & 0 & \phi_3(\mathbf{x}) & 0 \\ 0 & \phi_1(\mathbf{x}) & 0 & \phi_2(\mathbf{x}) & 0 & \phi_3(\mathbf{x}) \end{bmatrix}_{2 \times 6} \quad (5-35)$$

and $\mathbf{N}^p(\mathbf{x})$ stands for the shape function matrix for the interpolation of the pore fluid pressure variable within an element of interest:

$$\mathbf{N}^p(\mathbf{x})|_{\Omega_e} = [\phi_1(\mathbf{x}) \quad \phi_2(\mathbf{x}) \quad \phi_3(\mathbf{x})]_{1 \times 3} \quad (5-36)$$

$\bar{\mathbf{u}}$ and $\bar{\mathbf{p}}$ are vectors where the unknown nodal displacement and pressure values for an element of interest Ω_e are collected, respectively. The *Galerkin* weighting functions may be represented as:

$$\mathbf{v}^h(\mathbf{x})|_{\Omega_e} = \mathbf{N}^u(\mathbf{x})\mathbf{c}, \quad q^h(\mathbf{x})|_{\Omega_e} = \mathbf{N}^p(\mathbf{x})\bar{\mathbf{c}}. \quad (5-37)$$

where \mathbf{c} and $\bar{\mathbf{c}}$ collect arbitrary nodal weights.

5.4.2 Computation of the property matrixes

The discretised form of Equation 5-23 includes a global coefficient matrix comprising of diagonal and off-diagonal blocks representing the contribution of different phases of the porous media. The computation of each contributing matrix and the standard global matrix form are presented in this section.

The smoothed strain $\tilde{\boldsymbol{\epsilon}}^{(k)}$ over the smoothing domain Ω_k^s can be expressed by Equation 3-34. Similar to the previous chapters, S_s collects a set of q supporting nodes that contribute to the computation of the smoothed quantity of the interest over the smoothing domain Ω_k^s . The supporting nodes S_s , for the schematic inner smoothing

domain shown in Figure 5.1 is $S_s = \{A, B, C, D\}$ and for the boundary smoothing domain shown in the same figure is $S_s = \{A, B, C\}$. $\tilde{\mathbf{B}}_{1I}$ represents the smoothed strain-displacement matrix for arbitrary supporting node I of the smoothing domain Ω_k^s , given by the similar formulation given in Equation 3-35 along with its expanded form given in Equation 3-36.

As seen from Equation 3-37, the smoothed strain-displacement matrix is computed on the boundary of the smoothing domain Γ_k^s and the participation of the derivatives of the shape functions is eliminated. In ESFEM, the line integration of Equation 3-37 requires a sufficient number of Gauss points for numerical integration. As linear shape functions are adopted in this study, one Gauss point is adequate for each segment of the boundary of the smoothing domain ($\Gamma_{mb}^s \in \Gamma_k^s$). For linear ESFEM, the form of \tilde{b}_{1I} after including the numerical integration is the same as that presented in Equation 3-37. Same notations as presented in Chapter 3 are adopted in this chapter, except that $N_{gau} = 1$ is used per each segment of a smoothing domain boundary herein. The smoothed strain-displacement matrix for smoothing domain Ω_k^s ($\tilde{\mathbf{B}}_1$) is sequentially obtained in linear ESFEM by the standard assembly procedure and can be presented in the following form:

$$\tilde{\mathbf{B}}_1 = [\sum_{I \in S_s} \tilde{\mathbf{B}}_{1I}]_{3 \times 2q} \quad (5-38)$$

For the term $\nabla p(\mathbf{x})$ in the standard variational formulation (Equation 5-7), a similar procedure as presented in Chapter 3 (Equation 3-47) must be performed to obtain the smoothed pressure gradient.

Rewriting the discrete version of bilinear form (Equations 5-26) in matrix forms, yields:

$$\tilde{\mathbf{K}}_k^s = \int_{\Omega_k^s} \tilde{\boldsymbol{\varepsilon}}(\mathbf{v}^h) \boldsymbol{\sigma}'(\tilde{\boldsymbol{\varepsilon}}(\mathbf{u}^h)) d\Omega = \int_{\Omega_k^s} \tilde{\mathbf{B}}_1^T \mathbf{D}^{ep} \tilde{\mathbf{B}}_1 d\Omega = \tilde{\mathbf{B}}_1^T \mathbf{D}^{ep} \tilde{\mathbf{B}}_1 A_k^s \quad (5-39)$$

where A_k^s stands for the area of the smoothing domain Ω_k^s . The discrete form of Equation 5-27 is identical to that presented in Equation 3-42. One of the prominent features of ESFEM is that the numerical integration is performed with no mapping rule requirement, in contrast to the FEM. Omitting the need for the mapping rule ameliorates the difficulties associated with numerical integration when the mesh undergoes distortion.

The coupling matrix is calculated by Equation 3-52, represented here as:

$$\tilde{\mathbf{C}}_k^s = \int_{\Omega} p^h \tilde{\mathbf{V}} \cdot \mathbf{v}^h d\Omega = \int_{\Omega_k^s} \tilde{\mathbf{B}}_1^T \boldsymbol{\delta} \mathbf{N}^p d\Omega = \tilde{\mathbf{B}}_1^T \boldsymbol{\delta} \int_{\Omega_k^s} \mathbf{N}^p d\Omega . \quad (5-40)$$

The term $\int_{\Omega_k^s} \mathbf{N}^p d\Omega$ in Equation 5-40 is calculated over each smoothing domain, rather than the boundary of the smoothing domains, as no smoothing operation is applied to it. This numerical integration is performed by the subdivision of each of the interior smoothing domains into two sub-triangles and by using the standard Gauss integration method for the sub-triangular areas. Subdivision is not, however, required for the boundary smoothing domains. One Gauss point per sub-triangle located on its centroid is needed to attain adequate accuracy for numerical integrations. We can therefore write,

$$\tilde{\mathbf{C}}_k^s = \tilde{\mathbf{B}}_1^T \boldsymbol{\delta} \int_{\Omega_k^s} \mathbf{N}^p d\Omega = 2 \tilde{\mathbf{B}}_1^T \boldsymbol{\delta} \sum_{i=1}^{n_{tr}} A_i^{tr} \mathbf{N}_i^p w_i \quad (5-41)$$

where n_{tr} denotes the number of sub-triangles for the smoothing domain of interest and A_i^{tr} is the area of the triangle that hosts the Gauss points of interest. Finally, the fluid compressibility matrix (\mathbf{M}_k) is calculated over each smoothing domain in a manner similar to the standard FEM, because there is no smoothing operation involved in its definition. The vector of nodal fluxes \mathbf{T}_k and the vector of nodal forces \mathbf{F}_k are also calculated using Equations 3-44 and 3-45, respectively.

The standard assembly procedure is then performed to form the global property matrices and vectors of spatially discretised coupled flow-deformation equations as:

$$\tilde{\mathbf{K}} = \sum_{k=1}^{N_{SD}} \tilde{\mathbf{K}}_k^S \quad (5-42)$$

$$\tilde{\mathbf{H}} = \sum_{k=1}^{N_{SD}} \tilde{\mathbf{H}}_k^S \quad (5-43)$$

$$\tilde{\mathbf{C}} = \sum_{k=1}^{N_{SD}} \tilde{\mathbf{C}}_k^S \quad (5-44)$$

$$\mathbf{M} = \sum_{k=1}^{N_{SD}} \mathbf{M}_k \quad (5-45)$$

$$\mathbf{F} = \sum_{k=1}^{N_{SD}} \mathbf{F}_k \quad (5-46)$$

$$\mathbf{T} = \sum_{k=1}^{N_{SD}} \mathbf{T}_k \quad (5-47)$$

where $\tilde{\mathbf{K}}$, $\tilde{\mathbf{H}}$, $\tilde{\mathbf{C}}$, \mathbf{M} , \mathbf{F} and \mathbf{T} are already introduced in Chapter 3.

5.4.3 Linearisation

Equations 5-21 and 5-22, in general, express two nonlinear residual equations whose solution requires an appropriate iterative procedure. Here, the standard Newton-Raphson procedure is adopted. Accordingly, the coupled equations are linearly expanded about the configuration of interest. The residual forms of Equations 5-21 and 5-22 can be written as follows:

$$\Psi_u(\mathbf{u}^h, \mathbf{p}^h, \mathbf{v}^h) = \tilde{\mathbf{A}}(\mathbf{u}^h, \mathbf{v}^h) - \eta \tilde{\mathbf{B}}(\mathbf{v}^h, \mathbf{p}^h) - \mathbf{F}(\mathbf{v}^h) = 0 \quad (5-48)$$

$$\Psi_p(\mathbf{u}^h, \mathbf{p}^h, q^h) = \eta \tilde{\mathbf{B}}(\dot{\mathbf{u}}^h, q^h) + \frac{k_f}{\mu_f} \tilde{\mathbf{H}}(q^h, \mathbf{p}^h) + \alpha_f \mathbf{M}(q^h, \mathbf{p}^h) - \mathbf{T}(q^h) = 0 \quad (5-49)$$

Expanding Equations 5-48 and 5-49 about a trial solution $(\mathbf{u}_i^h, \mathbf{p}_i^h)$ results in:

$$\Psi_u(\mathbf{u}^h, p^h, \mathbf{v}^h) \approx \Psi_u(\mathbf{u}_i^h, p_i^h, \mathbf{v}^h) + \Delta\Psi_u(d\mathbf{u}_i^h, dp_i^h, \mathbf{v}^h) = \mathbf{0} \quad (5-49)$$

$$\Psi_p(\mathbf{u}^h, p^h, q^h) \approx \Psi_p(\mathbf{u}_i^h, p_i^h, q^h) + \Delta\Psi_p(d\mathbf{u}_i^h, dp_i^h, q^h) = \mathbf{0} \quad (5-50)$$

in which d represents the incremental variation of the quantity of interest used to update the unknown variables, i.e., $\mathbf{u}_{i+1}^h = \mathbf{u}_i^h + d\mathbf{u}_i^h$ and $p_{i+1}^h = p_i^h + dp_i^h$, and index i represents the i th iteration in the current time step. Δ represents the imbalance of the residuals due to the trial solutions not being perfect. The updated solution is sought by rendering the residuals zero, resulting in:

$$\Delta\Psi_u(d\mathbf{u}_i^h, dp_i^h, \mathbf{v}^h) = -\Psi_u(\mathbf{u}_i^h, p_i^h, \mathbf{v}^h) \quad (5-51)$$

$$\Delta\Psi_p(d\mathbf{u}_i^h, dp_i^h, q^h) = -\Psi_p(\mathbf{u}_i^h, p_i^h, q^h) \quad (5-52)$$

The Newton-Raphson standard procedure involves iteratively linearising the left-hand side of Equations 5-52 and 5-53, and solving the ensuing linear problems to find the approximated solutions so that the residuals approach zero. Before obtaining the corresponding linear equations explicitly, the system of equations needs to be discretised in the time domain too. In this study, a three-point time discretisation technique with variable time steps is adopted [143], except for the first time step, in which a standard forward Euler scheme is utilised. In this technique, the estimation of the time derivative of a function of interest f at time $t + \alpha\Delta t$ is made based on the function values at times $t - \Delta t$, t and $t + \alpha\Delta t$, using Equation 3-55 associated with its relevant defined coefficients presented in Equation 3-56.

Equations 5-48 and 5-49 are now rewritten in the fully discretised forms at the current time step $t + \alpha\Delta t$ in the following way:

$$(\Psi_u)^{t+\alpha\Delta t} = \int_{\Omega} \tilde{\mathbf{B}}_1^T(\boldsymbol{\sigma}')^{t+\alpha\Delta t} d\Omega - \eta \tilde{\mathbf{C}}\mathbf{P}^{t+\alpha\Delta t} - \mathbf{F}^{t+\alpha\Delta t} = \mathbf{0} \quad (5-53)$$

$$(\Psi_p)^{t+\alpha\Delta t} = \eta \tilde{\mathbf{C}}^T (A\mathbf{U}^{t+\alpha\Delta t} - B\mathbf{U}^t + C\mathbf{U}^{t-\Delta t}) + \Delta t \tilde{\mathbf{H}}\mathbf{P}^{t+\alpha\Delta t} + a_f \mathbf{M} (A\mathbf{P}^{t+\alpha\Delta t} - B\mathbf{P}^t + C\mathbf{P}^{t-\Delta t}) - \Delta t \mathbf{T}^{t+\alpha\Delta t} = \mathbf{0} \quad (5-54)$$

where \mathbf{U} and \mathbf{P} are the global nodal displacement and nodal pressure vectors, respectively, in which all nodal displacement and pressure components for a discretised domain are stored. The term $\int_{\Omega} \tilde{\mathbf{B}}_1^T(\boldsymbol{\sigma}')^{t+\alpha\Delta t} d\Omega$ represents another form of $\tilde{\mathbf{K}}_T \mathbf{U}^{t+\alpha\Delta t}$ when the material nonlinearity is included. The subscript T in $\tilde{\mathbf{K}}_T$ implies that the stiffness matrix is calculated based on the tangent elasto-plastic constitutive model, as follows:

$$\mathbf{D}^{ep} = \frac{\partial \boldsymbol{\sigma}'_k}{\partial \boldsymbol{\varepsilon}_k} \quad (5-55)$$

Refinement to the trial solutions needs to be performed to achieve the nodal displacements and pore fluid pressures that satisfy Equations 5-53 and 5-54. An iterative procedure is therefore required at the current time step, in the form of:

$$(\Psi_u)_{i+1}^{t+\alpha\Delta t} = \int_{\Omega} \tilde{\mathbf{B}}_1^T(\boldsymbol{\sigma}')_{i+1}^{t+\alpha\Delta t} d\Omega - \eta \tilde{\mathbf{C}}\mathbf{P}_{i+1}^{t+\alpha\Delta t} - (\mathbf{F})_{i+1}^{t+\alpha\Delta t} = \mathbf{0} \quad (5-56)$$

$$(\Psi_p)_{i+1}^{t+\alpha\Delta t} = \eta \tilde{\mathbf{C}}^T (A\mathbf{U}_{i+1}^{t+\alpha\Delta t} - B\mathbf{U}^t + C\mathbf{U}^{t-\Delta t}) + \Delta t \tilde{\mathbf{H}}\mathbf{P}_{i+1}^{t+\alpha\Delta t} + a_f \mathbf{M} (A\mathbf{P}_{i+1}^{t+\alpha\Delta t} - B\mathbf{P}^t + C\mathbf{P}^{t-\Delta t}) - \Delta t (\mathbf{T})_{i+1}^{t+\alpha\Delta t} = \mathbf{0} \quad (5-57)$$

Using Taylor series expansion, the following equations can be developed to find the solution at $(i + 1)th$ iteration using the solution obtained at ith iteration:

$$\begin{Bmatrix} (\Psi_u)_{i+1}^{t+\alpha\Delta t} \\ (\Psi_p)_{i+1}^{t+\alpha\Delta t} \end{Bmatrix} = \begin{Bmatrix} (\Psi_u)_i^{t+\alpha\Delta t} \\ (\Psi_p)_i^{t+\alpha\Delta t} \end{Bmatrix} + J_i \begin{Bmatrix} d\mathbf{U}_{i+1}^{t+\alpha\Delta t} \\ d\mathbf{P}_{i+1}^{t+\alpha\Delta t} \end{Bmatrix} = \mathbf{0} \quad (5-58)$$

in which the Jacobian matrix is defined as:

$$J = \begin{bmatrix} \frac{\partial \Psi_u}{\partial U} & \frac{\partial \Psi_u}{\partial P} \\ \frac{\partial \Psi_p}{\partial U} & \frac{\partial \Psi_p}{\partial P} \end{bmatrix} \quad (5-59)$$

A more explicit form of the Jacobian matrix can be expressed as:

$$J_i = \begin{bmatrix} (\tilde{\mathbf{K}}_T)_i^{t+\alpha\Delta t} & -\eta\tilde{\mathbf{C}} \\ A\eta\tilde{\mathbf{C}}^T & (A\alpha_f\mathbf{M} + \Delta t\tilde{\mathbf{H}}) \end{bmatrix} \quad (5-60)$$

The Jacobian matrix will be independent of the iteration number if a linear elastic constitutive model is adopted.

The incremental displacement vector $d\mathbf{U}_{i+1}^{t+\alpha\Delta t}$ and pressure vector $d\mathbf{P}_{i+1}^{t+\alpha\Delta t}$ at iteration $i+1$ are then computed using the following equation:

$$\begin{Bmatrix} d\mathbf{U}_{i+1}^{t+\alpha\Delta t} \\ d\mathbf{P}_{i+1}^{t+\alpha\Delta t} \end{Bmatrix} = -J_i^{-1} \begin{Bmatrix} (\Psi_u)_i^{t+\alpha\Delta t} \\ (\Psi_p)_i^{t+\alpha\Delta t} \end{Bmatrix} \quad (5-61)$$

Numerical algorithms and convergence criteria similar to those used in [148] were adopted in this study to perform the Newton-Raphson iterations at each time step.

5.5 Consistently stabilised mixed ESFEM

It is reported in the literature [e.g., [38, 46, 167, 306]] that in general, the formulation presented based on equal-order \mathbf{S}_u^h and S_p^h subspaces leads to volumetric locking and the presence of severe oscillation in the approximated pressure solution in the case of (nearly) incompressible material. In this sense, ESFEM suffers from the same deficiencies as the standard FEM. In this section, the root of these instabilities is discussed, and a stabilised ESFEM is developed to overcome them.

5.5.1 The inf–sup condition

The linearised smoothed matrix from of the flow-deformation equation (Equation 5-58) produces stable solutions if and only if a pair of subspaces $(\mathbf{V}_u, \mathbf{V}_p)$ satisfies the inf–sup condition [1, 2, 27]:

$$\inf_{q^h \in V_p, q^h \neq 0} \sup_{\mathbf{v}^h \in \mathbf{V}_u, \mathbf{v}^h \neq 0} \frac{\tilde{B}(\mathbf{v}^h, q^h)}{\|\mathbf{v}^h\|_{G_1} \|q^h\|_{G_1}} = k_h \geq k_h^{min} > 0 \quad (5-62)$$

in which k_h^{min} is a constant independent of the mesh size h . This condition equivalently implies that the coupling matrix $\tilde{\mathbf{C}}_k^s$ must be uniformly of full row rank with respect to the mesh size approaching zero [53, 167, 306, 307]. There are many pairs of subspaces for displacements and fluid pressure that results in an unstable solution, including the equal-order interpolation functions with respect to the same triangulation, which is perhaps the simplest choice. In addition, there are other combinations of spaces (such as bilinear–constant pairs) used for interpolation of the discretised *Stokes* equation that show severe instability when is employed in the *Galerkin* formulation [38, 40, 41, 167, 306]. The primary incentive to design stabilised methods is to permit attainment of stable and accurate solutions by simple pairs of spaces, offering additional computational benefits (e.g., uniform data structures and local mass conservation).

5.5.2 Consistently stabilised smoothed *Galerkin* methods

The general form of the consistently stabilised smoothed *Galerkin* methods can be stated as families of the bilinear forms for the Biot’s equations in the following form:

$$\begin{aligned} \tilde{Q}(\mathbf{u}^h, p^h; \mathbf{v}^h, q^h) + \langle \dot{\mathbf{R}}_m(\mathbf{u}^h, p^h), \dot{\mathbf{W}}_m(\mathbf{v}^h, q^h) \rangle_m + \langle \dot{\mathbf{R}}_c(\mathbf{u}^h, p^h), \dot{\mathbf{W}}_c(\mathbf{v}^h, q^h) \rangle_c = \\ L(\mathbf{v}^h, q^h) \quad \forall (\mathbf{v}^h, q^h) \in \mathbf{V}_{v,0}^h \times V_{q,0}^h \end{aligned} \quad (5-63)$$

where $\dot{\mathbf{R}}_m(\mathbf{u}^h, p^h)|_{\Omega_e}$ and $\dot{\mathbf{R}}_c(\mathbf{u}^h, p^h)|_{\Omega_e}$ stand for the smoothing domain-based, rate-dependent residual of the equilibrium equation and the fluid continuity equation in the coupled flow-deformation formulation, respectively, expressed in the following forms:

$$\dot{\mathbf{R}}_m(\mathbf{u}^h, p^h)|_{\Omega_e} = \mathbf{L}_d^T \dot{\boldsymbol{\sigma}}(\mathbf{u}^h, p^h) + \dot{\bar{\rho}} \bar{\mathbf{g}} \quad (5-64)$$

$$\dot{\mathbf{R}}_c(\mathbf{u}^h, p^h)|_{\Omega_e} = \nabla \cdot \left[\frac{k_f}{\mu_f} (-\nabla p^h + \rho_f \bar{\mathbf{g}}) \right] + \alpha_f \dot{p}^h + \nabla \cdot \dot{\mathbf{u}}^h \quad (5-65)$$

$\langle \cdot \rangle_m$ and $\langle \cdot \rangle_c$ denote *discrete* inner L^2 products for the residuals of the equilibrium and continuity equations, respectively, which are associated with $\mathbf{W}_m(\mathbf{v}^h, q^h)$ and $\dot{\mathbf{W}}_c(\mathbf{v}^h, q^h)$, the corresponding forms of the weighting functions.

Equation 5-63 presents the consistently stabilised smoothed *Galerkin* method in its most general form. In the formulations to follow, the weighting function corresponding to the residual of the continuity equation is set to zero ($\mathbf{W}_c = 0$) since studies show that the stabilisation resulting from these terms cannot effectively alleviate the fluid pressure instabilities when a porous medium with compressible constituents is considered [193]. For the weighting function corresponding to the residual of the equilibrium equation, the following form is adopted:

$$\mathbf{W}_m(\mathbf{v}^h, q^h)|_{\Omega_k^s} = \mathbf{L}_d^T \boldsymbol{\sigma}(\alpha \mathbf{v}^h, \beta q^h) \quad (5-66)$$

where $\boldsymbol{\sigma}(\alpha \mathbf{v}^h, \beta q^h) = \boldsymbol{\sigma}'(\alpha \mathbf{v}^h) - \eta \beta q^h \boldsymbol{\delta}$, α can take values of ± 1 or 0, and the value of β can be either 1 or -1. The discrete inner product in Equation 5-64 is defined as the weighted summation of the integrations over the smoothing domains, as follows:

$$\langle \mathbf{u}^h, \mathbf{v}^h \rangle_m = \sum_{\Omega_k^s \in \Omega} \tau(\mathbf{u}^h, \mathbf{v}^h)_{0, \Omega_k^s} \quad (5-67)$$

The positive, real-value τ is known as the stabilisation parameter, whose value must be properly selected to ensure stability in consistently stable *Galerkin* methods. The stabilisation parameter will be quantified and discussed later in this chapter.

The consistently stabilised SFEM adopted in this study can then be represented as follows:

$$\tilde{Q}_{\alpha\beta}(\mathbf{u}^h, p^h; \mathbf{v}^h, q^h) = L_{\alpha\beta}(\mathbf{v}^h, q^h) \quad \forall (\mathbf{v}^h, q^h) \in \mathbf{V}_{v,0}^h \times V_{q,0}^h \quad (5-68)$$

where, $\tilde{Q}_{\alpha\beta}$ stands for the globally stabilised smoothed bilinear form, parameterised by α and β , and $L_{\alpha\beta}$ denotes the associated linear functional. $\tilde{Q}_{\alpha\beta}$ has the following form:

$$\begin{aligned} \tilde{Q}_{\alpha\beta}(\mathbf{u}^h, p^h; \mathbf{v}^h, q^h) &= \tilde{A}(\mathbf{u}^h, \mathbf{v}^h) - \tilde{B}(\mathbf{v}^h, p^h) + \beta \tilde{B}(\mathbf{u}^h, q^h) \\ &+ \sum_{\Omega_k^s \in \Omega} (\mathbf{L}_d^T \boldsymbol{\sigma}(\alpha \mathbf{v}^h, \beta q^h), \tau (\mathbf{L}_d^T \dot{\boldsymbol{\sigma}}(\mathbf{u}^h, p^h) + \dot{\bar{\rho}} \bar{\mathbf{g}}))_{0, \Omega_k^s} \end{aligned} \quad (5-69)$$

and the linear functional is defined as follows:

$$L_{\alpha\beta}(\mathbf{v}^h, q^h) = F(\mathbf{v}^h) + H(q^h) - \sum_{\Omega_k^s \in \Omega} (\dot{\bar{\rho}} \bar{\mathbf{g}}, \mathbf{L}_d^T \boldsymbol{\sigma}(\alpha \mathbf{v}^h, \beta q^h))_{0, \Omega_k^s} \quad (5-70)$$

Depending on the selected values for α , different consistently stabilised *Galerkin* methods can be obtained. For $\alpha = 1, 0, -1$ along with $\beta = 1$ the stabilised method corresponds, respectively, to the *Galerkin least squares (GLS) method* [308], the *pressure-Poisson stabilised Galerkin method* [46], and the *absolute stabilised method* of Douglas and Wang [172]. Different values of β equal to either 1 or -1 may result in obtaining different global algebraic systems, which might possess either strong coercivity or weak coercivity properties [53]; however, they will result in identical numerical results for displacement and pressure variables if the same α is chosen [53]. GLS has been successfully applied in the numerical modelling of geomechanical

problems, ignoring the flow-deformation process in [50]. The *pressure-Poisson stabilised Galerkin* was proposed in association with simplifying assumptions compared to the GLS method, and has, to date, been adopted for the flow-deformation analysis of both saturated and unsaturated porous media [51, 195], which has much less computational costs without losing the desired accuracy. However, the abrupt change in the displacement and pressure contours can be observed in numerical results presented in [50]. Furthermore, the effectiveness of the *pressure-Poisson* stabilisation technique is highly sensitive to the selection of the stabilisation parameter.

The added stabilisation term, in general, contains the abstract notion of the residual of the differential equilibrium equation. The consistency is, hence, provided by term $L_d^T \boldsymbol{\sigma}(\mathbf{u}^h, p^h)$ which vanishes as the mesh size approaches zero. The advantageous property of the methods represented by Equation 5-64 is that all stabilising terms are implementable at the smoothing domain level.

The added stabilising term is based solely on the residual of the equilibrium equation, but the coupling between the displacement and pressure variables, naturally provided through Terzaghi's effective stress principle, results in effective alleviation of fluid pressure oscillations in the numerical results when consistently equilibrium-based stabilised methods are used.

The introduction of stabilising terms to the governing bilinear form of the problem results in appearance of additional bilinear terms in the governing bilinear form. Adopting a linearisation similar to that used for the original governing equations, Equation 5-77 can be rewritten as follows:

$$\begin{aligned} \tilde{Q}_{\alpha\beta}(\mathbf{u}^h, p^h; \mathbf{v}^h, q^h) = & \tilde{A}(\mathbf{u}^h, \mathbf{v}^h) - \tilde{B}(\mathbf{v}^h, p^h) + \beta \tilde{B}(\mathbf{u}^h, q^h) + \alpha D(\mathbf{u}^h, \mathbf{v}^h) + \\ & \alpha O(\mathbf{v}^h, q^h) + \beta O(\mathbf{u}^h, q^h) + \beta Y(p^h, q^h) \end{aligned} \quad (5-71)$$

where D , O and Y are the bilinear forms corresponding to stabilising contributions arising from the discretisation of the added residual of equilibrium equation. They contribute to the stiffness, coupling and permeability blocks in the global matrix system, respectively. In this chapter, the method similar to the one proposed by Douglas and Wang [172] is adopted (i.e., $\alpha = -1, \beta = 1$) as it offers unconditional stability, regardless of the value of the stabilisation parameter τ [53].

Equation 5-69 can thus be restricted to the form of:

$$\tilde{Q}_{-1,1}(\mathbf{u}^h, p^h; \mathbf{v}^h, q^h) = L_{-1,1}(\mathbf{v}^h, q^h) \quad \forall (\mathbf{v}^h, q^h) \in \mathbf{V}_{v,0}^h \times V_{q,0}^h \quad (5-72)$$

where

$$\begin{aligned} \tilde{Q}_{-1,1}(\mathbf{u}^h, p^h; \mathbf{v}^h, q^h) = & \tilde{A}(\mathbf{u}^h, \mathbf{v}^h) - \tilde{B}(\mathbf{v}^h, p^h) + \tilde{B}(\mathbf{u}^h, q^h) + D(\mathbf{u}^h, \mathbf{v}^h) + \\ & O(\mathbf{v}^h, p^h) + O(\mathbf{u}^h, q^h) + Y(p^h, q^h) \end{aligned} \quad (5-73)$$

It can be easily identified that the yet non-smoothed bilinear terms D and O that are added to the globally smoothed bilinear form contain second-order derivatives of the displacement and its corresponding weight function. As a result, simple equal-order linear interpolation functions for displacement and fluid pressure cannot be effectively used if this bilinear form of the governing equations is adopted, because the added stabilising terms of the displacement variable are vanished in this case, and the stabilisation term is reduced to $\sum_{\Omega_k^s \in \Omega} (\nabla q^h, \tau \nabla p^h)_{0, \Omega_k^s}$, which corresponds to the inconsistently stabilised method proposed in [44]. This method was compared with the other stabilisation methods proposed in geomechanics in [37, 50, 51, 193] and was shown that has sub-optimal convergence rate and poor accuracy. The deterioration of accuracy intensifies as the pressure variable is exposed to an incorrect natural boundary condition as the naturally induced boundary condition term $\sum_{\Omega_k^s \in \Omega} (\Delta \mathbf{u}^h, \tau \nabla q^h)_{0, \Omega_k^s}$

vanishes when employing equal-order linear interpolation functions. This problem is gracefully circumvented by smoothing the additional bilinear terms over the smoothing domains, as discussed later in this chapter.

5.5.3 Stabilisation parameter

A dimensional analysis shows that τ has the unit of $m^2/\frac{kN}{m^2}$. The basic scalar form of the stabilisation parameter introduced in [46] is adopted in this study:

$$\tau = \frac{\alpha^e (h^e)^2}{2G_i} \quad (5-74)$$

where h^e is the size of the smoothing domain which has the directional character, computed in the direction of the current pressure gradient vector by the method proposed in [193], as edge-based smoothing domains are four-sided convex non-regular areas. G_i stands for the current shear modulus of the smoothing domain of interest. This corresponds to elastic shear modulus G when material linearity is considered, and to the component of $D_{33,i}^{ep}$ of the tangent elasto-plastic matrix \mathbf{D}^{ep} in a general elasto-plastic material behaviour [ref]. The stabilisation parameter therefore accounts for the variation of the shear modulus during a materially nonlinear analysis of a porous medium. Another method for accounting for the variation of the stabilisation parameter with the shear modulus was proposed in [52]. However, based on this thesis's investigations, this method is not effective in severely nonlinear cases; especially for the computation of the collapse load of footings.

Equation 5-75 is indeed a simple form for calculation of the stabilisation parameter. There are more complex forms suggested for quantification of the stabilisation

parameters in the literature, for example for the stabilisation of the transient analysis of advection-diffusion problems in computational fluid dynamics [309, 310], and for the stabilisation of the flow-deformation discretised equations [193], which are also adopted in [51]. It has to be noted that the time step has also a major influence in the numerical results of a stabilised numerical method as reported in [311, 312], which show that the time step should have a proportionality relationship with the mesh size. The aforementioned references show that when a relatively very small time step is taken, even the consistently stabilised methods may either generate pressure oscillations or diverge from the exact solutions. However, accurate results can be achieved when time step sizes are chosen in proportion to the mesh size, using both time step-dependent stabilisation parameter and the simple form of the stabilisation parameter presented above [53, 311, 312].

5.5.4 Spatial and temporal discretisation of the proposed stabilisation method

The term that has been added to the global smoothed bilinear form (\tilde{Q}) for the stabilisation can be presented in the following form:

$$\sum_{\Omega_k^s \in \Omega} ((\mathbf{L}_d^T \boldsymbol{\sigma}(-\mathbf{v}^h, q^h)), \tau(\mathbf{L}_d^T \dot{\boldsymbol{\sigma}}(\mathbf{u}^h, p^h) + \bar{\rho} \mathbf{g}))_{0, \Omega_k^s} \quad (5-75)$$

Considering the general case that includes material nonlinearity, the weighting part of Equation 5-76, $\mathbf{L}_d^T \boldsymbol{\sigma}(-\mathbf{v}^h, q^h)$, can be expanded in the following form:

$$\mathbf{L}_d^T \boldsymbol{\sigma}(-\mathbf{v}^h, q^h) = \mathbf{L}_d^T (\mathbf{D}^e(\boldsymbol{\varepsilon}(-\mathbf{v}^h, q^h) - \boldsymbol{\varepsilon}^p(-\mathbf{v}^h)) - \eta \boldsymbol{\delta} q^h) \quad (5-76)$$

According to [50, 51], the contribution of the plastic strain embedded in the displacement weighting function can be ignored compared to that of the elastic strain,

and therefore omitted in order to avoid unnecessary linearisation of the weighting function, and to prevent undue difficulties that would otherwise arise in the calculation of the global matrix system. Thus, Equation 5-76 can be simplified to the following spatially discretised form:

$$\sum_{\Omega_k^s \in \Omega} \int_{\Omega_k^s} [-\mathbf{G}_{el}^u \bar{\mathbf{v}} - \eta \nabla \mathbf{N}^p \bar{q}]^T \tau [\mathbf{L}_d^T \dot{\boldsymbol{\sigma}}(\mathbf{u}^h, p^h) + \bar{\rho} \dot{\mathbf{g}}] d\Omega \quad (5-77)$$

where \mathbf{G}_{el}^u is the stabilising matrix representing the contribution of the weighting function of the displacement variable in the proposed stabilisation formulation. The body forces are assumed independent of time in this study, therefore, the term $\bar{\rho} \dot{\mathbf{g}}$ is omitted from the formulation in the rest of this chapter.

The residual of the equilibrium equation term $\mathbf{L}_d^T \dot{\boldsymbol{\sigma}}(\mathbf{u}^h, p^h)$ can be written in terms of unknown nodal values of displacement and pressure variables in the following form:

$$\mathbf{L}_d^T \dot{\boldsymbol{\sigma}}(\mathbf{u}^h, p^h) = (\mathbf{G}_{ep}^u \dot{\mathbf{u}} - \eta \nabla \mathbf{N}^p \dot{p}) \quad (5-78)$$

in which \mathbf{G}_{ep}^u denotes the contributing matrix resulted from the displacement variable in the proposed stabilisation formulation.

For the standard FEM formulation, \mathbf{G}_{ep}^u and \mathbf{G}_{el}^u can be expressed in the following form:

$$\mathbf{G}_{ep}^u = \mathbf{L}_d^T \mathbf{D}^{ep} \mathbf{B} \quad (5-79)$$

$$\mathbf{G}_{el}^u = \mathbf{L}_d^T \mathbf{D}^e \mathbf{B} \quad (5-80)$$

where \mathbf{B} stands for the standard strain-displacement matrix containing the first-order derivatives of the shape functions. \mathbf{G}_{ep}^u is equivalent to \mathbf{G}_{el}^u when elastic linear material is assumed in the analysis.

As can be seen, the contributing matrices associated with displacement and its weighting function (\mathbf{G}_{ep}^u and \mathbf{G}_{el}^u) would vanish if a linear interpolation function is adopted for the displacement variable, due to the existence of second-order derivatives in \mathbf{G}_{ep}^u and \mathbf{G}_{el}^u . Accordingly, the proposed formulation would lose most of its benefits, and reduce to the inconsistent stabilisation method proposed in [44] when linear interpolations are used. To overcome this difficulty, the next section presents a new technique for computation of \mathbf{G}_{ep}^u and \mathbf{G}_{el}^u .

5.5.5 Computation of the smoothed \mathbf{G}_{ep}^u and \mathbf{G}_{el}^u

Ensuring the effective contribution of the displacement and its weighting function in the proposed formulation even when linear interpolation functions are used, requires the elimination of derivatives from their corresponding stabilising matrices. To this end, the smoothing gradient technique is applied to the standard formulations of \mathbf{G}_{ep}^u and \mathbf{G}_{el}^u (Equations 5-79 and 5-80). However, given that the smoothed stress is constant over the smoothing domains, \mathbf{G}_{ep}^u and \mathbf{G}_{el}^u cannot be directly obtained. The smoothing gradient technique is applicable to \mathbf{G}_{ep}^u and \mathbf{G}_{el}^u provided that the smoothed stress over the smoothing domain of interest is first expressed in terms of its supporting nodal values. Thus, a technique is proposed here to obtain the smoothed nodal stresses by means of global projection. This technique is based on replacing the constant smoothed stress over the smoothing domains with an equivalent nodal smoothed stress in such a way that the global error associated with this replacement is minimized over the domain of the problem of interest in the formulation.

We define $\tilde{\boldsymbol{\epsilon}}^{*(k)}$ as the vector of the *recovered* smoothed strain at any point of interest (\mathbf{x}_k) within its corresponding smoothing domain (Ω_k^S), as follows:

$$\tilde{\boldsymbol{\epsilon}}^{*(k)} = \mathbf{N}^{u*}(\mathbf{x}_k) \bar{\boldsymbol{\epsilon}}^{(k)} \quad (5-81)$$

where \mathbf{N}^{u*} is the matrix of interpolation functions over the smoothing domain of interest, relating the recovered smoothed strain to its corresponding recovered nodal values, defined as follows:

$$\mathbf{N}^{u*}(\mathbf{x}_k) = [\sum_{I \in \mathcal{S}_s} \mathbf{N}_I^{u*}(\mathbf{x}_k)]_{3 \times 3q} \quad (5-82)$$

$$\mathbf{N}_I^{u*}(\mathbf{x}_k) = \begin{pmatrix} \phi_I(\mathbf{x}_k) & 0 & 0 \\ 0 & \phi_I(\mathbf{x}_k) & 0 \\ 0 & 0 & \phi_I(\mathbf{x}_k) \end{pmatrix}_{I \in \mathcal{S}_s} \quad (5-83)$$

where $\bar{\boldsymbol{\epsilon}}^{(k)}$ is the vector of *recovered* nodal strains which defined over each smoothing domain as:

$$\bar{\boldsymbol{\epsilon}}^{(k)} = \mathbf{W}^{(k)} \tilde{\boldsymbol{\epsilon}}^{(k)} \quad (5-84)$$

where $\mathbf{W}^{(k)}$ contains the rows and columns that correspond to the smoothing domain k , deduced from the globally computed \mathbf{W} matrix, given as:

$$\mathbf{W} = \left(\int_{\Omega} \mathbf{N}^{gl,u*T} \mathbf{N}^{gl,u*} d\Omega \right)^{-1} \left(\int_{\Omega} \mathbf{N}^{gl,u*T} d\Omega \right) \quad (5-85)$$

\mathbf{W} relates the recovered nodal smoothed strain globally computed over the problem domain ($\bar{\boldsymbol{\epsilon}}$) to its corresponding smoothed strain of all smoothing domains ($\tilde{\boldsymbol{\epsilon}}$) in the following form:

$$\bar{\boldsymbol{\epsilon}} = \mathbf{W} \tilde{\boldsymbol{\epsilon}} \quad (5-86)$$

so that it minimises the global error associated with using the recovered smoothed strain instead of the smoothed strain on the domain of interest. \mathbf{N}^{gl,u^*} stands for the globally assembled form of \mathbf{N}^{u^*} computed over each smoothing domain.

The terms of \mathbf{N}^{u^*} are evaluated by numerical integration over the corresponding smoothing domain using the Gauss points at the centroids of the sub-triangles, which are also used for the integration of some of the property matrixes (e.g., compressibility matrix \mathbf{M}_k). Then, the standard assembly procedure is performed to obtain the global matrix \mathbf{N}^{gl,u^*} as follows:

$$\mathbf{N}^{gl,u^*} = \bigcup_{k=1}^{NSD} \mathbf{N}^{u^*} \quad (5-87)$$

And we then have:

$$\tilde{\boldsymbol{\epsilon}}^* = \mathbf{N}^{gl,u^*} \bar{\boldsymbol{\epsilon}} \quad (5-88)$$

The variation of the recovered smoothed strain ($\delta\tilde{\boldsymbol{\epsilon}}^*$) is also evaluated in a similar fashion and is expressed as:

$$\delta\tilde{\boldsymbol{\epsilon}}^* = \mathbf{N}^{gl,u^*} \delta\bar{\boldsymbol{\epsilon}} \quad (5-89)$$

The global error associated with using the recovered smoothed strain instead of the smoothed strain can be defined as follows:

$$\tilde{\boldsymbol{\epsilon}} = \tilde{\boldsymbol{\epsilon}}^* - \boldsymbol{\epsilon} \quad (5-90)$$

To minimise this error, we enforce the orthogonality of the projection of the space of the recovered smoothed strain variation to that of the relevant error, mathematically expressed as follows:

$$\int_{\Omega} \delta\tilde{\boldsymbol{\epsilon}}^{*T} \tilde{\boldsymbol{\epsilon}} d\Omega = \int_{\Omega} \delta\tilde{\boldsymbol{\epsilon}}^{*T} (\tilde{\boldsymbol{\epsilon}}^* - \boldsymbol{\epsilon}) d\Omega = 0 \quad \forall \delta\tilde{\boldsymbol{\epsilon}}^* \quad (5-91)$$

Inserting Equations 5-89, 5-90 and 5-87 into Equation 5-91 results in the following form:

$$\delta \bar{\boldsymbol{\varepsilon}}^T \int_{\Omega_k^s} \mathbf{N}^{gl, u^*T} (\mathbf{N}^{gl, u^*} \bar{\boldsymbol{\varepsilon}} - \mathbf{W}^{-1} \bar{\boldsymbol{\varepsilon}}) d\Omega = 0 \quad \forall \delta \tilde{\boldsymbol{\varepsilon}}^{*(k)} \quad (5-92)$$

where, the global matrix \mathbf{W} can be readily obtained by some simple manipulations presented in Equation 5-85. As a result, the corresponding terms related to the specific smoothing domain $\mathbf{W}^{(k)}$ can be extracted from the globally computed matrix \mathbf{W} . The smoothed effective stress is also defined over each smoothing domain as:

$$\tilde{\boldsymbol{\sigma}}'^{(k)} = \mathbf{D} \tilde{\boldsymbol{\varepsilon}}^{(k)} = \mathbf{D} \tilde{\mathbf{B}}_1 \bar{\mathbf{u}} \quad (5-93)$$

The residual term $\mathbf{L}_d^T \dot{\boldsymbol{\sigma}}(\mathbf{u}^h, \mathbf{p}^h)$ can be viewed as the rate of the residual of the equilibrium equation at any point of interest within its associated smoothing domain. The term $\dot{\boldsymbol{\sigma}}(\mathbf{u}^h, \mathbf{p}^h)$ must consequently be presented in terms of the rate of the *recovered* smoothed effective stress $\dot{\tilde{\boldsymbol{\sigma}}}^{*(k)}$ which is variable over each smoothing domain. To obtain the recovered smoothed effective stress at any point of interest within its associated smoothing domain, a definition similar to that used for the recovered strain can be adopted, as follows:

$$\tilde{\boldsymbol{\sigma}}'^{*(k)} = \mathbf{N}^{u^*}(\mathbf{x}_k) \bar{\boldsymbol{\sigma}}'^{(k)} \quad (5-94)$$

where the assigned nodal values of the recovered smoothed effective stress can be formulated as follows:

$$\bar{\boldsymbol{\sigma}}'^{(k)} = \mathbf{D} \bar{\boldsymbol{\varepsilon}}^{(k)} = \mathbf{D} \mathbf{W}^{(k)} \tilde{\boldsymbol{\varepsilon}}^{(k)} = \mathbf{D} \mathbf{W}^{(k)} \tilde{\mathbf{B}}_1 \bar{\mathbf{u}} \quad (5-95)$$

Then, Equation 5-78 can be written in the following form:

$$\mathbf{L}_d^T \dot{\tilde{\boldsymbol{\sigma}}}^{*(k)}(\mathbf{u}^h, \mathbf{p}^h) = \mathbf{L}_d^T (\mathbf{N}^{u^*}(\mathbf{x}_k) \dot{\tilde{\boldsymbol{\sigma}}}^{*(k)}) - \eta \nabla \mathbf{N}^p \dot{\tilde{\mathbf{p}}}} \quad (5-96)$$

The term representing the contribution of the displacement variable in Equation 5-96 can be smoothed over each smoothing domain, as follows:

$$\begin{aligned} \frac{1}{A_k^s} \int_{\Omega_k^s} \mathbf{L}_d^T \dot{\boldsymbol{\sigma}}'^{(k)}(\mathbf{u}^h, p^h) d\Omega &= \frac{1}{A_k^s} \int_{\Omega_k^s} (\mathbf{L}_d^T(\mathbf{N}^{u*}(\mathbf{x}_k)) d\Omega) \dot{\boldsymbol{\sigma}}'^{(k)} = \\ \frac{1}{A_k^s} \int_{\Gamma_k^s} \mathbf{L}_n^T(\mathbf{N}^{u*}(\mathbf{x})) d\Gamma \dot{\boldsymbol{\sigma}}'^{(k)} & \end{aligned} \quad (5-97)$$

Thus, the smoothed forms of \mathbf{G}_{ep}^u and \mathbf{G}_{el}^u can be defined as follows:

$$\tilde{\mathbf{G}}_{ep}^u = \frac{1}{A_k^s} \int_{\Gamma_k^s} \mathbf{L}_n^T(\mathbf{N}^{u*}(\mathbf{x})) d\Gamma \mathbf{D}_i^{ep} \mathbf{W}^{(k)} \tilde{\mathbf{B}}_1 \quad (5-98)$$

$$\tilde{\mathbf{G}}_{el}^u = \frac{1}{A_k^s} \int_{\Gamma_k^s} \mathbf{L}_n^T(\mathbf{N}^{u*}(\mathbf{x})) d\Gamma \mathbf{D}^e \mathbf{W}^{(k)} \tilde{\mathbf{B}}_1 \quad (5-99)$$

As can be seen, all derivatives in conjunction with the standard variational statement of \mathbf{G}_{ep}^u and \mathbf{G}_{el}^u are eliminated by performing the smoothing gradient technique, allowing the linear interpolations to be used effectively.

The numerical integrations over the boundary of the smoothing domains can be performed in Equations 5-98 and 5-99 similar to that used to obtain the strain-displacement matrix (Equation 3-37). Therefore, components of $\tilde{\mathbf{G}}_{ep}^u$ and $\tilde{\mathbf{G}}_{el}^u$ for supporting node I of the smoothing domain Ω_k^s can be calculated as:

$$\tilde{\mathbf{G}}_{epI}^u = \frac{1}{2A_k^s} \sum_{m=1}^{n_{gau}} (w_m \mathbf{L}_{nm}^T(\mathbf{N}^{u*}(\mathbf{x}_m)) l_m^{(k)}) \mathbf{D}_i^{ep} \mathbf{W}_I^{(k)} \tilde{\mathbf{B}}_{1I} \quad (5-100)$$

$$\tilde{\mathbf{G}}_{elI}^u = \frac{1}{2A_k^s} \sum_{m=1}^{n_{gau}} (w_m \mathbf{L}_{nm}^T(\mathbf{N}^{u*}(\mathbf{x}_m)) l_m^{(k)}) \mathbf{D}^e \mathbf{W}_I^{(k)} \tilde{\mathbf{B}}_{1I} \quad (5-101)$$

where the notations have been introduced according to those used in Equation 3-37.

then,

$$\tilde{\mathbf{G}}_{ep}^u = \left[\sum_{I \in S_s} \tilde{\mathbf{G}}_{epI}^u \right]_{2q \times 2q} \quad (5-102)$$

$$\tilde{\mathbf{G}}_{el}^u = \left[\sum_{I \in S_s} \tilde{\mathbf{G}}_{elI}^u \right]_{2q \times 2q} \quad (5-103)$$

A similar procedure is performed to eliminate derivatives from for term ∇N^p to achieve a globally consistent formulation. The same formulation as used in Equation 3-47 is adopted here:

$$\tilde{\nabla} N^p \bar{\mathbf{p}}_I = \sum_{I \in S_s} \tilde{\mathbf{B}}_{2I}(\mathbf{x}_k) \bar{\mathbf{p}}_I \quad (5-104)$$

The spatially discretised form of the stabilisation term (Equation 5-76) at iteration $i+1$ for the current time step $t + \alpha\Delta t$ can, therefore, be written in the following form:

$$\sum_{\Omega_k^s \in \Omega} \int_{\Omega_k^s} \left((-\tilde{\mathbf{G}}_{el}^u \bar{\mathbf{v}} - \eta \tilde{\mathbf{B}}_2 \bar{\mathbf{q}})^T, \tau (\tilde{\mathbf{G}}_{ep}^u \dot{\mathbf{u}}_{i+1}^{t+\alpha\Delta t} - \eta \tilde{\mathbf{B}}_2 \dot{\bar{\mathbf{p}}}_{i+1}^{t+\alpha\Delta t}) \right)_{0, \Omega_k^s} \quad (5-105)$$

Straightforward manipulations lead to the introduction of the following stabilising matrices:

$$\tilde{\mathbf{K}}_{stab}^{SD} = \int_{\Omega_k^s} \tilde{\mathbf{G}}_{el}^{uT} \tau \tilde{\mathbf{G}}_{ep}^u d\Omega = \tilde{\mathbf{G}}_{el}^{uT} \tau \tilde{\mathbf{G}}_{ep}^u A_k^s \quad (5-106)$$

$$\tilde{\mathbf{H}}_{stab}^{SD} = \int_{\Omega_k^s} \tilde{\mathbf{B}}_2^T \tau \tilde{\mathbf{B}}_2 d\Omega = \tilde{\mathbf{B}}_2^T \tau \tilde{\mathbf{B}}_2 A_k^s \quad (5-107)$$

$$\tilde{\mathbf{C}}_{stab}^{SD} = \int_{\Omega_k^s} \tilde{\mathbf{G}}_{el}^{uT} \tau \tilde{\mathbf{B}}_2 d\Omega = \tilde{\mathbf{G}}_{el}^{uT} \tau \tilde{\mathbf{B}}_2 A_k^s \quad (5-108)$$

$$\tilde{\mathbf{C}}_{stab}^{*,SD} = \int_{\Omega_k^s} \tilde{\mathbf{G}}_{ep}^{uT} \tau \tilde{\mathbf{B}}_2 d\Omega = \tilde{\mathbf{G}}_{ep}^{uT} \tau \tilde{\mathbf{B}}_2 A_k^s \quad (5-109)$$

As can be seen, all the contributing matrices are derived directly in Equations 5-16 to 5-109, with no need for any mapping, by taking advantage of the smoothing technique. It

is worth noting that contribution matrixes defined in Equations 5-106 to 5-109 are constant over each smoothing domain.

Having obtained the contributing stabilisation matrices, Equation 5-106 can be rewritten as follows:

$$\sum_{\Omega_k^s \in \Omega} (-\tilde{\mathbf{K}}_{stab}^{SD} \dot{\mathbf{u}}_{i+1}^{t+\alpha\Delta t} + \eta \tilde{\mathbf{C}}_{stab}^{SD} \dot{\mathbf{p}}_{i+1}^{t+\alpha\Delta t} - \eta \tilde{\mathbf{C}}_{stab}^{*,SD\ T} \dot{\mathbf{u}}_{i+1}^{t+\alpha\Delta t} + \eta^2 \tilde{\mathbf{H}}_{stab}^{SD} \dot{\mathbf{p}}_{i+1}^{t+\alpha\Delta t}) \quad (5-110)$$

The linearised residuals (Equations 5-56 and 5-57) at the current time step $t + \alpha\Delta t$ can then be modified into the following forms:

$$\begin{aligned} (\boldsymbol{\Psi}_{u,stab})_{i+1}^{t+\alpha\Delta t} &= \int_{\Omega} \tilde{\mathbf{B}}_1^T(\boldsymbol{\sigma}')_{i+1}^{t+\alpha\Delta t} d\Omega - \tilde{\mathbf{K}}_{stab} \left(\frac{AU_{i+1}^{t+\alpha\Delta t} - BU^t + CU^{t-\Delta t}}{\Delta t} \right) - \eta \tilde{\mathbf{C}} \mathbf{P}_{i+1}^{t+\alpha\Delta t} + \\ \eta \tilde{\mathbf{C}}_{stab} \left(\frac{AP_{i+1}^{t+\alpha\Delta t} - BP^t + CP^{t-\Delta t}}{\Delta t} \right) - (\mathbf{F})_{i+1}^{t+\alpha\Delta t} &= \mathbf{0} \end{aligned} \quad (5-111)$$

$$\begin{aligned} (\boldsymbol{\Psi}_{p,stab})_{i+1}^{t+\alpha\Delta t} &= \eta \tilde{\mathbf{C}}^T \left(\frac{AU_{i+1}^{t+\alpha\Delta t} - BU^t + CU^{t-\Delta t}}{\Delta t} \right) - \eta \tilde{\mathbf{C}}_{stab}^{*T} \left(\frac{AU_{i+1}^{t+\alpha\Delta t} - BU^t + CU^{t-\Delta t}}{\Delta t} \right) + \\ \tilde{\mathbf{H}} \mathbf{P}_{i+1}^{t+\alpha\Delta t} + \eta^2 \tilde{\mathbf{H}}_{stab} \left(\frac{AP_{i+1}^{t+\alpha\Delta t} - BP^t + CP^{t-\Delta t}}{\Delta t} \right) + \alpha_f \mathbf{M} \left(\frac{AP_{i+1}^{t+\alpha\Delta t} - BP^t + CP^{t-\Delta t}}{\Delta t} \right) - (\mathbf{T})_{i+1}^{t+\alpha\Delta t} &= \mathbf{0} \end{aligned} \quad (5-112)$$

A similar Newton-Raphson procedure discussed earlier can be adopted for solving the global matrix system to obtain the nodal displacements $\mathbf{U}_{i+1}^{t+\alpha\Delta t}$ and the nodal pore pressures $\mathbf{P}_{i+1}^{t+\alpha\Delta t}$. The solution procedure can then be rewritten for the stabilised formulation as follows:

$$\begin{Bmatrix} (\boldsymbol{\Psi}_{u,stab})_{i+1}^{t+\alpha\Delta t} \\ (\boldsymbol{\Psi}_{p,stab})_{i+1}^{t+\alpha\Delta t} \end{Bmatrix} = \begin{Bmatrix} (\boldsymbol{\Psi}_{u,stab})_i^{t+\alpha\Delta t} \\ (\boldsymbol{\Psi}_{p,stab})_i^{t+\alpha\Delta t} \end{Bmatrix} + \mathbf{J}_{stab,i} \begin{Bmatrix} d\mathbf{U}_{i+1}^{t+\alpha\Delta t} \\ d\mathbf{P}_{i+1}^{t+\alpha\Delta t} \end{Bmatrix} = \mathbf{0} \quad (5-113)$$

in which the stabilised Jacobian matrix \mathbf{J}_{stab} is formulated as:

$$\mathbf{J}_{stab} = \begin{bmatrix} \frac{\partial \Psi_{u,stab}}{\partial \mathbf{U}} & \frac{\partial \Psi_{u,stab}}{\partial \mathbf{P}} \\ \frac{\partial \Psi_{p,stab}}{\partial \mathbf{U}} & \frac{\partial \Psi_{p,stab}}{\partial \mathbf{P}} \end{bmatrix}. \quad (5-114)$$

The linearisation of the stabilised Jacobian matrix can be represented in the following form:

$$\mathbf{J}_{stab,i} = \begin{bmatrix} ((\tilde{\mathbf{K}}_T)_i)^{t+\alpha\Delta t} - \frac{A}{\Delta t} \tilde{\mathbf{K}}_{stab} & \eta(-\tilde{\mathbf{C}} + \frac{A}{\Delta t} \tilde{\mathbf{C}}_{stab}) \\ \frac{A\eta}{\Delta t} (\tilde{\mathbf{C}} - \tilde{\mathbf{C}}_{stab})^T & (\frac{A\alpha_f}{\Delta t} \mathbf{M} + \tilde{\mathbf{H}} + \frac{A\eta^2}{\Delta t} \tilde{\mathbf{H}}_{stab}) \end{bmatrix} \quad (5-115)$$

The incremental displacement vector $d\mathbf{U}_{i+1}^{t+\alpha\Delta t}$ and pressure vector $d\mathbf{P}_{i+1}^{t+\alpha\Delta t}$ at iteration $i+1$ can then be computed as follows:

$$\begin{Bmatrix} d\mathbf{U}_{i+1}^{t+\alpha\Delta t} \\ d\mathbf{P}_{i+1}^{t+\alpha\Delta t} \end{Bmatrix} = -\mathbf{J}_{stab,i}^{-1} \begin{Bmatrix} (\Psi_{u,stab})_i^{t+\alpha\Delta t} \\ (\Psi_{p,stab})_i^{t+\alpha\Delta t} \end{Bmatrix} \quad (5-116)$$

5.6 Polynomial pressure projection method

To date, the pressure projection stabilisation method has been successfully applied to numerical solutions of Darcy's equation [177], and coupled flow-deformation problems in geomechanics [52]. In this section of the chapter, the polynomial pressure projection stabilisation method [58,64] is applied to the standard FEM with equal low-order interpolation functions. This method is presented here for the sake of completeness, because it has been used as the benchmark when the stabilisation method proposed in this chapter is numerically examined later.

The polynomial pressure projection method can be viewed as a non-residual stabilisation method as it stabilizes the global bilinear form of the governing equations without resorting to the residual terms. Thus, the method is considered as an

inconsistent stabilisation method in the sense that the resulting discretised governing equations may not be exactly satisfied by the exact solution. Although different variations of the inconsistent stabilisation methods, commonly known as *local pressure projection methods*, exist, they are all based on the stabilisation framework proposed by Brezzi and Fortin [42]. The first specific version of this general stabilisation framework is the pioneering work of Silvester [197]. An extensive theoretical and numerical investigation of the local pressure projection methods were later presented by Becker and Brack [174].

The main idea behind all classes of local pressure projection methods is decomposition of pressure space into two parts, \hat{V}_p^h and $V_p^h \setminus \hat{V}_p^h$, in such a way that the inf-sup condition is satisfied for the displacement/pressure subspaces $V_u^h \times \hat{V}_p^h$. Therefore, robust and accurate numerical solutions can be obtained if the other part of the pressure space ($V_p^h \setminus \hat{V}_p^h$) is stabilised. An operator is then needed to project the pressure from the richer space V_p^h to the smaller space \hat{V}_p^h , which can be symbolically shown as:

$$\mathbf{\Pi}: V_p^h \rightarrow \hat{V}_p^h \quad (5-117)$$

where $\mathbf{\Pi}$ is known as the projection operator.

The bilinear form of the stabilisation term in polynomial pressure projection method can be generally expressed as follows:

$$S_{pp}(p^h, q^h) = \sum_{\Omega_e \in \mathcal{T}_h} \tau \overline{(p^h - \mathbf{\Pi} p^h, q^h - \mathbf{\Pi} q^h)}_{0, \Omega_e} \quad (5-118)$$

where $S_p(p^h, v^h)$ is the stabilisation term added to the global FEM standard bilinear form of coupled flow-deformation equations (Equation 5-14), resulting in:

$$Q_{PP}(\mathbf{u}^h, p^h; \mathbf{v}^h, p^h) = Q(\mathbf{u}^h, p^h; \mathbf{v}^h, p^h) + S_{pp}(p^h, q^h) \quad (5-119)$$

where $Q_{PP}(\mathbf{u}^h, p^h; \mathbf{v}^h, q^h)$ stands for the global bilinear form of the flow-deformation equations that is stabilised by the polynomial pressure projection method. When equal linear order interpolation functions are used, the projection operator is defined as follows:

$$\mathbf{\Pi}: L_2(\Omega) \rightarrow R_0 \quad (5-120)$$

where, R_0 denotes a set of piecewise constants. A pressure projection with a range of piecewise constants can be given in the following form:

$$\mathbf{\Pi}p^h|_{\Omega^e} = \frac{1}{A_k^s} \int_{\Omega^e} p^h d\Omega \quad (5-121)$$

in which the constants correspond to the average of p^h over the elements when the linear interpolation function is employed.

Having defined $S_{PP}(p^h, q^h)$ and $\mathbf{\Pi}$, [200] showed that the inherent deficiency associated with using equal-order linear interpolation functions that prevents the fulfilment of the inf-sup condition is overcome by the appearance of an additional $C_2 \|q^h - \mathbf{\Pi}q^h\|_0$ term in the original inf-sup condition. Consequently, the weak inf-sup condition is satisfied, shown as:

$$\sup_{\mathbf{v}^h \in \mathbf{V}_u, \mathbf{v}^h \neq 0} \frac{B(\mathbf{v}^h, q^h)}{\|\mathbf{v}^h\|_1} \geq C_1 \|q^h\|_1 - C_2 \|q^h - \mathbf{\Pi}q^h\|_0 \quad (5-122)$$

The contributing stabilisation matrix produced by bilinear $S_{PP}(p^h, q^h)$ is then presented in the following form:

$$\mathbf{M}_{PP} = \int_{\Omega_e} \tau (\mathbf{N}^p - \mathbf{\Pi}(\mathbf{N}^p))^T (\mathbf{N}^p - \mathbf{\Pi}(\mathbf{N}^p)) d\Omega \quad (5-123)$$

Note that the numerical integration of Equation 5-124 is performed similar to that of the compressibility matrix \mathbf{M} .

When applying the pressure projection technique to the standard variational form, the equilibrium residual (Ψ_u) remains unchanged, but the fluid continuity residual changes and takes the following form (after discretisation):

$$(\Psi_p)_{PP,i+1}^{t+\alpha\Delta t} = \eta \mathbf{C}^T (A\mathbf{U}_{i+1}^{t+\alpha\Delta t} - B\mathbf{U}^t + C\mathbf{U}^{t-\Delta t}) + \Delta t \mathbf{H}\mathbf{P}_{i+1}^{t+\alpha\Delta t} + \alpha_f (\mathbf{M} + \mathbf{M}_{PP}) (A\mathbf{P}_{i+1}^{t+\alpha\Delta t} - B\mathbf{P}^t + C\mathbf{P}^{t-\Delta t}) - \Delta t (\mathbf{F}_p)_{i+1}^{t+\alpha\Delta t} = \mathbf{0} \quad (5-124)$$

in which $(\Psi_p)_{PP,i+1}^{t+\alpha\Delta t}$ represents the linearised residual of the fluid continuity equation at the time step $t + \alpha\Delta t$, stabilised by the pressure projection method. All contributing matrices, in conjunction with the coupled-flow deformation analysis, are then formulated by the standard FEM procedure [2].

The resulting discretised system of equations can again be solved using the standard Newton-Raphson procedure, similar to the procedure explained before:

$$\begin{Bmatrix} (\Psi_u)_{i+1}^{t+\alpha\Delta t} \\ (\Psi_p)_{PP,i+1}^{t+\alpha\Delta t} \end{Bmatrix} = \begin{Bmatrix} (\Psi_u)_i^{t+\alpha\Delta t} \\ (\Psi_p)_{PP,i}^{t+\alpha\Delta t} \end{Bmatrix} + J_{PP,i} \begin{Bmatrix} d\mathbf{U}_{i+1}^{t+\alpha\Delta t} \\ d\mathbf{P}_{i+1}^{t+\alpha\Delta t} \end{Bmatrix} = \mathbf{0} \quad (5-125)$$

in which the Jacobian matrix is:

$$J_{PP,i} = \begin{bmatrix} (\mathbf{K}_T)_i^{t+\alpha\Delta t} & -\eta \mathbf{C} \\ A\eta \mathbf{C}^T & (A\alpha_f (\mathbf{M} + \mathbf{M}_{PP}) + \Delta t \mathbf{H}) \end{bmatrix} \quad (5-126)$$

As can be seen, the stabilising matrix \mathbf{M}_{PP} eliminates the zero-diagonal block that may otherwise exist at very early stages of the flow-deformation process due to initial incompressibility of the porous media. The polynomial pressure projection method retains the sparsity of the matrix system, as \mathbf{M}_{PP} is created by the same shape functions that are used for other contributing matrices.

5.7 Numerical Examples

Three benchmark numerical examples are presented in this section to study the validity and robustness of the consistent stabilisation method proposed in this study and to compare the performance of the proposed method to the performance of the polynomial pressure projection method.

5.7.1 One dimensional consolidation

The first example presented in this section concerns Terzaghi's one-dimensional problem. The example includes a linear-elastic soil mass with a height of $h = 30$ m and a width of $a = 1$ m with a low permeability of $k = 10^{-6}$ m/sec, as shown in Figure 5.2(a). The soil column is composed of 80 triangular elements associated with 63 nodes, as shown in Figure 5.2(b). The lower boundary of the soil column is rigidly restricted both vertically and horizontally, while its lateral boundaries are only horizontally fixed. The upper boundary of the soil medium is assumed to be fully drained ($p = 0$). However, the lateral sides and the base of the soil column are impermeable. The assigned boundary conditions of the soil column are also shown in Figure 5.2(a).

According to Terzaghi's formulation, an instantaneous increase in excess pore water pressure can be expected in the column as result of a sudden surface-distributed load of $q = 1$ kPa at the top of the soil column. After the instantaneous increase, the excess pore water pressure gradually dissipates over time.

The linear properties of the soil column are the elastic modulus of $E = 1$ kPa and Poisson's ratio of $\nu = 0.0$. Other relevant parameters used in numerical modelling

include: an initial time step of $\Delta t_0 = 1$ s, the time step growth factor of $\alpha = 1.1$, the porosity of $n = 0.2$, the solid grain compressibility of $C_s = 0$ and the fluid compressibility of $C_f = 0.454 \times 10^{-6} \text{ kPa}^{-1}$. The densities of the fluid (ρ_f) is 10 kN/m^3 . Regarding the material properties used in this numerical example, the soil column can be thought of as a nearly incompressible medium. The scalar value of α^e is taken as 0.05.

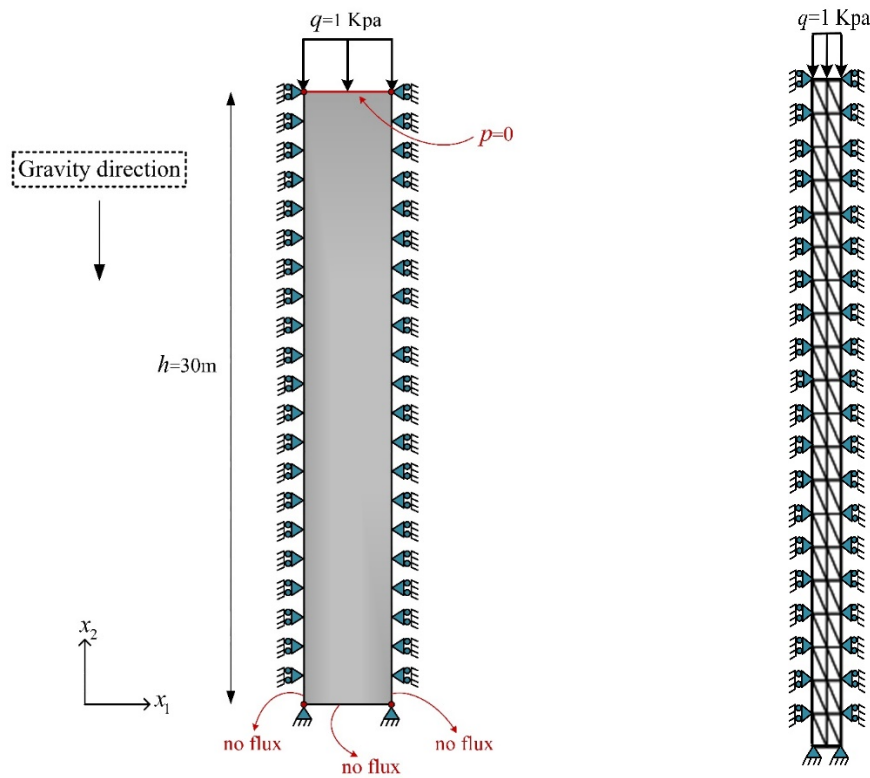


Figure 5.2. A schematic representation of (a) the soil column with its assigned boundary conditions (not to scale), and (b) the discretisation used for the numerical analyses.

Figure 5.3 shows the pressure profile of the soil column along its height after the initial time step for the standard ESFEM. It also shows the numerical results obtained with the proposed consistent stabilisation method and numerical results obtained with the polynomial pressure projection method. According to Terzaghi's consolidation theory, pore pressure throughout the soil column must be equal to overburden stress; however, the ESFEM produced a pathological profile of excess pore pressure and wild node-to-node pressure oscillations throughout the domain of the column. This is because of the violation of the inf-sup condition as a result of using equal-order linear interpolation functions for pressure and displacement variables.

The numerical results obtained with the proposed stabilised ESFEM perfectly match the reference solution [313], as can be clearly seen in Figure 5.3. The added stabilisation term led to a successful fulfilment of the inf-sup condition. The results obtained with the polynomial pressure projection method do not alleviate pressure oscillation near the drainage boundary of the soil medium due to a sharp gradient of pressure near the surface of the soil column. The numerical results, therefore, concur with [36] regarding the failure of the polynomial pressure projection method in terms of the complete elimination of pressure oscillation in a numerical flow-deformation analysis.

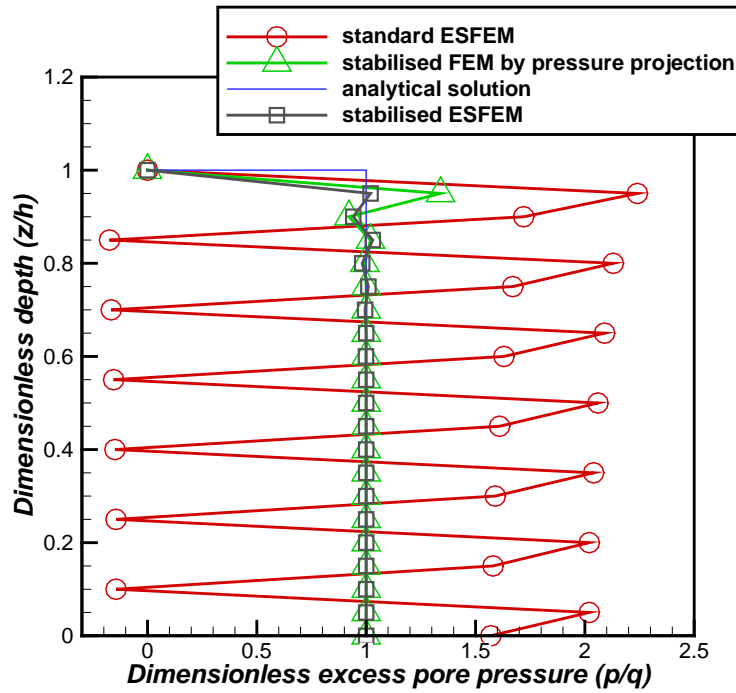


Figure 5.3. A pressure profile, along the height of the soil column, presented with the stabilised ESFEM proposed in this study, the standard ESFEM and the stabilised FEM obtained with the polynomial pressure projection method.

Contrary to stabilisation parameters proposed in other studies [51, 193], the simple steady-state based stabilisation parameter used in this study managed to tune the size of the stabilisation terms to alleviate erratic pressure oscillation without a need to include the time step size and its associated growth factor into the stabilisation parameter. The influence of the time step and its relevant growth factor directly appear in the resultant stabilised matrix system in this study through the existence of the coefficient $A/\Delta t$ in all blocks of the global matrix system.

According to Equation 5-115, it can be seen that the size of the required time step size must be large enough, relative to the element size, to be used in an analysis of interest. Thus, the formulation proposed in this chapter confirms the findings of other studies that state that the size of the time step needs to be larger than a certain value depending

on the mesh size; otherwise, it could lead to the appearance of either pressure oscillation or a Divergence of the converged solution from an adequately accurate numerical approximation [53, 311, 312]. Indeed, these were found even with the absolute stabilisation method associated with *Stokes* problems that was proposed by Douglas and Wang [172].

The numerical experiments in this study shows that the necessity of using time-dependent stabilisation parameters in methods proposed in other studies [51, 193] likely stems from failures to provide sufficient amount of weighting function related to the added stabilisation terms due to the exclusion of the displacement weight function. Thus, added residual terms only affects the discretised fluid continuity equation. This approach can, however, be erroneous because the discretised equilibrium equation remains unchanged, and the influence of stabilising terms, which can be produced by the inclusion of the displacement weight function is overlooked. Therefore, introducing the size of the time step to the stabilisation parameter somehow tries to compensate for elimination of the displacement weight functions in the aforementioned stabilisation methods to provide sufficient amount of stabilisation and to avoid the destabilising effects of overly diffusive terms caused by inappropriately chosen stabilisation parameter. Such an approach is, however, not rigorous and may not work all the time

Figure 5.4 depicts the contours of excess pore pressure obtained using the standard ESFEM and the proposed stabilised ESFEM after three sequential time steps for the three rows of the triangular elements from the top of the soil column. The representation of the pressure contours is restricted to the top of the column since for the rest of the column, a uniform pressure distribution was obtained for the numerical results associated with the stabilised ESFEM and a repeatedly erratic pressure contour was

obtained using the standard ESFEM. As can be seen, a wildly erroneous pressure contour pattern across the domain was substantially ameliorated using the proposed stabilisation method, and the stabilised numerical results perfectly agree to the Terzaghi's consolidation theory.

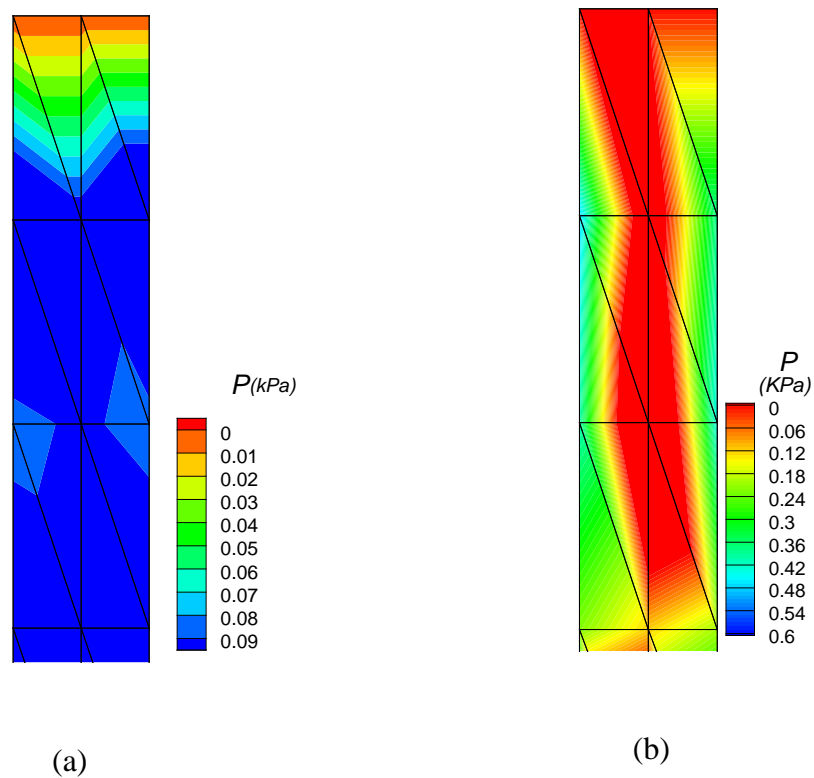


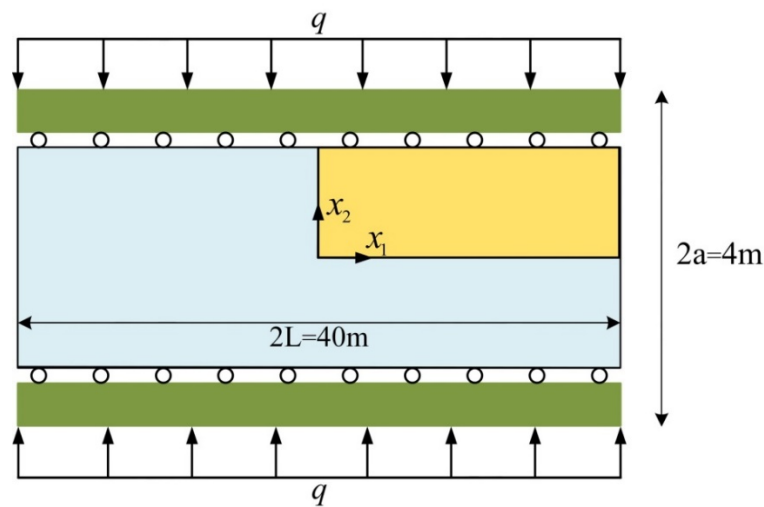
Figure 5.4. The contours of the approximated pressure solutions (kPa) for three elements on the top of the soil column obtained by (a) stabilised ES-FEM and (b) standard ES-FEM after three initially subsequent time steps.

5.7.2 Mandel's problem

The second example presented in this section examines the proposed method by studying a well-known benchmark example: Mandel's problem. It consists of a long

saturated soil slab with a length of $2L = 40$ m and a width of $2a = 4$ m confined by two rigid plates at the top and bottom of the slab, which are assumed to be frictionless and impermeable, as shown in Figure 5.5(a). The rigidity of each plate causes equal vertical displacements for all nodes directly connected the plate, while the nodes are horizontally unconstrained. The fluid and soil constituents of the medium are assumed to be incompressible.

The plates are subjected to a distributed load of $q = 2$ kPa, which is compressively applied and results in the appearance of an initial excess pore pressure of $p = 2$ kPa throughout the medium, except for at the drainage boundaries at $x_1 = \pm L$ according to Mandel's analytical solution [298]. A quarter of the medium is modelled due to symmetry. The discretisation of the medium is performed using 606 triangular elements created by 1,000 nodes, as shown in Figure 5.5(b). It is worth noting that the adopted mesh is more refined at the right side of the domain to attain better accuracy. The elastic parameters are $E = 10^4$ kPa and $\nu = 0.0$, which correspond to the consolidation coefficient $c_v = 1$ and the permeability coefficient $k = 10^{-4}$ m/sec. The soil porosity is assumed $n = 0.2$. The scalar value of α^e was assumed to be 0.072.



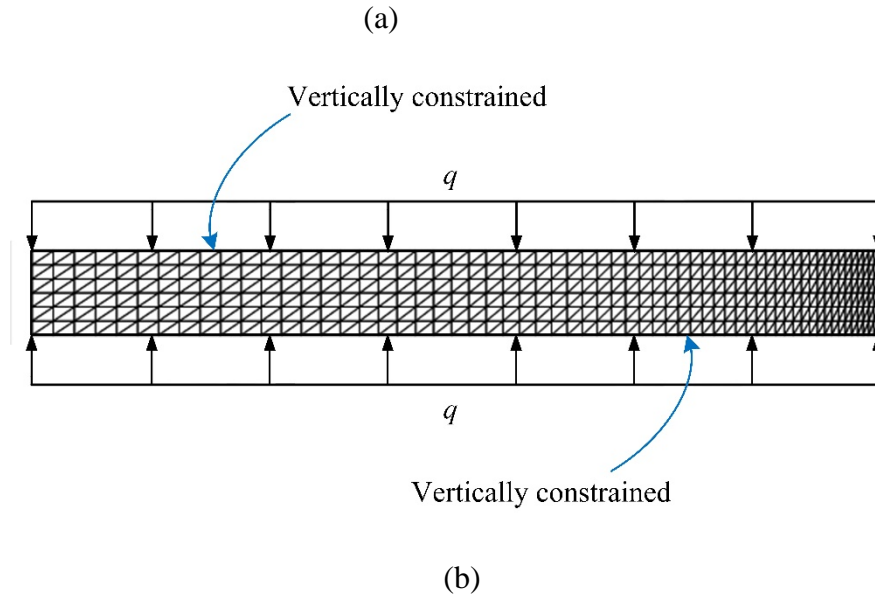


Figure 5.5. (a) a schematic (not to scale) representation of the geometry of Mandel's problem (b) the discretisation used for modelling a quarter of the domain.

Figure 5.6 shows that variations in the pressure profile at time $t = 0.004$ sec corresponded to the dimensionless time $t_d = 1 \times 10^{-5}$ calculated by $t_d = \frac{Ekt}{2\mu_f(1+\nu)(1-2\nu)L^2}$, which was obtained using the standard FEM, the standard ES-FEM and their stabilised counterparts. Due to symmetry, the pressure variation is one-dimensional with no change along any vertical line, therefore pressure variations are depicted only along horizontal direction. The dimensionless length is defined as x_1/L while the dimensionless pressure is p/p_0 . It can be seen that utilising standard formulations with equal-order interpolation functions for both primary variables produces pressure oscillations that are intensified in the vicinity of the drainage boundary. The proposed stabilised ES-FEM was able to produce a smoothly realistic pressure profile, which agrees well with Mandel's analytical solution [298].

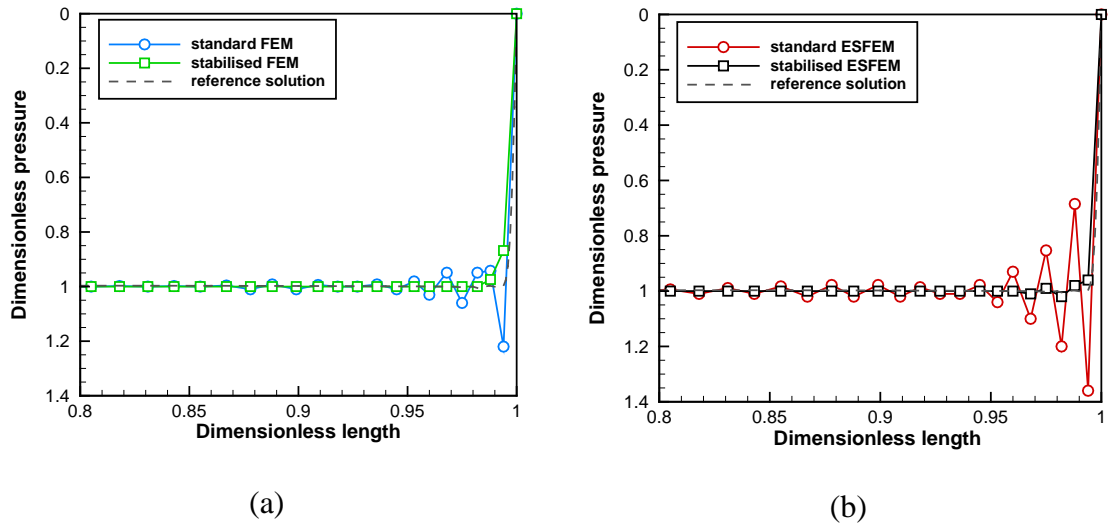
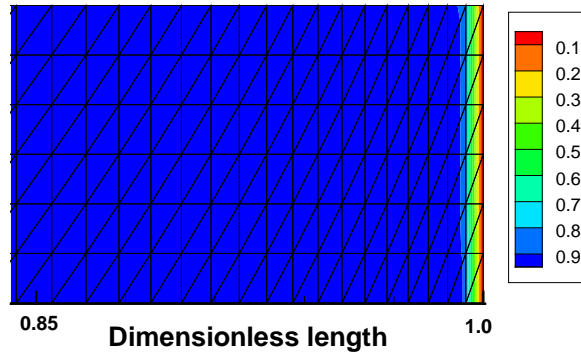
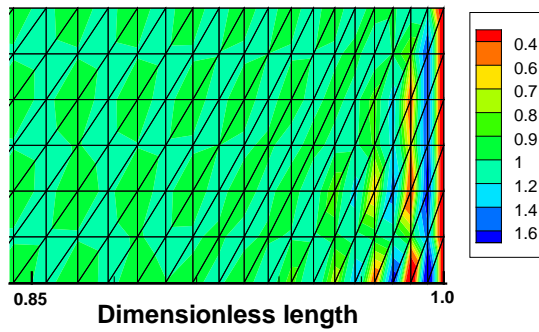


Figure 5.6. The variation of the dimensionless excess pore pressure along the dimensionless length of the soil medium at dimensionless time $t_d = 1 \times 10^{-5}$ for (a) standard and stabilised FEM and (b) for standard ES-FEM and proposed method for the stabilisation of ESFEM.

Figure 5.7 shows pressure contours in part of the domain obtained using the numerical results of the standard ESFEM and the proposed stabilised ESFEM. As aforementioned, the standard formulation shows wild pressure oscillations near the drainage boundary that are associated with unrealistic vertical variations of pressure in some regions. In contrast, the pressure distribution obtained using the stabilised formulation is stable and accurate.



(a)



(b)

Figure 5.7. The contours of dimensionless pressure distribution after the first time step of $\Delta t_0 = 0.01$ sec for (a) standard ESFEM, and (b) stabilised ESFEM

5.7.3 Bearing capacity of a strip footing

Volumetric locking at a fully developed plastic flow is one of the most challenging issues of computational elastoplasticity, especially when a computation of a collapse load, which is prone to large errors, must be considered [314]. Various techniques have been proposed, which will briefly introduced, to address mesh locking induced by elastoplastic constitutive models which results in overestimation of the collapse load.

The simplest solution is the reduced integration method that under-integrates internal force vectors and subsequently under-integrates relevant stiffness matrices [315]. The technique employs an integration scheme one order lower than a sufficient order needed to evaluate an exact integration. However, the approach leads to the appearance of spurious kinematic modes with no rises in internal energy. The propagation of spurious kinematic modes into adjacent elements with the reduced integration method was reported in [316].

Another approach that has been proposed is the selective integration, known as the B-concept, which differentiates Gauss points used for integrations of shear strain and Gauss points used to integrate volumetric strain [317]. Nonetheless, it has been shown that the B-concept fails to address the mesh locking issue for the general case of $\psi \neq 0$ where ψ denotes a dilation angle [315].

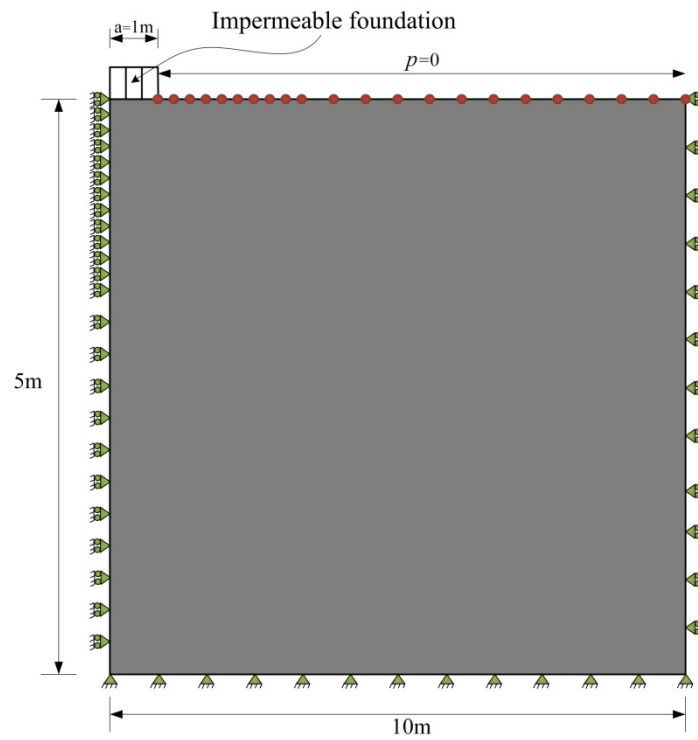
Another possible solution that has been proposed is the enhanced assumed strain approach, which was suggested by Simo and Rifai [318]. The approach includes augmentations of the standard strain fields obtained using continuous displacement fields with local element-based strain fields. However, this approach has spurious modes in the analyses of interest when material nonlinearity (damage or plasticity) is assumed. This failure to produce accurate results, when material nonlinearity is

included, happens with other mixed formulations as well, such as the \mathbf{u}/p formulation adopted in this thesis [315].

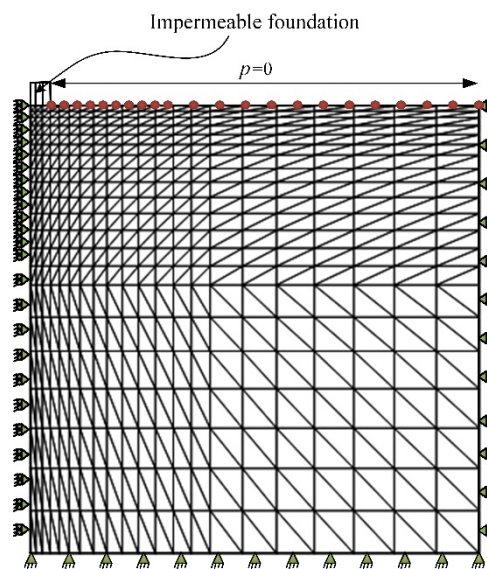
The effectiveness and robustness of the proposed stabilisation method, in regard to overcoming the volumetric locking issue, is investigated in the third numerical example in this section. The investigation incorporates material nonlinearity by using Mohr-Coulomb's nonlinear constitutive model. The model is used to compute the bearing capacity of a strip footing placed on a soil medium.

The example includes a smooth flexible impervious strip footing laid on a saturated low-permeable soil medium with a thickness of 5 m that extends laterally 10 m from the footing's axis of symmetry, as shown in Figure 5.8(a). It is assumed that the soil medium is weightless and the underlying rigid bedrock is impervious. Non-associativity for the soil medium is also with a friction angle of $\phi = 30^\circ$ and a dilation angle of $\psi = 0$. The cohesion is $c = 1$ kPa, and free drainage is assumed for the ground surface. Due to symmetry only half of the medium is modelled.

The elastic modulus and Poisson's ratio are assumed to be $E = 100$ kPa and $\nu = 0.25$, respectively, and the coefficient of permeability is assumed $k = 3.2 \times 10^{-9}$ m/sec. These parameters correspond to a consolidation coefficient of $c_v = 1 \times 10^{-6}$ m²/sec. The porosity is assumed $n = 0.2$, and both solid and fluid ingredients are assumed to be incompressible. The soil medium is discretised using a set of triangular elements, which contains 441 elements and 800 nodes, as shown in Figure 5.8(b). The scalar stabilisation parameter α^e is taken as 0.055 in this example.



(a)



(b)

Figure 5.8. (a) The geometry of the strip footing (not to scale) and the saturated porous medium used to estimate the collapse load and (b) the discretisation adopted for the numerical solution.

The surface load acts on the strip footing at the length $a = 1$ m, as shown in Figure 5-8(a). The vertical surface load instantaneously increases from $q = 0$ kPa to $q = 3.14$ kPa, which corresponds to an elastic limit load, as per an analytical solution by Prandtl [319], equal to $q_e = \pi C$. The elastic limit load is applied in five subsequent time steps with equal dimensionless lengths of $t_d = 4 \times 10^{-8}$ where $t_d = \frac{Ekt}{2\mu_f(1+v)(1-2v)a^2}$. Then, the load is increased in steps of $0.005q_e$ until failure occurs, which should correspond to the ultimate limit load of $q_{ult} = (\pi + 2)C$. The time step size and its corresponding growth factor is $\Delta t_0 = 1.5$ sec and $\alpha = 1$, respectively.

Figure 5.9 shows pressure variations along the axis of symmetry beneath the strip footing at the dimensionless time $t_d = 5 \times 10^{-8}$, which is equal to $t = 1.25$ sec. The pressure variations are obtained using the standard FEM, the standard ESFEM and their corresponding stabilised formulations. Elegant numerical results are attained by adopting stabilised formulations contrary to their standard counterparts, which show poor accuracy. It is important to note that the standard ESFEM produced more oscillatory pressure results than the standard FEM.

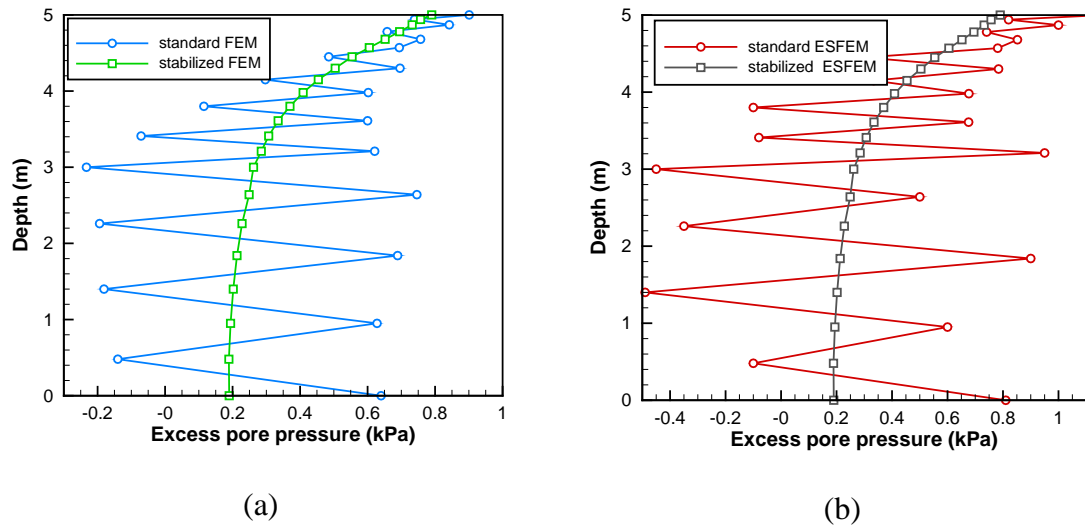


Figure 5.9. Pressure variations along the axis of symmetry beneath the strip footing at the dimensionless time $t_v = 5 \times 10^{-8}$, obtained by (a) standard and stabilised FEM and (b) standard ESFEM and proposed stabilised ESFEM.

Figure 5.10 compares variations in the vertical load versus variations in the vertical displacement just below the strip footing obtained using different approaches. The figure also compares the computed collapse loads of the standard FEM, ESFEM and their stabilised counterparts, and also Prandtl's analytical solution. As can be seen, the standard FEM produced the worst numerical results and had the most overestimations of collapse loads ($1.07q_{ult}$). The proposed stabilised ES-FEM successfully overcame the volumetric locking issue and was the most accurate method in terms of computations of the strip-footing collapse load with respect to the analytical solution ($1.008 q_{ult}$).

The standard ESFEM was softer than the standard FEM, as was expected based on various studies [91, 92, 94]; with the computed collapse load of $1.04 q_{ult}$. Nonetheless, in regards to polynomial pressure projections, the stabilised FEM was unable to address volumetric locking inherent in the standard FEM and to accurately predict strip-footing

collapse load ($1.036 q_{ult}$). The same failure, relevant to the computation of the collapse load, was observed with a slightly better accuracy when polynomial pressure projections were adopted for the standard ESFEM. projections were adopted for the standard ESFEM.

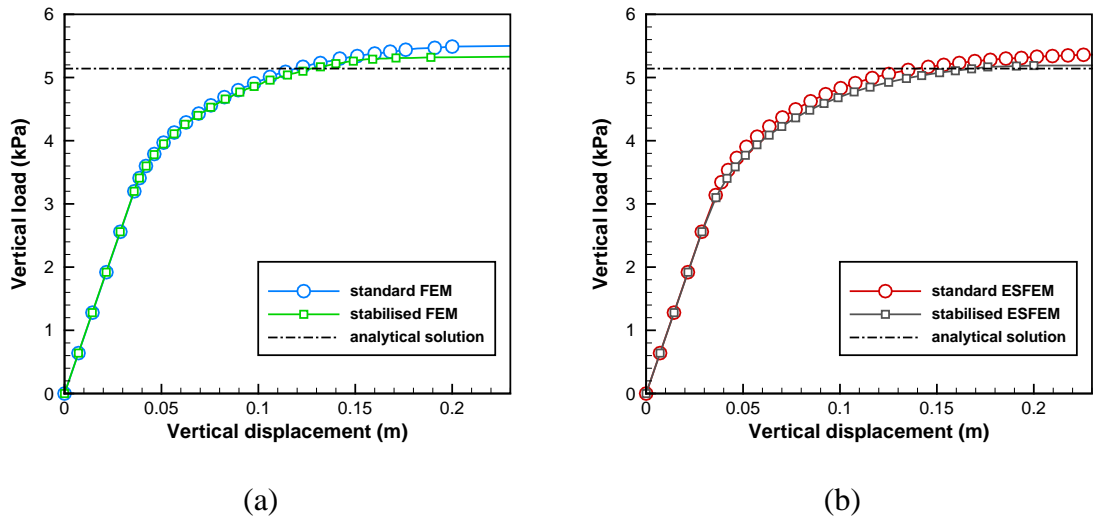


Figure 5.10. Vertical load variations with respect to vertical displacements just below the strip footing, plotted for (a) the standard and stabilised FEM and (b) the standard ESFEM and the stabilised ESFEM using the method proposed in this study.

Figure 5.11 shows the pressure contours obtained in the last convergent step of the analysis, just before collapse occurs with the standard ESFEM and the stabilised ESFEM, corresponding to approximated pressure solutions at the dimensionless times $t_d = 5.4 \times 10^{-6}$ and $t_d = 5.64 \times 10^{-6}$, respectively. It can be seen that the stabilised method proposed in this study has resolved the violation of the inf-sup condition, which is the root cause of the erroneous estimation of the pressure distribution across the soil medium. Moreover, this study's method successfully produces realistic pressure contours, as can be seen in the figure.

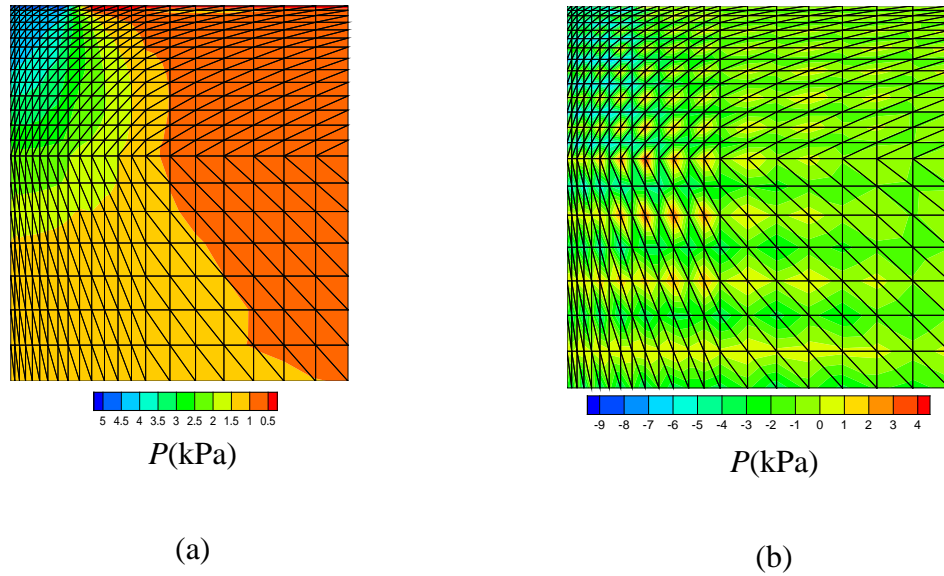


Figure 5.11. Pressure contours, at the last convergent step, obtained using (a) the proposed stabilised ESFEM at the dimensionless time $t_d = 5.64 \times 10^{-6}$ and (b) the standard ESFEM at the dimensionless time $t_d = 5.4 \times 10^{-6}$.

5.8 Conclusion

A consistent stabilisation method has been proposed in this study. The proposed stabilised technique has been introduced within the ESFEM framework as perhaps the simplest form of edge-based SPIM to prove the viability and the robustness of the proposed method. A novel technique based on the combination of the global strain projection along with the application of the smoothing gradient technique has been exploited in order to retrieve the use of equal-order linear interpolation functions for approximations of the primary variables, the displacement and the pore pressure. An unconditional stable consistent method based on that proposed in [172] has been applied to satisfy the inf-sup condition irrespective of the chosen stabilisation parameter, resulting in the elimination of the pathological oscillatory pore pressure behaviour and the overestimation of the collapse load in computational geomechanics. The versatility and the accuracy of the proposed stabilisation method have been shown by the

simulation of the number of geotechnical examples, including both linear and nonlinear cases. It has also numerically proven that proposed method exhibit the superior performance that its contender (pressure projection method) when equal-order linear interpolations are used. The superiority was rooted to the better estimation of the collapse load in the strip footing and the efficient vanishing the pathological pattern of the pore pressure distribution near the drainage boundary.

6 An Enriched smoothed point interpolation method for the flow-deformation analysis of saturated porous media with embedded interfaces

6.1 Preface

An enriched smoothed point interpolation method is proposed for the numerical simulation of saturated porous media containing embedded interfaces. Embedded interfaces are those in which the underlying bulk discretisation is not aligned with the interface geometries. The well-established coupled flow-deformation equations developed by Biot (presented in Chapter 3) govern the behaviour of a saturated porous medium away from a discontinuity. A viscous fluid represents the flow within a discontinuity at the microscale while restoring the momentum and mass couplings to the coupled flow-deformation equations of a saturated porous medium with the assumption of validity on a macroscopic scale. In this chapter, the formulation proposed to describe the interfacial inflow exploits the aperture-dependent permeability of the discontinuity cavity in addition to the utilisation of the standard Darcy flow. The proposed formulation enables the incorporation of both the opening and the enforcement of the closure mode, where either the fluid exchange is recovered or the contact condition is imposed at the interface of interest. The presence of interfaces on the approximation of the primary and secondary variables is inserted by augmenting the shape functions (PIM and RPIM) with properly defined enrichment functions and by exploiting the partition-of-unity (PU) property of the adopted shape functions. The penalty method is used to present the contact behaviour in which the solid and fluid phases are subjected to

relevant constraints. It is shown that the smoothing gradient technique eliminates the need for the sub-division of supporting domains crossed by discontinuity. Temporal discretisation is performed using the three-point time discretisation scheme. The resultant algebraic system is non-linear due to the nonlinearity of the coupling terms, and is solved by application of a consistent Newton–Raphson iterative algorithm. The chapter concludes by a rigorous numerical examination of the proposed method using a set of benchmark examples.

6.2 Governing equations of saturated porous media with interfaces

The partial differential equations developed in [161] govern the coupled solid deformation and saturating fluid flow in a saturated porous medium surrounding a discontinuity, which includes the linear momentum balance equation (the equilibrium equation) in association with the entire porous medium and the continuity equation of flow that describes the saturating fluid phase. The forms of coupled flow-deformation equations are similar to Equations 3-1 and 3-2.

The essential and natural boundary conditions identical to those presented in Equations 3-4 to 3-7 are specified to close the boundary value problems away from a discontinuity. The imposed boundary conditions are assumed to apply on the complementary parts of the boundary, satisfying the conditions presented in Equation 3-9 and Equation 3-10. Throughout this chapter, linear elastic behaviour is assumed for the medium away from an interface as represented by Equation 3-11 and Equation 3-12.

A schematic representation of a saturated porous medium with inclusion of an internal interface (Γ_d) is provided in Figure 6.1. In this figure, $n_{\Gamma_d^+}$ and $n_{\Gamma_d^-}$ are the unit normal

vectors directed to Ω^- and Ω^+ , respectively, where the signs + and - above Γ_d indicate the two sub-domains of the discontinuity. The internal interface is characterised by the outward unit normal vector to Γ_d pointing to Ω^+ with $\mathbf{n}_{\Gamma_d} = \mathbf{n}_{\Gamma_{d^-}} = -\mathbf{n}_{\Gamma_{d^+}}$, such that $\Gamma_d = \Gamma_{d^-} \cup \Gamma_{d^+}$. The interface enables the representation of a discontinuity in the field of either the secondary primary variables, such as strain and fluid flux, or the primary variables, which are the displacement and pore pressure fields. The former refers to weak discontinuity, such as material heterogeneity interfaces, and the latter refers to a strong discontinuity, such as a crack. The presence of geomechanical discontinuities (Γ_d) enforces the imposition of additional boundary conditions on the surface of the interface. These additional boundary conditions naturally appear in the weak form of the coupled flow-deformation equations of a saturated porous medium that contains an interface through the application of the Divergence theorem to the strong form of the equations.

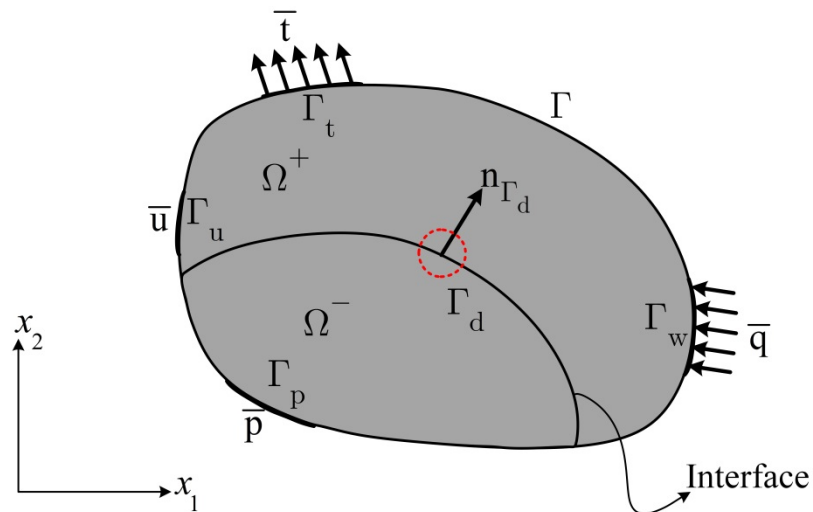


Figure 6.1. A schematic representation of a saturated porous medium Ω with internal boundary Γ_d

6.2.1 Weak forms

The derivation of weak forms that do not necessitate coincidence between the mesh topology and the interfacial geometry requires the definition of functional subspaces containing an embedded discontinuity. Thus, the subspaces chosen for the approximation of the displacement (\mathbf{u}) and pore pressure (p) are identically given as introduced in Equations 5-17 and 5-18 in addition to their corresponding test functions (\mathbf{v} and q) in Equations 5-19 and 5-20, respectively.

To build discontinuity into the weak forms of the coupled flow-deformation equations, the momentum balance (Equation 3-1) and the fluid mass balance (Equation 3-2) are multiplied by kinematically admissible test functions for displacement (\mathbf{v}) and for pore pressure (q), respectively. Introducing the internal boundary Γ_d , integrating over domain Ω , and applying the Divergence theorem accompanied by the specific boundary conditions (Equations 3-4 to 3-7) yields the explicit form of the corresponding weak forms:

$$\int_{\Omega} \boldsymbol{\varepsilon}^T(\mathbf{v}) \boldsymbol{\sigma}'(\boldsymbol{\varepsilon}(\mathbf{u})) d\Omega - \int_{\Gamma_d^+} \mathbf{v}^{+T} (\mathbf{n}_{\Gamma_d^+}^T \boldsymbol{\sigma}^+) d\Gamma - \int_{\Gamma_d^-} \mathbf{v}^{-T} (\mathbf{n}_{\Gamma_d^-}^T \boldsymbol{\sigma}^-) d\Gamma - \eta \int_{\Omega} p \nabla \cdot \mathbf{v} d\Omega - \int_{\Gamma_t} \mathbf{v}^T \bar{\mathbf{t}} d\Gamma - \int_{\Omega} \rho \mathbf{v}^T \mathbf{g} d\Omega = 0 \quad \forall \mathbf{v} \in V_{u,0} \quad (6-1)$$

$$\eta \int_{\Omega} q \nabla \cdot \dot{\mathbf{u}} d\Omega - \int_{\Gamma_d^+} q^+ (\mathbf{n}_{\Gamma_d^+}^T \mathbf{w}^+) d\Gamma - \int_{\Gamma_d^-} q^- (\mathbf{n}_{\Gamma_d^-}^T \mathbf{w}^-) d\Gamma + \frac{k_f}{\mu_f} \int_{\Omega} (\nabla q)^T \nabla p d\Omega + \alpha_f \int_{\Omega} q \dot{p} d\Omega - \int_{\Gamma_q} q \bar{q} d\Gamma = 0 \quad \forall q \in V_{p,0} \quad (6-2)$$

where \mathbf{w} is the fluid velocity, which is related to the pressure gradient through the Darcy law.

Based on Equations 6-1 and 6-2, the imposition of the constraints associated to an internal boundary Γ_d into the weak forms leads to the natural appearance of the external

tractions and the exchange of the fluid flux through the faces of the internal boundary. Indeed, these terms provide the hydro-mechanical couplings between a discontinuity and the surrounding saturated porous medium. The solvability of the constrained weak forms due to the presence of geomechanical discontinuity (Γ_d) requires appropriate imposition of additional boundary conditions that rely on the inherent nature of the discontinuity.

Assuming equilibrium between the cavity within a strong discontinuity and the surrounding medium, we can write,

$$\mathbf{n}_{\Gamma_d^+}^T \boldsymbol{\sigma}^+ = -\mathbf{n}_{\Gamma_d^-}^T \boldsymbol{\sigma}^- = \mathbf{t}_{\text{cont}} - p \mathbf{n}_{\Gamma_d} \quad (6-3)$$

where \mathbf{t}_{cont} denotes the frictional contact tractions on $\Gamma_{\text{cont}} \subset \Gamma_d$, where Γ_{cont} expresses the active contact surface of the discontinuity. Appropriate contact numerical algorithms should be imposed to quantify the likely effects of the opening/closing and sticking/slipping modes of the discontinuity faces. In this study, the contact constraints are established by two nested *Kuhn–Tucker* inequalities, which will be elaborated later. The term $p \mathbf{n}_{\Gamma_d}$ in Equation 6-3 recovers the influence of the fluid-induced traction acting on the faces of a strong discontinuity, which arises from the presence of the fluid within the cavity. The fluid-induced traction and the frictional contact traction provide mechanical coupling between the discontinuity and the surrounding bulk.

Using Equation 6-3, the compact form of the equilibrium equation (Equation 6-1) is obtained as follows:

$$\int_{\Omega} \boldsymbol{\varepsilon}^T(\mathbf{v}) \boldsymbol{\sigma}'(\boldsymbol{\varepsilon}(\mathbf{u})) d\Omega + \int_{\Gamma_d} \llbracket \mathbf{v} \rrbracket^T (\mathbf{t}_{\text{cont}} - p \cdot \mathbf{n}_{\Gamma_d}) d\Gamma - \eta \int_{\Omega} p \boldsymbol{\nabla} \cdot \mathbf{v} d\Omega - \int_{\Gamma_t} \mathbf{v}^T \bar{\mathbf{t}} d\Gamma - \int_{\Omega} \rho \mathbf{v}^T \mathbf{g} d\Omega = 0 \quad \forall \mathbf{v} \in \mathbf{V}_{u,0} \quad (6-4)$$

where $[[*]]$ is the jump operator that indicates the difference of the variable of interest $*$ between the two faces of internal boundary, i.e., $[[*]] = *^+ - *^-$.

It is assumed that the equilibrium between the cavity and the surrounding porous medium as well as the uniqueness of the frictional contact traction values at the faces of a discontinuity result in the attainment of the same value relevant to the pressure field at the faces of a discontinuity [320, 321]. Therefore, the same values obtained for the pressure weighting functions $q = q^+ = q^-$ are inevitably admitted.

Considering the same pressure weighting functions at both faces of the discontinuity, Equation 6-2 is modified as follows:

$$\eta \int_{\Omega} q \nabla \cdot \dot{\mathbf{u}} d\Omega - \int_{\Gamma_d} q [[\mathbf{w}]]^T \mathbf{n}_{\Gamma_d} d\Gamma + \frac{k_f}{\mu_f} \int_{\Omega} (\nabla q)^T \nabla p d\Omega + \alpha_f \int_{\Omega} q \dot{p} d\Omega - \int_{\Gamma_q} q \bar{q} d\Gamma = 0 \quad \forall q \in V_{p0} \quad (6-5)$$

The jump in the flux $[[\mathbf{w}]]$ is introduced in Equation 6-5, multiplied by \mathbf{n}_{Γ_d} , indicating that the normal flow to the faces of a strong discontinuity may be discontinuous. Thus, the mass balance coupling stemming from the exchange of flow between the cavity and the surrounding porous medium naturally appears in the weak form of the fluid continuity equation were $[[\mathbf{w}]]$ implies that some of the fluid can be stored within the cavity or transported in a tangential direction to a strong discontinuity.

Considering the weak discontinuity caused by the contrast in the material properties, the terms including jumps in Equations 6-4 and 6-5, would be eliminated, i.e.,

$$\int_{\Gamma_d} [[\mathbf{v}]]^T (\mathbf{t}_{cont} - p \cdot \mathbf{n}_{\Gamma_d}) d\Gamma = 0 \quad (6-6)$$

and

$$\int_{\Gamma_d} q [[\mathbf{w}]]^T \mathbf{n}_{\Gamma_d} d\Gamma = 0 \quad (6-7)$$

and Equations 6-4 and 6-5 default to those with discontinuities only in the secondary variable (i.e., strain).

6.2.2 Fluid flow formulation within a strong discontinuity

The continuity equation for the fluid inside a fully open discontinuity is as follows:

$$\nabla \cdot \mathbf{w} + \eta \nabla \cdot \dot{\mathbf{u}} + c_f \dot{p} = 0 \quad (6-8)$$

where η and c_f are defined in section 3.2 of this thesis. The Darcy velocity vector, \mathbf{w} , is related to pressure gradient as follows:

$$\mathbf{w} = k_{cr} (-\nabla p + \rho_f \bar{\mathbf{g}}) \quad (6-9)$$

where k_{cr} is the crack permeability with respect to the fluid. It is assumed that a viscous fluid flow with Newtonian rheology fills the cavity of the discontinuity. Assuming isotropy inside the discontinuity, The well-known cubic law [264] is adopted to estimate the opening-dependent crack permeability as follows:

$$k_{cr} = \frac{1}{\kappa} \frac{h^2}{12\mu_f} \quad (6-10)$$

where h denotes the discontinuity (crack) opening and κ is a coefficient that varies from 1.04 to 1.65, to account for the unrealistic assumption of the parallel faces condition [322].

The weak form of the fluid continuity within the crack is then developed to obtain the coupling between fluid flow within the discontinuity and the surrounding porous

medium. To this end, the pressure test function q is multiplied in Equation 6-8 and integrated over the discontinuity domain Ω' , as follows:

$$\int_{\Omega'} q(\nabla \cdot \mathbf{w} + \eta \nabla \cdot \dot{\mathbf{u}} + c_f \dot{p}) d\Omega = 0 \quad (6-11)$$

Inserting Equation 6-9 into Equation 6-11 then yields the following:

$$\int_{\Omega'} q(\nabla \cdot [k_{cr}(-\nabla p + \rho_f \bar{\mathbf{g}})] + \eta \nabla \cdot \dot{\mathbf{u}} + c_f \dot{p}) d\Omega = 0 \quad (6-12)$$

Introducing an appropriate form of the Divergence theorem with discontinuities into Equation 6-12, the weak form of Equation 6-8 is obtained as follows:

$$\begin{aligned} \int_{\Omega'} q \eta \nabla \cdot \dot{\mathbf{u}} d\Omega - \int_{\Gamma_d} q [\mathbf{w}]^T \mathbf{n}_{\Gamma_d} d\Gamma + \int_{\Omega'} (\nabla q)^T k_{cr} \nabla p d\Omega + \int_{\Omega'} q c_f \dot{p} d\Omega - \\ \int_{\Omega} (\nabla q)^T k_{cr} \rho_f \bar{\mathbf{g}} d\Omega = 0 \end{aligned} \quad (6-13)$$

Hence, the mass coupling term is systematically obtained by the relation established through Equation 6-13 as follows:

$$\begin{aligned} \int_{\Gamma_d} q [\mathbf{w}]^T \mathbf{n}_{\Gamma_d} d\Gamma = - \underbrace{\int_{\Omega'} (\nabla q)^T k_{cr} \nabla p d\Omega}_{Integral (I)} - \underbrace{\int_{\Omega'} q c_f \dot{p} d\Omega}_{Integral (II)} - \underbrace{\int_{\Omega'} q \eta \nabla \cdot \dot{\mathbf{u}} d\Omega}_{Integral (III)} + \\ \underbrace{\int_{\Omega} (\nabla q)^T k_{cr} \rho_f \bar{\mathbf{g}} d\Omega}_{Integral (IV)} \end{aligned} \quad (6-14)$$

The evaluation of Equation 6-14 is investigated under the local Cartesian coordinate system (x', y') , in which the coordinate system coincides with the tangent and normal directions of the strong discontinuity as shown in Figure 6.2. It is assumed the equilibrium between the cavity and the surrounding porous medium results in the association of the uniform fluid pressure with its corresponding test function across the width of the discontinuity [66]. Therefore, derivations of integrals of (I)-(IV) in Equation 6-14 are performed in the following manner:

$$\underbrace{\int_{\Omega'} \nabla q^T k_{cr} \nabla p d\Omega}_{Integral (I)} = \int_{\Gamma_d} \int_{-\frac{h}{2}}^{+\frac{h}{2}} \nabla q^T k_{cr} \nabla p dy' dx' = \int_{\Gamma_d} \int_{-\frac{h}{2}}^{+\frac{h}{2}} k_{cr} \left(\frac{\partial q}{\partial x'} \frac{\partial p}{\partial x'} + \frac{\partial q}{\partial y'} \frac{\partial p}{\partial y'} \right) dy' dx' = \int_{\Gamma_d} k_{cr}(h) \frac{\partial q}{\partial x'} \frac{\partial p}{\partial x'} dx' \quad (6-15)$$

$$\underbrace{\int_{\Omega'} q c_f \dot{p} d\Omega}_{Integral (II)} = \int_{\Gamma_d} \int_{-\frac{h}{2}}^{+\frac{h}{2}} q c_f \dot{p} dy' dx' = \int_{\Gamma_d} q(h) c_f \dot{p} dx' \quad (6-16)$$

$$\underbrace{\int_{\Omega'} q \eta \nabla \cdot \dot{\mathbf{u}} d\Omega}_{Integral (III)} = \int_{\Gamma_d} \int_{-\frac{h}{2}}^{+\frac{h}{2}} q \eta \nabla \cdot \dot{\mathbf{u}} dy' dx' = \int_{\Gamma_d} \int_{-\frac{h}{2}}^{+\frac{h}{2}} q \eta \left(\frac{\partial \dot{u}_{x'}}{\partial x'} + \frac{\partial \dot{u}_{y'}}{\partial y'} \right) dy' dx' = \int_{\Gamma_d} q \eta(h) \frac{1}{2} \left(\frac{\partial \dot{u}_{x'}}{\partial x'} \Big|_{+\frac{h}{2}} + \frac{\partial \dot{u}_{x'}}{\partial x'} \Big|_{-\frac{h}{2}} \right) dx' + \int_{\Gamma_d} q \eta \left(\dot{u}_{y'} \Big|_{+\frac{h}{2}} - \dot{u}_{y'} \Big|_{-\frac{h}{2}} \right) dx' = \int_{\Gamma_d} q \eta(h) \left\langle \frac{\partial \dot{u}_{x'}}{\partial x'} \right\rangle dx' + \int_{\Gamma_d} q \eta \llbracket \dot{u}_{y'} \rrbracket dx' \quad (6-17)$$

$$\underbrace{\int_{\Omega'} (\nabla q)^T k_{cr} \rho_f \bar{\mathbf{g}} d\Omega}_{Integral (IV)} = \int_{\Gamma_d} \int_{-\frac{h}{2}}^{+\frac{h}{2}} \frac{\partial q}{\partial x'} \bar{g}_{x'} + \frac{\partial q}{\partial y'} \bar{g}_{y'} dy' dx' = \int_{\Gamma_d} k_{cr} \rho_f(h) \frac{\partial q}{\partial x'} \bar{g}_{x'} dx' \quad (6-18)$$

where $\dot{u}_{x'}$ and $\dot{u}_{y'}$ stand for the projected solid velocity on the local longitudinal (x') and tangential axes (y'), respectively. In the above derivations, a linear variation of $\dot{u}_{x'}$ and $\frac{\partial \dot{u}_{x'}}{\partial x'}$ is assumed with respect to y' direction over the width of the discontinuity[66]. Also, the derivatives of fluid pressure in conjunction with its test function in the y' direction are eliminated because of the uniform pressure distribution over the width of the discontinuity h arising from the equilibrium between the cavity and the surrounding

medium. $\langle * \rangle$ obtains the average value of the quantity of the interest $*$ at the discontinuity faces. Substitution of Equations 6-15 to 6-18 into Equation 6-14 yields:

$$\int_{\Gamma_d} q \llbracket \mathbf{w} \rrbracket^T \mathbf{n}_{\Gamma_d} dx' = - \int_{\Gamma_d} k_{cr}(h) \frac{\partial q}{\partial x'} \frac{\partial p}{\partial x'} dx' - \int_{\Gamma_d} q(h) c_f \dot{p} dx' - \int_{\Gamma_d} q \eta(h) \langle \frac{\partial \dot{u}_{x'}}{\partial x'} \rangle dx' - \int_{\Gamma_d} q^T \eta \llbracket \dot{u}_{y'} \rrbracket dx' + \int_{\Gamma_d} k_{cr} \rho_f(h) \frac{\partial q}{\partial x'} \bar{g}_{x'} dx' \quad (6-19)$$

Equation 6-19 expresses the fluid leak-off between a discontinuity and the surrounding saturated porous media. It is worth noting that the contribution term related to integral II is conventionally eliminated from Equation 6-19 based on the assumption of incompressible fluid within the cavity. The term $\int_{\Gamma_d} q \llbracket \mathbf{w} \rrbracket^T \mathbf{n}_{\Gamma_d} dx'$ produces a strong nonlinearity in the global equation system because of the dependence of the crack permeability as well as other terms in Equation 6-19 to the width of discontinuity h , which is *a priori* unknown. The width of discontinuity is equal to $\llbracket u_{y'} \rrbracket$ and can be simply related to the displacement field as follows:

$$h = \llbracket u_{y'} \rrbracket = \mathbf{n}_{\Gamma_d}^T \llbracket \mathbf{u} \rrbracket \quad (6-20)$$

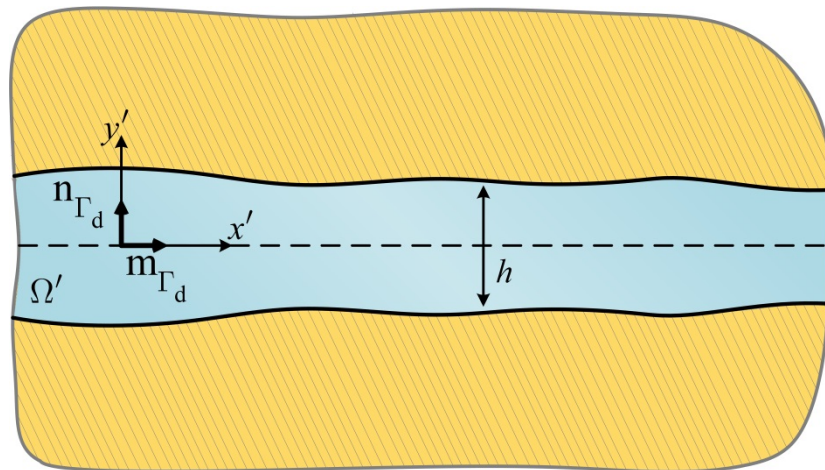


Figure 6.2. A schematic representation of the geometry and the corresponding local coordinate system in the cavity

6.3 Enriched SPIM for saturated porous media with interfaces

To capture the hydro-mechanical coupling that stems from the contact tractions acting on the discontinuity faces and the fluid exchange from the strong discontinuity into the surrounding medium, the displacement and fluid pressure fields must be enhanced to reproduce the physical discontinuities. The nonalignment of the material heterogeneity boundaries with the underlying mesh topology is also captured by the enhancement of the displacement derivative field (i.e., strain). The existence of a crack implies a discontinuity on the displacement field in conjunction with the normal discontinuous fluid flux to the crack. The pressure field can be assumed to be continuous across the crack, which is the case in this chapter based on the discussion presented in previous sections. Based on the type of discontinuity, appropriate enrichment functions are carefully selected to enable physical representation the discontinuities. In this chapter, the *Heaviside* function is chosen to represent the displacement discontinuity over the crack faces. The fluid pressure is modelled using a proper function of the level set function (i.e., the ridge function) to accommodate the flux discontinuity normal to the crack faces caused by the transport and storage of the fluid flow in the tangential direction of the discontinuity. Because of the weak discontinuity in the fluid phase, the ridge function is also adopted as the displacement variable.

Inspired by the extrinsically enriched functions applied in XFEM [242, 250, 323, 324], the enriched approximations of displacement and pressure variables are proposed as follows:

$$\mathbf{u}^h(\mathbf{x}) = \sum_{I \in S_s} \mathbf{N}_I^u(\mathbf{x}) \bar{\mathbf{u}}_I + \sum_{J \in S_s^{enr}} \mathbf{N}_J^{u,enr}(\mathbf{x}) \bar{\mathbf{a}}_J \quad (6-21)$$

$$p^h(\mathbf{x}) = \sum_{I \in S_s} \mathbf{N}_I^p(\mathbf{x}) \bar{p}_I + \sum_{J \in S_s^{enr}} \mathbf{N}_J^{p,enr}(\mathbf{x}) \bar{\mathbf{b}}_J \quad (6-22)$$

where \mathbf{N}^u and \mathbf{N}^p correspond to standard shape functions for the displacement and pressure variables, respectively. They are created by either PIM or RPIM, as presented in section 3.4 of this thesis, using the collection of supporting nodes in S_s . $\mathbf{N}^{u, enr}$ and $\mathbf{N}^{p, enr}$ stand for the contributing functions that are relevant to the enriched part of the displacement and pressure approximations, respectively. S_s^{enr} collects the nodes whose supporting domains are intersected by the discontinuity which can be taken equal to S_s . $\bar{\mathbf{a}}_j$ and $\bar{\mathbf{b}}_j$ are the vectors that collect additional nodal degrees of freedom assigned to enriched supporting nodes for the displacement and pressure approximations, respectively. The contributing enriched functions are as follows:

$$\mathbf{N}_j^{u, enr}(\mathbf{x}) = \mathbf{N}_j^u(\mathbf{x})(\psi^{u, enr}(\mathbf{x}) - \psi^{u, enr}(\mathbf{x}_j)) \quad (6-23)$$

$$\mathbf{N}_j^{p, enr}(\mathbf{x}) = \mathbf{N}_j^p(\mathbf{x})(\psi^{p, enr}(\mathbf{x}) - \psi^{p, enr}(\mathbf{x}_j)) \quad (6-24)$$

where $\psi^{u, enr}$ and $\psi^{p, enr}$ are the enrichment function for the displacement and pressure fields, respectively. As mentioned previously in this chapter, $\psi^{u, enr}$ can represent either the *Heaviside* function to capture strong discontinuity or the ridge function when only the discrepancy in material properties exists, whereas $\psi^{p, enr}$ can only possess the ridge function to represent the presence of the discontinuity of the pressure gradient normal to crack faces. The enrichment functions are shifted by the subtraction of $\psi^{u, enr}(\mathbf{x}_j)$ and $\psi^{p, enr}(\mathbf{x}_j)$ to preserve the Kronecker delta property, which leads to the achievement of the real nodal values when the point of interest coincides any node ($\mathbf{u}^h(\mathbf{x}_j)$ and $p^h(\mathbf{x}_j)$). Similar to standard interpolation functions that possess partition of unity (PU), the enriched approximations presented in this chapter are a PU. The enrichment functions used in this chapter will be introduced in the following sections.

6.3.1 The signed distance function

The well-established level set method [322] which allows quantification of the existence of interfaces using implicit functions is adopted here. A domain is split into two sub-domains Ω^+ and Ω^- by the interface Γ_d as previously shown in Figure 6.3. The positions of the points on Γ_d are set at zero. The positions of other points over the domains can be defined with respect to the zero iso-contour (i.e., the interface position). The most conventional level set function is the signed distance function, which is represented as follows:

$$d(\mathbf{x}) = \min \|\mathbf{x} - \mathbf{x}^*\| \text{sign}((\mathbf{x} - \mathbf{x}^*) \cdot \mathbf{n}_{\Gamma_d}) \quad (6-25)$$

where \mathbf{x}^* is the point on the discontinuity that is the closest distance from point \mathbf{x} . $\|\cdot\|$ stands for the Euclidean norm where $\|\mathbf{x} - \mathbf{x}^*\|$ expresses the distance between the point of interest \mathbf{x} and the interface Γ_d . Based on Equation 6-25, two sides of an interface are differentiated by the assignment of different signs. This definition implicitly determines the position of the discontinuity as the zero iso-contour of the level set function as follows:

$$d(\mathbf{x}) \begin{cases} > 0 \text{ if } \mathbf{x} \in \Omega^+ \\ = 0 \text{ if } \mathbf{x} \in \Gamma_d \\ < 0 \text{ if } \mathbf{x} \in \Omega^- \end{cases} \quad (6-26)$$

The schematic representation of signed distance function is shown in Figure 6.3.

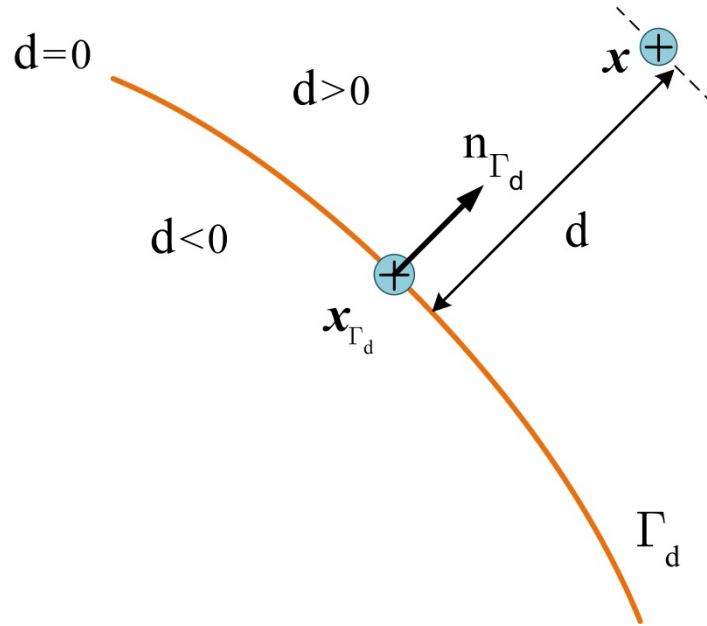


Figure 6.3. A signed distance function applied to quantify the position of a node with respect to the interface

6.3.2 Heaviside function

A strong discontinuity (crack) occurs because of different displacements on the faces of the discontinuity. The kinematic representation of the strong discontinuity can be recovered by exploiting the *Heaviside* function. The form of the *Heaviside* function applied in this chapter is as follows:

$$\psi^{u, enr}(\mathbf{x}) = H(\mathbf{x}) = \begin{cases} +1 & d(\mathbf{x}) \geq 0 \\ 0 & d(\mathbf{x}) < 0 \end{cases} \quad (6-27)$$

6.3.3 Ridge function

The incorporation of weak discontinuities requires the introduction of appropriate continuous functions that belong to C^0 space, but not to C^1 space. This requirement implies the utilisation of a non-differentiable function with respect to its first order differentiation to kinematically represent the weak discontinuity. A weak discontinuity

can be properly captured by using the modified abs-enrichment function, which is commonly known as the ridge enrichment function, expressed as follows:

$$\psi^{i, enr}(\mathbf{x}) = \sum_{J \in S_s^{enr}} \mathbf{N}_J^p(\mathbf{x}) |d_J| - \left| \sum_{J \in S_s^{enr}} \mathbf{N}_J^p(\mathbf{x}) d_J \right| \quad i=u, p \quad (6-28)$$

where d_J is the value of the signed distance function at node J , and superscript i indicates that the ridge function can be included to both primary displacement and pressure variables under the required circumstances. The use of ridge enrichment is advantageous compared with the commonly used alternative $|d(\mathbf{x})|$ because it prevents the violation of the PU property in the smoothing domains adjacent to the enriched smoothing domain that contain no interfaces (blending smoothing domains) [6]. Blending smoothing domains violates the PU property because a mix of the enriched and standard field nodes contributes to the creation of the interpolation function over blending smoothing domains. The ridge function vanishes at the field nodes of the blending smoothing domains and therefore the PU is restored [250, 254, 323]. The one-dimensional representation of the ridge function, the enriched nodes, and the standard nodes are depicted in Figure 6.4.

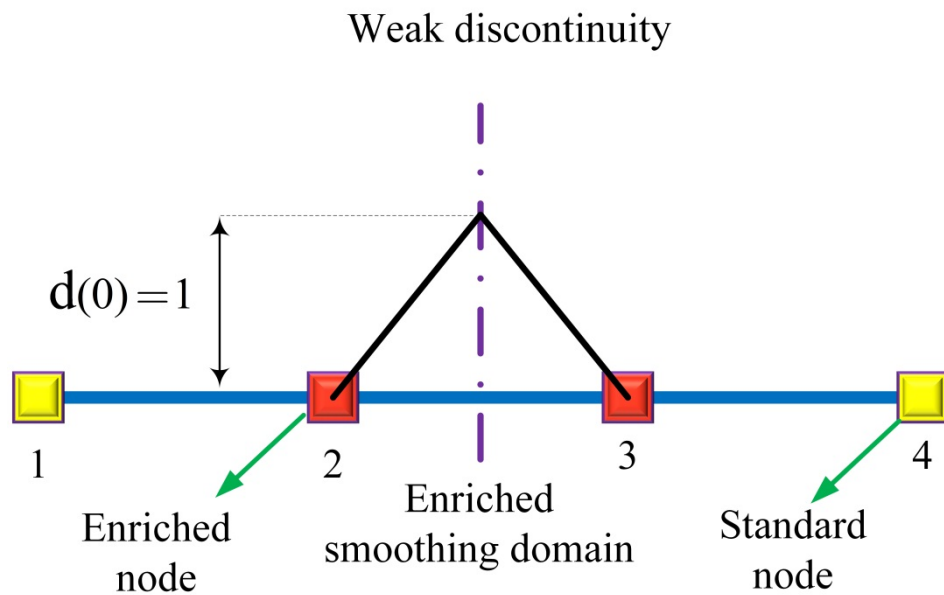


Figure 6.4. Schematic representation of the ridge function to reproduce a weak discontinuity

6.3.4 Domain discretisation

In SPIM/SRPIM, the problem domain is partitioned into N_{SD} smoothing domains that satisfy the conditions expressed by Equations 3-31 and 3-32. The smoothing domains can be created using a triangular background mesh in different ways, which results in different types of SPIMs/SRPIMs [15, 16, 20, 101, 105]. Following the formulation presented in Chapter 3, the cells of the background mesh are again used directly as the smoothing domains in this chapter, which results in the development of the Enriched cell-based SPIM/SRPIM (CSPIM/CSRPIM).

6.3.5 Supporting node selection schemes

In Enriched CSPIM/CSRPIM, the selection of supporting nodes at each point of interest is not arbitrary. It must be performed so that the resulting approximation function is square-integrable on the boundary of the smoothing domains [101]. Two node selection

schemes, T4 and T2L, which are described in section 3.4.2, are adopted in this chapter. Only two supporting nodes are again adopted where the Gauss point of interest is located on the boundary of the domain.

6.3.6 Creation of standard shape functions

In this chapter, the PIM and RPIM [88] are adopted to construct the standard nodal shape functions. A procedure similar to that presented in section 3.4.1 is performed to obtain the standard shape functions (N^u and N^p) to present the standard part of the enriched approximation.

6.3.7 Computation of smoothed strain and pressure gradient in Enriched SPIM

Because the cells of the background mesh serve as the smoothing domains in CSPIM/CSRPIM, the smoothed gradient of the displacement field (i.e., smoothed strain) is computed for each cell using the smoothing operation technique [90] and the Divergence theorem as shown by Equation 3-29.

From Equation 6-21, the smoothed strain can be obtained as follows:

$$\tilde{\boldsymbol{\varepsilon}}^{(k)} = \sum_{I \in S_s} \tilde{\mathbf{B}}_{1I} \bar{\mathbf{u}}_I + \sum_{J \in S_s^{enr}} \tilde{\mathbf{B}}_{1J}^{enr} \bar{\mathbf{a}}_J \quad (6-29)$$

where $\tilde{\mathbf{B}}_1$ is the standard smoothed strain-displacement matrix as previously formulated in Chapter 3 (Equation 3-35), obtained by applying the smoothing gradient technique (Equation 3-27). In a similar manner, the enriched part of the strain-displacement matrix ($\tilde{\mathbf{B}}_1^{enr}$) is computed as follows [325, 326]:

$$\tilde{\mathbf{B}}_{1j}^{enr} = \begin{bmatrix} \tilde{b}_{jx_1}^{u,enr} & 0 \\ 0 & \tilde{b}_{jx_2}^{u,enr} \\ \tilde{b}_{jx_2}^{enr} & \tilde{b}_{jx_1}^{enr} \end{bmatrix} \quad (6-30)$$

$$\tilde{\mathbf{B}}_1^{enr} = \begin{bmatrix} \tilde{b}_{1x_1}^{u,enr} & 0 & & \tilde{b}_{qx_1}^{u,enr} & 0 \\ 0 & \tilde{b}_{1x_2}^{u,enr} & \dots & 0 & \tilde{b}_{qx_2}^{u,enr} \\ \tilde{b}_{1x_2}^{u,enr} & \tilde{b}_{1x_1}^{u,enr} & & \tilde{b}_{qx_2}^{u,enr} & \tilde{b}_{qx_1}^{u,enr} \end{bmatrix}_{3 \times 2q} \quad (6-31)$$

where numerical integration must be performed over all segments of the boundaries associated with the smoothing sub-domain of interest created as the original smoothing domain is cut by an interface as shown in Figure 6.5. Summing the contributions related to the entries of $\tilde{\mathbf{B}}_1^{enr}$ over all Gauss points along the boundary segments, $\tilde{b}_{jl}^{u,enr}$ results in the following:

$$\tilde{b}_{jl}^{u,enr} = \frac{1}{2A_{sub,k}^s} \sum_{m=1}^{N_{seg}} \left[L_m^k \sum_{n=1}^{N_{gau}} w_n \phi_l(\mathbf{x}_{mn}) \left(\psi^{u,enr}(\mathbf{x}_{mn}) - \psi^{u,enr}(\mathbf{x}_j) \right) n_l(\mathbf{x}_{mn}) \right] \quad (l = x_1, x_2) \quad (6-32)$$

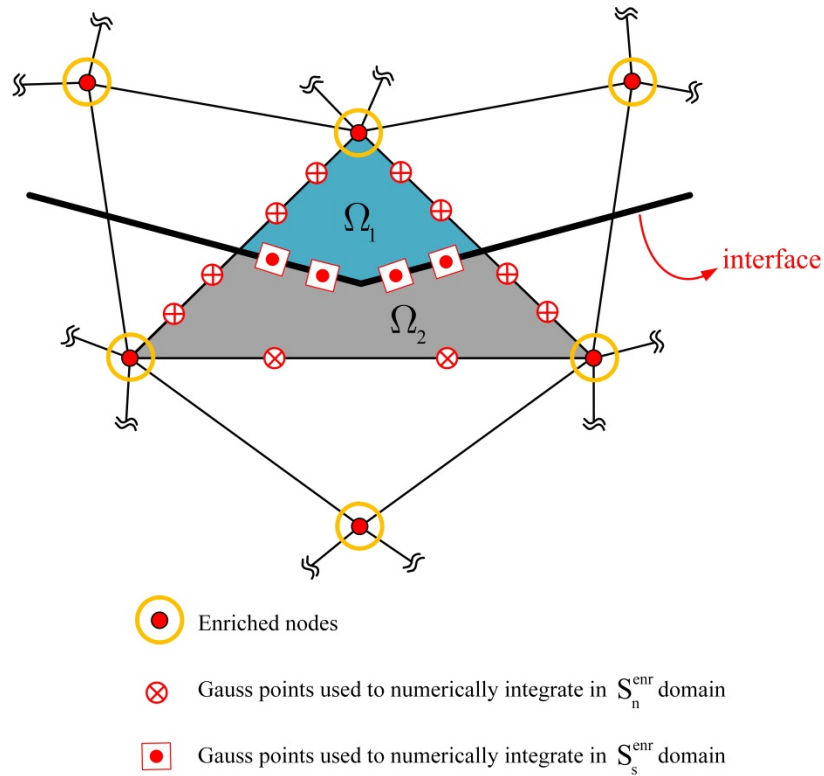


Figure 6.5. A supporting domain cut by an interface and its associated Gauss points used in the numerical integrations

in which the notations are the same as those presented in section 3.5.3 of chapter 3. $A_{sub,k}^s$ indicates the area of either subdomains Ω_1 or Ω_2 when the smoothing domain is cut by an interface. It is worth noting that the numerical integration using the Gauss points along the interface is performed by the inclusion of all the supporting nodes contributing to the creation of the standard shape functions of the nodes of the smoothing domain of interest (S_s). The numerical integration using the Gauss points along the boundaries of the background mesh are, however, performed based on the supporting nodes selected by the chosen T-scheme for the specific boundary (S_n) as depicted in Figure 3-3. In this chapter, N_{gau} is taken as two in all chosen T-schemes.

From Equation 6-24, the pressure gradient is obtained in a similar fashion as follows:

$$\tilde{\mathbf{V}}P = \sum_{I \in S_s} \tilde{\mathbf{B}}_{2I} \bar{\mathbf{p}}_I + \sum_{J \in S_s^{enr}} \tilde{\mathbf{B}}_{2J}^{enr} \bar{\mathbf{b}}_J \quad (6-33)$$

As discussed in Chapter 3, $\tilde{\mathbf{B}}_2$ has identical entries to $\tilde{\mathbf{B}}_1$, but with different arrangements of them (Equation 3-48). Similarly, $\tilde{\mathbf{B}}_2^{enr}$ has a different arrangement of entries compared to its counterpart $\tilde{\mathbf{B}}_1^{enr}$. It also contains different components with respect to $\tilde{\mathbf{B}}_1^{enr}$ when a strong discontinuity is considered.

The matrix $\tilde{\mathbf{B}}_{2J}^{enr}$ associated with the node of interest J takes the form expressed as follows:

$$\tilde{\mathbf{B}}_{2J}^{enr} = \begin{bmatrix} \tilde{b}_{Jx_1}^{p,enr} \\ \tilde{b}_{Jx_2}^{p,enr} \end{bmatrix} \quad (6-34)$$

Consequently,

$$\tilde{\mathbf{B}}_2^{enr} = \begin{bmatrix} \tilde{b}_{1x_1}^{p,enr} & \dots & \tilde{b}_{qx_1}^{p,enr} \\ \tilde{b}_{1x_2}^{p,enr} & & \tilde{b}_{qx_2}^{p,enr} \end{bmatrix}_{2 \times q} \quad (6-35)$$

where the components of $\tilde{\mathbf{B}}_2^{enr}$ are computed in the following form:

$$\tilde{b}_{Jl}^{p,enr} = \frac{1}{2A_{sub,k}^s} \sum_{m=1}^{N_{seg}} \left[L_m^k \sum_{n=1}^{N_{gau}} w_n \phi_l(\mathbf{x}_{mn}) \left(\psi^{p,enr}(\mathbf{x}_{mn}) - \psi^{p,enr}(\mathbf{x}_J) \right) n_l(\mathbf{x}_{mn}) \right]$$

$$(l = x_1, x_2) \quad (6-36)$$

Introducing the SPIM framework with the extrinsic enrichment results in the elimination of complexities associated with the sub-integration in XFEM [322] by transforming the integration over the smoothing sub-domains into that along the boundaries of the smoothing sub-domains (including material interfaces and cracks). In addition, as will be shown later in the numerical examples, the enriched SPIM

formulated above offers a substantial improvement in terms of stress calculation, which poses difficulties in XFEM especially near the crack tips where the computations of stress intensity factors are of importance [326].

The original mapping–rule independency of SPIM is restored when enrichment functions are selected in such a way that $\tilde{\mathbf{B}}_1^{enr}$ and $\tilde{\mathbf{B}}_2^{enr}$ are constant over the smoothing domains. Consequently, the contribution of $\tilde{\mathbf{B}}_1^{enr}$ and $\tilde{\mathbf{B}}_2^{enr}$ can be taken out from the numerical integration over the smoothing domains without resorting to the mapping rule, which otherwise would require a significant level of computational expenses especially when the number of Gauss points is discernibly increased compared to the corresponding standard formulation, which is the case in XFEM because the elements are sub-patriated [322].

6.4 Contact behaviour along interfaces

The evaluation of the contact forces in fractured saturated porous media with the occurrence of a discontinuity closure mode requires the imposition of the contact constraints to solid and fluid phases. The treatment of the contact constraints in XFEM has been investigated in solid mechanics [258, 261, 323] as well as in saturated and unsaturated porous media [62, 65, 67, 327, 328]. In this section, a penalty method accompanied by enriched SPIM is adopted to computationally estimate the frictional contact forces stemming from the closing mode of a strong discontinuity. The proposed contact algorithm accounts for both normal forces and frictional contact forces with the inclusion of the stick and slip modes.

6.4.1 Contact conditions: the *Kuhn–Tucker* rule

Figure 6.6 shows two solid bodies, referred to as a master body and a slave body. Their initial domains are denoted by Ω^{Master} and Ω^{Slave} , respectively. The jump notation can be exploited to represent the relative displacement from an arbitrary point S located on the surface of the slave body Γ^{Slave} with respect to an arbitrary point M on the surface of the master body Γ^{Master} [322]:

$$[[\mathbf{u}]] = \mathbf{u}^{\text{Slave}} - \mathbf{u}^{\text{Master}} \text{ on } \Gamma = \Gamma^{\text{Slave}} \cup \Gamma^{\text{Master}} \quad (6-37)$$

where $\mathbf{u}^{\text{Slave}}$ and $\mathbf{u}^{\text{Master}}$ are the absolute displacements with respect to the origin of the assigned Cartesian coordinate in association with the slave point S and master point M, respectively. Representing the outward unit vector normal to the surface of the master body by $\mathbf{n}_{\Gamma_{\text{cont}}}$, the gap functions can be defined in the normal direction in the following form:

$$g_N \equiv \mathbf{n}_{\Gamma_{\text{cont}}}^T [[\mathbf{u}]] \text{ on } \Gamma = \Gamma^{\text{Slave}} \cup \Gamma^{\text{Master}} \quad (6-38)$$

as well as the gap function in a tangential direction, given by:

$$g_T = [[\mathbf{u}]] \mathbf{m}_{\Gamma_{\text{cont}}} \equiv (\mathbf{I} - \mathbf{n}_{\Gamma_{\text{cont}}}^T \mathbf{n}_{\Gamma_{\text{cont}}}) [[\mathbf{u}]] \text{ on } \Gamma = \Gamma^{\text{Slave}} \cup \Gamma^{\text{Master}} \quad (6-39)$$

where $\mathbf{n}_{\Gamma_{\text{cont}}}^T \mathbf{n}_{\Gamma_{\text{cont}}}$ denotes the projection matrix of the normal direction, in a two-dimensional setting, and \mathbf{I} is the identity matrix. The non-penetration condition can be stated by $g_N \geq 0$ where $g_N = 0$ indicates the contact condition, in which a compressive normal contact force is produced, which is indicated by $t_{\text{cont},N} \leq 0$ on the master body. The mathematical description of the contact interface can be written by $\Gamma_{\text{cont}} = \Gamma^{\text{Slave}} \cap \Gamma^{\text{Master}}$. The existence of a gap between two contacting bodies is stated as $g_N \geq 0$ and

$t_{cont,N} = 0$. Hence, the mathematical form of the contact conditions can be defined as follows:

$$g_N \leq 0, t_{cont,N} \geq 0, g_N t_{cont,N} = 0 \quad (6-40)$$

which is commonly known as the *Kuhn–Tucker* inequality [72]. The first statement of Equation 6-40 prevents the interpenetration of the contacting bodies, and the second statement expresses the development of a compressive contact force that arise from the onset of a closed gap. The last relation in Equation 6-40 assures the elimination of the contact tractions pertaining to the onset of the opening mode. Hence, Equation 6-40 provides a robust means of handling contact problems under the constrained optimisation framework, which is well-established for imposing a contact constraint to variational statement.

The term Γ_{cont} is unknown within a time step, and the complementary part of the strong discontinuity is subjected to a fully open mode under traction-free condition, with active contact surface being unknown. An iterative solution strategy is then adopted to handle the kinematic quantities in a nonlinear algebraic system that is exposed to a contact constraint.

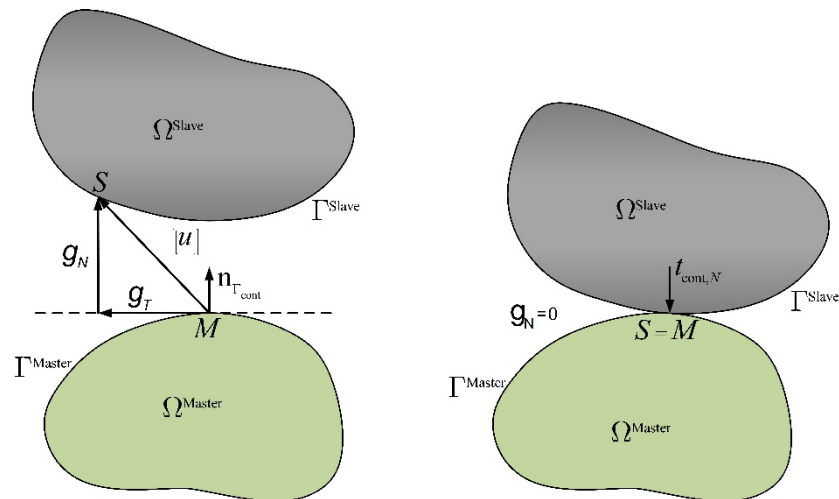


Figure 6.6. Schematic representation of two bodies in contact in association with gap functions in normal and transversal directions with the constrained condition [322]

6.4.2 Coulomb theory of frictional contact

As shown in Figure 6.7, when two contacting bodies, a master and a slave, have no normal gap and therefore are in contact, only a tangential relative displacement between them is allowed. A decomposition of the relative displacement into normal and tangential components that are analogous to those used in classical plasticity is needed. By preserving the nearly constant $\mathbf{n}_{\Gamma_{\text{cont}}}$ throughout the sliding process during the contact and sliding of the two bodies, the normal and tangential loads $t_{\text{cont},N}$ and $t_{\text{cont},T}$ are defined on the contact surface of the master body

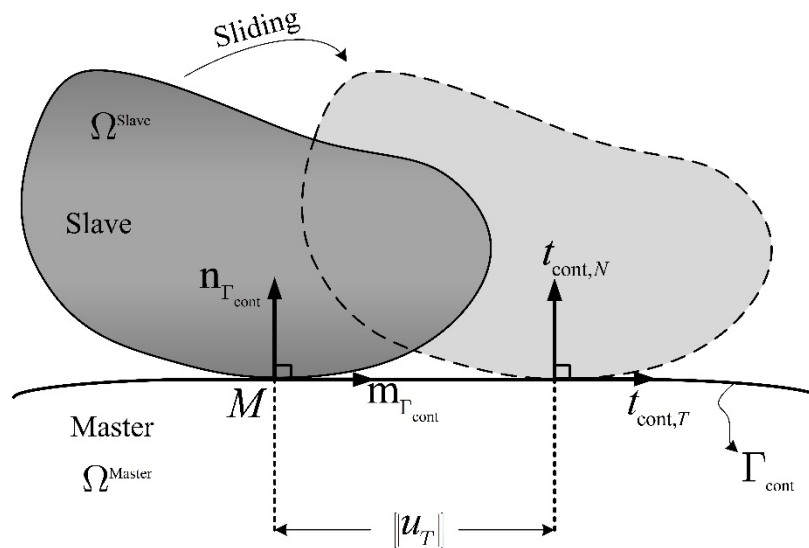


Figure 6.7. A sliding slave body with respect to a master body undergoing a relative tangential displacement[322]

The frictional behaviour is formulated here based on the stick-slip condition introduced by Curnier [329]. According to the stick-slip theory, the relative displacement at the surfaces in contact is decomposed into two parts: one part, the stick, is reversible, which can be interpreted as the elastic deformation; the other part, the slip, is irreversible,

which can be interpreted as plastic deformation. For a slip along Γ_{cont} , the decomposition of the relative tangential displacement can be performed as follows:

$$[[\mathbf{u}_T]] = [[\mathbf{u}_T^e]] + [[\mathbf{u}_T^p]] \text{ on } \Gamma_{cont} \quad (6-41)$$

where $[[\mathbf{u}_T]]$ stands for the relative displacement in the tangential direction shown by $[[\mathbf{u}_T]] = (\mathbf{I} - \mathbf{n}_{\Gamma_{cont}}^T \mathbf{n}_{\Gamma_{cont}})[[\mathbf{u}]]$. In Equation 6-41, the superscripts e and p indicate the stick/elastic and slip/ plastic parts of $[[\mathbf{u}_T]]$, respectively.

In this chapter, the resultant unilateral contact condition is established by the imposition of constraints through the implementation of the penalty method. This method, unlike the Lagrangian multiplier method [38], avoids introducing additional unknown variables in the formulation. In the penalty method, the non-penetration constraint is established by embedding extremely stiff springs on the active contacting surfaces. As a result, the normal contact forces $t_{cont,N}$ can be attained through the multiplication of the penalty parameter k_N by the relative displacement in the normal direction $[[\mathbf{u}_N]]$. The elastic part of the contact force in the tangential direction $t_{cont,T}$ is calculated in a similar manner. The penalty parameters k_N and k_T can be thought of as the normal and tangential amplitudes of stiffness, which are *a priori* selected at the contact surface. Consequently, the constitutive law that relates the normal and tangential relative displacements to their corresponding contact loads can be elaborated as follows:

$$t_{cont,N} = (\mathbf{D}_f^e)_N [[\mathbf{u}^e]] \quad (6-42)$$

$$t_{cont,T} = (\mathbf{D}_f^e)_T [[\mathbf{u}^e]] \quad (6-43)$$

where $(\mathbf{D}_f^e)_T$ and $(\mathbf{D}_f^e)_N$ indicate the parts of the elastic modulus contributing to the normal and tangential directions as follows:

$$(\mathbf{D}_f^e)_N = k_N(\mathbf{n}_{\Gamma_{\text{cont}}}^T \mathbf{n}_{\Gamma_{\text{cont}}}) \quad (6-44)$$

$$(\mathbf{D}_f^e)_T = k_T (\mathbf{I} - \mathbf{n}_{\Gamma_{\text{cont}}}^T \mathbf{n}_{\Gamma_{\text{cont}}}) \quad (6-45)$$

where k_N and k_T represent the constant normal and tangential stiffness, respectively. The decomposition of the relative tangential displacements into stick and slip parts requires the use of a slip criterion in the formulation. The slip criterion is needed to build a theoretical description that expresses the relationship between the stress and stick-slip movement at the body surfaces in contact. In the stick condition, the relative movement between the contacting bodies is assumed to be zero in the tangential direction, whereas in the sliding condition, a relative movement is allowed at the point of interest in the tangential direction at the interface. In this chapter, the well-established Coulomb's friction law is applied to capture the frictional contact behaviour as a function of contact forces \mathbf{t}_{cont} , which has been used, frequently and successfully, to represent frictional contact behaviour. Coulomb's friction law defined as a function of the contact force \mathbf{t}_{cont} is simply shown as follows:

$$F_f(\mathbf{t}_{\text{cont}}, w) = \|\mathbf{t}_{\text{cont},T}\| - \mu_f(\mathbf{t}_{\text{cont},N}, w) \|\mathbf{t}_{\text{cont},N}\| \begin{cases} = 0 & \text{slip} \\ < 0 & \text{stick} \end{cases} \quad (6-46)$$

where μ_f denotes the Coulomb friction coefficient calculated by $\mu_f = \tan \varphi_f$, where φ_f indicates the friction angle at the interface of interest. The friction coefficient μ_f is assumed to rely on two parameters: the frictional work parameter w , and the normal contact force $\mathbf{t}_{\text{cont},N}$. $F_f < 0$ implies that a stick situation governs the relative displacement between two contacting bodies; $F_f \geq 0$ implies a slip situation between two bodies in contact where the shear stress is restricted to the value satisfying $F_f = 0$.

The slip criterion dictates the dependency of shear stress on the normal contact force $\mathbf{t}_{cont,N}$ when slip condition is satisfied.

According to the conventional plasticity theory, the slip direction is determined by an appropriate slip rule, which can be specified by the gradient of a convex potential function, Z . Assuming associative rule, the potential function Z can be replaced by the slip criterion F_f . However, despite its convenience, the assumption of associativity may engender an erroneous normal force that could cause an unrealistic separation between the contacting surfaces. The avoidance of the anomalies related to the separation from the surfaces in contact requires the adoption of a non-associative slip rule [329]. Hence, in this chapter, a non-associative slip potential function, represented by $Z = \|\mathbf{t}_{cont,T}\|$, is applied for an isotropic frictional contact, in which the outward normal to the slip potential function determines the slip direction. Consequently, the tangential plastic deformation $[[\mathbf{u}_T^p]]$ is obtained by defining the slip rule as follows:

$$[[\mathbf{u}_T^p]] = d\gamma \frac{\partial Z}{\partial \mathbf{t}_{cont,T}} = d\gamma \mathbf{m}_{\Gamma_{cont}} \quad (6-47)$$

where $d\gamma$ stands for the plastic multiplier representing the magnitude of the slip increment with respect to the outward normal to the potential Z , and $\mathbf{m}_{\Gamma_{cont}} = \mathbf{t}_{cont,T} / \|\mathbf{t}_{cont,T}\|$ is the unit tangential vector.

The tangent stiffness matrix, \mathbf{D}_f^{ep} , is unsymmetrical because of the non-associativity induced by the slip rule. Assuming that the contact tractions in horizontal and tangential directions are decoupled, independent constitutive expressions can be established between the normal and tangential contact tractions and the relative displacements in the following forms:

$$d\mathbf{t}_{cont,N} = (\mathbf{D}_f)_N d[\mathbf{u}] \quad (6-48)$$

$$d\mathbf{t}_{cont,T} = (\bar{\mathbf{D}}_f)_T d[\mathbf{u}] \quad (6-49)$$

where $(\mathbf{D}_f)_N = k_N((\mathbf{n}_{\Gamma_{cont}}^T \mathbf{n}_{\Gamma_{cont}}))$ and $(\bar{\mathbf{D}}_f)_T = \bar{k}_T(\mathbf{I} - \mathbf{n}_{\Gamma_{cont}}^T \mathbf{n}_{\Gamma_{cont}})$, where \bar{k}_T is the tangential stiffness parameter. The stick-slip condition can be determined by a careful selection of \bar{k}_T derived from a stick-slip relationship for the contact. In the stick condition, no contact tangential movement results in the attainment of the contact friction forces. In this case, the stick tangential stiffness $\bar{k}_T = k_T > 0$ can be directly obtained from the relationship between $\|\mathbf{t}_{cont,T}\|$ and $\|\mathbf{g}_T\|$ for the contact. At the threshold of slippage, the frictional forces are derived directly from the restriction induced by $F_f = 0$, resulting in the attainment of a constant value of $\mu_f \|\mathbf{t}_{cont,N}\|$. Consequently, the slip tangential stiffness $\bar{k}_T = 0$ is adopted in the slip mode.

The incremental total contact traction can, therefore, be written as follows:

$$d\mathbf{t}_{cont} = d\mathbf{t}_{cont,N} + d\mathbf{t}_{cont,T} = (\mathbf{D}_f)_N d[\mathbf{u}] + (\bar{\mathbf{D}}_f)_T d[\mathbf{u}] = \bar{\mathbf{D}}_f^{ep} d[\mathbf{u}] \quad (6-50)$$

where

$$\bar{\mathbf{D}}_f^{ep} = k_N (\mathbf{n}_{\Gamma_{cont}}^T \mathbf{n}_{\Gamma_{cont}}) + \bar{k}_T ((\mathbf{I} - \mathbf{n}_{\Gamma_{cont}}^T \mathbf{n}_{\Gamma_{cont}})) \quad (6-51)$$

The conventional predictor–corrector algorithm frequently adopted in the classical plasticity theory along with a return mapping algorithm can be adopted efficiently to solve the nonlinear contact problem formulated above. The adopted predictor–corrector algorithm leads to a smooth transition from the stick condition to the slip condition when tangential forces increase. The step-by-step implementation of the predictor–corrector algorithm is given in Table 6-1.

Table 6-1. The predictor–corrector algorithm for a frictional contact problem (superscript n or $n + 1$ indicates trial number) [322].

<p>1) Compute the normal traction by</p> $\mathbf{t}_{\text{cont},N}^{n+1} = \mathbf{t}_{\text{cont},N}^n + (\mathbf{D}_f^e)_N [[\Delta \mathbf{u}]]^n$ <p>2) Set $\bar{\mathbf{k}}_T = \mathbf{k}_T^{\text{Stick}}$ and evaluate the trial magnitude of the elastic frictional traction</p> $(\mathbf{t}_{\text{cont},T}^{n+1})^{\text{trial}} = \mathbf{t}_{\text{cont},T}^n + (\bar{\mathbf{D}}_f^e)_T [[\Delta \mathbf{u}]]^n$ <p>3) If $\mathbf{F}_f = \ (\mathbf{t}_{\text{cont},N}^{n+1})^{\text{trial}}\ - \mu_f \ \mathbf{t}_{\text{cont},N}^{n+1}\ < 0$,</p> <p>Then $\mathbf{t}_{\text{cont},T}^{n+1} = (\mathbf{t}_{\text{cont},T}^{n+1})^{\text{trial}}$ and exit</p> <p>Else, Go to step 4.</p> <p>4) Adjust the frictional traction estimated by the trial amplitude, and the friction stiffness by</p> $\mathbf{t}_{\text{cont},T}^{n+1} = \mu_f \ \mathbf{t}_{\text{cont},N}^{n+1}\ \frac{\Delta \mathbf{g}_T^{n+1}}{\ \Delta \mathbf{g}_T^{n+1}\ } \text{ and } \bar{\mathbf{k}}_T = \frac{\mu_f \ \mathbf{t}_{\text{cont},N}^{n+1}\ - \ \mathbf{t}_{\text{cont},T}^{n+1}\ }{\ \Delta \mathbf{g}_T^{n+1}\ }$
--

6.4.3 The Enriched SPIM formation for contact modelling

In this section, the enriched SPIM formulation proposed for the incorporation of contact modelling in solid mechanics is presented. This formulation, commonly applied in computational contact mechanics, is described here to ensure completeness. In subsequent sections, the proposed contact formulation will be included in the coupled flow-deformation analysis of saturated porous media with an embedded interface.

For a solid body with a contacting interface within its domain, the overall static equilibrium can be expressed as:

$$\nabla \cdot \boldsymbol{\sigma} + \mathbf{b} = 0 \quad (6-52)$$

with the boundary condition as presented in Equations 3-4 and 3-5. A procedure similar to that presented in section 6.2.1 is performed to obtain the weak form of Equation 6-52,

$$\begin{aligned} & \int_{\Omega_k^s} \boldsymbol{\varepsilon}^T(\mathbf{v}) \tilde{\boldsymbol{\sigma}}(\boldsymbol{\varepsilon}(\mathbf{u})) d\Omega - \int_{\Gamma_{\text{cont}}^+} \mathbf{v}^{+T} (\mathbf{n}_{\Gamma_{d^+}}^T \tilde{\boldsymbol{\sigma}}^+) d\Gamma - \int_{\Gamma_{\text{cont}}^-} \mathbf{v}^{-T} (\mathbf{n}_{\Gamma_{d^-}}^T \tilde{\boldsymbol{\sigma}}^-) d\Gamma - \\ & \int_{\Gamma_t} \mathbf{v}^T \bar{\mathbf{t}} d\Gamma - \int_{\Omega_k^s} \rho \mathbf{v}^T \mathbf{g} d\Omega = 0 \quad \forall \mathbf{v} \in \mathbf{V}_{u,0} \end{aligned} \quad (6-53)$$

A simple manipulation then results in the compact form of Equation 6-53, as follows:

$$\begin{aligned} & \int_{\Omega_k^s} \boldsymbol{\varepsilon}^T(\mathbf{v}) \tilde{\boldsymbol{\sigma}}(\boldsymbol{\varepsilon}(\mathbf{u})) d\Omega + \int_{\Gamma_{\text{cont}}} \llbracket \mathbf{v} \rrbracket^T \mathbf{n}_{\Gamma_{\text{cont}}}^T \tilde{\boldsymbol{\sigma}} d\Gamma - \int_{\Gamma_t} \mathbf{v}^T \bar{\mathbf{t}} d\Gamma - \int_{\Omega_k^s} \rho \mathbf{v}^T \mathbf{g} d\Omega = 0 \\ & \forall \mathbf{v} \in \mathbf{V}_{u,0} \end{aligned} \quad (6-54)$$

with the boundary condition $\mathbf{n}_{\Gamma_{\text{cont}}}^T \tilde{\boldsymbol{\sigma}} = \mathbf{t}_{\text{cont}}$.

Using Equation 6-21 and introducing the *Heaviside* enrichment function to represent the strong discontinuity in contact problems, the jump in the displacement field is elaborated as follows:

$$\begin{aligned} \llbracket \mathbf{u} \rrbracket &= \llbracket \mathbf{N}^u(\mathbf{x}) \bar{\mathbf{u}} + \mathbf{N}^{u, \text{enr}}(\mathbf{x}) \bar{\mathbf{a}} \rrbracket = \llbracket \mathbf{N}^u(\mathbf{x}) \bar{\mathbf{u}} \rrbracket + \llbracket \mathbf{N}^{u, \text{enr}}(\mathbf{x}) \bar{\mathbf{a}} \rrbracket = \llbracket \mathbf{N}^{u, \text{enr}}(\mathbf{x}) \bar{\mathbf{a}} \rrbracket = \\ & \mathbf{N}^u(\mathbf{x}) \llbracket H(\mathbf{x}) - H(\mathbf{x}_j) \rrbracket \bar{\mathbf{a}} \equiv \mathbf{N}^u(\mathbf{x}) \bar{\mathbf{a}} \end{aligned} \quad (6-55)$$

The enriched displacement weight function \mathbf{v} can be expressed in terms of the corresponding nodal values as follows:

$$\mathbf{v}(\mathbf{x}) = \sum_{I \in S_s} \mathbf{N}_I^u(\mathbf{x}) \bar{\mathbf{c}}_I + \sum_{J \in S_s^{\text{enr}}} \mathbf{N}_J^{u, \text{enr}}(\mathbf{x}) \delta \bar{\mathbf{a}}_J \quad (6-56)$$

where $\bar{\mathbf{c}}$ denotes an arbitrary unknown weight vector related to the standard approximation of the displacement variable, and $\delta \bar{\mathbf{a}}$ corresponds the weight vector of the enrichment displacement approximation. Substituting Equations 6-21, 6-29, 6-55

and 6-56 into Equation 6-54, the weak form incorporating the discretised contact constraint is obtained, as follows:

$$\int_{\Omega} (\tilde{\mathbf{B}}_1 \bar{\mathbf{c}} + \tilde{\mathbf{B}}_1^{enr} \delta \bar{\mathbf{a}})^T \tilde{\boldsymbol{\sigma}}(\boldsymbol{\varepsilon}(\mathbf{u})) d\Omega + \int_{\Gamma_{\text{cont}}} \llbracket \mathbf{N}^u \bar{\mathbf{c}} + \mathbf{N}^{u,enr} \delta \bar{\mathbf{a}} \rrbracket^T \mathbf{t}_{\text{cont}} d\Gamma - \int_{\Gamma_t} (\mathbf{N}^u \bar{\mathbf{c}} + \mathbf{N}^{u,enr} \delta \bar{\mathbf{a}})^T \bar{\mathbf{t}} d\Gamma - \int_{\Omega} (\mathbf{N}^u \bar{\mathbf{c}} + \mathbf{N}^{u,enr} \delta \bar{\mathbf{a}})^T \mathbf{b} d\Omega = 0 \quad (6-57)$$

A manipulation similar to Equation 6-55 is performed on the second term of Equation 6-57 as follows:

$$\int_{\Gamma_{\text{cont}}} \llbracket \mathbf{N}^u \bar{\mathbf{c}} + \mathbf{N}^{u,enr} \delta \bar{\mathbf{a}} \rrbracket^T \mathbf{t}_{\text{cont}} d\Gamma = \int_{\Gamma_{\text{cont}}} \delta \bar{\mathbf{a}}^T (\mathbf{N}^u)^T \mathbf{t}_{\text{cont}} d\Gamma \quad (6-58)$$

Given that 6-57 must hold for any arbitrary $\bar{\mathbf{c}}$ and $\delta \bar{\mathbf{a}}$, it can be rearranged to yield the expanded residual forms as follows:

$$\boldsymbol{\Psi}_1^u(\bar{\mathbf{u}}, \bar{\mathbf{a}}) \equiv \int_{\Omega_k^s} \tilde{\mathbf{B}}_1^T \tilde{\boldsymbol{\sigma}}(\boldsymbol{\varepsilon}(\mathbf{u})) d\Omega - \int_{\Gamma_t} (\mathbf{N}^u)^T \bar{\mathbf{t}} d\Gamma - \int_{\Omega_k^s} (\mathbf{N}^u)^T \mathbf{b} d\Omega = \mathbf{0} \quad (6-59)$$

$$\begin{aligned} \boldsymbol{\Psi}_2^u(\bar{\mathbf{u}}, \bar{\mathbf{a}}) &\equiv \int_{\Omega_k^s} (\tilde{\mathbf{B}}_1^{enr})^T \tilde{\boldsymbol{\sigma}} d\Omega + \int_{\Gamma_{\text{cont}}} (\mathbf{N}^u)^T \mathbf{t}_{\text{cont}} d\Gamma - \int_{\Gamma_t} (\mathbf{N}^{u,enr})^T \bar{\mathbf{t}} d\Gamma - \\ &\int_{\Omega_k^s} (\mathbf{N}^{u,enr})^T \mathbf{b} d\Omega = \mathbf{0} \end{aligned} \quad (6-60)$$

Equations 6-59 and 6-60 present the residual of the nonlinear weak form attributed to a single-phase problem with the inclusion of an internal interface that is subjected to a contact constraint. The nonlinearity of the resultant algebraic system arising from the frictional contact constraint necessitates the adoption of an iterative procedure. In this study, the well-established Newton–Raphson iterative algorithm, similar to that presented in section 5.4.3, is adopted. Therefore, at iteration $i + 1$ in each time step, we have,

$$\tilde{\mathbf{K}}_i^{t_{n+1}} \begin{Bmatrix} d\bar{\mathbf{u}}_{i+1} \\ d\bar{\mathbf{a}}_{i+1} \end{Bmatrix} = \begin{bmatrix} \tilde{\mathbf{K}}_{uu} & \tilde{\mathbf{K}}_{ua} \\ \tilde{\mathbf{K}}_{au} & \tilde{\mathbf{K}}_{aa} \end{bmatrix}_i \begin{Bmatrix} d\bar{\mathbf{u}}_{i+1} \\ d\bar{\mathbf{a}}_{i+1} \end{Bmatrix} = - \begin{Bmatrix} \boldsymbol{\Psi}_1^u \\ \boldsymbol{\Psi}_2^u \end{Bmatrix}_i \quad (6-61)$$

where $\tilde{\mathbf{K}}$ stands for the smoothed stiffness matrix that is composed of four sub-matrices as seen in Equation 6-61. The smoothed sub-matrix $\tilde{\mathbf{K}}_{uu}$ contains only contributing entities derived from the standard degrees of freedom, whereas the smoothed sub-matrix $\tilde{\mathbf{K}}_{aa}$ is related to the additional degrees of freedom with no relation to the standard degrees of freedom. The off-diagonal sub-matrices $\tilde{\mathbf{K}}_{ua}$ and $\tilde{\mathbf{K}}_{au}$ present the coupling stiffness effects due to the interaction of standard and additional degrees of freedom. The sub-matrices are derived in the standard manner conventionally adopted in nonlinear problems, as follows:

$$\tilde{\mathbf{K}}_{uu} = \frac{\partial \Psi_1^u}{\partial \bar{\mathbf{u}}} = \int_{\Omega_k^s} \tilde{\mathbf{B}}_1^T \frac{\partial \tilde{\sigma}}{\partial \bar{\mathbf{u}}} d\Omega \quad (6-62)$$

$$\tilde{\mathbf{K}}_{ua} = \frac{\partial \Psi_1^u}{\partial \bar{\mathbf{a}}} = \int_{\Omega_k^s} (\tilde{\mathbf{B}}_1^{enr})^T \frac{\partial \tilde{\sigma}}{\partial \bar{\mathbf{a}}} d\Omega \quad (6-63)$$

$$\tilde{\mathbf{K}}_{au} = \frac{\partial \Psi_2^u}{\partial \bar{\mathbf{u}}} = \int_{\Omega_k^s} (\tilde{\mathbf{B}}_1^{enr})^T \frac{\partial \tilde{\sigma}}{\partial \bar{\mathbf{u}}} d\Omega \quad (6-64)$$

$$\tilde{\mathbf{K}}_{aa} = \frac{\partial \Psi_2^u}{\partial \bar{\mathbf{a}}} = \int_{\Omega_k^s} (\tilde{\mathbf{B}}_1^{enr})^T \frac{\partial \tilde{\sigma}}{\partial \bar{\mathbf{a}}} d\Omega + \int_{\Gamma_{\text{cont}}} (\mathbf{N}^u)^T \frac{\partial \mathbf{t}_{\text{cont}}}{\partial \bar{\mathbf{a}}} d\Gamma \quad (6-65)$$

Consequently, the full smoothed stiffness matrix takes the following form:

$$\tilde{\mathbf{K}}_i = \left[\begin{array}{cc} \int_{\Omega_k^s} \tilde{\mathbf{B}}_1^T \mathbf{D} \tilde{\mathbf{B}}_1 d\Omega & \int_{\Omega_k^s} \tilde{\mathbf{B}}_1^T \mathbf{D} \tilde{\mathbf{B}}_1^{enr} d\Omega \\ \int_{\Omega_k^s} (\tilde{\mathbf{B}}_1^{enr})^T \mathbf{D} \tilde{\mathbf{B}}_1 d\Omega & \int_{\Omega_k^s} (\tilde{\mathbf{B}}_1^{enr})^T \mathbf{D} \tilde{\mathbf{B}}_1^{enr} d\Omega + \underbrace{\int_{\Gamma_{\text{cont}}} (\mathbf{N}^u)^T \mathbf{D}_f^{ep} \mathbf{N}^u d\Gamma}_{\mathbf{K}^{con}} \end{array} \right]_i \quad (6-66)$$

The terms \mathbf{K}^{con} and $\int_{\Gamma_{\text{cont}}} (\mathbf{N}^u)^T \mathbf{t}_{\text{cont}} d\Gamma$ (Equation 6-58) can be thought of as the contact stiffness and the contact force vector, which incorporate the contact constraint into the Enriched CSPIM formulation. According to the linear elastic assumption related to material behaviour, the incremental stress-strain relation can be elaborated as follows:

$$d\tilde{\sigma} = \mathbf{D}d\tilde{\epsilon} \equiv \mathbf{D}\tilde{\mathbf{B}}_1 d\bar{\mathbf{u}} + \mathbf{D}\tilde{\mathbf{B}}_1^{enr} d\bar{\mathbf{a}} \quad (6-67)$$

A similar constitutive model was established in the previous section (Equation 6-50) to characterise the nonlinearity induced by the existence of the frictional contact behavior, given as:

$$d\mathbf{t}_{\text{cont}} = \bar{\mathbf{D}}_f^{ep} d[\mathbf{u}] \equiv \bar{\mathbf{D}}_f^{ep} \mathbf{N}^u d\bar{\mathbf{a}} \quad (6-68)$$

The numerical integration of sub-matrices included in $\tilde{\mathbf{K}}$ does not require a mapping to perform numerical integrations because both $\tilde{\mathbf{B}}_1$ and $\tilde{\mathbf{B}}_1^{enr}$ are constant over each smoothing domain:

$$\tilde{\mathbf{K}}_{uu} = \int_{\Omega_k^s} \tilde{\mathbf{B}}_1^T \mathbf{D} \tilde{\mathbf{B}}_1 d\Omega = \tilde{\mathbf{B}}_1^T \mathbf{D} \tilde{\mathbf{B}}_1 A_k^s \quad (6-69)$$

$$\tilde{\mathbf{K}}_{ua} = \int_{\Omega_k^s} \tilde{\mathbf{B}}_1^T \mathbf{D} \tilde{\mathbf{B}}_1^{enr} d\Omega = \tilde{\mathbf{B}}_1^T \mathbf{D} \tilde{\mathbf{B}}_1^{enr} A_k^s \quad (6-70)$$

$$\tilde{\mathbf{K}}_{au} = \int_{\Omega_k^s} (\tilde{\mathbf{B}}_1^{enr})^T \mathbf{D} \tilde{\mathbf{B}}_1 d\Omega = (\tilde{\mathbf{B}}_1^{enr})^T \mathbf{D} \tilde{\mathbf{B}}_1 A_k^s \quad (6-71)$$

$$\tilde{\mathbf{K}}_{aa} = \int_{\Omega_k^s} (\tilde{\mathbf{B}}_1^{enr})^T \mathbf{D} \tilde{\mathbf{B}}_1^{enr} d\Omega = (\tilde{\mathbf{B}}_1^{enr})^T \mathbf{D} \tilde{\mathbf{B}}_1^{enr} A_k^s \quad (6-72)$$

The evaluation of the contact stiffness matrix \mathbf{K}^{con} and the contact force vector (Equation 5-58) needs a proper numerical integration scheme over the contact surface Γ_{cont} . To this end, the contact discontinuity is first partitioned to a set of straight lines, and the intersection of the contact surface and the cut smoothing domains are identified, as depicted in Figure 6.8. The same Gauss points used to calculate $\tilde{\mathbf{B}}_1$ and $\tilde{\mathbf{B}}_1^{enr}$ are adopted to perform the numerical integration over each sub-smoothing domain, requiring no additional Gauss points. The already-computed shape functions involved in the calculation of $\tilde{\mathbf{B}}_1$ and $\tilde{\mathbf{B}}_1^{enr}$ are also used for the numerical evaluation of the contact stiffness and the contact force vector.

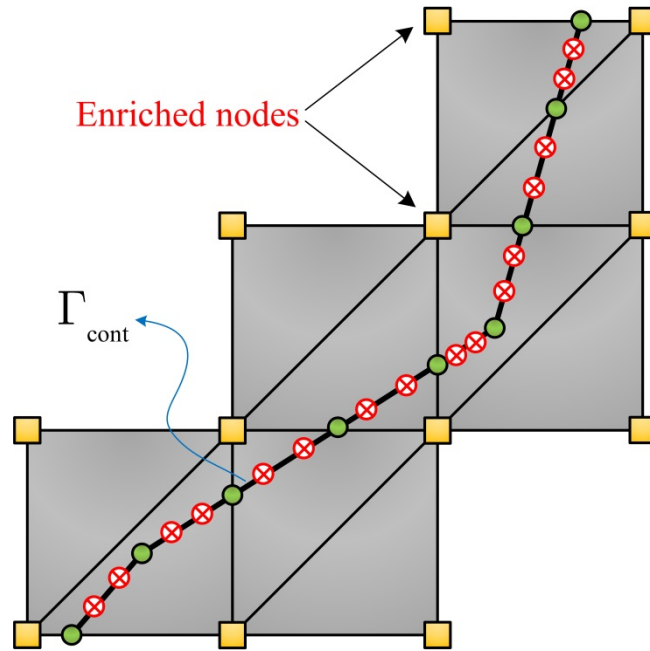


Figure 6.8. A schematic representation of the partitioning of the contact interface and the relevant Gauss points on the contact surface used for the numerical integration.

Finally, the convergence of the iterative solution is evaluated by the following criterion:

$$\eta = \left(\left\| (\Psi_1^u)^T \Psi_2^u \right\| / \|F_{ext}\| \right) \leq \eta_{aim} \quad (6-73)$$

where η_{aim} is a previously chosen percentage error. Because the penalty method is adopted in this chapter, the contact term is determined in association with the Gauss points on the active contact surface on which the normal opening g_N attains a negative value within the Newton–Raphson iterative scheme. The predictor-corrector algorithm presented in Table 6-1 is adopted to differentiate between the stick and slip conditions.

6.5 The fully discretised Enriched cell-based SPIM formulation for saturated porous media with an embedded interface

According to the formulation presented in section 6.4 and the weak forms of the coupled flow-deformation of porous media along with the fluid continuity equation within a cavity, it is possible to derive a comprehensive formulation that simultaneously demonstrates all potential effects induced by the existence of an embedded interface. The coupled flow-deformation weak form of saturated porous media with the inclusion of the contact behaviour is obtained in this section by extending that presented in section 6-4.

To arrive at the discretised weak forms, including the equilibrium and flow continuity equations, the spatially interpolation functions introduced in sections 3.4.1 and 6.3 are inserted into Equations 6-4 and 6-5 in the *Galerkin* sense, in which the test functions \mathbf{v} and q and their corresponding, equal order, trial functions are chosen from appropriate subspaces. By fulfilling the requirement that the weak form must remain valid for all kinematically admissible test functions, the discrete form of the residuals related to solid and fluid phases at the current time step $t + \alpha\Delta t$ are obtained as follows:

$$\Psi_u^{enr} = \mathbf{K}\bar{\mathbf{U}} - \mathbf{C}_{total}\bar{\mathbf{P}} + \mathbf{F}_{\Gamma_d} - \mathbf{F}_{ext} = \mathbf{0} \quad (6-74)$$

$$\Psi_p^{enr} = \mathbf{C}_{total}^T \dot{\bar{\mathbf{U}}} + \mathbf{H}_{total}\bar{\mathbf{P}} + \mathbf{M}_{total}\dot{\bar{\mathbf{P}}} - \mathbf{q}_{ext} = \mathbf{0} \quad (6-75)$$

where,

$$\mathbf{K} = \tilde{\mathbf{K}} + \mathbf{K}^{con}, \mathbf{C}_{total} = \tilde{\mathbf{C}} + \mathbf{C}_{\Gamma_d}, \mathbf{H}_{total} = \tilde{\mathbf{H}} + \mathbf{H}_{\Gamma_d} + \mathbf{H}_{closure}, \mathbf{M}_{total} = \mathbf{M} + \mathbf{M}_{\Gamma_d} \quad (6-76)$$

Ψ_u^{enr} and Ψ_p^{enr} are the residual forms of the nonlinear equations corresponding to the solid and fluid phases, respectively. $\bar{\mathbf{U}}$ and $\bar{\mathbf{P}}$ are the collection of the standard and enriched degrees of freedom for the solid phase and fluid phase, respectively. The global $\tilde{\mathbf{K}}$, $\tilde{\mathbf{C}}$, $\tilde{\mathbf{H}}$, and \mathbf{M} matrices were computed in Chapter 3 for an elastic linear medium with no discontinuity. In the presence of a discontinuity, the definition of these matrices must be updated to accommodate the effect of the additional degrees of freedom due to enrichment functions, as follows,

$$\tilde{\mathbf{K}} = \begin{bmatrix} \int_{\Omega_k^s} \tilde{\mathbf{B}}_1^T \mathbf{D} \tilde{\mathbf{B}}_1 d\Omega & \int_{\Omega_k^s} \tilde{\mathbf{B}}_1^T \mathbf{D} \tilde{\mathbf{B}}_1^{enr} d\Omega \\ \int_{\Omega_k^s} (\tilde{\mathbf{B}}_1^{enr})^T \mathbf{D} \tilde{\mathbf{B}}_1 d\Omega & \int_{\Omega_k^s} (\tilde{\mathbf{B}}_1^{enr})^T \mathbf{D} \tilde{\mathbf{B}}_1^{enr} d\Omega \end{bmatrix} \quad (6-77)$$

$$\tilde{\mathbf{C}} = \begin{bmatrix} \int_{\Omega_k^s} (\tilde{\mathbf{B}}_1)^T \eta \delta \mathbf{N}^p d\Omega & \int_{\Omega_k^s} \tilde{\mathbf{B}}_1^T \eta \delta \mathbf{N}^{p,enr} d\Omega \\ \int_{\Omega_k^s} (\tilde{\mathbf{B}}_1^{enr})^T \eta \delta \mathbf{N}^p d\Omega & \int_{\Omega_k^s} (\tilde{\mathbf{B}}_1^{enr})^T \eta \delta \mathbf{N}^{p,enr} d\Omega \end{bmatrix} \quad (6-78)$$

$$\tilde{\mathbf{H}} = \begin{bmatrix} \int_{\Omega_k^s} \tilde{\mathbf{B}}_2^T \frac{k_f}{\mu_f} \tilde{\mathbf{B}}_2 d\Omega & \int_{\Omega_k^s} \tilde{\mathbf{B}}_2^T \frac{k_f}{\mu_f} \tilde{\mathbf{B}}_2^{enr} d\Omega \\ \int_{\Omega_k^s} (\tilde{\mathbf{B}}_2^{enr})^T \frac{k_f}{\mu_f} \tilde{\mathbf{B}}_2 d\Omega & \int_{\Omega_k^s} (\tilde{\mathbf{B}}_2^{enr})^T \frac{k_f}{\mu_f} \tilde{\mathbf{B}}_2^{enr} d\Omega \end{bmatrix} \quad (6-79)$$

$$\mathbf{M} = \begin{bmatrix} \int_{\Omega_k^s} (\mathbf{N}^p)^T \alpha_f \mathbf{N}^p d\Omega & \int_{\Omega_k^s} (\mathbf{N}^p)^T \alpha_f \mathbf{N}^{p,enr} d\Omega \\ \int_{\Omega_k^s} (\mathbf{N}^{p,enr})^T \alpha_f \mathbf{N}^p d\Omega & \int_{\Omega_k^s} (\mathbf{N}^{p,enr})^T \alpha_f \mathbf{N}^{p,enr} d\Omega \end{bmatrix} \quad (6-80)$$

where the numerical integrations are performed in a similar manner to that described in Chapter 3. The Gauss points used for the numerical integrations of the enriched smoothed matrices and their corresponding interpolation functions to represent the approximation of the enriched part of displacement and pressure variables are the same as those used for the calculation of the standard property matrices, as shown in Figure 3-4.

Introducing the fluid continuity equation within a strong discontinuity into the global flow-deformation equation of a saturated porous medium introduces two important effects into the global behaviour of the saturated porous media: hydraulic coupling and mechanical coupling. Hydraulic coupling is introduced to the global equation because of the fluid exchange between the discontinuity and the surrounding permeable porous medium. Consequently, it affects the pressure-pressure block as well as the pressure-displacement block of the global coefficient matrix through the appearance of \mathbf{C}_{Γ_d} , \mathbf{H}_{Γ_d} , and \mathbf{M}_{Γ_d} as the contributing matrices, which are expressed as follows:

$$\mathbf{C}_{\Gamma_d} = \begin{bmatrix} \mathbf{0} & \mathbf{0} \\ \int_{\Gamma_d} (\mathbf{N}^u)^T \mathbf{n}_d \mathbf{N}^p d\Gamma & \int_{\Gamma_d} (\mathbf{N}^u)^T \mathbf{n}_d \tilde{\mathbf{N}}^p d\Gamma \end{bmatrix} \quad (6-81)$$

$$\mathbf{H}_{\Gamma_d} = \begin{bmatrix} \int_{\Gamma_d} \tilde{\mathbf{B}}_2^T \mathbf{k}_{\Gamma_d} \tilde{\mathbf{B}}_2 h d\Gamma & \int_{\Gamma_d} \tilde{\mathbf{B}}_2^T \mathbf{k}_{\Gamma_d} \tilde{\mathbf{B}}_2^{enr} h d\Gamma \\ \int_{\Gamma_d} (\tilde{\mathbf{B}}_2^{enr})^T \mathbf{k}_{\Gamma_d} \tilde{\mathbf{B}}_2 h d\Gamma & \int_{\Gamma_d} (\tilde{\mathbf{B}}_2^{enr})^T \mathbf{k}_{\Gamma_d} \tilde{\mathbf{B}}_2^{enr} h d\Gamma \end{bmatrix} \quad \text{with} \quad \begin{cases} \mathbf{k}_{\Gamma_d} = \mathbf{m}_d k_{cr} \mathbf{m}_d^T \\ k_{cr} = h^2 / 12 \mu_f \end{cases} \quad (6-82)$$

$$\mathbf{M}_{\Gamma_d} = \begin{bmatrix} \int_{\Omega_k^s} (\mathbf{N}^p)^T c_f \mathbf{N}^p h d\Omega & \int_{\Omega_k^s} (\mathbf{N}^p)^T c_f \mathbf{N}^{p,enr} h d\Omega \\ \int_{\Omega_k^s} (\mathbf{N}^{p,enr})^T c_f \mathbf{N}^p h d\Omega & \int_{\Omega_k^s} (\mathbf{N}^{p,enr})^T c_f \mathbf{N}^{p,enr} h d\Omega \end{bmatrix} \quad (6-83)$$

The hydraulic coupling effects are complemented by the involvement of an additional flux term induced by the weight of the existing fluid within the cavity. This term, which is added to the natural flux term of the standard weak form of the governing equations, is expressed as follows:

$$\mathbf{q}_{ext} = \left\{ \int_{\Gamma_w} (\mathbf{N}^p)^T \bar{q} d\Gamma \right\} + \left\{ \int_{\Omega_k^s} \tilde{\mathbf{B}}_2^T \frac{k_f}{\mu_f} \rho_f \bar{\mathbf{g}} d\Omega \right. \\ \left. \int_{\Omega_k^s} (\tilde{\mathbf{B}}_2^{enr})^T \frac{k_f}{\mu_f} \rho_f \bar{\mathbf{g}} d\Omega \right\} \quad (6-84)$$

The mechanical coupling effects arise from the tractions induced by either the exerted fluid pressure within the strong discontinuity or the development of frictional contact forces due to the appearance of the closure mode in the strong discontinuity. The force vector induced by the mechanical coupling effect is added into the solid residual term by the following expression:

$$\mathbf{F}_{\Gamma_d} = \left[\begin{array}{c} 0 \\ \Sigma \left(\int_{\Gamma_{cont}} \mathbf{N}^T \mathbf{t}_{cont} d\Gamma + \int_{\Gamma_d} (\mathbf{N}^u)^T \mathbf{p} d\Gamma \right) \end{array} \right] \quad (6-85)$$

where $\int_{\Gamma_{cont}} (\mathbf{N}^u)^T \mathbf{t}_{cont} d\Gamma$ indicates the contact forces, and $\int_{\Gamma_d} (\mathbf{N}^u)^T \mathbf{p} d\Gamma$ is due to the forces induced by the fluid pressure within the cavity, both of which are enforced at the crack faces. The elaboration of $\int_{\Gamma_{cont}} (\mathbf{N}^u)^T \mathbf{t}_{cont} d\Gamma$ was presented in the previous section. It is worth noting that the closure mode of the crack results in introducing the frictional contact stiffness, \mathbf{K}^{con} added to the global stiffness matrix and applied by the penalty method using the formulation described for the single-phase problems in the previous section.

The onset of the closure mode in a strong discontinuity necessitates the elimination of the enriched pressure degrees of freedom, which is mathematically expressed as follows:

$$\mathbf{p}^{enr} = 0 \quad \text{on } \Gamma_{cont} \quad (6-86)$$

This is captured by incorporating a penalisation term into the weak form of the fluid continuity equation, resulting in:

$$(\mathbf{K}_{\Gamma_{con}})^f = \int_{\Gamma_{con}} (\tilde{\mathbf{N}}^p)^T \bar{\mathbf{E}}_N \tilde{\mathbf{N}}^p d\Gamma \quad (6-87)$$

where $\bar{\epsilon}_N$ is a scalar penalty parameter for imposing the essential boundary conditions related to \mathbf{p}^{enr} . This matrix, which resembles the permeability matrix, is added to the discretised formulation through $\mathbf{H}_{closure}$ matrix (see Equation 6-76) defined in the following form:

$$\mathbf{H}_{closure} = \begin{bmatrix} 0 & 0 \\ 0 & (\mathbf{K}_{\Gamma_{con}})^f \end{bmatrix} \quad (6-88)$$

The external forces corresponding to the standard and additional degrees of freedom related to the solid phase can be calculated by the following expression: $\mathbf{F}_{ext} =$

$$\begin{bmatrix} \sum \left(\int_{\Gamma^k} \mathbf{N}^T \bar{\mathbf{t}} d\Gamma + \int_{\Omega^k} \mathbf{N}^T \rho \mathbf{g} d\Omega \right) \\ \sum \left(\int_{\Gamma^k} (\mathbf{N}^{enr})^T \bar{\mathbf{t}} d\Gamma + \int_{\Omega^k} (\mathbf{N}^{enr})^T \rho \mathbf{g} d\Omega \right) \end{bmatrix} \quad (6-89)$$

For temporal discretisation of Equation 6-75, a three-point time discretisation technique with variable time steps detailed in Chapter 3 is again adopted in this chapter. consequently, the fully discretised forms of Equations 5-48 and 5-49 can be obtained at the current time step $t + \alpha\Delta t$ as follows:

$$(\boldsymbol{\Psi}_u^{enr})^{t+\alpha\Delta t} = \mathbf{K}\bar{\mathbf{U}}^{t+\alpha\Delta t} - \mathbf{C}_{total}\bar{\mathbf{P}}^{t+\alpha\Delta t} - \mathbf{F}_{\Gamma_d}^{t+\alpha\Delta t} - \mathbf{F}_{ext}^{t+\alpha\Delta t} = \mathbf{0} \quad (6-90)$$

$$(\boldsymbol{\Psi}_p^{enr})^{t+\alpha\Delta t} = \mathbf{C}_{total}^T (A\bar{\mathbf{U}}^{t+\alpha\Delta t} - B\bar{\mathbf{U}}^t + C\bar{\mathbf{U}}^{t-\Delta t}) + \Delta t \mathbf{H}_{total} \bar{\mathbf{P}}^{t+\alpha\Delta t} +$$

$$\mathbf{M}_{total} (A\bar{\mathbf{P}}^{t+\alpha\Delta t} - B\bar{\mathbf{P}}^t + C\bar{\mathbf{P}}^{t-\Delta t}) - \Delta t \mathbf{q}_{ext}^{t+\alpha\Delta t} = \mathbf{0} \quad (6-91)$$

A similar Newton-Raphson procedure discussed earlier can be adopted for solving the above nonlinear global matrix system to obtain the nodal displacements $\bar{\mathbf{U}}_{i+1}^{t+\alpha\Delta t}$ and the nodal pore pressure $\bar{\mathbf{P}}_{i+1}^{t+\alpha\Delta t}$ at $(i + 1)$ th iteration at time $t + \alpha\Delta t$. The solution procedure can be rewritten as follows:

$$\begin{Bmatrix} (\Psi_u^{enr})_{i+1}^{t+\alpha\Delta t} \\ (\Psi_p^{enr})_{i+1}^{t+\alpha\Delta t} \end{Bmatrix} = \begin{Bmatrix} (\Psi_u^{enr})_i^{t+\alpha\Delta t} \\ \Psi_p^{enr}{}^i{}^{t+\alpha\Delta t} \end{Bmatrix} + J_{enr,i} \begin{Bmatrix} d\bar{U}_{i+1}^{t+\alpha\Delta t} \\ d\bar{P}_{i+1}^{t+\alpha\Delta t} \end{Bmatrix} = \mathbf{0} \quad (6-92)$$

in which the enriched Jacobian matrix J_{enr} is formulated as:

$$J_{enr,i} = \begin{bmatrix} \mathbf{K} & -\mathbf{C}_{total} \\ A(\mathbf{C}_{total})^T & (A\mathbf{M}_{total} + \Delta t\mathbf{H}_{total})_i \end{bmatrix} \quad (6-93)$$

The convergence of the solution is evaluated by checking the following criterion:

$$\eta = \left(\|(\Psi_u^{enr})^T \Psi_p^{enr}\| / \|\mathbf{F}_{ext}\| \right) \leq \eta_{aim} \quad (6-94)$$

where η_{aim} is *a priori* chosen error tolerance.

6.6 Numerical verifications

The robustness and efficiency of the proposed Enriched SPIM are examined in this section through the simulation of a set of numerical examples, which include both single-phase and saturated porous media. The numerical examples are selected such that all aspects of the formulation are tested. The numerical results are presented for both structured and unstructured triangulations. For all numerical examples, the alignment of the triangular boundaries with the interfaces is not preserved. All examples are evaluated under the plane-strain condition. The problems are simulated through different node selection schemes (T-schemes) to investigate the influence of different number of supporting nodes on the overall behaviour of the problem of interest.

6.6.1 Single-phase medium with an inclined interface subjected to compressive loading

The first example involves simulation of a plate $1 \text{ m} \times 1 \text{ m}$ with an inclined interface, following a Columbian frictional model subjected to compressive loading induced by a uniform vertical displacement of $u_{x_2} = -0.1 \text{ m}$ acting on the top edge of the medium, as sketched in Figure 6.9. The material interface Γ_d splits the domain into two sub-domains, where the level set is specified by the equation of an inclined plane $d(\mathbf{x}) = x_2 - 0.2x_1 - 0.4586$, in which the position of the material interface is defined by $d(\mathbf{x}) = 0$. The boundary conditions adopted in this examples are also depicted in Figure 6.9.

The interfacial inclination is represented by the slope of the line equal to $\theta = \tan^{-1}(0.2)$, as shown in Figure 6.9. Identical material properties are assumed for both sub-domains on both sides of the material interface. The elastic modulus is taken as $E_1 = E_2 = 10^4 \text{ MPa}$, while assuming the Poisson's ratio of $\nu_1 = \nu_2 = 0.3$. The inclined interface is characterized by two discernible frictional coefficients, $\mu = 0.21$ and $\mu = 0.19$, for two different simulations indicating the stick and slip conditions, respectively, according to the classical problem of a rigid block laid on a rough surface. Given $\theta = \tan^{-1}(0.2)$, a sliding response is expected with $\mu = 0.19$, while a stick condition is expected otherwise.

The square domain is discretised by a structured triangulation of 2,450 triangular background elements, as shown in Figure 6.9. The imposition of the contact constraint is made by applying the penalty method using the Enriched cell-based SPIM/SRPIM proposed in this chapter. The penalty stiffness in both horizontal and tangential directions are identically taken as $k_N = k_T = 1 \times 10^{12} \frac{\text{MPa}}{\text{m}^3}$.

The entire load is applied in one load step, and the resulting numerical solutions are shown in Figure 6.10 and Figure 6.11. Perfectly matched numerical results are achieved compared to numerical reference solutions presented by Annavarapu and Hautefeuille [330], which is consistent with theoretical expectations. As can be seen in Figure 6.10, the sliding response is recovered when the frictional coefficient between the blocks is taken as less than the tangent of the inclined interface ($\mu = 0.19$), while the stick state is observed with the larger assigned frictional coefficient ($\mu = 0.21$). The convergent solutions were achieved within a maximum of 6 iterations. The specified tolerance is set to $\eta_{aim} = 1.5 \times 10^{-8}$.

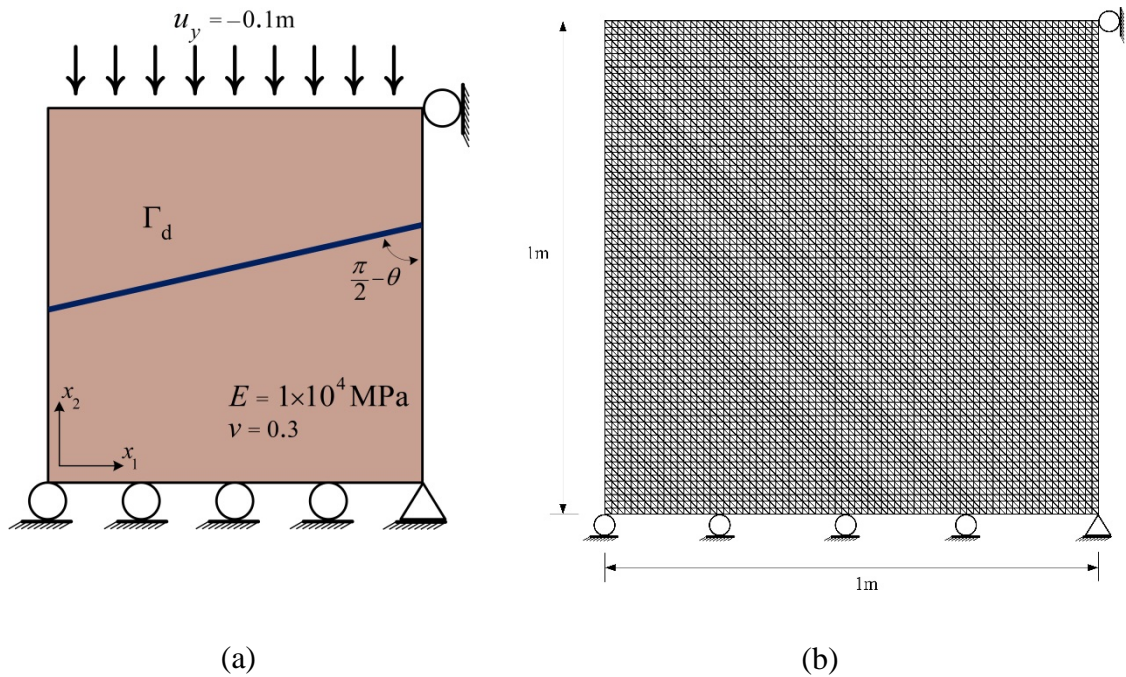
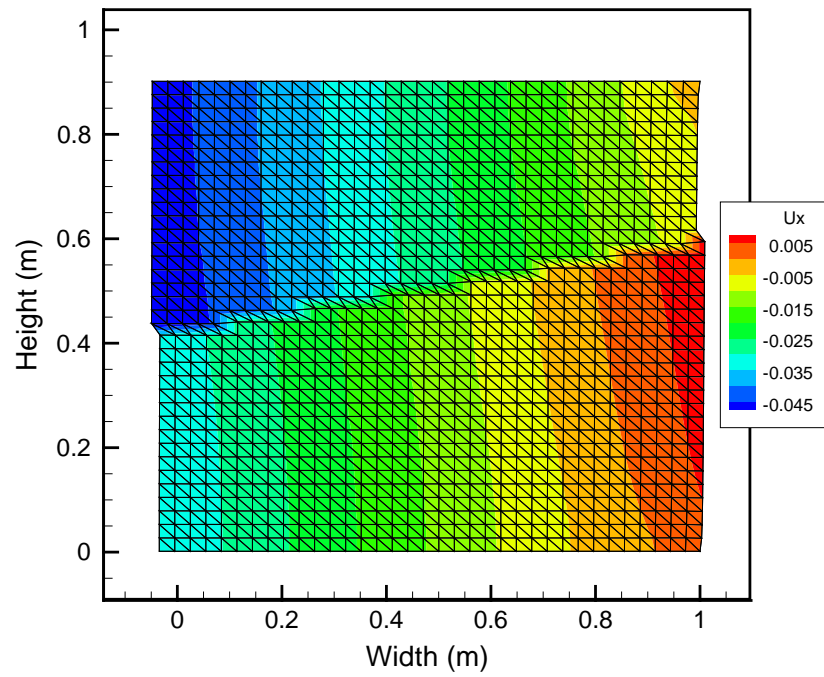
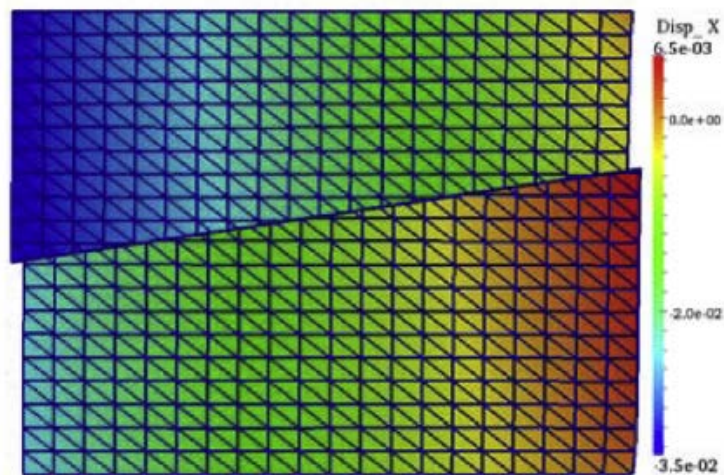


Figure 6.9. (a) A schematic representation of the unit square geometry with a frictional interface. (b) The discretization used for the computations [261].

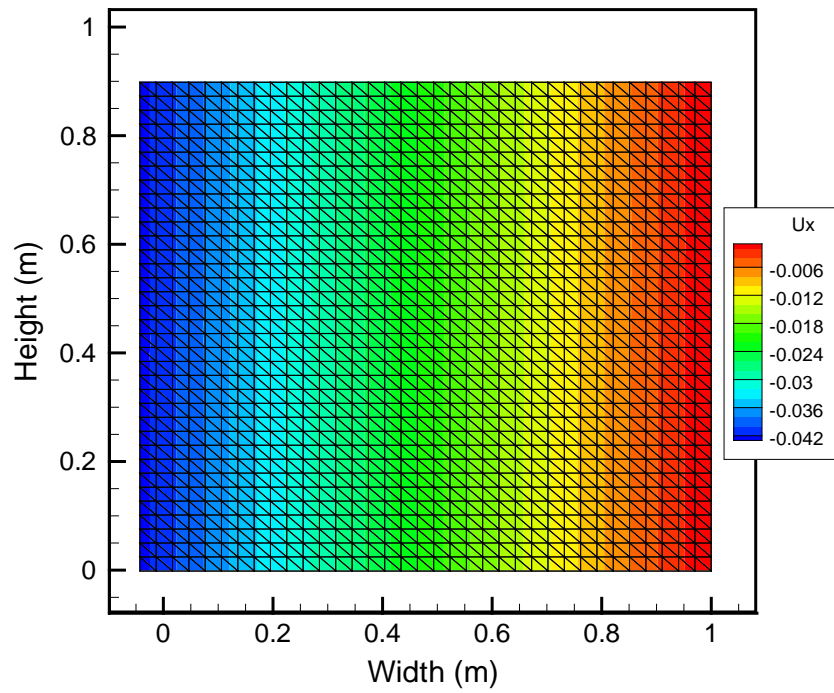


(a)

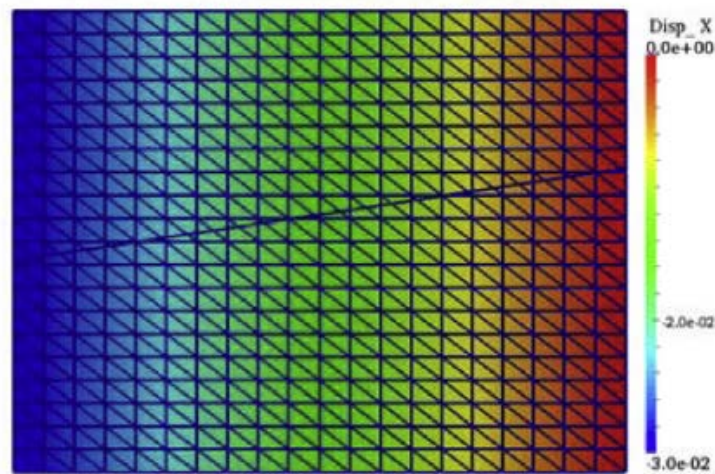


(b)

Figure 6.10. The contours of the horizontal displacement associated with the deformed medium with an inclined interface subjected to compressive loading when $\mu < \tan \theta$, slipping state for (a) the Enriched CSRPIIM-T2L of this study, and (b) the numerical result presented in [330].



(a)



(b)

Figure 6.11. The contours of the horizontal displacement associated with the deformed medium with an inclined interface subjected to the compressive loading when $\mu > \tan \theta$, stick condition for (a) the Enriched CSRPIIM-T2L of this study and (b) the numerical result presented in [330].

6.6.2 Single-phase medium with the horizontal interface subjected to non-uniform compression

The second numerical example concerns a unit square medium containing an interface, characterized by the level set as $d(\mathbf{x}) = x_2 - 0.5$. The interface decomposes the medium into two sub-domains, where the material properties are identical for both sides of the medium as $E_1 = E_2 = 10^4$ MPa and $\nu_1 = \nu_2 = 0.3$. The investigation of stick/slip behaviour is performed by assigning two different frictional coefficient values of $\mu = 0.1$ and $\mu = 0.4$. The bottom surface of the medium is horizontally and vertically constrained, while the top of the medium is subjected to a non-uniform vertical displacement specified as $u_{x_2} = 0.09 x_1 - 0.1$ m as well as a uniform horizontal displacement of $u_{x_1} = 0.05$ m, as depicted in Figure 6.12. The sides of the domain are unconstrained. The discretisation of the medium is performed by a uniform structured triangulation of 2,450 smoothing domains (elements). The normal and tangential penalty parameters were assumed $k_N = k_T = 1 \times 10^{10} \frac{\text{MPa}}{\text{m}^3}$, respectively. A trial and error analysis is performed to fine-tune the values of the penalty parameters ensuring that the non-penetration constraint is accurately enforced, while preventing the emergence of oscillatory behaviour as encountered when too-high values for the penalty parameters are selected. The geometry of the unit square and the imposed boundary conditions, together with the mesh topology used in this study, are depicted in Figure 6.12. The specified tolerance is set to $\eta_{aim} = 1 \times 10^{-10}$.

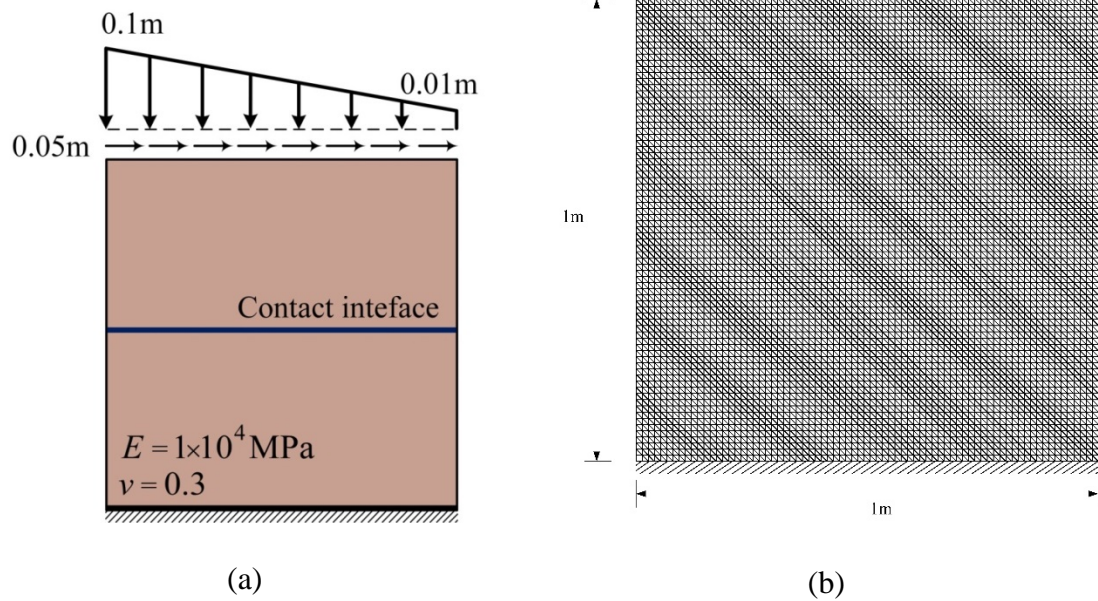


Figure 6.12. (a) A unit squared medium compressively loaded and sheared at the top edge and fixed at the bottom edge. (b) The underlying discretisation used in this study.

Figure 6.13 and Figure 6.14 depict the profiles of normal contact stress and the variation of tangential sliding for the cases of $\mu = 0.1$ and $\mu = 0.4$, respectively. The attained numerical results are presented for both Enriched CSPIM T4 and CSRPIIM T2L and are compared with those presented by Hirmand and Vahab [261]. It is evident that the numerical results attained by the proposed methods in this chapter are in excellent agreement with the results presented in [261].

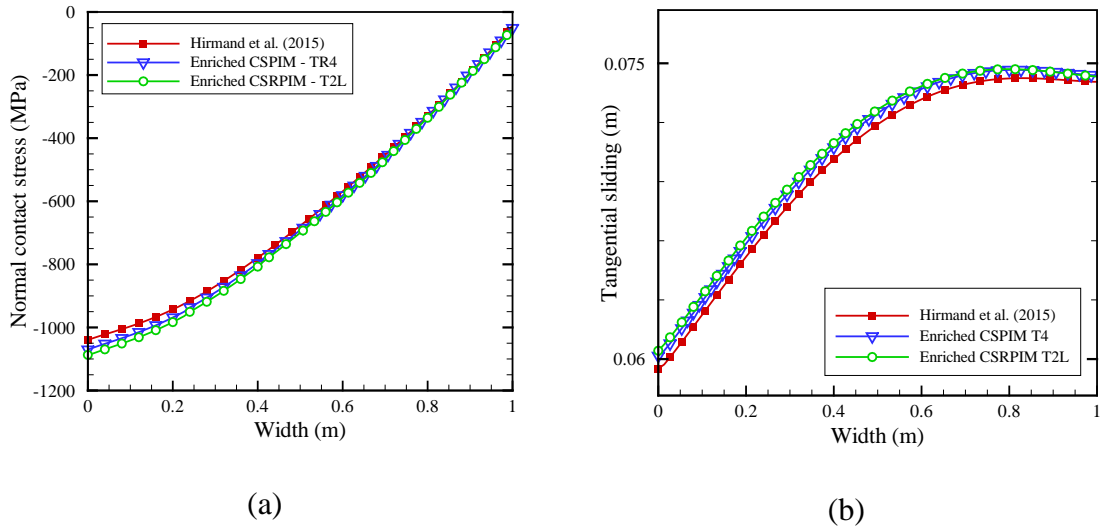


Figure 6.13. The profile of normal contact stress (a) and the variation of tangential sliding with respect to the interfacial length for the case where the frictional coefficient is $\mu = 0.1$, which corresponds to the slipping condition.

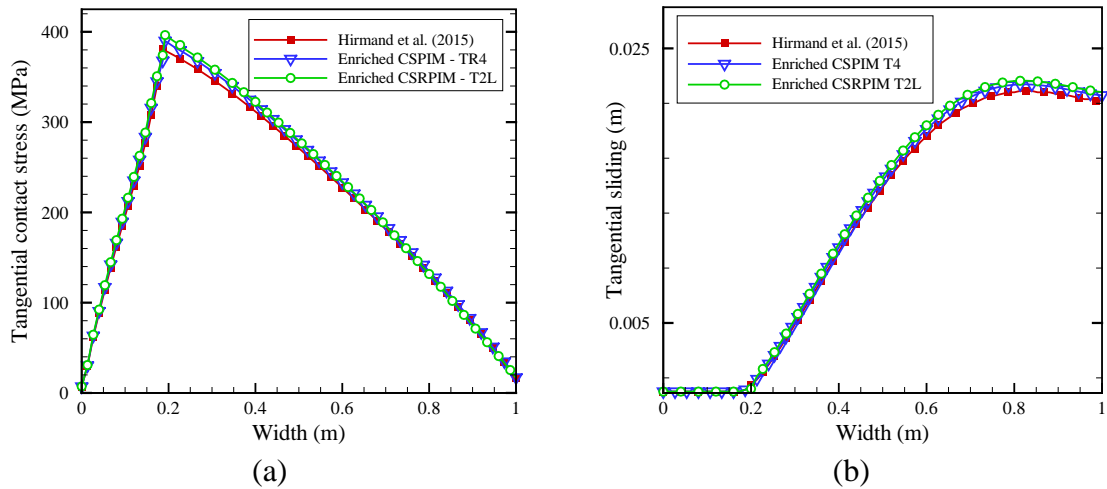
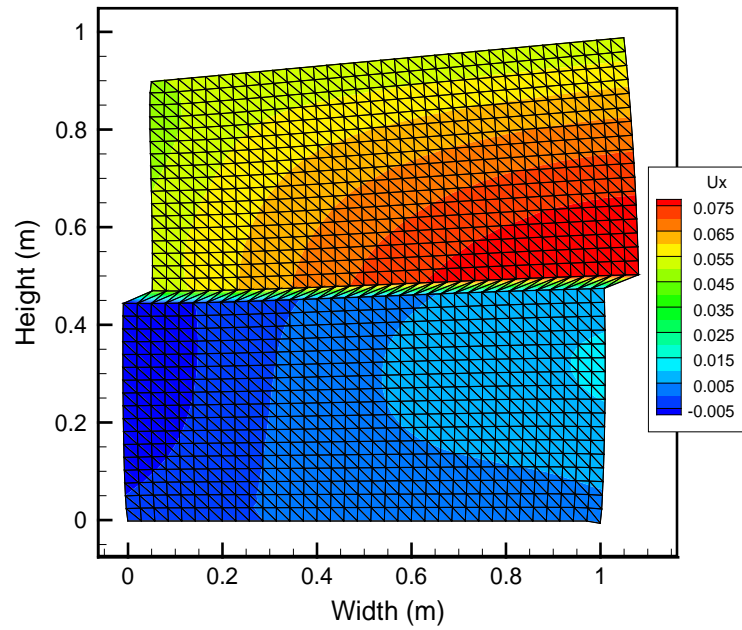


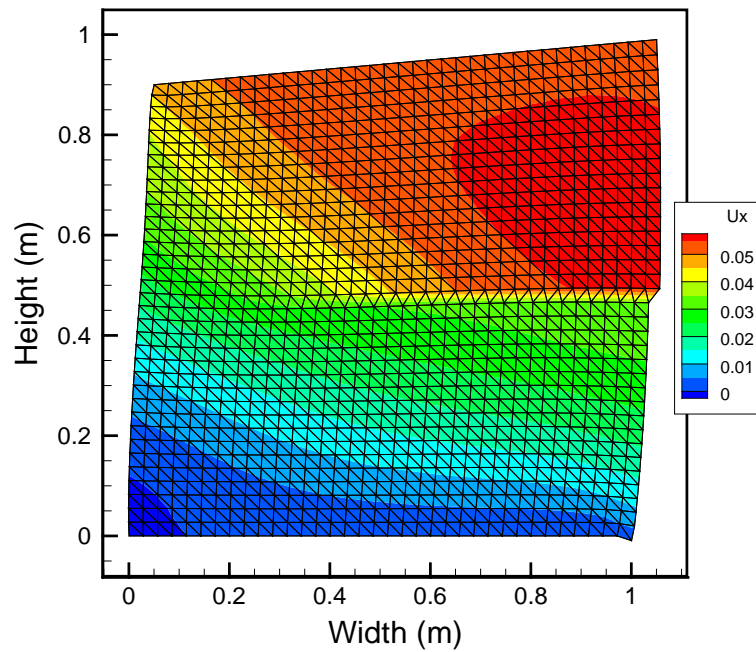
Figure 6.14. The profile of normal contact stress (a) and the variation of tangential sliding with respect to the interfacial length for the case where the frictional coefficient is taken as $\mu = 0.4$, which corresponds to the stick and slip conditions.

The horizontal displacement of the deformed medium is shown in Figure 6.15 for both the cases analysed ($\mu = 0.1$ and $\mu = 0.4$). In the case with $\mu = 0.1$, the threshold of the slip limit is readily reached by the mobilised frictional contact forces, which results in

the development of the slip condition along the entire length of the interface. The tangential contact forces are then directly computed by the amplitude of the normal contact forces, which aligns with the tangential sliding direction. However, the specification of a higher frictional coefficient value of $\mu = 0.4$ lead to the appearance of two distinct regions. The region where the high amplitude of the prescribed vertical displacement prevents the onset of slip, and no relative displacement occurs between the bodies in contact. The other region is where the frictional stress exceeds the slip limit and the tangential contact mode switches to the slipping mode. As a result, relative displacement between the two contacting bodies occurs in this region, and the frictional stresses are obtained according to the Coulomb's frictional constitutive model between the contacting bodies.



(a)



(b)

Figure 6.15. The horizontal displacement contours on the deformed medium of a unit square subjected to non-uniform compression with the frictional coefficient (a) $\mu = 0.1$ and (b) $\mu = 0.4$.

6.6.3 Multi-layered elastic foundation

The next example examines a multi-layered flexible foundation with the assumption of linear behaviour of the soil medium away from the interfaces subjected to a surface step loading of $350 \frac{\text{kN}}{\text{m}^2}$. The soil stratum contains vertical and horizontal material interfaces, through which the medium is decomposed into three subdomains. This problem was previously used to study strain localisation in [331], and modelling weak discontinuity by XFEM in [61] under dynamic loading. For this example, a quasi-static step loading on the foundation is assumed as shown in Figure 6.16. The foundation is $30 \times 30 \text{ m}$, and the corresponding essential and natural boundary conditions are shown in Figure 6.16.

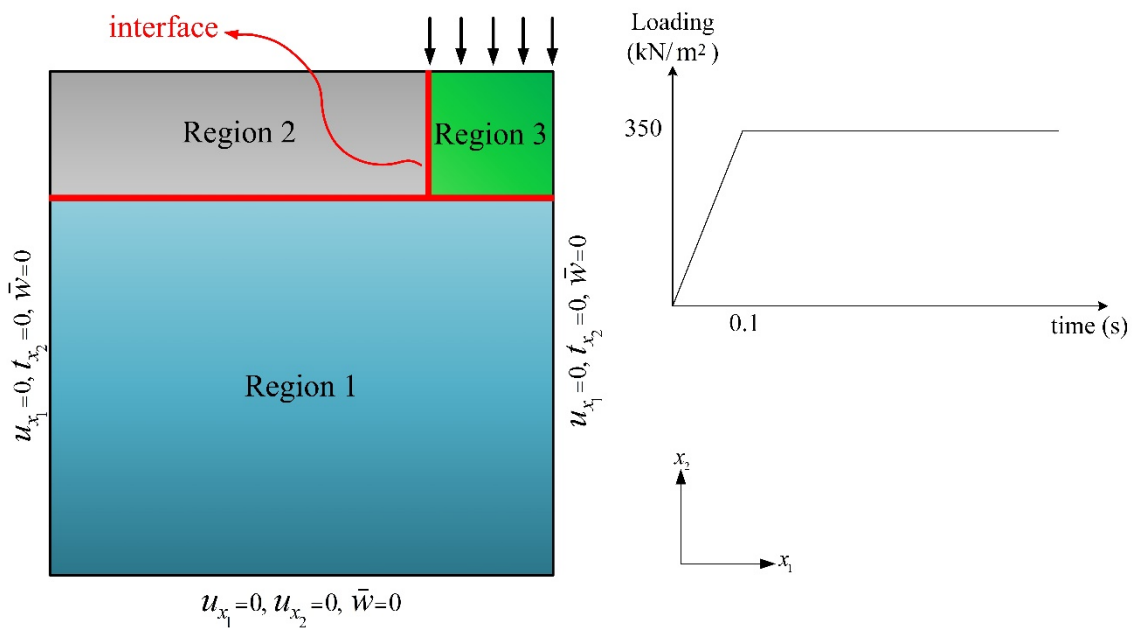


Figure 6.16. The representation of the multi-layered saturated porous medium with interfacial geometries, along with the corresponding boundary conditions [61].

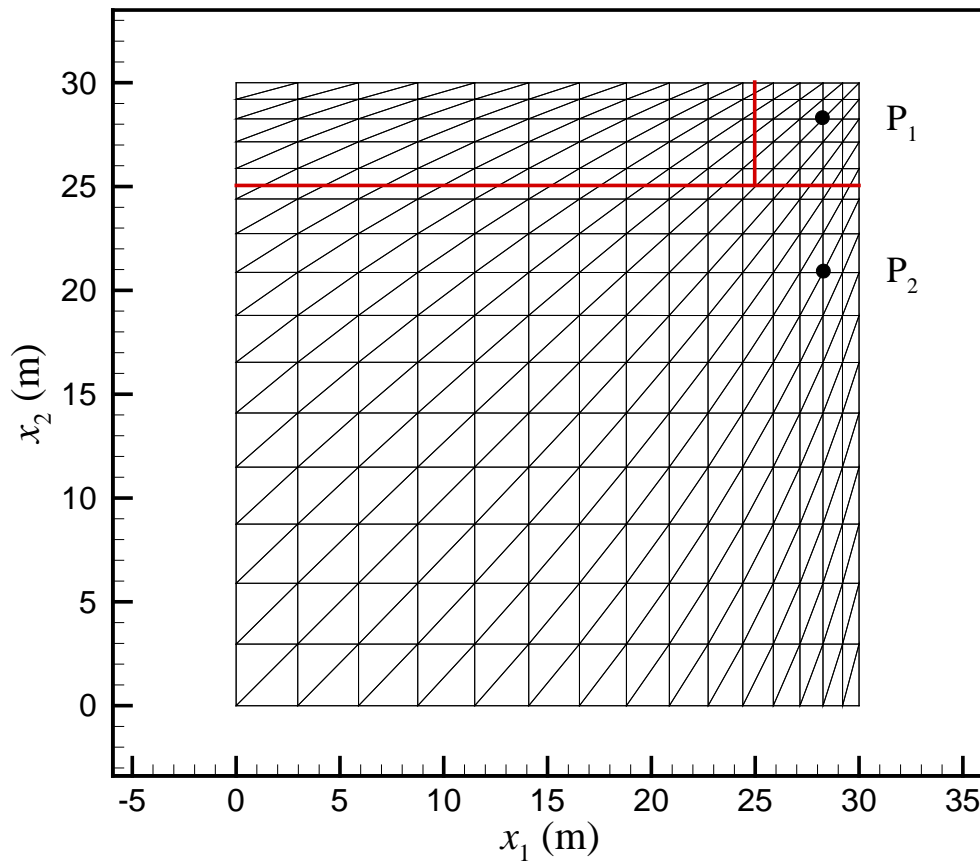


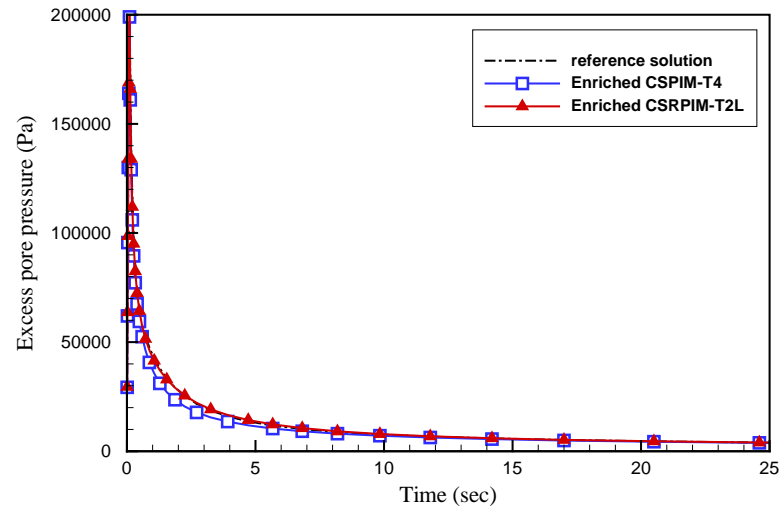
Figure 6.17. The triangulation adopted for the proposed Enriched CSPIM/CRPIM for the simulation of the multi-layered saturated porous medium, together with the coordinates of the nodes of interest for the examination of numerical results.

The domain is partitioned using a mesh composed of 450 smoothing domains generated by 256 nodes. The domain discretisation, with interfacial geometries and the positions of the nodes of interest which are used for the representation of the numerical results, are depicted in Figure 6.17. The coordinates of point \mathbf{P}_1 are (28.26 m, 28.26 m), and \mathbf{P}_2 are (28.26 m, 20.86 m). The assigned material properties for the three sub-domains are listed in Table 6-2. The larger regions are numbered first.

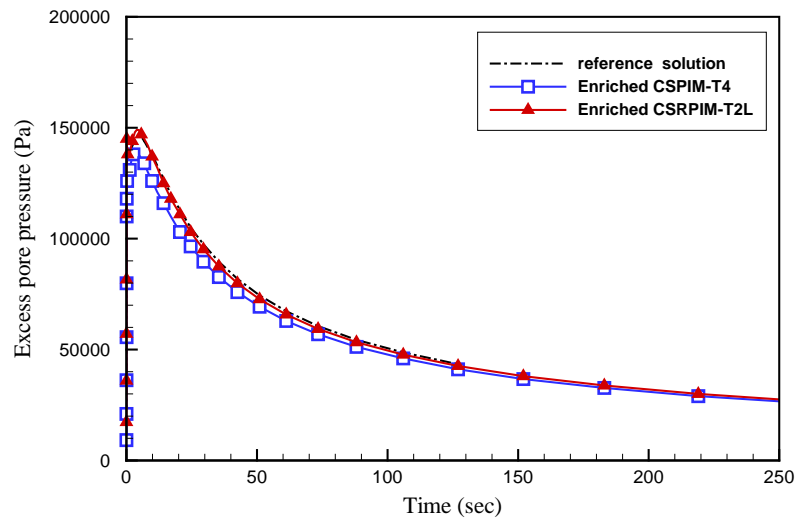
Table 6-2. Material properties assigned for the numerical simulation of the multi-layered elastic foundation.

Material properties	Region 1	Region 2	Region 3
Young's modulus E (kPa)	20×10^3	40×10^3	100×10^3
Poisson ratio ν	0.2	0.2	0.2
Solid density ρ_s (kN/m³)	20	20	20
Fluid density ρ_f (kN/m³)	10	10	10
Fluid compressibility c_f (1/Pa)	0.91×10^{-9}	0.91×10^{-9}	0.91×10^{-9}
Solid compressibility c_s (1/Pa)	1.0×10^{-20}	1.0×10^{-20}	1.0×10^{-20}
Porosity n	0.25	0.3	0.35
Permeability k (m/sec)	1.0×10^{-5}	5.0×10^{-5}	19.6×10^{-4}

The numerical results are verified against the reference solutions obtained by the FEM simulation using a very fine mesh. In the FEM simulation, the mesh conformity with the interfacial geometries is enforced, while in the proposed Enriched SPIM/SRPIM simulations, the interfaces cut through the smoothing domains, as can be see in Figure 6.17. The initial time step is set to $\Delta t_0 = 0.01$ sec with time-step growth factor coefficient $\alpha = 1.2$. Figure 6.18 presents the variation of pore pressure with respect to time at nodes \mathbf{P}_1 and \mathbf{P}_2 defined earlier. As can be seen from this figure, the numerical results obtained by the proposed method are in excellent agreement with the reference FEM solution. The variation of vertical displacement at nodes \mathbf{P}_1 and \mathbf{P}_2 obtained by the proposed Enriched cell-based SPIM/SRPIM, along with the corresponding FEM results as the reference solution, are also plotted in Figure 6.19.

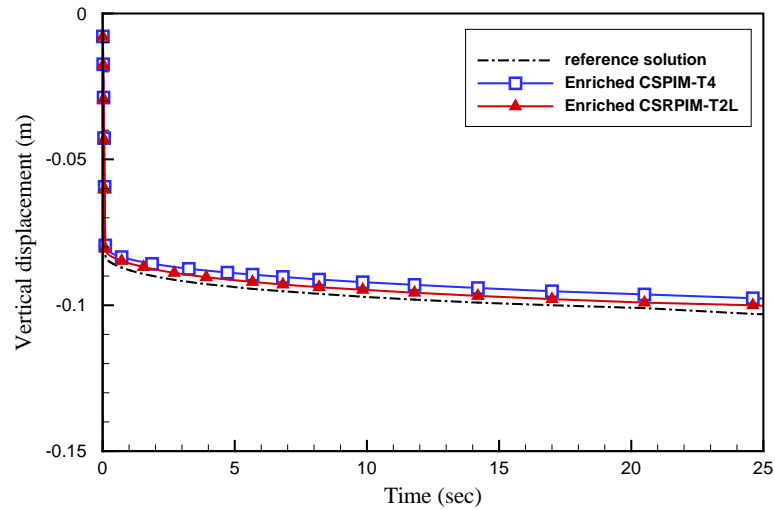


P_1

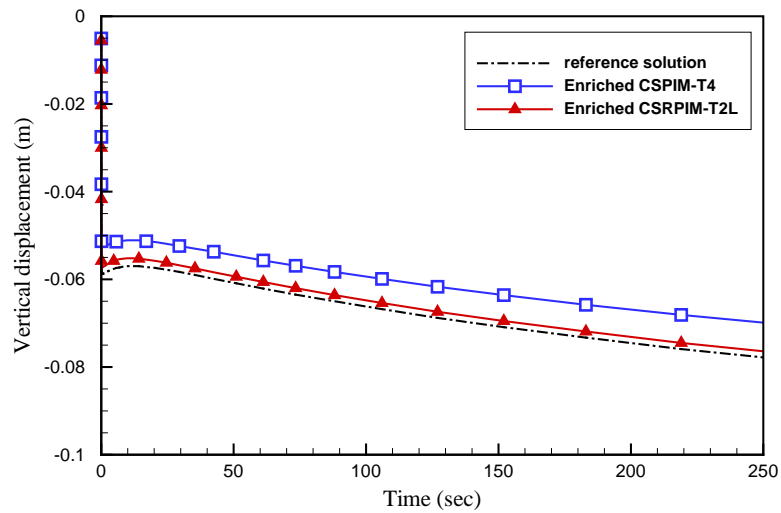


P_2

Figure 6.18. The variation of excess pore water pressure with time at nodes P_1 and P_2 .



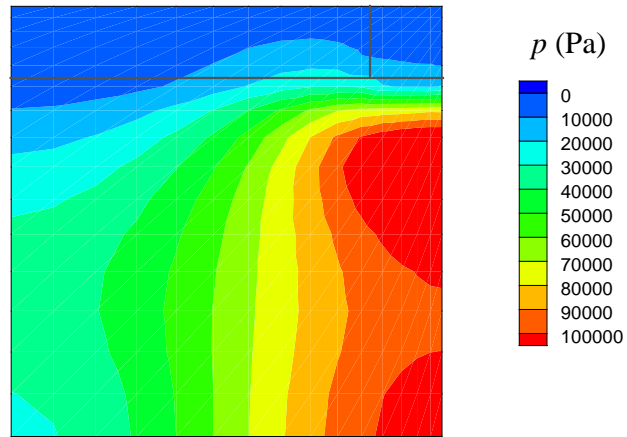
P_1



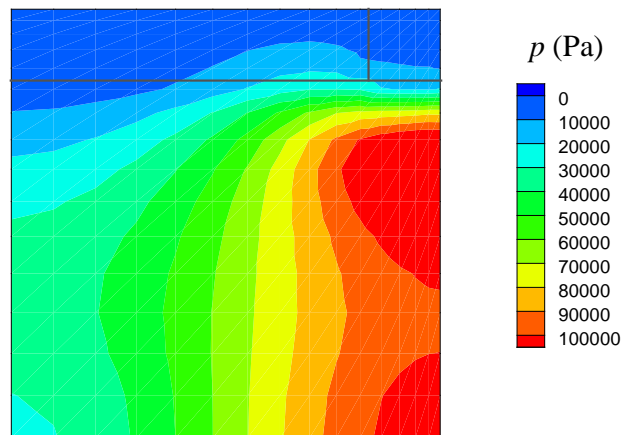
P_2

Figure 6.19. The variation of vertical displacement with respect to time at nodes P_1 and P_2 .

Figure 6.20 and Figure 6.21 graphically compare the contours of the excess pore pressure and displacement obtained by the Enriched CSRPIM-T2L and the reference FEM solution, respectively at an arbitrary time $t = 20.47$ sec. It is clear from these figures that the two solutions agree very well, qualitatively, over the whole domain.



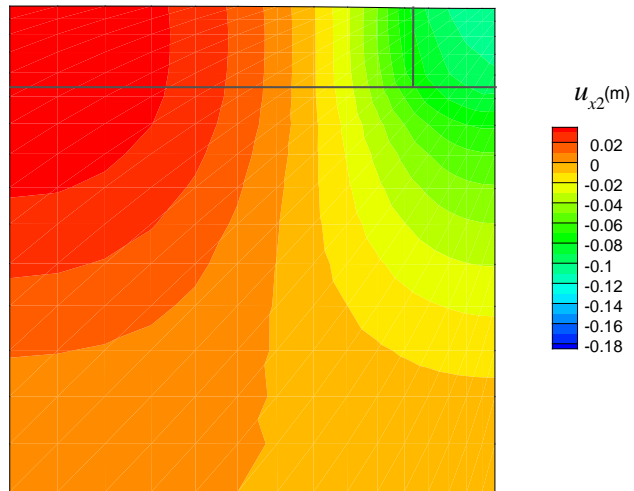
(a)



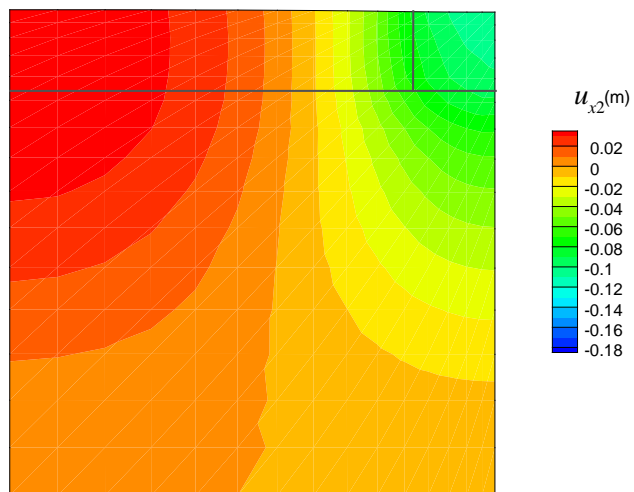
(b)

Figure 6.20. The excess pore pressure contours obtained by (a) FEM and (b) CSRPIIM-T2L at

$t = 20.47$ sec.



(a)



(b)

Figure 6.21. The displacement contours obtained by (a) FEM and (b) CSRPIIM-T2L at time $t = 20.47$ sec.

6.6.4 Saturated porous rectangular block with vertical discontinuity

The last example concerns planestrain consolidation of a saturated porous medium of $1m \times 1m$ with a strong vertical discontinuity passing through the middle of the medium, as shown in Figure 6.22(a). In this case, the flow and deformation patterns no longer followed the standard one-dimensional consolidation. There is no theoretical solution for this problem, hence the verification of the proposed method is performed through comparison of the numerical results obtained in this study with those presented by Khoei and Vahab [65], who exploited the LATIN iterative procedure together with the penalty method adapted to an XFEM framework.

The permeability along the vertical discontinuity is aperture-dependent, as discussed earlier in this chapter, and could be highly variable over time. The possible closure of the crack was recovered by the adoption of the contact active set strategy accompanied by the fulfilment of the contact constraint with the application of the penalty method.

The geometry of the rectangular saturated porous medium, along with its corresponding boundary conditions, are depicted in Figure 6.22(a). Figure 6.22(b) shows the mesh topology, which in this example was composed of 242 triangular smoothing domains created by 144 nodes. The top edge of the medium allowed drainage, while other boundaries are set to be impermeable. The lateral boundaries are horizontally constrained and the bottom of the medium was restricted in both directions. A uniformly distributed surcharge of $w = 10$ kPa acted on the top of the medium. The material properties of the discontinuous rectangular saturated porous medium are listed in Table 6-3.

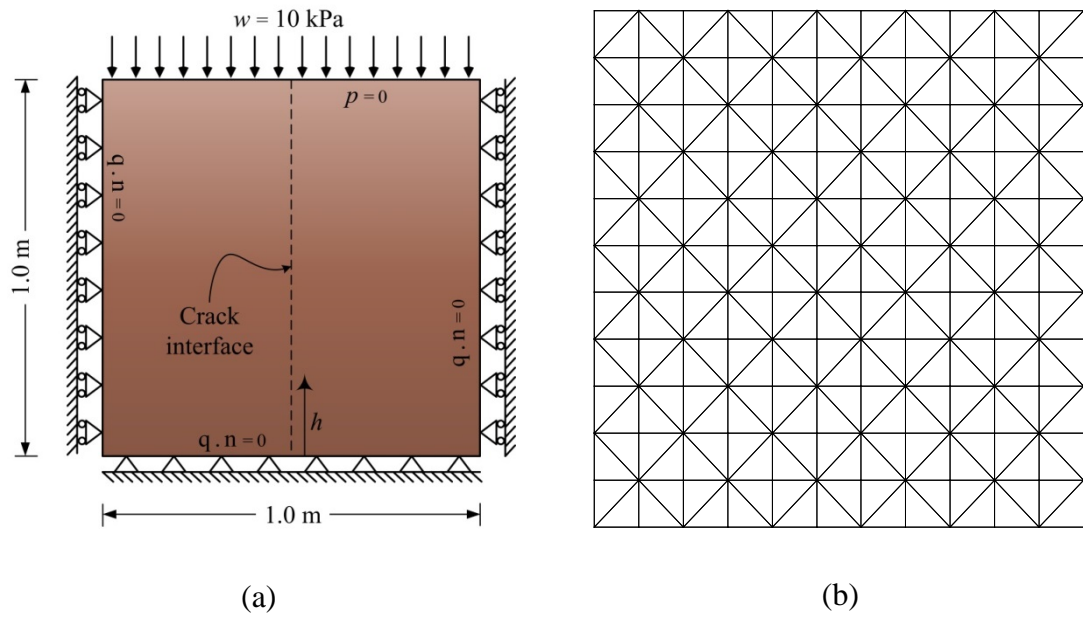


Figure 6.22. (a) Geometry of the discontinuous saturated porous block [65] and (b) the domain discretisation used in the numerical simulation.

Table 6-3. The material properties assigned to the consolidation problem of the discontinues saturated porous medium [65].

Elasticity modulus	$E = 1000 \text{ kPa}$
Poisson ratio	$\nu = 0.2$
Biot's constant	$\alpha = 1$
Porosity	$n = 0.3$
Solid grain density	$\rho_s = 2000 \text{ kg/m}^3$
Water density	$\rho_w = 1000 \text{ kg/m}^3$
Water compressibility	$\alpha_f = 0.33 \times 10^{-9} \text{ Pa}^{-1}$
Permeability	$k_f = 1.157 \times 10^{-9} \text{ m}^3/\text{N s}$
Water viscosity	$\mu_f = 1 \times 10^{-3} \text{ Pa s}$

Figure 6.25 depicts the profile of the dimensionless pore water pressure ($\frac{p}{w}$) obtained by the Enriched CSPIM-T4 over the height of the medium along the strong discontinuity at four different times during the consolidation process: $t = 0.0007$ days, $t = 0.0021$ days, $t = 0.0035$ days and $t = 0.007$ days. Also included in the figure are the solutions presented in [65], and also the results for the case without the existence of the crack. Convergent solutions were achieved within 14 iterations (at most) under Newton-Raphson iterative scheme adopted in this chapter.

Figure 6.24 shows the amount of the discontinuity opening along the height of the discontinuity at the same four times as those presented in the previous paragraph. The evolution of the general flow pattern in the domain, with and without the discontinuity, at different times is also shown in Figure 6.25.

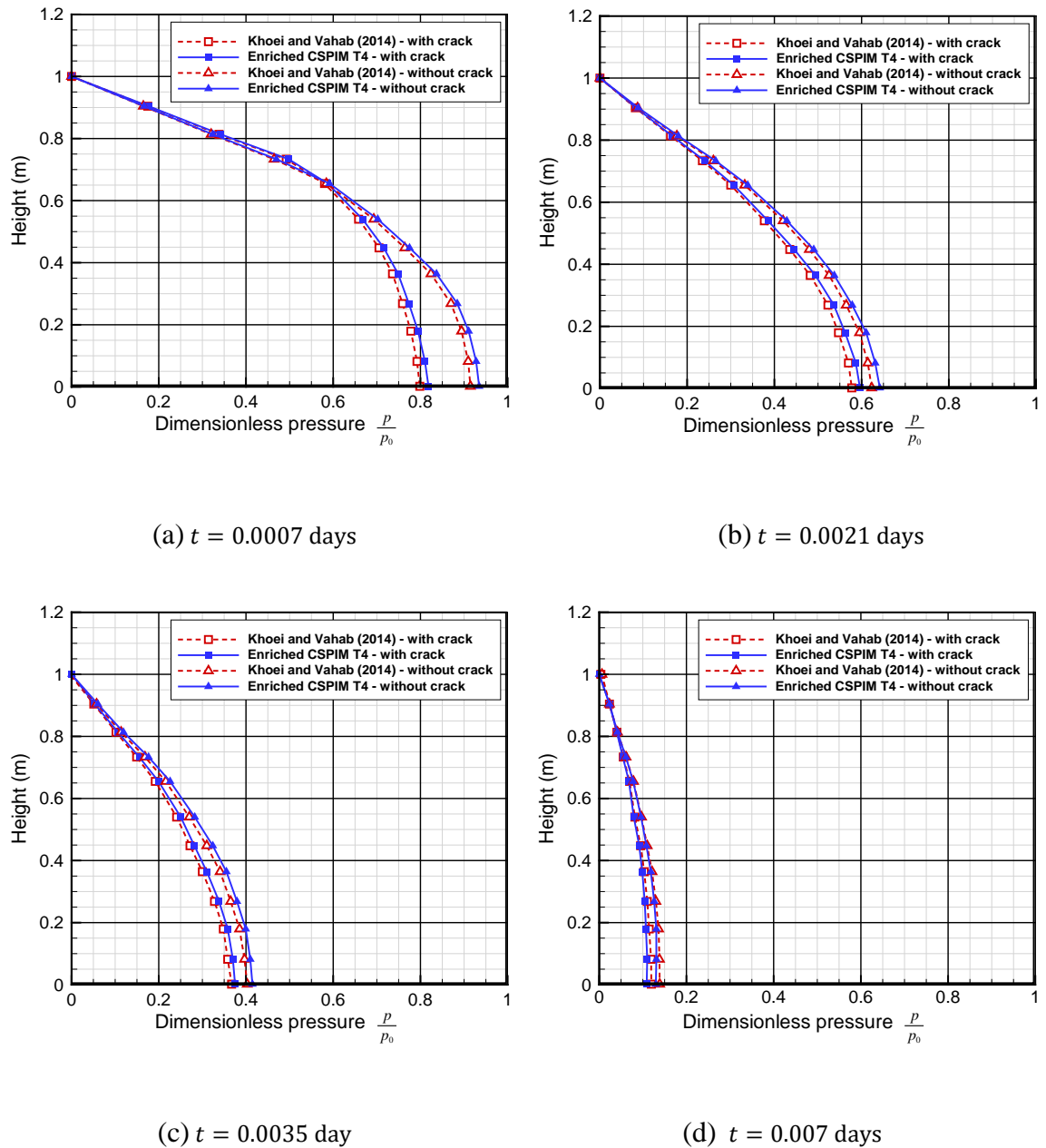


Figure 6.23. The dimensionless excess pore pressure profiles along the strong discontinuity at time (a) $t = 0.0007$ days; (b) $t = 0.0021$ days; (c) $t = 0.0035$ days; and (d) $t = 0.007$ days

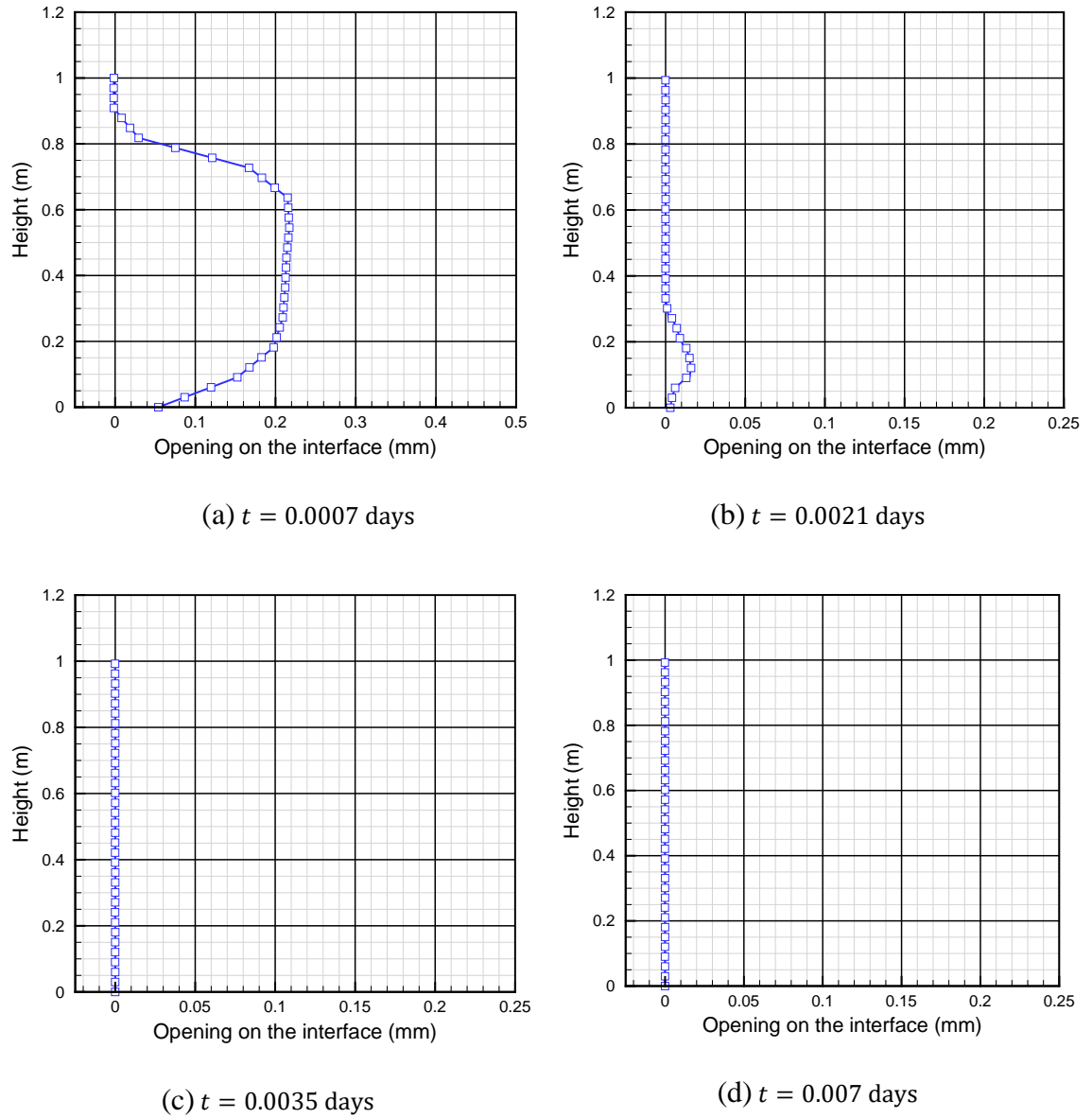
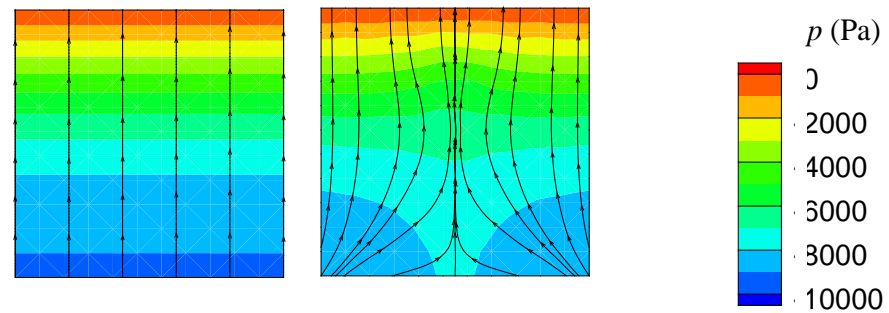
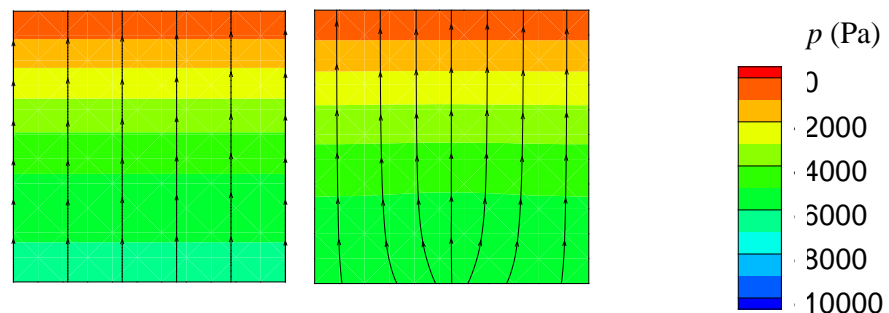


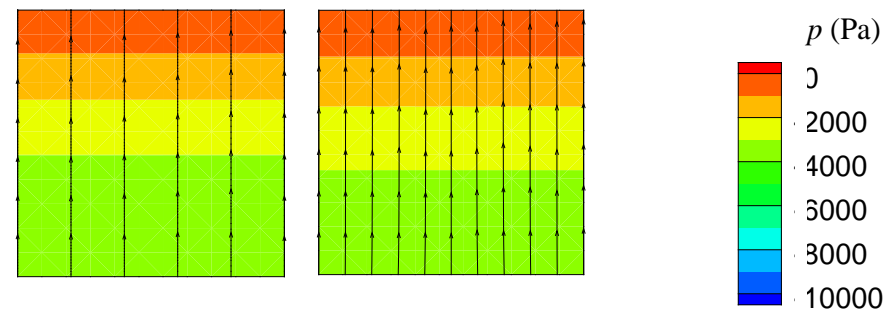
Figure 6.24. The evolution of the opening at the strong discontinuity for time (a) $t = 0.0007$ days; (b) $t = 0.0021$ days; (c) $t = 0.0035$ days; and (d) $t = 0.007$ days, obtained by CSRPI-M-T2L.



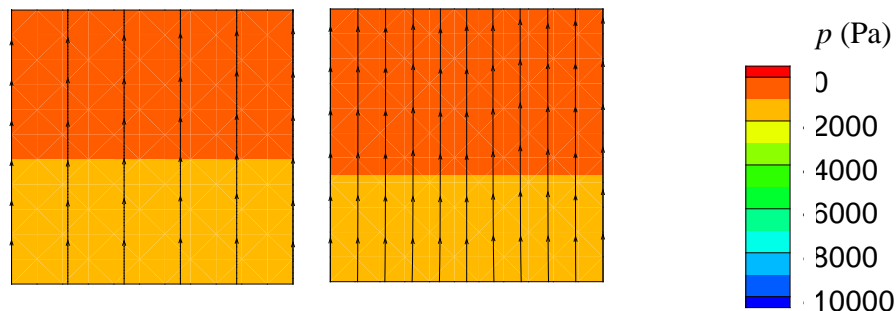
(a) $t = 0.0007$ days



(b) $t = 0.0021$ days



(c) $t = 0.0035$ days



(d) $t = 0.007$ days

(1) without crack

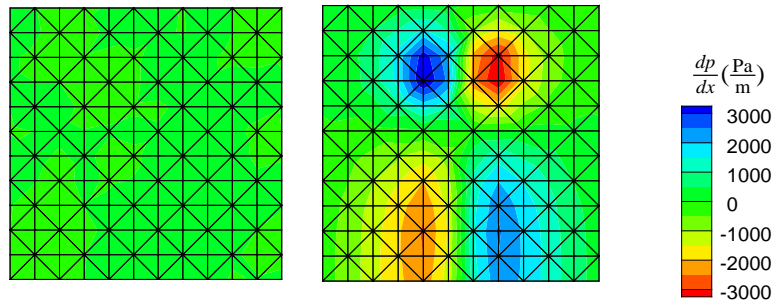
(2) with crack

Figure 6.25. The evolution of the consolidation process for time (a) $t = 0.0007$ days; (b) $t = 0.0021$ days; (c) $t = 0.0035$ days; and (d) $t = 0.007$ days in (1) a continuous saturated porous block and (2) a discontinuous saturated porous block. The arrows are flow lines.

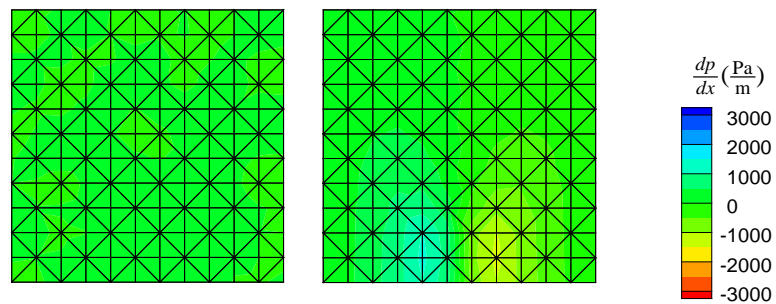
In this example, the dissipation of the excess pore pressure is strongly dependent on the coupling between the flow through the discontinuity and that of the surrounding porous medium. As can be clearly seen in Figure 6.23(a) and Figure 6.25(a), the excess pore pressure initially dissipated faster in the strong discontinuity and its surrounding medium, compared to the identical saturated porous medium without a crack. This is because the crack is initially opened as can be seen from Figure 6.24(a), resulting in a higher permeability in the discontinuity compared to the surrounding porous medium. The opened crack shortens the drainage path, resulting in higher rate of consolidation. However, as the consolidation process proceeds, starting from the upper edge of the soil block where the drainage is allowed, the permeability of the discontinuous medium decreases because of the development of the closure mode in the discontinuity. The closure mode starts from the upper region, where soil consolidates first, and develops downwards, as can be seen in Figure 6.24. The figure shows that the strong discontinuity closes rapidly (in the upper region first and then along the whole length of the discontinuity) and thereafter could not drain the water from the surrounding porous medium. Once the crack is fully closed, the discontinuous media indeed becomes a porous medium with no discontinuity and is therefore consolidated with the same rate as a continuous porous medium. At the early stage of the consolidation, when the crack is partly open, a preferential path for the flow in the lower region of the medium is developed which results in an increase of the water pressure in the upper region of the domain and a decrease of the water pressure in the lower region of the domain, compared to that of a porous medium with no discontinuity, as clearly seen from Figure 6.25(a).

The effect of the discontinuity on the flow path during consolidation can be seen from Figure 6.25. For further clarification, the contours of horizontal (x_1 direction) fluid flux

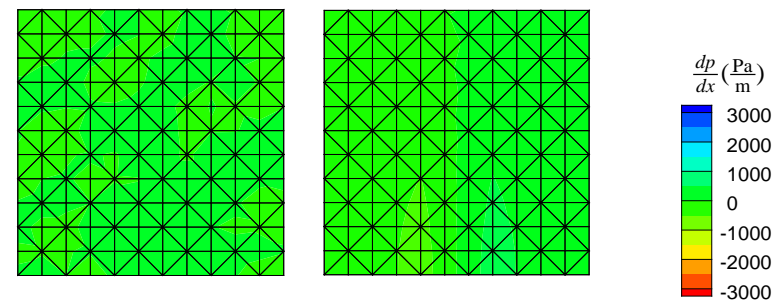
is shown in Figure 6.26 at the four different times used for the previous representation of the numerical results. It is apparent that fluid exchange between the surrounding medium and the crack exists at the early stage of the consolidation process when the crack is still open. The development of the closure mode results in the satisfaction of the fluid continuity condition across the contacting faces of the discontinuity, and thereafter, the medium acts as an intact porous medium without the crack, resulting in zero horizontal flux in the medium.



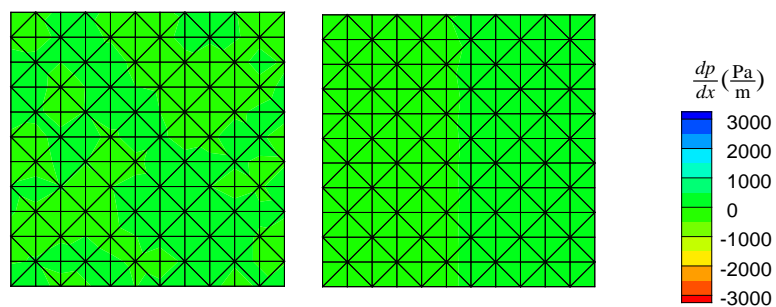
(a) $t = 0.0007$ days



(b) $t = 0.0021$ days;



(c) $t = 0.0035$ days



(d) $t = 0.007$ days

(1) without crack

(2) with crack

Figure 6.26. The variation of the fluid flux in x_1 direction for time (a) $t = 0.0007$ days; (b) $t = 0.0021$ days; (c) $t = 0.0035$ days; and (d) $t = 0.007$ days for the saturated porous medium (1) without crack and (2) with crack.

6.7 Conclusion

A novel mesh-independent methodology was formulated to properly include interfaces such as cracks, material heterogeneities, and shear bands in the coupled formulation of a porous medium. In this formulation, the interfacial geometry (embedded interface) can be located arbitrarily in the domain, irrespective of the underlying discretisation. The influence of the interfaces on the approximation of the variables of interest was considered through the enhancement of the shape functions by physically appropriate enrichment functions.

A proper form of the Divergence theorem was adopted to include the effects of the interfaces, which led to the appearance of additional terms arising from the hydraulic and mechanical couplings between the interface and the surrounding porous medium. A two-scale approach was formulated, in which the representative fluid continuity equation included the presence of fluid flow within the cavity (micro-scale), independent from the fluid flow in the surrounding porous medium (macro-scale). The weak forms of the governing equations were obtained and discretised adopting a cell-based SPIM based on a set of standard and enriched shape functions chosen based on the type of the discontinuity of interest. The *Heaviside* and ridge functions were used as the enrichment functions to represent strong and weak discontinuities, respectively, which observe partition of unity concept.

A frictional contact numerical algorithm with a robust method for inclusion of the closure mode in the pre-existing cracks was developed. The development of the frictional tractions was included through implementation of the penalty method. The resultant global matrix system was obtained which included all the coupling effects. The smoothing gradient technique was adopted for quantification of the property matrixes, removing the need for sub-dividing the supporting domains (elements) cut by the discontinuity for numerical integrations. This results in a marked drop in the number of Gauss points required for the numerical integration compared to methods like XFEM, with no loss of accuracy. A number of numerical examples, including both weak and strong discontinuities under stick-slip and opening and closure modes, were analysed and verified the proposed Enriched SPIM.

7 Conclusions and further work

This thesis was devoted to the development of a numerical SPIM procedure applied to a coupled flow-deformation analysis of saturated media. The contributions and findings made in this thesis are briefly presented in the following sections. Possible future research avenues are also discussed.

There were some research limitations encountered during this research. The most challenging limitation was to handle the large-scale problems because some numerical methods adopted in this study were time-consuming as much more supporting nodes were involved for the approximation of the unknown variables compared to the conventional methods such as FEM. In some cases, it was almost impossible to handle complex large-scale numerical simulations with fine mesh sizes, such as the Noordbergum problem presented in chapter 4, without appealing to the implementation of the advanced algebraic solvers to significantly reduce computational expenses. This was rooted in the increase in the bandwidths of the property matrices and in interrupting the sparsity of the property matrices. Another difficulty was related to the over-softness of the some SPIM stiffness matrices where a numerical analysis approached the collapse state in a nonlinear analysis of porous media under either an undrained condition or the drained condition. This was because of applying smoothing gradient technique to the standard variational formulations, resulting in the reduction in the estimation of the stiffness property compared to those approaches which employ the compatible strain concept. Consequently, the achievement of the convergence near the collapse state needed some careful treatments such as more iterations or smaller time steps needed to attain the accurate collapse loads; otherwise, the analysis would be suddenly terminated

before the realistic collapse state was reached and would result in the underestimation of the collapse load for some numerical methods such as CSR-PIM-T2L or ES-FEM-T3.

7.1 Contributions and findings

7.1.1 Application of cell-based smoothed point interpolation methods in the flow-deformation analysis of saturated porous media

A novel cell-based smoothed point interpolation method for the flow-deformation analysis of saturated porous media was studied in which the primary variables were estimated using PIM shape functions (polynomial PIM or radial PIM). The derivatives of the primary variables were smoothed by applying the smoothing gradient technique. Careful node selection techniques, commonly known as T-schemes, for the creation of shape functions were exploited to ensure the solvability of the algebraic system. Upon introducing different T-schemes, various cell-based SPIM have been created, each of which exhibits discernible superiority compared to conventional numerical methods, such as the FEM and PIM/RPIM. An extensive numerical investigation was performed to compare the performance of the proposed method with its contenders. This included studying a set of benchmark problems with analytical solutions adopting the proposed methods, the FEM and PIM/RPIM.

A comprehensive error analysis performed for each benchmark example showed that the proposed method provides better accuracy in terms of primary variables and energy error norms in comparison with the FEM and PIM/RPIM when considering the flow-deformation analysis of saturated porous media. In terms of primary variables, i.e.

displacement and the excess pore pressure, CSPIM-T4 showed superiority among all the numerical methods studied, with CSRPIIM-T4 being a close second. Theoretically proven higher convergence rates of SPIMs compared to the FEM and PIM/RPIM were confirmed by error analysis of the numerical results.

CSRPIIM-T2L produced the best results in terms of both accuracy and convergence rate of the energy norms. The superior performance of CSRPIIM-T2L can be attributed to the adaptation of higher-order shape functions and a reduced numerical integration given the number of supporting nodes involved in the creation of shape functions, intensifying the softness of the model which often results in a close-to-exact stiffness. The accuracy of CSRPIIM-T2L was, however, highly influenced by the fineness of the background mesh, as the softening effects were considerably hampered when a coarse mesh is used due to a high number of boundary cells (compared to total number of cells), which stiffens the behaviour of the model.

7.1.2 A novel approach for application of smoothed point interpolation methods to axisymmetric problems in poroelasticity

A novel approach was introduced to overcome the singularity problem arises when SPIM is used in an axisymmetric setting, due to the existence of the Gauss points on the axisymmetric axes. To this end, a heuristic decomposition technique was proposed to obtain the property matrices of the discretised form of the coupled flow-deformation equations, in which the submatrix that does not contain derivative of the primary variables is distinguished from those containing differentiation terms. The smoothing operation was then applied only to the submatrices with derivative terms, while the other submatrix was treated in a standard manner using the Gauss integration method

over each smoothing domain. With this approach, the avoidance of the singularity was ensured, while the same level of computational expense was involved, in comparison with the proposed SPIM formulation for plain strain problems. The validity and robustness of the proposed method in axisymmetric coupled problems was investigated through simulation of a set of axisymmetric coupled problems, which included both theoretical and practical problems. The attained numerical results were compared with their corresponding reference solutions. In all cases, the numerical performance of the proposed method exhibited superiority. A proper error analysis in terms of primary variables was performed. It was shown that the proposed method retains the appealing feature of SPIM when adapting to an axisymmetric setting. Among various cell-based SPIM, CSRPIIM-T2L showed slightly better performance in terms of both displacement and excess pore pressure variables, followed closely by CSPIM-T4.

7.1.3 A stabilised, low-order smoothed point interpolation method for numerical analyses in geomechanics

An approach for consistently stabilising SPIM was proposed for both linear and nonlinear numerical analysis in geomechanics. The presented method facilitated the utilisation of equal-order linear interpolations in the context of consistently stabilised *Galerkin* methods in computational geomechanics, which would otherwise result in a sub-optimal convergence rate. The adoption of a smoothing gradient technique together with an unconditionally consistent stabilised method provided a stabilisation parameter-independent method while discretising the field domain with the simplest form of triangulation. The consistency was retained as the smoothing gradient technique removes all derivatives that exists in the standard stabilisation formulation that if

untreated, would incur the elimination of the contributing terms in association with the displacement variable and its test function. The proposed approach was implemented through a simple form of the edge-based SPIM, which is often known as edge-based smoothed finite element method (SFEM). The integrations of the interested quantities over the elements were transformed to those over the edges of the sub-triangles constructed based on the shared boundaries of triangular elements, commonly known as edge-based smoothing domains. The implementation of the smoothing technique in the proposed method requires the attainment of the smoothed strain nodal values from the the smoothed strains over smoothing domains. A novel projection technique was proposed to obtain this by minimising the error in conjunction with the use of smoothed strain nodal values. The proposed method stabilised the solution independent of *a priori* chosen stabilisation parameter, unlike many other consistent stabilised techniques applied in computational geomechanics. The robustness and accuracy of the proposed method were investigated by comparing the attained numerical results with their corresponding reference solutions for several benchmark coupled problems with both linear and nonlinear constitutive models. It was also shown that the stabilisation parameter is a purely spatial parameter with the objective of providing sufficient coercivity to the weak form of the governing equations, and therefore should be independent form the time step. The simplest form of the stabilisation method was used in this study and successfully tuned the required amount of weighting function to ensure the fulfilment of the inf-sup condition. It was shown that complex forms of stabilisation parameter are unnecessary and can be avoided if the weighting functions associated with the displacement variable are considered in the added stabilisation terms.

7.1.4 An enriched smoothed point interpolation method for flow-deformation analysis of saturated porous media with embedded interfaces

A novel mesh-independent methodology was formulated to properly include interfaces such as cracks, material heterogeneities and shear bands in the analysis of porous medium. In this formulation, the interfacial geometry can be arbitrary located, irrespective of the underlying discretisation. To include the effect of interfaces, the shape functions were enhanced by the physically reasonable enrichment functions. A proper form of the Divergence theorem was adopted to represent the interfaces, which led to the appearance of the additional terms arising from the hydro-mechanical couplings between the interface and the surrounding porous medium. The representative fluid continuity equation was successfully formulated to quantify the coupling between an interface and the surrounding porous bulk. The weak forms were discretised using SPIM with a set of standard and enriched shape functions which are chosen based on the type of the discontinuity of interest. The *Heaviside* and ridge functions were used as the enrichment functions to represent strong and weak discontinuities, respectively, which uphold the partition of unity condition, similar to the FEM shape functions. A frictional contact numerical algorithm was adopted to provide a robust mean for inclusion of the closure mode of discontinuities. The frictional tractions were included in the formulation through implementation of the penalty method applied to both solid and fluid phases. The smoothing gradient technique was applied to all relevant contributing matrices, which, unlike XFEM, removes the need for sub-dividing the supporting domains (elements) hosting discontinuity for the evaluation of the numerical integrations. It was shown that when smoothing gradient technique is adopted, the number of Gauss points required for numerical integrations of the matrices of a discontinuous medium increases only slightly compared to those of a continuous

medium due to the use of the same Gauss points for the numerical integration of the property matrices and the frictional contact tractions, as well as the elimination of sub-partitioning commonly used in XFEM. A number of numerical examples, including both weak discontinuity and strong discontinuity under stick-slip and opening and closure modes, were analysed and confirmed the efficiency of the proposed Enriched SPIM.

7.2 Future research

In line with the studies presented in this thesis, future research work can be carried out in the following areas:

- ❖ A comprehensive assessment of the stabilisation techniques proposed in computational geomechanics. Various stabilisations techniques have been proposed to apply to different geotechnical problems routinely encountered in practice. According to the literature, they perform differently under various circumstances. As an example, pressure projection method proposed in [52] fails to recover the excess pore pressure response near drainage boundary at early stage of the consolidation process. In addition, the ability of the pressure projection method to efficiently capture the failure condition is still undetermined. An extensive comparison study would be desirable to investigate all well-established stabilisation techniques applied to various problems, such as the analysis of shear bands, stability of vertical cut, hydraulic fracturing, etc. For each stabilisation approach, a set of sensitivity analysis with respect to the quality of the variables of interest can be performed as the stabilisation

parameter varies to specify the robustness of the proposed method and to obtain proper bounds for the stabilisation parameters.

- ❖ Development of the proposed Enriched SPIM methods towards crack propagation problems. The majority of the problems with the cracks necessitate a proper criterion to take into account the possible crack propagation in an arbitrary direction which may change during time. The complexities associated with the application of the FEM to crack propagation problems, such as a need for successive remeshing and subsequent data transfer that deteriorates the quality of the numerical results, leave room for the efficient use of a mesh-independent Enriched SPIM to benefit from desirable features of both the smoothing gradient technique and the mathematically implicit representation of interfaces through employing enrichment functions. Applying Enriched SPIM delivers unique benefits for crack propagation problems, such as the elimination of sub-partitioning which is quite time-consuming in XFEM.

- ❖ Implementation of the Lagrange multiplier method to impose the contact constraint. The efficiency of the penalty method presented in this thesis hinges on the proper selection of the stiffness value assigned to both horizontal and tangential directions, which would otherwise lead to an ill-conditioned resultant matrix if too-high values are assigned. However, the Lagrange multiplier approach eliminates the necessity of *a priori* specified stiffness values, as it satisfies the contact condition exactly by introducing additional unknown variables which present the contact fluxes. Any Lagrange multiplier implementation must be formulated in such a way to satisfy the inf-sup

condition, which would restrict using the same spaces for additional variables and primary variables.

- ❖ An extension towards assuming independent pressure degrees of freedom across a strong discontinuity in the flow-deformation analysis of fractured porous media. The simplified assumption regarding the pressure continuity between the strong discontinuity faces arises from the equilibrium assumption hold between the cavity and the surrounding porous medium. The relaxation of the equilibrium assumption at the faces of the cavity can be made by assigning different pressure degrees of freedom, which is more realistic when a low-permeable cavity is considered [212, 262]. The drop of this assumption in Enriched SPIM proposed in this thesis results in a more comprehensive formulation which would be well-settled in hydraulic fracturing analysis.
- ❖ An extension toward three-dimensional settings. It is evident that all proposed methods in this study are limited to two-dimensional setting. To apply the proposed methods to three-dimensional settings, the strain-displacement matrix should include additional rows that represent the deformation along another axis. The derivation of the formulation could then be straightforward; however, including discontinuity is not a trivial task because enriching the proposed method in three-dimensional settings would encounter some difficulties, including the implementation of the level-set method and representing the curve discontinuities in three-dimensional settings. These difficulties have been reported frequently in relation to the application of XFEM in three-dimensional setting. Consequently, it is recommended that more advanced techniques be

developed to represent discontinuities by adjusting the potential function, including the phase field, of the SPIM.

References

- [1] Jardine R, Potts D, Fourie A, Burland J. Studies of the influence of non-linear stress-strain characteristics in soil-structure interaction. *Geotechnique*. 1986;36(3):377-96.
- [2] Potts DM, Zdravkovic L, Zdravković L. *Finite element analysis in geotechnical engineering: application*: Thomas Telford, 2001.
- [3] Meroi E, Schrefler B, Zienkiewicz O. Large strain static and dynamic semisaturated soil behaviour. *International Journal for Numerical and Analytical Methods in Geomechanics*. 1995;19(2):81-106.
- [4] Zienkiewicz OC, Taylor RL. *The finite element method: Solid mechanics*: Butterworth-Heinemann, 2000.
- [5] Belytschko T, Krongauz Y, Organ D, Fleming M, Krysl P. Meshless methods: an overview and recent developments. *Computer methods in applied mechanics and engineering*. 1996;139(1):3-47.
- [6] Fries T-P, Matthies HG. *Classification and overview of meshfree methods*. Department of Mathematics and Computer Science, Technical University of Braunschweig. 2003.
- [7] Kumar RP, Dodagoudar G. Two-dimensional modelling of contaminant transport through saturated porous media using the radial point interpolation method (RPIM). *Hydrogeology Journal*. 2008;16(8):1497-505.
- [8] Zhuang X, Augarde C, Mathisen K. Fracture modeling using meshless methods and level sets in 3D: framework and modeling. *International Journal for Numerical Methods in Engineering*. 2012;92(11):969-98.
- [9] Samimi S, Pak A. Three-dimensional simulation of fully coupled hydro-mechanical behavior of saturated porous media using Element Free Galerkin (EFG) method. *Computers and Geotechnics*. 2012;46(75-83).
- [10] Bui H, Fukagawa R, Sato K. Smoothed particle hydrodynamics for soil mechanics. *proceedings of Numerical Methods in Geotechnical Engineering, Graz*. 2006:275-81.
- [11] Bui H, Fukagawa R, Sako K, Wells J. Slope stability analysis and discontinuous slope failure simulation by elasto-plastic smoothed particle hydrodynamics (SPH). *Géotechnique*. 2011;61(7):565-74.
- [12] Belytschko T, Lu YY, Gu L. Element-free Galerkin methods. *International journal for numerical methods in engineering*. 1994;37(2):229-56.
- [13] Liu G. AG space theory and a weakened weak (W2) form for a unified formulation of compatible and incompatible methods: Part I theory. *International Journal for Numerical Methods in Engineering*. 2010;81(9):1093-126.
- [14] Liu G. AG space theory and a weakened weak (W 2) form for a unified formulation of compatible and incompatible methods: Part II applications to solid mechanics problems. *International journal for numerical methods in engineering*. 2010;81(9):1127.
- [15] Liu G, Zhang G. Upper bound solution to elasticity problems: A unique property of the linearly conforming point interpolation method (LC-PIM). *International Journal for Numerical Methods in Engineering*. 2008;74(7):1128-61.
- [16] Liu G, Zhang G. Edge-based smoothed point interpolation methods. *International Journal of Computational Methods*. 2008;5(04):621-46.
- [17] Liu G, Chen L, Nguyen-Thoi T, Zeng K, Zhang G. A novel singular node-based smoothed finite element method (NS-FEM) for upper bound solutions of fracture problems. *International Journal for Numerical Methods in Engineering*. 2010;83(11):1466-97.

- [18] Zhang G, Liu G, Nguyen T, Song C, Han X, Zhong Z, et al. The upper bound property for solid mechanics of the linearly conforming radial point interpolation method (LC-RPIM). *International Journal of Computational Methods*. 2007;4(03):521-41.
- [19] Chen L, Nguyen-Xuan H, Nguyen-Thoi T, Zeng K, Wu S. Assessment of smoothed point interpolation methods for elastic mechanics. *International Journal for Numerical Methods in Biomedical Engineering*. 2010;26(12):1635-55.
- [20] Liu G, Zhang G. A normed G space and weakened weak (W2) formulation of a cell-based smoothed point interpolation method. *International Journal of Computational Methods*. 2009;6(01):147-79.
- [21] Cui X, Feng S, Li G. A cell-based smoothed radial point interpolation method (CS-RPIM) for heat transfer analysis. *Engineering Analysis with Boundary Elements*. 2014;40(147-53).
- [22] Cui X, Liu G, Li G. A cell-based smoothed radial point interpolation method (CS-RPIM) for static and free vibration of solids. *Engineering analysis with boundary elements*. 2010;34(2):144-57.
- [23] Cui X, Liu G, Li G. A smoothed Hermite radial point interpolation method for thin plate analysis. *Archive of Applied Mechanics*. 2011;81(1):1-18.
- [24] Cui X, Liu G, Li G. Analysis of Mindlin–Reissner plates using cell-based smoothed radial point interpolation method. *International Journal of Applied Mechanics*. 2010;2(03):653-80.
- [25] Liu G, Jiang Y, Chen L, Zhang G, Zhang Y. A singular cell-based smoothed radial point interpolation method for fracture problems. *Computers & Structures*. 2011;89(13):1378-96.
- [26] Liu G, Wang Z, Zhang G, Zong Z, Wang S. An edge-based smoothed point interpolation method for material discontinuity. *Mechanics of Advanced Materials and Structures*. 2012;19(1-3):3-17.
- [27] Liu G, Zhang G, Zong Z, Li M. Meshfree cell-based smoothed alpha radial point interpolation method (CS- α RPIM) for solid mechanics problems. *International Journal of Computational Methods*. 2013;10(04):1350020.
- [28] Tang Q, Zhang G, Liu G, Zhong Z, He Z. An efficient adaptive analysis procedure using the edge-based smoothed point interpolation method (ES-PIM) for 2D and 3D problems. *Engineering Analysis with Boundary Elements*. 2012;36(9):1424-43.
- [29] Wu S, Liu G, Cui X, Nguyen T, Zhang G. An edge-based smoothed point interpolation method (ES-PIM) for heat transfer analysis of rapid manufacturing system. *International Journal of Heat and Mass Transfer*. 2010;53(9):1938-50.
- [30] Wu S, Liu G, Zhang H, Zhang G. A node-based smoothed point interpolation method (NS-PIM) for thermoelastic problems with solution bounds. *International Journal of Heat and Mass Transfer*. 2009;52(5-6):1464-71.
- [31] Xu X, Liu G-R, Gu Y. A novel quadratic edge-based smoothed conforming point interpolation method (ES-CPIM) for elasticity problems. *International Journal of Computational Methods*. 2012;9(02):1240033.
- [32] Yao L, Li Y, Li L. A Cell-Based Smoothed Radial Point Interpolation—Perfectly Matched Layer Method For Two-Dimensional Acoustic Radiation Problems. *Journal of Pressure Vessel Technology*. 2016;138(2):021301.
- [33] Zhang G, Liu G. Meshfree cell-based smoothed point interpolation method using isoparametric PIM shape functions and condensed RPIM shape functions. *International Journal of Computational Methods*. 2011;8(04):705-30.

- [34] Soares D. Iterative dynamic analysis of linear and nonlinear fully saturated porous media considering edge-based smoothed meshfree techniques. *Computer Methods in Applied Mechanics and Engineering*. 2013;253(73-88).
- [35] Soares Jr D. Dynamic elastoplastic analyses by smoothed point interpolation methods. *International Journal of Computational Methods*. 2013;10(05):1350030.
- [36] Preisig M, Prévost JH. Stabilization procedures in coupled poromechanics problems: A critical assessment. *International Journal for Numerical and Analytical Methods in Geomechanics*. 2011;35(11):1207-25.
- [37] Pastor M, Li T, Liu X, Zienkiewicz O, Quecedo M. A fractional step algorithm allowing equal order of interpolation for coupled analysis of saturated soil problems. *Mechanics of Cohesive-frictional Materials*. 2000;5(7):511-34.
- [38] Brezzi F. On the existence, uniqueness and approximation of saddle-point problems arising from Lagrangian multipliers. *Revue française d'automatique, informatique, recherche opérationnelle Analyse numérique*. 1974;8(R2):129-51.
- [39] Arnold DN. Mixed finite element methods for elliptic problems. *Computer Methods in Applied Mechanics and Engineering*. 1990;82(1-3):281-300.
- [40] Arnold DN, Brezzi F, Fortin M. A stable finite element for the Stokes equations. *Calcolo*. 1984;21(4):337-44.
- [41] Brezzi F, Douglas J. Stabilized mixed methods for the Stokes problem. *Numerische Mathematik*. 1988;53(1):225-35.
- [42] Brezzi F, Fortin M. A minimal stabilisation procedure for mixed finite element methods. *Numerische Mathematik*. 2001;89(3):457-91.
- [43] Brezzi F, Hughes TJ, Marini LD, Masud A. Mixed discontinuous Galerkin methods for Darcy flow. *Journal of Scientific Computing*. 2005;22(1):119-45.
- [44] Brezzi F, Pitkäranta J. On the stabilization of finite element approximations of the Stokes equations. *Efficient solutions of elliptic systems*: Springer, 1984. p. 11-9.
- [45] Hughes T, Franca L. A new finite element formulation for CFD: VI The I Stokes problem with various well-posed boundary conditions: Symmetric formulations that converge for all velocity/pressure spaces. *Comput Methods Appl Mech Engng*. 1987;65(85-97).
- [46] Hughes TJ, Franca LP, Balestra M. A new finite element formulation for computational fluid dynamics: V. Circumventing the Babuška-Brezzi condition: a stable Petrov-Galerkin formulation of the Stokes problem accommodating equal-order interpolations. *Computer Methods in Applied Mechanics and Engineering*. 1986;59(1):85-99.
- [47] Hughes TJ, Franca LP, Hulbert GM. A new finite element formulation for computational fluid dynamics: VIII. The Galerkin/least-squares method for advective-diffusive equations. *Computer Methods in Applied Mechanics and Engineering*. 1989;73(2):173-89.
- [48] Hughes TJ, Masud A, Wan J. A stabilized mixed discontinuous Galerkin method for Darcy flow. *Computer Methods in Applied Mechanics and Engineering*. 2006;195(25):3347-81.
- [49] Commend S. Stabilized finite elements in geomechanics. 2001.
- [50] Commend S, Truty A, Zimmermann T. Stabilized finite elements applied to elastoplasticity: I. Mixed displacement–pressure formulation. *Computer methods in applied mechanics and engineering*. 2004;193(33):3559-86.
- [51] Truty A, Zimmermann T. Stabilized mixed finite element formulations for materially nonlinear partially saturated two-phase media. *Computer methods in applied mechanics and engineering*. 2006;195(13):1517-46.

- [52] White JA, Borja RI. Stabilized low-order finite elements for coupled solid-deformation/fluid-diffusion and their application to fault zone transients. *Computer Methods in Applied Mechanics and Engineering*. 2008;197(49):4353-66.
- [53] Barth T, Bochev P, Gunzburger M, Shadid J. A taxonomy of consistently stabilized finite element methods for the Stokes problem. *SIAM Journal on Scientific Computing*. 2004;25(5):1585-607.
- [54] Khoei A, Azami A, Haeri S. Implementation of plasticity based models in dynamic analysis of earth and rockfill dams: A comparison of Pastor–Zienkiewicz and cap models. *Computers and Geotechnics*. 2004;31(5):384-409.
- [55] Pastor M, Zienkiewicz O, Li T, Xiaoqing L, Huang M. Stabilized finite elements with equal order of interpolation for soil dynamics problems. *Archives of Computational Methods in Engineering*. 1999;6(1):3.
- [56] Zienkiewicz O, Chang C, Bettess P. Drained, undrained, consolidating and dynamic behaviour assumptions in soils. *Geotechnique*. 1980;30(4):385-95.
- [57] Zienkiewicz O, Shiomi T. Dynamic behaviour of saturated porous media; the generalized Biot formulation and its numerical solution. *International journal for numerical and analytical methods in geomechanics*. 1984;8(1):71-96.
- [58] Jansen KE, Collis SS, Whiting C, Shaki F. A better consistency for low-order stabilized finite element methods. *Computer Methods in Applied Mechanics and Engineering*. 1999;174(1-2):153-70.
- [59] Melenk JM, Babuška I. The partition of unity finite element method: basic theory and applications. *Computer methods in applied mechanics and engineering*. 1996;139(1):289-314.
- [60] Khoei A, Barani O, Mofid M. Modeling of dynamic cohesive fracture propagation in porous saturated media. *International Journal for Numerical and Analytical Methods in Geomechanics*. 2011;35(10):1160-84.
- [61] Khoei A, Haghighat E. Extended finite element modeling of deformable porous media with arbitrary interfaces. *Applied Mathematical Modelling*. 2011;35(11):5426-41.
- [62] Khoei A, Hirmand M, Vahab M, Bazargan M. An enriched FEM technique for modeling hydraulically driven cohesive fracture propagation in impermeable media with frictional natural faults: Numerical and experimental investigations. *International Journal for Numerical Methods in Engineering*. 2015;104(6):439-68.
- [63] Khoei A, Hosseini N, Mohammadnejad T. Numerical modeling of two-phase fluid flow in deformable fractured porous media using the extended finite element method and an equivalent continuum model. *Advances in water resources*. 2016;94(5):10-28.
- [64] Khoei A, Moallemi S, Haghighat E. Thermo-hydro-mechanical modeling of impermeable discontinuity in saturated porous media with X-FEM technique. *Engineering Fracture Mechanics*. 2012;96(7):1-23.
- [65] Khoei A, Vahab M. A numerical contact algorithm in saturated porous media with the extended finite element method. *Computational Mechanics*. 2014;54(5):1089-110.
- [66] Khoei A, Vahab M, Haghighat E, Moallemi S. A mesh-independent finite element formulation for modeling crack growth in saturated porous media based on an enriched-FEM technique. *International Journal of Fracture*. 2014;188(1):79-108.
- [67] Khoei A, Vahab M, Hirmand M. An enriched–FEM technique for numerical simulation of interacting discontinuities in naturally fractured porous media. *Computer Methods in Applied Mechanics and Engineering*. 2018;331(1):197-231.
- [68] Irzal F, Remmers JJ, Huyghe JM, de Borst R. A large deformation formulation for fluid flow in a progressively fracturing porous material. *Computer Methods in Applied Mechanics and Engineering*. 2013;256(29):37.

- [69] Rethore J, Borst Rd, Abellan MA. A two-scale approach for fluid flow in fractured porous media. *International Journal for Numerical Methods in Engineering*. 2007;71(7):780-800.
- [70] Goudarzi M, Mohammadi S. Weak discontinuity in porous media: an enriched EFG method for fully coupled layered porous media. *International Journal for Numerical and Analytical Methods in Geomechanics*. 2014.
- [71] Goudarzi M, Mohammadi S. Analysis of cohesive cracking in saturated porous media using an extrinsically enriched EFG method. *Computers and Geotechnics*. 2015;63(183-98).
- [72] Wriggers P, Laursen TA. *Computational contact mechanics*: Springer, 2006.
- [73] Khoshghalb A. *Meshfree analysis of unsaturated porous media including hydraulic hysteresis and large deformations*: The University of New South Wales Sydney, Australia, 2011.
- [74] Lucy LB. A numerical approach to the testing of the fission hypothesis. *The astronomical journal*. 1977;82(1013-24).
- [75] Gingold RA, Monaghan JJ. Smoothed particle hydrodynamics: theory and application to non-spherical stars. *Monthly notices of the royal astronomical society*. 1977;181(3):375-89.
- [76] Libersky LD, Petschek AG, Carney TC, Hipp JR, Allahdadi FA. High strain Lagrangian hydrodynamics: a three-dimensional SPH code for dynamic material response. *Journal of computational physics*. 1993;109(1):67-75.
- [77] Liu WK, Jun S, Zhang YF. Reproducing kernel particle methods. *International journal for numerical methods in fluids*. 1995;20(8-9):1081-106.
- [78] Duarte CA, Oden JT. Hp clouds-an hp meshless method. *Numerical methods for partial differential equations*. 1996;12(6):673-706.
- [79] Atluri S, Zhu T. A new meshless local Petrov-Galerkin (MLPG) approach in computational mechanics. *Computational mechanics*. 1998;22(2):117-27.
- [80] Liu G-R, Gu Y-T. *An introduction to meshfree methods and their programming*: Springer, 2005.
- [81] Lancaster P, Salkauskas K. Surfaces generated by moving least squares methods. *Mathematics of computation*. 1981;37(155):141-58.
- [82] Taylor R, Simo J, Zienkiewicz O, Chan A. The patch test—a condition for assessing FEM convergence. *International journal for numerical methods in engineering*. 1986;22(1):39-62.
- [83] Blanc T, Pastor M. A stabilized fractional step, Runge–Kutta Taylor SPH algorithm for coupled problems in geomechanics. *Computer Methods in Applied Mechanics and Engineering*. 2012;221(41-53).
- [84] Nguyen-Thanh N, Rabczuk T, Nguyen-Xuan H, Bordas SP. A smoothed finite element method for shell analysis. *Computer Methods in Applied Mechanics and Engineering*. 2008;198(2):165-77.
- [85] Dolbow J, Belytschko T. Numerical integration of the Galerkin weak form in meshfree methods. *Computational mechanics*. 1999;23(3):219-30.
- [86] Liu G-R. *Meshfree methods: moving beyond the finite element method*: CRC press, 2010.
- [87] Liu G-R, Gu Y. A point interpolation method for two-dimensional solids. *International Journal for Numerical Methods in Engineering*. 2001;50(4):937-51.
- [88] Wang J, Liu G. A point interpolation meshless method based on radial basis functions. *International Journal for Numerical Methods in Engineering*. 2002;54(11):1623-48.

- [89] Liu G. On G space theory. *International Journal of Computational Methods*. 2009;6(02):257-89.
- [90] Liu G-R, Zhang G-Y. Smoothed point interpolation methods: G space theory and weakened weakforms2013.
- [91] Liu G, Dai K, Nguyen T. A smoothed finite element method for mechanics problems. *Computational Mechanics*. 2007;39(6):859-77.
- [92] Liu G, Nguyen T, Dai K, Lam K. Theoretical aspects of the smoothed finite element method (SFEM). *International journal for numerical methods in Engineering*. 2007;71(8):902-30.
- [93] Chen J-S, Wu C-T, Yoon S, You Y. A stabilized conforming nodal integration for Galerkin mesh-free methods. *International Journal for Numerical Methods in Engineering*. 2001;50(2):435-66.
- [94] Liu G, Nguyen-Thoi T, Lam K. An edge-based smoothed finite element method (ES-FEM) for static, free and forced vibration analyses of solids. *Journal of Sound and Vibration*. 2009;320(4):1100-30.
- [95] Liu G, Nguyen-Thoi T, Nguyen-Xuan H, Lam K. A node-based smoothed finite element method (NS-FEM) for upper bound solutions to solid mechanics problems. *Computers & structures*. 2009;87(1):14-26.
- [96] Nguyen-Xuan H, Bordas S, Nguyen-Dang H. Smooth finite element methods: convergence, accuracy and properties. *International Journal for Numerical Methods in Engineering*. 2008;74(2):175-208.
- [97] Cui X, Liu G, Li G, Zhao X, Nguyen-Thoi T, Sun G. A smoothed finite element method (SFEM) for linear and geometrically nonlinear analysis of plates and shells. *Comput Model Eng Sci*. 2008;28(2):109-25.
- [98] Nguyen-Thoi T, Liu G, Lam K, Zhang G. A face-based smoothed finite element method (FS-FEM) for 3D linear and geometrically non-linear solid mechanics problems using 4-node tetrahedral elements. *International Journal for Numerical Methods in Engineering*. 2009;78(3):324-53.
- [99] Nguyen-Xuan H, Nguyen-Thoi T. A stabilized smoothed finite element method for free vibration analysis of Mindlin–Reissner plates. *Communications in Numerical Methods in Engineering*. 2009;25(8):882-906.
- [100] Nguyen-Xuan H, Rabczuk T, Bordas S, Debonnie J-F. A smoothed finite element method for plate analysis. *Computer Methods in Applied Mechanics and Engineering*. 2008;197(13):1184-203.
- [101] Liu G, Zhang G, Dai K, Wang Y, Zhong Z, Li G, et al. A linearly conforming point interpolation method (LC-PIM) for 2D solid mechanics problems. *International Journal of Computational Methods*. 2005;2(04):645-65.
- [102] Liu G, Li Y, Dai K, Luan M, Xue W. A linearly conforming radial point interpolation method for solid mechanics problems. *International Journal of Computational Methods*. 2006;3(04):401-28.
- [103] Wang S, Liu G, Zhang G, Chen L. Design of asymmetric gear and accurate bending stress analysis using the ES-PIM with triangular mesh. *International Journal of Computational Methods*. 2011;8(04):759-72.
- [104] Soares Jr D. Time-domain electromagnetic wave propagation analysis by edge-based smoothed point interpolation methods. *Journal of Computational Physics*. 2013;234(472-86).
- [105] Cheng J, Liu G, Li T-C, Wu S-C, Zhang G-Y. ES-PIM with cell death and birth technique for simulating heat transfer in concrete dam construction process. *Journal of Engineering Mechanics*. 2011;138(1):133-42.

- [106] Modaressi H, Aubert P. Coupled FEM-EFGM for consolidation modelling. *Numerical Models in Geomechanics*. 1995:417-22.
- [107] Murakami A, Kawabata H, Aoyama S. EFGM analysis for saturated soil. *Computer methods and advances in geomechanics*. 2000;1(153-6).
- [108] Oliaei M, Pak A. Element Free Galerkin Mesh-Less Method for Fully Coupled Analysis of a Consolidation Process. *Scientia Iranica, Transaction A*. 2009;16(1):65-77.
- [109] Oliaei MN, Soga K, Pak A. Some numerical issues using element-free Galerkin mesh-less method for coupled hydro-mechanical problems. *International journal for numerical and analytical methods in geomechanics*. 2009;33(7):915-38.
- [110] Samimi S, Pak A. A novel three-dimensional element free Galerkin (EFG) code for simulating two-phase fluid flow in porous materials. *Engineering Analysis with Boundary Elements*. 2014;39(53-63).
- [111] Sheu G. Characterizing soil properties by the meshless local Petrov-Galerkin method. *Geotechnical and Geological Engineering*. 2007;25(4):473-86.
- [112] Soares D, Sladek V, Sladek J. Modified meshless local Petrov-Galerkin formulations for elastodynamics. *International Journal for Numerical Methods in Engineering*. 2012;90(12):1508-828.
- [113] Soares Jr D. Dynamic Analysis of Porous Media Considering Unequal Phase Discretization by Meshless Local Petrov-Galerkin Formulations. *Computer Modeling in Engineering & Sciences(CMES)*. 2010;61(2):177-200.
- [114] Abe K, Nakamura S, Nakamura H, Shiomi K. Numerical study on dynamic behavior of slope models including weak layers from deformation to failure using material point method. *Soils and Foundations*. 2017;57(2):155-75.
- [115] Bhandari T, Hamad F, Moormann C, Sharma K, Westrich B. Numerical modelling of seismic slope failure using MPM. *Computers and Geotechnics*. 2016;75(126-34).
- [116] Coetzee C, Vermeer P, Basson A. The modelling of anchors using the material point method. *International journal for numerical and analytical methods in geomechanics*. 2005;29(9):879-95.
- [117] Bandara S, Soga K. Coupling of soil deformation and pore fluid flow using material point method. *Computers and Geotechnics*. 2015;63(199-214).
- [118] Bardenhagen S, Brackbill J, Sulsky D. The material-point method for granular materials. *Computer methods in applied mechanics and engineering*. 2000;187(3-4):529-41.
- [119] Jassim I, Stolle D, Vermeer P. Two-phase dynamic analysis by material point method. *International journal for numerical and analytical methods in geomechanics*. 2013;37(15):2502-22.
- [120] Soga K, Alonso E, Yerro A, Kumar K, Bandara S. Trends in large-deformation analysis of landslide mass movements with particular emphasis on the material point method. *Géotechnique*. 2015;66(3):248-73.
- [121] Ceccato F, Beuth L, Simonini P. Analysis of piezocone penetration under different drainage conditions with the two-phase material point method. *Journal of Geotechnical and Geoenvironmental Engineering*. 2016;142(12):04016066.
- [122] Cundall PA, Strack OD. A discrete numerical model for granular assemblies. *geotechnique*. 1979;29(1):47-65.
- [123] Gabrieli F, Cola S, Calvetti F. Use of an up-scaled DEM model for analysing the behaviour of a shallow foundation on a model slope. *Geomechanics and Geoengineering: An International Journal*. 2009;4(2):109-22.

- [124] Jiang M, Yin Z-Y. Analysis of stress redistribution in soil and earth pressure on tunnel lining using the discrete element method. *Tunnelling and Underground Space Technology*. 2012;32(251-9).
- [125] Lim KW, Andrade JE. Granular element method for three-dimensional discrete element calculations. *International Journal for Numerical and Analytical Methods in Geomechanics*. 2014;38(2):167-88.
- [126] Jefferies A, Kuhnert J, Aschenbrenner L, Giffhorn U. Finite pointset method for the simulation of a vehicle travelling through a body of water. *Meshfree Methods for Partial Differential Equations VII*: Springer, 2015. p. 205-21.
- [127] Kuhnert J, Ostermann I. The finite pointset method (FPM) and an application in soil mechanics. *Mathematics of Planet Earth*: Springer, 2014. p. 815-8.
- [128] Michel I, Kuhnert J, Kolymbas D. Meshfree simulation of avalanches with the Finite Pointset Method (FPM). *EGU General Assembly Conference Abstracts2017*. p. 13203.
- [129] Uhlmann E, Gerstenberger R, Kuhnert J. Cutting simulation with the meshfree finite pointset method. *Procedia CIRP*. 2013;8(391-6).
- [130] Blanc T, Pastor M. Numerical simulation of debris flows with the 2D-SPH depth integrated model. *EGU General Assembly Conference Abstracts2009*. p. 1978.
- [131] Bui HH, Fukagawa R. An improved SPH method for saturated soils and its application to investigate the mechanisms of embankment failure: Case of hydrostatic pore-water pressure. *International Journal for Numerical and Analytical Methods in Geomechanics*. 2013;37(1):31-50.
- [132] Bui H, Kodikara J, Pathegama R, Bouazza A, Haque A. Large deformation and post-failure simulations of segmental retaining walls using mesh-free method (SPH). *arXiv preprint arXiv:150104000*. 2015.
- [133] Peng C, Wu W, Yu H-s, Wang C. A SPH approach for large deformation analysis with hypoplastic constitutive model. *Acta Geotechnica*. 2015;10(6):703-17.
- [134] Holmes DW, Williams JR, Tilke P, Leonardi CR. Characterizing flow in oil reservoir rock using SPH: absolute permeability. *Computational Particle Mechanics*. 2016;3(2):141-54.
- [135] Hu M, Liu M, Xie M, Liu G. Three-dimensional run-out analysis and prediction of flow-like landslides using smoothed particle hydrodynamics. *Environmental Earth Sciences*. 2015;73(4):1629-40.
- [136] Komoróczy A, Abe S, Urai JL. Meshless numerical modeling of brittle–viscous deformation: first results on boudinage and hydrofracturing using a coupling of discrete element method (DEM) and smoothed particle hydrodynamics (SPH). *Computational Geosciences*. 2013;17(2):373-90.
- [137] Carbonell JM, Oñate E, Suárez B. Modelling of tunnelling processes and rock cutting tool wear with the particle finite element method. *Computational Mechanics*. 2013;52(3):607-29.
- [138] Oñate E, Idelsohn SR, Celigueta MA, Rossi R, Marti J, Carbonell J, et al. Advances in the particle finite element method (PFEM) for solving coupled problems in engineering. *Particle-Based Methods*: Springer, 2011. p. 1-49.
- [139] Wang J, Liu G, Wu Y. A point interpolation method for simulating dissipation process of consolidation. *Computer Methods in Applied Mechanics and Engineering*. 2001;190(45):5907-22.
- [140] Wang J, Liu G, Lin P. Numerical analysis of Biot's consolidation process by radial point interpolation method. *International Journal of Solids and Structures*. 2002;39(6):1557-73.

- [141] Wang W, Wang J, Wang Z, Nogami T. An unequal-order radial interpolation meshless method for Biot's consolidation theory. *Computers and Geotechnics*. 2007;34(2):61-70.
- [142] Khoshghalb A, Khalili N. A stable meshfree method for fully coupled flow-deformation analysis of saturated porous media. *Computers and Geotechnics*. 2010;37(6):789-95.
- [143] Khoshghalb A, Khalili N, Selvadurai A. A three-point time discretization technique for parabolic partial differential equations. *International Journal for Numerical and Analytical Methods in Geomechanics*. 2011;35(3):406-18.
- [144] Khoshghalb A, Khalili N. A meshfree method for fully coupled analysis of flow and deformation in unsaturated porous media. *International Journal for Numerical and Analytical Methods in Geomechanics*. 2013;37(7):716-43.
- [145] Khoshghalb A, Khalili N. An alternative approach for quasi-static large deformation analysis of saturated porous media using meshfree method. *International Journal for Numerical and Analytical Methods in Geomechanics*. 2015.
- [146] Wang J, Zhang B, Nogami T. Wave-induced seabed response analysis by radial point interpolation meshless method. *Ocean Engineering*. 2004;31(1):21-42.
- [147] Wang J, Nogami T, Dasari G, Lin P. A weak coupling algorithm for seabed-wave interaction analysis. *Computer methods in applied mechanics and engineering*. 2004;193(36-38):3935-56.
- [148] Ghaffaripour O, Khoshghalb A, Khalili N. An edge-based smoothed point interpolation method for elasto-plastic coupled hydro-mechanical analysis of saturated porous media. *Computers and Geotechnics*. 2017;82(99-109).
- [149] Chen C-H. Development of Soft Particle Code (SPARC): Logos Verlag Berlin GmbH, 2015.
- [150] Schneider-Muntau B, Chen C-H, Bathaeian SI. Simulation of shear bands with Soft PARTicle Code (SPARC) and FE. *GEM-International Journal on Geomathematics*. 2017;8(1):135-51.
- [151] Ullah Z, Augarde C. Solution of elasto-statics problems using the element-free galerkin method with local maximum entropy shape functions. 2010.
- [152] Ullah Z, Augarde CE, Crouch RS, Coombs WM. FE-EFGM coupling using maximum entropy shape functions and its application to small and finite deformation. 19th UK Conference of the Association for Computational Mechanics in Engineering (ACME), Heriot-Watt University, Edinburgh, UK2011. p. 277-80.
- [153] Ullah Z, Augarde C, Coombs W. Local maximum entropy shape functions based FE-EFGM coupling. 2013.
- [154] Kardani O, Nazem M, Kardani M, Sloan S. On the application of the maximum entropy meshfree method for elastoplastic geotechnical analysis. *Computers and Geotechnics*. 2017;84(68-77).
- [155] Ullah Z, Coombs W, Augarde C. An adaptive finite element/meshless coupled method based on local maximum entropy shape functions for linear and nonlinear problems. *Computer methods in applied mechanics and engineering*. 2013;267(111-32).
- [156] Zhu H, Miao Y, Cai Y. Meshless natural neighbour method and its application in elasto-plastic problems. *Computational Methods: Springer*, 2006. p. 1465-75.
- [157] Obermayr M, Dressler K, Vrettos C, Eberhard P. A bonded-particle model for cemented sand. *Computers and Geotechnics*. 2013;49(299-313).
- [158] Schenkengel K-U, Vrettos C. „Modelling of liquefaction-induced lateral spreading using the Lattice Boltzmann Method “. 5th International Conference on Earthquake Geotechnical Engineering2011.

- [159] Wu C-T, Chen J-S, Chi L, Huck F. Lagrangian meshfree formulation for analysis of geotechnical materials. *Journal of engineering mechanics*. 2001;127(5):440-9.
- [160] Terzaghi K. *Erdbaumechanik auf bodenphysikalischer Grundlage*. 1925.
- [161] Biot MA. General theory of three-dimensional consolidation. *Journal of applied physics*. 1941;12(2):155-64.
- [162] Ghaboussi J, Wilson EL. Flow of compressible fluid in porous elastic media. *International Journal for Numerical Methods in Engineering*. 1973;5(3):419-42.
- [163] Zienkiewicz O. Soils and other saturated media under transient, dynamic conditions; General formulation and the validity of various simplifying assumptions. *Soil mechanics-transient and cyclic loads*. 1982:1-16.
- [164] Zienkiewicz O. Basic formulation of static and dynamic behaviour of soil and other porous media. *Numerical methods in geomechanics*. 1982;92(39-55).
- [165] Zienkiewicz O, Xie Y, Schrefler B, Ledesma A, Bicanic N. Static and dynamic behaviour of soils: a rational approach to quantitative solutions. II. Semi-saturated problems. *Proceedings of the Royal Society of London A: Mathematical, Physical and Engineering Sciences: The Royal Society*, 1990. p. 311-21.
- [166] Gawin D, Schrefler BA, Galindo M. Thermo-hydro-mechanical analysis of partially saturated porous materials. *Engineering Computations*. 1996;13(7):113-43.
- [167] Brezzi F, Bathe K-J. A discourse on the stability conditions for mixed finite element formulations. *Computer methods in applied mechanics and engineering*. 1990;82(1-3):27-57.
- [168] Girault V, Raviart P-A. *Finite element methods for Navier-Stokes equations: theory and algorithms*: Springer Science & Business Media, 2012.
- [169] Jha B, Juanes R. A locally conservative finite element framework for the simulation of coupled flow and reservoir geomechanics. *Acta Geotechnica*. 2007;2(3):139-53.
- [170] Burman E, Hansbo P. A unified stabilized method for Stokes' and Darcy's equations. *Journal of Computational and Applied Mathematics*. 2007;198(1):35-51.
- [171] Behr MA, Franca LP, Tezduyar TE. Stabilized finite element methods for the velocity-pressure-stress formulation of incompressible flows. *Computer Methods in Applied Mechanics and Engineering*. 1993;104(1):31-48.
- [172] Douglas J, Wang JP. An absolutely stabilized finite element method for the Stokes problem. *Mathematics of computation*. 1989;52(186):495-508.
- [173] Franca LP, Frey SL, Hughes TJ. Stabilized finite element methods: I. Application to the advective-diffusive model. *Computer Methods in Applied Mechanics and Engineering*. 1992;95(2):253-76.
- [174] Becker R, Braack M. A finite element pressure gradient stabilization¶ for the Stokes equations based on local projections. *Calcolo*. 2001;38(4):173-99.
- [175] Codina R, Blasco J. Analysis of a pressure-stabilized finite element approximation of the stationary Navier-Stokes equations. *Numerische Mathematik*. 2000;87(1):59-81.
- [176] Kechkar N, Silvester D. Analysis of locally stabilized mixed finite element methods for the Stokes problem. *Mathematics of Computation*. 1992;58(197):1-10.
- [177] Bochev PB, Dohrmann CR. A computational study of stabilized, low-order C^0 finite element approximations of Darcy equations. *Computational Mechanics*. 2006;38(4):323-33.
- [178] Burman E. Pressure projection stabilizations for Galerkin approximations of Stokes' and Darcy's problem. *Numerical Methods for Partial Differential Equations*. 2008;24(1):127-43.

- [179] Burman E, Hansbo P. Stabilized Crouzeix-Raviart element for the Darcy-Stokes problem. *Numerical Methods for Partial Differential Equations*. 2005;21(5):986-97.
- [180] Franca LP, Harder C, Valentin F. On a residual local projection method for the Darcy equation. *Comptes Rendus Mathematique*. 2009;347(17-18):1105-10.
- [181] Masud A, Hughes TJ. A stabilized mixed finite element method for Darcy flow. *Computer methods in applied mechanics and engineering*. 2002;191(39):4341-70.
- [182] Chorin AJ. A numerical method for solving incompressible viscous flow problems. *Journal of computational physics*. 1997;135(2):118-25.
- [183] Salomoni V, Schrefler B. A CBS-type stabilizing algorithm for the consolidation of saturated porous media. *International journal for numerical methods in engineering*. 2005;63(4):502-27.
- [184] Blanc T, Pastor M. A stabilized smoothed particle hydrodynamics, Taylor-Galerkin algorithm for soil dynamics problems. *International Journal for Numerical and Analytical Methods in Geomechanics*. 2013;37(1):1-30.
- [185] Oñate E. Derivation of stabilized equations for numerical solution of advective-diffusive transport and fluid flow problems. *Computer methods in applied mechanics and engineering*. 1998;151(1-2):233-65.
- [186] Onate E. A stabilized finite element method for incompressible viscous flows using a finite increment calculus formulation. *Computer methods in applied mechanics and engineering*. 2000;182(3):355-70.
- [187] Onate E, Taylor RL, Zienkiewicz OC, Rojek J. A residual correction method based on finite calculus. *Engineering Computations*. 2003;20(5/6):629-58.
- [188] Onate E, Rojek J, Taylor RL, Zienkiewicz OC. Finite calculus formulation for incompressible solids using linear triangles and tetrahedra. *International Journal for Numerical Methods in Engineering*. 2004;59(11):1473-500.
- [189] Oñate E, Idelsohn SR, Felippa CA. Consistent pressure Laplacian stabilization for incompressible continua via higher-order finite calculus. *International Journal for Numerical Methods in Engineering*. 2011;87(1-5):171-95.
- [190] Oñate E, Franci A, Carbonell JM. Lagrangian formulation for finite element analysis of quasi-incompressible fluids with reduced mass losses. *International Journal for Numerical Methods in Fluids*. 2014;74(10):699-731.
- [191] de-Pouplana I, Oñate E. A FIC-based stabilized mixed finite element method with equal order interpolation for solid-pore fluid interaction problems. *International Journal for Numerical and Analytical Methods in Geomechanics*. 2017;41(1):110-34.
- [192] Bochev P, Gunzburger M. An absolutely stable pressure-Poisson stabilized finite element method for the Stokes equations. *SIAM Journal on Numerical Analysis*. 2004;42(3):1189-207.
- [193] Truty A. A Galerkin/least-squares finite element formulation for consolidation. *International Journal for Numerical Methods in Engineering*. 2001;52(8):763-86.
- [194] Shibata T, Murakami A. A stabilization procedure for soil-water coupled problems using the element-free Galerkin method. *Computers and Geotechnics*. 2011;38(5):585-97.
- [195] Aguilar G, Gaspar F, Lisbona F, Rodrigo C. Numerical stabilization of Biot's consolidation model by a perturbation on the flow equation. *International journal for numerical methods in engineering*. 2008;75(11):1282-300.
- [196] Bochev PB, Dohrmann CR, Gunzburger MD. Stabilization of low-order mixed finite elements for the Stokes equations. *SIAM Journal on Numerical Analysis*. 2006;44(1):82-101.
- [197] Silvester D. Optimal low order finite element methods for incompressible flow. *Computer methods in applied mechanics and engineering*. 1994;111(3-4):357-68.

- [198] Blasco J, Codina R. Space and time error estimates for a first order, pressure stabilized finite element method for the incompressible Navier–Stokes equations. *Applied Numerical Mathematics*. 2001;38(4):475-97.
- [199] Codina R, Blasco J. Stabilized finite element method for the transient Navier–Stokes equations based on a pressure gradient projection. *Computer Methods in Applied Mechanics and Engineering*. 2000;182(3):277-300.
- [200] Dohrmann CR, Bochev PB. A stabilized finite element method for the Stokes problem based on polynomial pressure projections. *International Journal for Numerical Methods in Fluids*. 2004;46(2):183-201.
- [201] Silvester DJ, Kechkar N. Stabilised bilinear-constant velocity-pressure finite elements for the conjugate gradient solution of the Stokes problem. *Computer Methods in Applied Mechanics and Engineering*. 1990;79(1):71-86.
- [202] Choo J, Borja RI. Stabilized mixed finite elements for deformable porous media with double porosity. *Computer Methods in Applied Mechanics and Engineering*. 2015;293(131-54).
- [203] Liu F, Gordon P, Meier H, Valiveti D. A stabilized extended finite element framework for hydraulic fracturing simulations. *International Journal for Numerical and Analytical Methods in Geomechanics*. 2017;41(5):654-81.
- [204] Wei H, Chen J-S, Hillman M. A stabilized nodally integrated meshfree formulation for fully coupled hydro-mechanical analysis of fluid-saturated porous media. *Computers & Fluids*. 2016;141(105-15).
- [205] Nakshatrala K, Masud A, Hjelmstad K. On finite element formulations for nearly incompressible linear elasticity. *Computational Mechanics*. 2008;41(4):547-61.
- [206] Nguyen-Xuan H, Liu G. An edge-based smoothed finite element method softened with a bubble function (bES-FEM) for solid mechanics problems. *Computers & Structures*. 2013;128(14-30).
- [207] Wu C, Hu W, Liu G. Bubble-enhanced smoothed finite element formulation: a variational multi-scale approach for volume-constrained problems in two-dimensional linear elasticity. *International Journal for Numerical Methods in Engineering*. 2014;100(5):374-98.
- [208] Ong TH, Heaney CE, Lee C-K, Liu G, Nguyen-Xuan H. On stability, convergence and accuracy of bES-FEM and bFS-FEM for nearly incompressible elasticity. *Computer Methods in Applied Mechanics and Engineering*. 2015;285(315-45).
- [209] Ng K, Small J. Behavior of joints and interfaces subjected to water pressure. *Computers and Geotechnics*. 1997;20(1):71-93.
- [210] Noorishad J, Ayatollahi M, Witherspoon P. A finite-element method for coupled stress and fluid flow analysis in fractured rock masses. *International Journal of Rock Mechanics and Mining Sciences & Geomechanics Abstracts: Elsevier*, 1982. p. 185-93.
- [211] Segura J, Carol I. On zero-thickness interface elements for diffusion problems. *International journal for numerical and analytical methods in geomechanics*. 2004;28(9):947-62.
- [212] Segura JM, Carol I. Coupled HM analysis using zero-thickness interface elements with double nodes. Part I: Theoretical model. *International journal for numerical and analytical methods in geomechanics*. 2008;32(18):2083-101.
- [213] Segura J, Carol I. Coupled HM analysis using zero-thickness interface elements with double nodes—Part II: Verification and application. *International Journal for Numerical and Analytical Methods in Geomechanics*. 2008;32(18):2103-23.
- [214] Guiducci C, Pellegrino A, Radu J-P, Collin F, Charlier R. Numerical modeling of hydro-mechanical fracture behavior. *Numerical models in Geomechanics*. 2002:293-9.

- [215] Centeno Lobão M, Eve R, Owen D, de Souza Neto EA. Modelling of hydro-fracture flow in porous media. *Engineering Computations*. 2010;27(1):129-54.
- [216] Carrier B, Granet S. Numerical modeling of hydraulic fracture problem in permeable medium using cohesive zone model. *Engineering fracture mechanics*. 2012;79(3):12-28.
- [217] Watanabe N, Wang W, Taron J, Görke U, Kolditz O. Lower-dimensional interface elements with local enrichment: application to coupled hydro-mechanical problems in discretely fractured porous media. *International Journal for Numerical Methods in Engineering*. 2012;90(8):1010-34.
- [218] Leong E, Randolph M. A model for rock interfacial behaviour. *Rock mechanics and rock engineering*. 1992;25(3):187-206.
- [219] Van den Berg P. Analysis of soil penetration: TU Delft, Delft University of Technology, 1994.
- [220] Liyanapathirana D, Deeks A, Randolph M. Numerical modelling of large deformations associated with driving of open-ended piles. *International Journal for Numerical and Analytical Methods in Geomechanics*. 2000;24(14):1079-101.
- [221] Hughes TJ, Taylor RL, Sackman JL, Curnier A, Kanoknukulchai W. A finite element method for a class of contact-impact problems. *Computer methods in applied mechanics and engineering*. 1976;8(3):249-76.
- [222] Katona MG. A simple contact–friction interface element with applications to buried culverts. *International Journal for Numerical and Analytical Methods in Geomechanics*. 1983;7(3):371-84.
- [223] Sheng D, Sun D-A, Matsuoka H. Cantilever sheet-pile wall modelled by frictional contact. *Soils and foundations*. 2006;46(1):29-37.
- [224] Sheng D, Wriggers P, Sloan SW. Improved numerical algorithms for frictional contact in pile penetration analysis. *Computers and Geotechnics*. 2006;33(6-7):341-54.
- [225] Laursen TA. Computational contact and impact mechanics: fundamentals of modeling interfacial phenomena in nonlinear finite element analysis: Springer Science & Business Media, 2013.
- [226] Simo JC, Wriggers P, Taylor RL. A perturbed Lagrangian formulation for the finite element solution of contact problems. *Computer methods in applied mechanics and engineering*. 1985;50(2):163-80.
- [227] Papadopoulos P, Taylor RL. A mixed formulation for the finite element solution of contact problems. *Computer Methods in Applied Mechanics and Engineering*. 1992;94(3):373-89.
- [228] Mabsout ME, Reese LC, Tassoulas JL. Study of pile driving by finite-element method. *Journal of geotechnical engineering*. 1995;121(7):535-43.
- [229] Belgacem FB, Hild P, Laborde P. The mortar finite element method for contact problems. *Mathematical and Computer Modelling*. 1998;28(4-8):263-71.
- [230] Ben Belgacem F. Numerical simulation of some variational inequalities arisen from unilateral contact problems by the finite element methods. *SIAM Journal on Numerical Analysis*. 2000;37(4):1198-216.
- [231] Hild P. Numerical implementation of two nonconforming finite element methods for unilateral contact. *Computer Methods in Applied Mechanics and Engineering*. 2000;184(1):99-123.
- [232] McDevitt T, Laursen T. A mortar-finite element formulation for frictional contact problems. *International Journal for Numerical Methods in Engineering*. 2000;48(10):1525-47.
- [233] Sabetamal H, Nazem M, Sloan SW, Carter JP. Frictionless contact formulation for dynamic analysis of nonlinear saturated porous media based on the mortar method.

- International Journal for Numerical and Analytical Methods in Geomechanics. 2016;40(1):25-61.
- [234] Sabetamal H, Nazem M, Carter J. Numerical analysis of torpedo anchors. Proceedings of the Third International Symposium on Computational Geomechanics: ComGeo III, Krakow, Poland 2013.
- [235] Fischer KA, Sheng D, Abbo AJ. Modeling of pile installation using contact mechanics and quadratic elements. Computers and Geotechnics. 2007;34(6):449-61.
- [236] Khishvand M, Nazem M, Sloan SW, Carter JP. Application of the third medium method for frictionless contact problems in geomechanics. Computers and Geotechnics. 2017;85(117-25).
- [237] Huang W, Sheng D, Sloan S, Yu H. Finite element analysis of cone penetration in cohesionless soil. Computers and Geotechnics. 2004;31(7):517-28.
- [238] Sheng D, Eigenbrod KD, Wriggers P. Finite element analysis of pile installation using large-slip frictional contact. Computers and Geotechnics. 2005;32(1):17-26.
- [239] Sheng D, Yamamoto H, Wriggers P. Finite element analysis of enlarged end piles using frictional contact. Soils and Foundations. 2008;48(1):1-14.
- [240] Simo JC, Laursen T. An augmented Lagrangian treatment of contact problems involving friction. Computers & Structures. 1992;42(1):97-116.
- [241] Béchet É, Moës N, Wohlmuth B. A stable Lagrange multiplier space for stiff interface conditions within the extended finite element method. International Journal for Numerical Methods in Engineering. 2009;78(8):931-54.
- [242] Dolbow J, Harari I. An efficient finite element method for embedded interface problems. International journal for numerical methods in engineering. 2009;78(2):229-52.
- [243] Ji H, Dolbow J. On strategies for enforcing interfacial constraints and evaluating jump conditions with the extended finite element method. International Journal for Numerical Methods in Engineering. 2004;61(14):2508-35.
- [244] Perić D, Owen D. Computational model for 3-D contact problems with friction based on the penalty method. International journal for numerical methods in engineering. 1992;35(6):1289-309.
- [245] Simoni L, Secchi S. Cohesive fracture mechanics for a multi-phase porous medium. Engineering Computations. 2003;20(5/6):675-98.
- [246] Schrefler BA, Secchi S, Simoni L. On adaptive refinement techniques in multi-field problems including cohesive fracture. Computer methods in applied mechanics and engineering. 2006;195(4-6):444-61.
- [247] Secchi S, Simoni L, A Schrefler B. Mesh adaptation and transfer schemes for discrete fracture propagation in porous materials. International journal for numerical and analytical methods in geomechanics. 2007;31(2):331-45.
- [248] Secchi S, Schrefler B. A method for 3-D hydraulic fracturing simulation. International journal of fracture. 2012;178(1-2):245-58.
- [249] Belytschko T, Black T. Elastic crack growth in finite elements with minimal remeshing. International journal for numerical methods in engineering. 1999;45(5):601-20.
- [250] Dolbow J, Belytschko T. A finite element method for crack growth without remeshing. Int J Numer Meth Engng. 1999;46(1):131-50.
- [251] Sukumar N, Moës N, Moran B, Belytschko T. Extended finite element method for three-dimensional crack modelling. International journal for numerical methods in engineering. 2000;48(11):1549-70.

- [252] Moës N, Gravouil A, Belytschko T. Non-planar 3D crack growth by the extended finite element and level sets—Part I: Mechanical model. *International Journal for Numerical Methods in Engineering*. 2002;53(11):2549-68.
- [253] Belytschko T, Moës N, Usui S, Parimi C. Arbitrary discontinuities in finite elements. *International Journal for Numerical Methods in Engineering*. 2001;50(4):993-1013.
- [254] Daux C, Moës N, Dolbow J, Sukumar N, Belytschko T. Arbitrary branched and intersecting cracks with the extended finite element method. *International journal for numerical methods in engineering*. 2000;48(12):1741-60.
- [255] Sukumar N, Chopp DL, Moës N, Belytschko T. Modeling holes and inclusions by level sets in the extended finite-element method. *Computer methods in applied mechanics and engineering*. 2001;190(46-47):6183-200.
- [256] Moës N, Cloirec M, Cartraud P, Remacle J-F. A computational approach to handle complex microstructure geometries. *Computer methods in applied mechanics and engineering*. 2003;192(28-30):3163-77.
- [257] Khoei A, Nikbakht M. An enriched finite element algorithm for numerical computation of contact friction problems. *International Journal of Mechanical Sciences*. 2007;49(2):183-99.
- [258] Liu F, Borja RI. A contact algorithm for frictional crack propagation with the extended finite element method. *International Journal for Numerical methods in engineering*. 2008;76(10):1489-512.
- [259] Nistor I, Guiton M, Massin P, Moës N, Geniaut S. An X-FEM approach for large sliding contact along discontinuities. *International Journal for Numerical Methods in Engineering*. 2009;78(12):1407-35.
- [260] Khoei A, Mousavi ST. Modeling of large deformation—Large sliding contact via the penalty X-FEM technique. *Computational Materials Science*. 2010;48(3):471-80.
- [261] Hirmand M, Vahab M, Khoei A. An augmented Lagrangian contact formulation for frictional discontinuities with the extended finite element method. *Finite Elements in Analysis and Design*. 2015;107(28-43).
- [262] De Borst R, Réthoré J, Abellan M-A. A numerical approach for arbitrary cracks in a fluid-saturated medium. *Archive of Applied Mechanics*. 2006;75(10-12):595-606.
- [263] Rethore J, De Borst R, Abellan MA. A discrete model for the dynamic propagation of shear bands in a fluid-saturated medium. *International journal for numerical and analytical methods in geomechanics*. 2007;31(2):347-70.
- [264] Réthoré J, Borst Rd, Abellan MA. A two-scale approach for fluid flow in fractured porous media. *International Journal for Numerical Methods in Engineering*. 2007;71(7):780-800.
- [265] Réthoré J, De Borst R, Abellan M-A. A two-scale model for fluid flow in an unsaturated porous medium with cohesive cracks. *Computational Mechanics*. 2008;42(2):227-38.
- [266] Mohammadnejad T, Khoei A. An extended finite element method for hydraulic fracture propagation in deformable porous media with the cohesive crack model. *Finite Elements in Analysis and Design*. 2013;73(77-95).
- [267] Mohammadnejad T, Khoei A. An extended finite element method for fluid flow in partially saturated porous media with weak discontinuities; the convergence analysis of local enrichment strategies. *Computational Mechanics*. 2013;51(3):327-45.
- [268] Mohammadnejad T, Khoei A. Hydro-mechanical modeling of cohesive crack propagation in multiphase porous media using the extended finite element method. *International Journal for Numerical and Analytical Methods in Geomechanics*. 2013;37(10):1247-79.

- [269] Prevost JH, Sukumar N. Faults simulations for three-dimensional reservoir-geomechanical models with the extended finite element method. *Journal of the Mechanics and Physics of Solids*. 2016;86(1-18).
- [270] Lecampion B. An extended finite element method for hydraulic fracture problems. *International Journal for Numerical Methods in Biomedical Engineering*. 2009;25(2):121-33.
- [271] Gordeliy E, Peirce A. Coupling schemes for modeling hydraulic fracture propagation using the XFEM. *Computer Methods in Applied Mechanics and Engineering*. 2013;253(305-22).
- [272] Gordeliy E, Peirce A. Implicit level set schemes for modeling hydraulic fractures using the XFEM. *Computer Methods in Applied Mechanics and Engineering*. 2013;266(125-43).
- [273] Gordeliy E, Peirce A. Enrichment strategies and convergence properties of the XFEM for hydraulic fracture problems. *Computer Methods in Applied Mechanics and Engineering*. 2015;283(474-502).
- [274] Gupta P, Duarte C. Simulation of non-planar three-dimensional hydraulic fracture propagation. *International Journal for Numerical and Analytical Methods in Geomechanics*. 2014;38(13):1397-430.
- [275] Remij E, Remmers J, Huyghe J, Smeulders D. The enhanced local pressure model for the accurate analysis of fluid pressure driven fracture in porous materials. *Computer Methods in Applied Mechanics and Engineering*. 2015;286(293-312).
- [276] Ren Q, Dong Y, Yu T. Numerical modeling of concrete hydraulic fracturing with extended finite element method. *Science in China Series E: Technological Sciences*. 2009;52(3):559-65.
- [277] Gracie R, Craig JR. Modelling well leakage in multilayer aquifer systems using the extended finite element method. *Finite Elements in Analysis and Design*. 2010;46(6):504-13.
- [278] Dahi-Taleghani A, Olson JE. Numerical modeling of multistranded-hydraulic-fracture propagation: Accounting for the interaction between induced and natural fractures. *SPE journal*. 2011;16(03):575-81.
- [279] Xiao Q-Z, Karihaloo BL. Improving the accuracy of XFEM crack tip fields using higher order quadrature and statically admissible stress recovery. *International Journal for Numerical Methods in Engineering*. 2006;66(9):1378-410.
- [280] Bordas S, Duflot M, Le P. A simple error estimator for extended finite elements. *International Journal for Numerical Methods in Biomedical Engineering*. 2008;24(11):961-71.
- [281] Aimene YE, Nairn JA. Modeling multiple hydraulic fractures interacting with natural fractures using the material point method. *SPE/EAGE European Unconventional Resources Conference and Exhibition 2014*.
- [282] Jenkins C, Ouenes A, Zellou A, Wingard J. Quantifying and predicting naturally fractured reservoir behavior with continuous fracture models. *AAPG bulletin*. 2009;93(11):1597-608.
- [283] Das R, Zhang Y, Schaub P, Cleary P. Modelling rock fracturing caused by magma intrusion using the smoothed particle hydrodynamics method. *Computational Geosciences*. 2014;18(6):927-47.
- [284] Oliaei MN, Pak A, Soga K. A coupled hydro-mechanical analysis for prediction of hydraulic fracture propagation in saturated porous media using EFG mesh-less method. *Computers and Geotechnics*. 2014;55(254-66).
- [285] Samimi S, Pak A. A fully coupled element-free Galerkin model for hydro-mechanical analysis of advancement of fluid-driven fractures in porous media.

- International Journal for Numerical and Analytical Methods in Geomechanics. 2016;40(16):2178-206.
- [286] Dolbow J, Belytschko T. Volumetric locking in the element free Galerkin method. International Journal for numerical methods in engineering. 1999;46(6):925-42.
- [287] Murakami A, Setsuyasu T, Arimoto S-i. Mesh-free method for soil-water coupled problem within finite strain and its numerical validity. Soils and foundations. 2005;45(2):145-54.
- [288] Soares Jr D, Sladek V, Sladek J, Zmindak M, Medvecky S. Porous media analysis by modified MLPG formulations. Computers Materials and Continua. 2012;27(2):101.
- [289] Soares Jr D, Schoenewald A, ESTORFF OV. An efficient smoothed point interpolation method for dynamic analyses. International Journal of Computational Methods. 2013;10(01):1340007.
- [290] Wang J, Liu G. On the optimal shape parameters of radial basis functions used for 2-D meshless methods. Computer methods in applied mechanics and engineering. 2002;191(23):2611-30.
- [291] Liu G. A generalized gradient smoothing technique and the smoothed bilinear form for Galerkin formulation of a wide class of computational methods. International Journal of Computational Methods. 2008;5(02):199-236.
- [292] Khalili N, Khabbaz M, Valliappan S. An effective stress based numerical model for hydro-mechanical analysis in unsaturated porous media. Computational mechanics. 2000;26(2):174-84.
- [293] Schiffman RL, Chen A, Jordan JC. An analysis of consolidation theories. Journal of Soil Mechanics & Foundations Div. 1969.
- [294] Selvadurai A, Carnaffan P. A transient pressure pulse method for the measurement of permeability of a cement grout. Canadian Journal of Civil Engineering. 1997;24(3):489-502.
- [295] Selvadurai A. Influence of residual hydraulic gradients on decay curves for one-dimensional hydraulic pulse tests. Geophysical Journal International. 2009;177(3):1357-65.
- [296] Tootoonchi A, Khoshghalb A, Liu G, Khalili N. A cell-based smoothed point interpolation method for flow-deformation analysis of saturated porous media. Computers and Geotechnics. 2016;75(159-73).
- [297] Cryer C. A comparison of the three-dimensional consolidation theories of Biot and Terzaghi. The Quarterly Journal of Mechanics and Applied Mathematics. 1963;16(4):401-12.
- [298] Mandel J. Consolidation des sols (étude mathématique)*. Geotechnique. 1953;3(7):287-99.
- [299] Gibson R, Schiffman R, Pu S. Plane strain and axially symmetric consolidation of a clay layer on a smooth impervious base. The Quarterly Journal of Mechanics and Applied Mathematics. 1970;23(4):505-20.
- [300] De Leeuw E. The theory of three-dimensional consolidation applied to cylindrical bodies. Proc 6th Int Conf Soil Mech and Found Engng 1965. p. 287-90.
- [301] Verruijt A. Theory and problems of poroelasticity. Delft University of Technology. 2013.
- [302] Verruijt A. Elastic storage of aquifers. Flow through porous media. 1969:331-76.
- [303] Rodrigues JD. The Noordbergum effect and characterization of aquitards at the Rio Maior mining project. Groundwater. 1983;21(2):200-7.
- [304] Kim J-M, Parizek RR. Numerical simulation of the Noordbergum effect resulting from groundwater pumping in a layered aquifer system. Journal of Hydrology. 1997;202(1):231-43.

- [305] Chen L, Rabczuk T, Bordas SPA, Liu G, Zeng K, Kerfriden P. Extended finite element method with edge-based strain smoothing (ESm-XFEM) for linear elastic crack growth. *Computer Methods in Applied Mechanics and Engineering*. 2012;209(250-65).
- [306] Brezzi F. Stability of saddle-points in finite dimensions. *Frontiers in Numerical Analysis*. 2003:17-61.
- [307] Bochev P, Lehoucq R. Regularization and stabilization of discrete saddle-point variational problems. *Electronic Transactions on Numerical Analysis*. 2006;22(97-113).
- [308] Hughes TJ, Franca LP. A new finite element formulation for computational fluid dynamics: VII. The Stokes problem with various well-posed boundary conditions: symmetric formulations that converge for all velocity/pressure spaces. *Computer Methods in Applied Mechanics and Engineering*. 1987;65(1):85-96.
- [309] Shakib F, Hughes TJ, Johan Z. A new finite element formulation for computational fluid dynamics: X. The compressible Euler and Navier-Stokes equations. *Computer Methods in Applied Mechanics and Engineering*. 1991;89(1-3):141-219.
- [310] Tezduyar TE, Osawa Y. Finite element stabilization parameters computed from element matrices and vectors. *Computer Methods in Applied Mechanics and Engineering*. 2000;190(3-4):411-30.
- [311] Bochev PB, Gunzburger MD, Lehoucq RB. On stabilized finite element methods for the Stokes problem in the small time step limit. *International Journal for Numerical Methods in Fluids*. 2007;53(4):573-97.
- [312] Bochev PB, Gunzburger MD, Shadid JN. On inf-sup stabilized finite element methods for transient problems. *Computer Methods in Applied Mechanics and Engineering*. 2004;193(15-16):1471-89.
- [313] Terzaghi K. *Theoretical soil mechanics*: Chapman And Hali, Limited John Wiler And Sons, Inc; New York, 1944.
- [314] Nagtegaal JC, Parks DM, Rice J. On numerically accurate finite element solutions in the fully plastic range. *Computer methods in applied mechanics and engineering*. 1974;4(2):153-77.
- [315] Crisfield MA, Remmers JJ, Verhoosel CV. *Nonlinear finite element analysis of solids and structures*: John Wiley & Sons, 2012.
- [316] Vermeer PA, De Borst R. Non-associated plasticity for soils, concrete and rock. *HERON*, 29 (3), 1984. 1984.
- [317] Hughes TJ. Generalization of selective integration procedures to anisotropic and nonlinear media. *International Journal for Numerical Methods in Engineering*. 1980;15(9):1413-8.
- [318] Simo JC, Rifai M. A class of mixed assumed strain methods and the method of incompatible modes. *International journal for numerical methods in engineering*. 1990;29(8):1595-638.
- [319] Prandtl L. Über die härte plastischer körper. *Nachrichten von der Gesellschaft der Wissenschaften zu Göttingen, Mathematisch-Physikalische Klasse*. 1920;1920(74-85).
- [320] D'Angelo C, Scotti A. A mixed finite element method for Darcy flow in fractured porous media with non-matching grids*. *ESAIM: Mathematical Modelling and Numerical Analysis*. 2012;46(2):465-89.
- [321] Formaggia L, Fumagalli A, Scotti A, Ruffo P. A reduced model for Darcy's problem in networks of fractures*. *ESAIM: Mathematical Modelling and Numerical Analysis*. 2014;48(4):1089-116.
- [322] Khoei AR. *Extended finite element method: theory and applications*: John Wiley & Sons, 2014.

- [323] Dolbow J, Moës N, Belytschko T. An extended finite element method for modeling crack growth with frictional contact. *Computer Methods in Applied Mechanics and Engineering*. 2001;190(51):6825-46.
- [324] Moës N, Dolbow J, Belytschko T. A finite element method for crack growth without remeshing. *International journal for numerical methods in engineering*. 1999;46(1):131-50.
- [325] Bordas S, Natarajan S, Kerfriden P, Augarde CE, Mahapatra DR, Rabczuk T, et al. On the performance of strain smoothing for quadratic and enriched finite element approximations (XFEM/GFEM/PUFEM). *International Journal for Numerical Methods in Engineering*. 2011;86(4-5):637-66.
- [326] Bordas SP, Rabczuk T, Hung N-X, Nguyen VP, Natarajan S, Bog T, et al. Strain smoothing in FEM and XFEM. *Computers & structures*. 2010;88(23-24):1419-43.
- [327] Khoei A, Vahab M, Hirmand M. Modeling the interaction between fluid-driven fracture and natural fault using an enriched-FEM technique. *International Journal of Fracture*. 2016;197(1):1-24.
- [328] Mohammadnejad T, Andrade J. Numerical modeling of hydraulic fracture propagation, closure and reopening using XFEM with application to in-situ stress estimation. *International Journal for Numerical and Analytical Methods in Geomechanics*. 2016;40(15):2033-60.
- [329] Curnier A. A theory of friction. *International Journal of Solids and Structures*. 1984;20(7):637-47.
- [330] Annavarapu C, Hautefeuille M, Dolbow JE. A Nitsche stabilized finite element method for frictional sliding on embedded interfaces. Part I: single interface. *Computer Methods in Applied Mechanics and Engineering*. 2014;268(417-36).
- [331] Khoei A, Gharehbaghi S, Tabarraie A, Riahi A. Error estimation, adaptivity and data transfer in enriched plasticity continua to analysis of shear band localization. *Applied Mathematical Modelling*. 2007;31(6):983-1000.